

POLITECNICO DI MILANO

Scuola di Ingegneria Industriale e dell'Informazione
Master's degree in Automation and Control Engineering
Dipartimento di Elettronica, Informazione e Bioingegneria



MODEL IDENTIFICATION AND CONTROL OF A WHEELED INVERTED PENDULUM VEHICLE DESIGNED FOR URBAN PACKAGE DELIVERY

Supervisor: Prof. Sergio Savaresi

Assistant supervisors: Prof. Matteo Corno
Ing. Stefano Sabatini

Master's thesis of:

Filippo Parravicini Matr. 864517
Andrea Rivolta Matr: 853631

Academic Year 2016-2017

ABSTRACT.....	13
ABSTRACT.....	14
ESTRATTO.....	15
CHAPTER 1 - INTRODUCTION.....	20
1.1 STATE OF THE ART AND PERSONAL CONTRIBUTIONS	21
1.2 THESIS STRUCTURE.....	23
CHAPTER 2 - VEHICLE SETUP.....	26
2.1 INTRODUCTION	26
2.2 MECHANICAL COMPONENTS:.....	27
2.2.1 <i>The chassis</i>	27
2.2.2 <i>The hulls</i>	28
2.2.3 <i>The wheels</i>	28
2.3 CONTROL ARCHITECTURE: GENERAL SCHEME	30
2.4 HARDWARE COMPONENTS:	31
2.4.1 <i>The mainboard</i>	31
2.4.2 <i>The NVIDIA GPU</i>	32
2.4.3 <i>The joystick</i>	33
2.5 PROPRIOCEPTIVE SENSORS.....	34
2.5.1 <i>IMU</i>	34
2.5.2 <i>Encoder</i>	35
2.5.3 <i>Lidars</i>	38
2.5.4 <i>Cameras</i>	39
2.6 CONCLUSIONS.....	39
CHAPTER 3 - DYNAMICAL MODEL.....	41
3.1 INTRODUCTION	41
3.2 NOMINAL MODEL	41
3.3 INPUT-OUTPUT TRANSFER FUNCTION	53
3.3.1 <i>From torque to pitch: $Gt\theta s$</i>	54
3.3.2 <i>From torque to speed: $Gtss$</i>	56
3.4 CONCLUSIONS.....	59
CHAPTER 4 - EFFECTS OF LOAD AND SLOPES	61
4.1 INTRODUCTION	61
4.2 EFFECTS OF LOADS	61
4.3 EFFECTS OF SLOPES	64
4.4 CONCLUSIONS.....	66
CHAPTER 5 - IMU CALIBRATION	68
5.1 INTRODUCTION	68
5.2 ERROR MODEL	68
5.3 CALIBRATION PROCEDURE	71
5.4 COMPENSATION PROCEDURE	76
5.5 CONCLUSIONS.....	81

CHAPTER 6 - STATE OBSERVERS	83
6.1 INTRODUCTION	83
6.2 PITCH ESTIMATION	83
6.3 PITCH RATE ESTIMATION.....	92
6.4 SPEED ESTIMATION.....	92
6.4.1 <i>The overflow.....</i>	94
6.5 YAW RATE ESTIMATION	95
6.6 CONCLUSIONS.....	96
CHAPTER 7 - PARAMETERS IDENTIFICATION	98
7.1 INTRODUCTION	98
7.2 DISSIPATION EFFECTS: FRICTION MODEL	98
7.2.1 <i>Static Friction.....</i>	100
7.2.2 <i>Dynamic friction</i>	102
7.2.3 <i>Rolling Friction.....</i>	106
7.2.4 <i>Friiction model: Conclusions.....</i>	107
7.3 MECHANICAL PARAMETERS:	108
7.3.1 <i>Direct Measure.....</i>	108
7.3.2 <i>Mechanical Parameters: Indirect Measure</i>	108
7.3.3 <i>Mechanical Parameters: Model Fitting</i>	108
7.4 CONCLUSION	111
CHAPTER 8 - CONTROL STRUCTURE.....	115
8.1 INTRODUCTION	115
8.2 REFERENCE FILTERING BLOCK	116
8.3 REGULATOR BLOCK	117
8.4 REGULATOR PERFORMANCE INDEXES	117
8.4.1 <i>Pitch Limitation</i>	118
8.4.2 <i>Start and station keeping</i>	119
8.4.3 <i>Turn-on-the-spot capabilities</i>	120
8.4.4 <i>Unbalanced Load handling.....</i>	121
8.4.5 <i>Uphill roads handling</i>	122
8.5 CONCLUSIONS.....	126
CHAPTER 9 - REFERENCE FILTERING.....	128
9.1 INTRODUCTION	128
9.2 RATE LIMITER.....	128
9.3 LOW-PASS FILTERING	130
9.4 CONCLUSIONS.....	131
CHAPTER 10 - LQ CONTROLLER.....	133
10.1 INTRODUCTION	133
10.2 LQR THEORY	133
10.3 LQ IMPLEMENTATION	136
10.4 LQ TUNING	138
10.5 STATION KEEPING.....	142

10.6	SPEED TRACKING	145
10.7	SPEED TRACKING: SLOPES.....	148
10.8	UNBALANCED LOAD	151
10.9	TURN ON THE SPOT	155
10.10	CONCLUSION ON THE CHOICE OF LQR	157
10.11	ROBUSTNESS ANALYSIS	158
10.11.1	<i>Mass variation test:</i>	158
10.11.2	<i>C.O.G height variation test:</i>	161
10.11.3	<i>Moment of Inertia</i>	163
10.11.4	<i>Package load test</i>	164
10.12	FEEDFORWARD	167
10.13	CONCLUSIONS.....	170
CHAPTER 11 -	CASCADE CONTROL.....	172
11.1	INTRODUCTION	172
11.2	CASCADE CONTROL: THEORY	172
11.3	CASCADE: PITCH LOOP	174
11.4	CASCADE: SPEED LOOP	179
11.5	STATION KEEPING.....	181
11.6	SPEED TRACKING	182
11.7	SPEED TRACKING: SLOPES.....	185
11.8	UNBALANCED LOAD	187
11.9	PITCH SATURATION	188
11.10	CONCLUSIONS.....	190
CHAPTER 12 -	CONCLUSIONS AND FUTURE DEVELOPMENTS.....	192
12.1	CONCLUSIONS.....	192
12.2	MODEL IDENTIFICATION.....	192
12.3	DISTURBS MODELLING	193
12.4	CONTROLLER DESIGN, STANDARD TECHNIQUES	193
12.5	CONTROLLER DESIGN, INNOVATIVE TECHNIQUES	194
12.6	FUTURE DEVELOPMENTS	194
12.6.1	<i>Pitch Saturation</i>	194
12.6.2	<i>Feed forward compensation of sloped roads</i>	195
12.6.3	<i>Feed forward compensation of unbalanced loads</i>	196
12.6.4	<i>Scheduled controller</i>	196
BIBLIOGRAPHY	198	

FIGURE 1-1 YAPE	20
FIGURE 1-2 PITCH PROFILE TRACKING WITH PITCH SATURATION AT 8° - CASCADE CONTROL	22
FIGURE 2-1 YAPE'S STRUCTURE.....	26
FIGURE 2-2 CHASSIS	27
FIGURE 2-3 HULLS.....	28
FIGURE 2-4 WHEEL	28
FIGURE 2-5 EMBEDDED MOTOR EXPLODED VIEW.....	29
FIGURE 2-6 GENERAL ARCHITECTURE	30
FIGURE 2-7 MAINBOARD	31
FIGURE 2-8 NVIDIA JETSON TX1	32
FIGURE 2-9 JOYSTICK	33
FIGURE 2-10 IDEAL VS REAL MEASUREMENT CURVE OF THE IMU	35
FIGURE 2-11 GEAR BOX EXPLODED VIEW	35
FIGURE 2-12 SCHEMATIC VIEW OF THE ENCODER BASED ON HALL SENSORS	36
FIGURE 2-13 SCHEMATIC VIEW OF THE GEAR TRANSMISSION	36
FIGURE 2-14 OCCURRENCE OF THE OVERFLOW ON ONE OF THE ENCODERS	37
FIGURE 2-15 LEDDARVU8	38
FIGURE 2-16 LOGITECH C920 HD PRO.....	39
FIGURE 3-1 WORLD FRAME AND VEHICLE FRAME	41
FIGURE 3-2 GRAPHICAL REPRESENTATION OF CURVILINEAR COORDINATE s AND YAW ANGLE ψ	42
FIGURE 3-3 GRAPHICAL REPRESENTATION OF PITCH ANGLE θ	42
FIGURE 3-4 GRAPHIC REPRESENTATION OF THE RELATIONSHIP BETWEEN sr, sl, s, ψ	43
FIGURE 3-5 MEANING OF MODEL PARAMETERS.....	44
FIGURE 3-6 FORCES AND TORQUES ACTING ON THE SYSTEM.....	44
FIGURE 3-7 FORCES AND TORQUES ACTING ON THE RIGHT WHEEL.....	45
FIGURE 3-8 FORCES AND TORQUES ACTING ON THE CHASSIS	46
FIGURE 3-9 FORCES AND TORQUES RESPONSIBLE FOR YAW MOTION	50
FIGURE 3-10 FORCES AND TORQUES RESPONSIBLE FOR YAW MOTION - SIMPLIFIED MODEL	50
FIGURE 3-11 BLOCK SCHEME WITH DECOUPLED DYNAMICS	54
FIGURE 3-12 INVERSE ROOT LOCUS OF $Gt\theta(s)$	55
FIGURE 3-13 SCHEMATIC REPRESENTATION OF THE EQUIVALENCE $Gtss = Gt\theta s G\theta s(s)$	56
FIGURE 3-14 NON-MINIMUM PHASE BEHAVIOUR.....	58
FIGURE 4-1 MODELLING OF UNBALANCED LOADS	62
FIGURE 4-2 FORCES AND TORQUES ACTING ON THE VEHICLE WHILE TRAVELLING ON UPHILL ROAD	64
FIGURE 4-3 GRAVITATIONAL ACCELERATION DECOMPOSITION IN UPHILL ROADS.....	66
FIGURE 5-1 SCHEMATIC REPRESENTATION OF IMU DoF	68
FIGURE 5-2 SCHEMATIC REPRESENTATION OF MISALIGNMENT BETWEEN IMU FRAME AND VEHICLE FRAME.....	70
FIGURE 5-3 NON-CALIBRATED IMU DATA.....	72
FIGURE 5-4 FOUR POSITION REQUIRED FOR IMU CALIBRATION	73
FIGURE 5-5 (A) UNCALIBRATED ACCELEROMETERS READINGS (B) CALIBRATED READINGS.....	74
FIGURE 5-6 RESULTANT OF GRAVITY ACCELERATION MEASURED BEFORE AND AFTER CALIBRATION	74
FIGURE 5-7 X-AXIS GYROMETER MEASUREMENTS BEFORE AND AFTER CALIBRATION.....	75
FIGURE 5-8 COMPENSATION PROCEDURE: (A) THE VEHICLE IS TILTED ON ONE SIDE AND THEN (B) IT IS TILTED ALL THE WAY TO THE OTHER SIDE	76
FIGURE 5-9 GRAVITY VECTOR IN STEADY POSITIONS	77
FIGURE 5-10 SYMMETRY OF θv_1 AND θv_2 WRT PLANE $YvZv$	78

FIGURE 5-11 GRAPHICAL EXPLANATION OF COMPENSATION PROCEDURE	79
FIGURE 5-12 ACCELEROMETERS READINGS: CALIBRATED DATA.....	80
FIGURE 5-13 ACCELEROMETERS READINGS: FIRST ROTATION	80
FIGURE 5-14 ACCELEROMETERS READINGS: SECOND ROTATION.....	81
FIGURE 6-1 GRAPHICAL EXPLANATION OF PITCH ANGLE.....	83
FIGURE 6-2 SPLIT FREQUENCY METHOD: GENERAL SCHEME	84
FIGURE 6-3 EXAMPLE OF WORKING PRINCIPLE OF SFM	85
FIGURE 6-4 DECOMPOSITION OF GRAVITY ON ACCELEROMETERS WHILE THE VEHICLE IS TILTING	86
FIGURE 6-5 SFM APPLIED IN PITCH ESTIMATION.....	87
FIGURE 6-6 TRADE OFF IN FILTER BANDWIDTH CHOICE	88
FIGURE 6-7 SCHEMATIC REPRESENTATION OF MOUNTED LASER SENSOR	88
FIGURE 6-8 COMPARISON BETWEEN LINEAR AND NON-LINEAR SOLUTION FOR PITCH ESTIMATION	90
FIGURE 6-9 TEST-1 COMPARISON BETWEEN PITCH LASER AND PITCH OBSERVED.	91
FIGURE 6-10 TEST-2 COMPARISON BETWEEN PITCH LASER AND PITCH OBSERVED.	91
FIGURE 6-11 GRAPHICAL EXPLANATION OF KINEMATIC RELATION (6.23)	93
FIGURE 6-12 SPEED ESTIMATION BEFORE AND AFTER LP FILTERING.....	93
FIGURE 6-13 OVERFLOW MANAGEMENT	94
FIGURE 6-14 GRAPHICAL EXPLANATION OF KINEMATIC RELATION (6.25)	95
FIGURE 6-15 SFM FOR YAWRATE ESTIMATION	96
FIGURE 7-1 FRICTION MODEL	99
FIGURE 7-2 ACASUAL FILTERING OF WHEEL MOTOR ARMATURE CURRENT.....	100
FIGURE 7-3 FRICTION MODEL – STRIBECK EFFECT	100
FIGURE 7-4 SETUP FRICTION TESTS.	101
FIGURE 7-5 BREAKAWAY CURRENT MEASUREMENTS	101
FIGURE 7-6 SPEED REFERENCE FOR EACH WHEEL IN VISCOUS FRICTION TESTS.....	103
FIGURE 7-7 FRICTION MODEL FITTING – RIGHT WHEEL	103
FIGURE 7-8 FRICTION MODEL FITTING – LEFT WHEEL.....	104
FIGURE 7-9 FRICTION MODEL (VISCOUS - ROOT SQUARED) FITTING – LEFT WHEEL.....	105
FIGURE 7-10 FRICTION MODEL (VISCOUS - ROOT SQUARED) FITTING – RIGHT WHEEL	105
FIGURE 7-11 SIMULATED AND MEASURED LIMIT CYCLE COMPARISON	107
FIGURE 7-12 GENERAL SCHEME FOR PARAMETERS ESTIMATION IN OPEN LOOP PROCEDURE	109
FIGURE 7-13 GENERAL SCHEME ADOPTED FOR PARAMETERS ESTIMATION	109
FIGURE 7-14 EXAMPLE OF RMSE SENSITIVITY TO C.O.G. HEIGHT VARIATIONS	110
FIGURE 7-15 EXAMPLE OF RMSE SENSITIVITY TO MOMENT OF INERTIA VARIATIONS	110
FIGURE 7-16 REAL SYSTEM VERSUS SIMULATOR IN FOLLOWING A TRAPEZOIDAL SPEED PROFILE. SPEED ANALYSIS	111
FIGURE 7-17 REAL SYSTEM VERSUS SIMULATOR IN FOLLOWING A TRAPEZOIDAL SPEED PROFILE. PITCH ANALYSIS	112
FIGURE 7-18 REAL SYSTEM VERSUS SIMULATOR IN FOLLOWING A TRAPEZOIDAL SPEED PROFILE. TORQUE ANALYSIS	112
FIGURE 8-1 CONTROL STRUCTURE WITH HUMAN DRIVING.	115
FIGURE 8-2 CONTROL STRUCTURE WITH AUTONOMOUS DRIVING.....	115
FIGURE 8-3 CONTROL SYSTEM EXPANDED SCHEME.....	116
FIGURE 8-4 CASCADE CONTROL ARCHITECTURE	117
FIGURE 8-5 PITCH ANGLE LIMIT.....	118
FIGURE 8-6 START-UP PROCEDURE SCHEMATIZATION	119
FIGURE 8-7 TWO WHEEL – FOUR WHEEL VEHICLE TURNING COMPARISON	120
FIGURE 8-8 SCHEMATIC VIEW OF BALANCED AND UNBALANCED LOAD.....	121
FIGURE 8-9 ANGLE OFFSET INTRODUCED BY UNBALANCED LOAD IN PITCH BEHAVIOUR.....	121

FIGURE 8-10 FORCES ACTING ON THE VEHICLE AT CONSTANT SPEED ON UPHILL ROAD.....	124
FIGURE 8-11 RESIDUAL CLEARANCE ANGLE WRT MASS VARIATIONS.....	125
FIGURE 8-12 RESIDUAL CLEARANCE ANGLE WRT C.O.G. HEIGHT VARIATIONS.....	125
FIGURE 8-13 CLEARANCE ANGLE OF THE UPHILL ROAD USED DURING EXPERIMENTAL TESTS.....	126
FIGURE 9-1 ACTION OF RATE LIMITER ON SPEED PROFILES	130
FIGURE 9-2 LOW PASS FILTER ON SPEED REFERENCE	131
FIGURE 9-3 OVERALL SCHEME OF REFERENCE FILTERING	131
FIGURE 10-1 CONTROL SCHEME WITH LQ REGULATOR	136
FIGURE 10-2 SCHEMATIC REPRESENTATION OF LQR IMPLEMENTATION	138
FIGURE 10-3 SPEED MEASURED DURING STABILIZATION: KLQ02.....	142
FIGURE 10-4 PITCH MEASURED DURING STABILIZATION: KLQ02.....	143
FIGURE 10-5 SPEED PROFILE USED IN EXPERIMENTAL TESTS	145
FIGURE 10-6 SPEED AND PITCH IN SPEED TRACKING TEST – KLQ 01 AND KLQ 06	145
FIGURE 10-7 SPEED AND PITCH IN SPEED TRACKING TEST – KLQ 02 AND KLQ 07	146
FIGURE 10-8 SPEED AND PITCH IN SPEED TRACKING TEST – KLQ 03 AND KLQ 08	146
FIGURE 10-9 SPEED AND PITCH IN SPEED TRACKING TEST – KLQ 04 AND KLQ 09	146
FIGURE 10-10 SPEED AND PITCH IN SPEED TRACKING TEST – KLQ 05 AND KLQ 10	147
FIGURE 10-11 SLOPE DURING EXPERIMENTAL TESTS	148
FIGURE 10-12 SPEED AND PITCH IN SPEED TRACKING TEST ON UPHILL ROAD– KLQ 01 AND KLQ 06	149
FIGURE 10-13 SPEED AND PITCH IN SPEED TRACKING TEST ON UPHILL ROAD– KLQ 02	149
FIGURE 10-14 SPEED AND PITCH IN SPEED TRACKING TEST ON UPHILL ROAD– KLQ 03 AND KLQ 08	149
FIGURE 10-15 SPEED AND PITCH IN SPEED TRACKING TEST ON UPHILL ROAD– KLQ 04 AND KLQ 09	150
FIGURE 10-16 SPEED AND PITCH IN SPEED TRACKING TEST ON UPHILL ROAD– KLQ 05 AND KLQ 10	150
FIGURE 10-17 STABLE POSITION IN CASE OF UNBALANCED LOAD	152
FIGURE 10-18 DISPLACEMENTS DURING STABILIZATION TESTS - LQR	153
FIGURE 10-19 PITCH DURING STABILIZATION TESTS	153
FIGURE 10-20 YAWRATE IN YAWRATE PROFILE TRACKING TEST - KLQ 11 AND KLQ 13	155
FIGURE 10-21 YAWRATE IN YAWRATE PROFILE TRACKING TEST - KLQ 12 AND KLQ 14	155
FIGURE 10-22 SPEED IN YAWRATE PROFILE TRACKING TEST - KLQ 11,12,13,14	156
FIGURE 10-23 KLQ_BEST: (A) SPEED DURING STABILIZATION (B) SPEED PROFILE TRACKING	157
FIGURE 10-24 KLQ_BEST: (A) YAWRATE PROFILE TRACKING (B) SPEED	157
FIGURE 10-25 SENSITIVITY OF THE SPEED WRT MASS VARIATIONS.....	158
FIGURE 10-26 SENSITIVITY OF THE PITCH WRT MASS VARIATIONS	159
FIGURE 10-27 SENSITIVITY OF THE TORQUE WRT MASS VARIATIONS.....	159
FIGURE 10-28 LOSS OF STABILITY IN CASE OF TOO HIGH MASS VARIATION	160
FIGURE 10-29 SENSITIVITY OF THE SPEED WRT C.O.G. HEIGHT VARIATIONS	161
FIGURE 10-30 SENSITIVITY OF THE PITCH WRT C.O.G. HEIGHT VARIATIONS	161
FIGURE 10-31 SENSITIVITY OF THE TORQUE WRT C.O.G. HEIGHT VARIATIONS	162
FIGURE 10-32 SENSITIVITY OF THE SPEED WRT TO INERTIA VARIATIONS.....	163
FIGURE 10-33 SENSITIVITY OF THE PITCH WRT TO INERTIA VARIATIONS	163
FIGURE 10-34 SENSITIVITY OF THE TORQUE WRT TO INERTIA VARIATIONS.....	164
FIGURE 10-35 RESPONSE WITH HYPOTHETICAL PACKAGE LOAD - SPEED	165
FIGURE 10-36 RESPONSE WITH HYPOTHETICAL PACKAGE LOAD - PITCH.....	165
FIGURE 10-37 RESPONSE WITH HYPOTHETICAL PACKAGE LOAD – TORQUE.....	166
FIGURE 10-38 PITCH FEEDFORWARD SCHEME.....	168
FIGURE 10-39 SPEED PROFILE TRACKING WITH PITCH FEEDFORWARD	169

FIGURE 10-40 PITCH PROFILE TRACKING	169
FIGURE 11-1 I/O REPRESENTATION OF CASCADE CONTROL.....	172
FIGURE 11-2 BLOCK SCHEME OF CASCADE CONTROL	173
FIGURE 11-3 BLOCK SCHEME OF CASCADE CONTROL: CLASSICAL FORM	173
FIGURE 11-4 PITCH CONTROL LOOP	174
FIGURE 11-5 INVERSE ROOT LOCUS OF $G\tau\theta(s)$	174
FIGURE 11-6 INVERSE ROOT LOCUS OF $G\tau\theta(s)$ AFTER POLE REPLACEMENT	175
FIGURE 11-7 BODE DIAGRAM OF CLOSED LOOP PITCH TRANSFER FUNCTION	177
FIGURE 11-8 BODE DIAGRAM OF CONTROL SENSITIVITY FUNCTION OF PITCH LOOP	178
FIGURE 11-9 OVERALL CONTROL SCHEME PITCH LOOP	178
FIGURE 11-10 SCHEME SPEED CONTROL LOOP	179
FIGURE 11-11 BODE DIAGRAMS OF $G\thetaRs(s)$	179
FIGURE 11-12 SPEED OPEN LOOP BODE DIAGRAM.....	180
FIGURE 11-13 SPEED TRACKING TEST – R01, R02, R03, R04 – SPEED.....	182
FIGURE 11-14 SPEED TRACKING TEST – R01, R02, R03, R04 – PITCH	183
FIGURE 11-15 SPEED TRACKING TEST – R05, R06, R07, R08 – SPEED	183
FIGURE 11-16 SPEED TRACKING TEST – R05, R06, R07, R08 – PITCH	184
FIGURE 11-17 PITCH PROFILE TRACKING R05	185
FIGURE 11-18 SPEED RESPONSE OF DIFFERENT REGULATORS ON UPHILL ROAD	185
FIGURE 11-19 PITCH RESPONSE OF DIFFERENT REGULATORS ON UPHILL ROAD.....	186
FIGURE 11-20 PITCH PROFILE TRACKING R05 UPHILL ROAD	186
FIGURE 11-21 DISPLACEMENTS DURING STABILIZATION TESTS - CASCADE.....	187
FIGURE 11-22 PITCH DURING STABILIZATION TESTS – CASCADE	187
FIGURE 11-23 SCHEME WITH PITCH REFERENCE SATURATION	189
FIGURE 11-24 SPEED PROFILE TRACKING WITH PITCH SATURATION	189
FIGURE 11-25 SPEED PROFILE TRACKING WITH PITCH SATURATION – PITCH ANALYSIS.....	190
FIGURE 12-1 FEED FORWARD COMPENSATION OF SLOPED ROADS.....	195
FIGURE 12-2 FEEDFORWARD COMPENSATION OF UNBALANCED LOADS.....	196

TABLE 2-1 MAINBOARD DATASHEET EXTRACT	31
TABLE 2-2 NVIDIA DATASHEET	32
TABLE 2-3 LIDARS DATASHEET	38
TABLE 2-4 CAMERA DATASHEET	39
TABLE 7-1 BREAKAWAY TORQUES	102
TABLE 7-2 ESTIMATED FRICTION MODEL PARAMETERS – LEFT WHEEL	104
TABLE 7-3 ESTIMATED FRICTION MODEL PARAMETERS – RIGHT WHEEL	104
TABLE 7-4 ESTIMATED FRICTION MODEL (VISCOSUS - ROOT SQUARED) PARAMETERS – LEFT WHEEL	106
TABLE 7-5 ESTIMATED FRICTION MODEL (VISCOSUS - ROOT SQUARED) PARAMETERS – RIGHT WHEEL	106
TABLE 7-6 ROLLING RESISTANCE – TEST RESULTS.....	106
TABLE 10-1 LIST OF CONTROLLER TESTED.....	141
TABLE 10-2 RESULTS OF STABILIZATION TESTS - LQR	144
TABLE 10-3 RESULTS OF SPEED PROFILE TRACKING TESTS - LQR	147
TABLE 10-4 RESULTS OF SPEED PROFILE TRACKING ON UPHILL ROAD TESTS - LQR	150
TABLE 10-5 RESULTS OF STABILIZATION WITH UNBALANCED LOAD TESTS - LQR	154
TABLE 10-6 COMPARISON WITH/WITHOUT PACKAGE	166
TABLE 11-1 LIST OF CASCADE CONTROLLER	181
TABLE 11-2 RESULTS OF STABILIZATION TESTS – CASCADE	181
TABLE 11-3 RESULTS OF STABILIZATION WITH UNBALANCED LOAD TESTS – CASCADE.....	188

Abstract

Questo progetto di tesi riguarda la modellizzazione e il controllo di un pendolo inverso su ruote, nell'ambito dello sviluppo di un veicolo autonomo per la consegna di pacchi in ambiente urbano. E' stata affrontata una prima fase di modellazione e identificazione dei parametri meccanici che caratterizzano il prototipo, e in seguito il progetto di due diversi controllori. Particolare attenzione è stata dedicata agli ostacoli presentati dal tipo di operazioni per il quale il veicolo è stato progettato e dall'ambiente urbano in cui queste devono essere portate a termine. Nello specifico sono state trattate le difficoltà derivanti dal trasporto di carichi, e quelle dovute alla possibilità di dover affrontare **tratti di strada in pendenza**. Entrambi gli approcci di controllo sono stati sperimentati con una serie di test volti a valutarne le performance e la capacità di affrontare i suddetti problemi. Entrambi gli approcci hanno fornito regolatori in grado di produrre il funzionamento desiderato nel veicolo, tanto in condizioni nominali quanto in presenza di disturbi. In particolare il progetto di un controllo in cascata ha consentito l'imposizione di vincoli sulla dinamica di beccheggio del veicolo, peculiarità particolarmente utile ad un veicolo dagli ingombri importanti e operante in un ambiente ricco di ostacoli come quello di cui ci siamo occupati.

Abstract

This thesis project is focused on model identification and control of a Wheeled Inverted Pendulum, in the context of the development of an autonomous vehicle for parcel delivery in urban environment. Our work was divided into two phases: the first was related to the computation and numerical assessment of a dynamical model of our prototype, whereas in the second two different controllers were developed. Particular attention was paid to the difficulties arising from carrying out parcel delivery tasks with a WIP vehicle, together with the main obstacles the urban environment presents. Namely, two main situations were examined: that in which the vehicle carries an unbalanced load and that in which it has to overcome a sloped stretch of road. Both the adopted control approaches were tested with a series of experiments aimed at evaluating their ability at driving the vehicle in an urban environment, possibly facing the aforementioned situations. The desired vehicle behaviour was obtained using each regulator, both in nominal and in perturbed situations. In particular, the design of a cascade regulator made it possible to impose a constraint on the maximum allowed pitch angle; that is a key peculiarity for our vehicle due to the significant clearances, and the necessity of achieving the maximum field of view for the exteroceptive sensors, which are mounted on the chassis and therefore impaired when the vehicle assumes too large pitch angles.

Estratto

Il presente lavoro si occupa di progettare un sistema di controllo per un pendolo inverso su ruote, e nasce dalla collaborazione con una azienda milanese, eNovia s.p.a., nell'ambito della progettazione e realizzazione di un veicolo autonomo per la consegna di pacchi in ambito urbano. L'obbiettivo che ci si è posti è quello di progettare un regolatore che permetta al veicolo di essere pilotato tramite riferimenti di velocità longitudinale e velocità di rotazione, nell'ottica di utilizzare tale controllore sia per la guida da remoto con pilota umano o sia come anello interno di una più ampia struttura di controllo che permetta al veicolo di operare in completa autonomia. Per fare questo, è stata necessaria innanzitutto una fase di modellazione delle dinamiche del veicolo. Utilizzando il Metodo di Newton, è stato possibile ricavare un modello non lineare che leggi le accelerazioni del veicolo alle coppie fornite dai due motori elettrici presenti all'interno del mozzo ruota. In seguito, si è proceduto alla linearizzazione ed analisi di tale modello, nella quale è stata messa in evidenza l'intrinseca instabilità della dinamica di beccheggio del telaio insieme ad alcune altre caratteristiche peculiari di veicoli di questo tipo, tra cui un comportamento a fase non minima della velocità longitudinale. In seguito, è stato necessario caratterizzare numericamente il modello perché rappresentasse correttamente il comportamento specifico del prototipo che ci era stato fornito. In particolare, sono state misurate le principali grandezze misurabili (masse, lunghezze, ...) ed è stata effettuata un'identificazione delle altre tramite fitting di risposte simulate e risposte misurate sul prototipo reale. Si è poi passati alla progettazione, implementazione e test di una serie di algoritmi di stima dello stato del veicolo basati sulle misurazioni provenienti dai sensori propriocettivi, nello specifico una IMU a sei gradi di libertà e due encoder rotativi montati nel mozzo ruota. In particolare è stato necessario realizzare uno stimatore dell'angolo di beccheggio, uno della velocità longitudinale e uno della velocità di imbardata. Una volta disponibile un modello accurato del prototipo insieme ad una stima accurata del suo stato dinamico in ogni istante è stato possibile progettare un regolatore che perseguisse l'obiettivo di controllo che era stato posto. Nel progetto di tale regolatore sono state percorse due diverse strade: la prima, ampiamente utilizzata in letteratura nel controllo di veicoli di questo tipo è basata sullo sviluppo di un regolatore LQ che controlli simultaneamente tutto lo stato del sistema; la seconda è un approccio in cascata, che è generalmente meno utilizzato in quanto di più difficile progettazione ma che ci ha consentito di imporre limitazioni alla dinamica di beccheggio del veicolo. Questa seconda scelta è stata dettata dalla mancanza nel controllo LQ di tecniche che permettano di imporre in modo agevole dei vincoli sugli stati del sistema; nello specifico, per un veicolo come quello di cui ci siamo occupati, è di particolare interesse la possibilità di imporre un valore massimo all'angolo di beccheggio, così da evitare l'impatto del veicolo contro il suolo. La scarsa considerazione di questo problema in letteratura è da imputarsi a diversi fattori, tra cui l'ampio margine di beccheggio presentato dalla maggior parte dei prototipi studiati e l'interesse puramente didattico che sottostà allo sviluppo di questi ultimi. Al contrario, il nostro veicolo presenta margine di beccheggio relativamente piccolo, ulteriormente limitato dalla presenza di ostacoli all'interno dell'ambiente in cui deve operare. Inoltre, poiché questo prototipo è progettato per essere effettivamente utilizzato a breve termine come robot porta pacchi in un vero ambiente urbano, la limitatezza delle dinamiche di beccheggio diviene un requisito fondamentale. Il controllo in cascata che viene presentato in questa tesi fornisce la possibilità di imporre tale limite, per quanto

un ulteriore studio sia ancora necessario per renderlo effettivamente operativo sul veicolo finale. Infine, nel progettare i vari regolatori, particolare attenzione è stata posta ad alcune problematiche relative al tipo di utilizzo per cui questo veicolo è stato concepito. Innanzitutto, sono stati considerati gli effetti della possibile presenza di pacchi sulla dinamica complessiva; sono state analizzate le **conseguenze della variazione di massa e dello spostamento del baricentro**, particolarmente rilevanti data la natura instabile dei veicoli di questo tipo. In secondo luogo sono state affrontate le **problematiche dinamiche e geometriche che sorgono nel momento in cui il veicolo si trova ad affrontare strade in pendenza**. Entrambi gli approcci di controllo si sono dimostrati efficaci a questo riguardo, e hanno permesso al veicolo di ottenere il funzionamento desiderato a dispetto della presenza di tali disturbi.

Ringraziamenti

Un ringraziamento particolare va al nostro relatore prof. Sergio Savaresi che ha fatto in modo che potessimo intraprendere questa esperienza interessante e formativa.

Un ringraziamento anche ai correlatori prof. Matteo Corno e Ing. Stefano Sabatini che ci hanno seguito e aiutato giorno per giorno ad affrontare questo percorso.

FIRMA

Filippo Parravicini:

Arrivato alla fine di cinque lunghi anni di ingegneria sono tante le persone che vorrei ringraziare. Purtroppo lo spazio e le mie abilità di scrittore sono alquanto limitate, ma cercherò comunque di mettere insieme un tentativo dignitoso.

Per primo non posso che ringraziare Andrea, amico e compagno di tesi, per le (esclusivamente sue) nottate di lavoro e la pazienza nel limitare le mie paranoie: senza di lui questa tesi non sarebbe mai stata conclusa.

Stefano, che da sempre mi sfida come solo un fratello maggiore può fare. Fosse per vincere una gara di biglie o per raggiungere i miei obiettivi nello studio, non avrei potuto chiedere modello migliore a cui aspirare.

Mia sorella Chiara, che sa che in fondo sono solo uno studente dello scientifico, e quanto fatico a trovare le parole giuste in questo momento. Di lei so che arriverà lontana qualunque sia la strada che sceglierà, bagnando il naso ad entrambi i suoi fratelloni.

Chiara, che ha la parte maggiore dei miei pensieri e del mio cuore. Che mi fa ridere come nessun altro, che sa sempre come consolarmi e come spronarmi, che mi ha dato più di quanto lei stessa immagini, e che è la mia più grande sicurezza e la mia più grande gioia.

I miei genitori, che mi hanno sempre supportato e spinto a ottenere il massimo in tutto quello che facevo. Papà, la cui saggezza ingegneristica mi ha sempre ispirato, e che spero di saper imitare nella bontà, la felicità e la sicurezza che ha sempre saputo trasmettermi. Mamma, che mi ha insegnato l'amore per i numeri e per le cose belle, e dalla quale non smetterò mai di imparare.

A tutti voi, e a chi non ho avuto lo spazio per ricordare, va il mio grazie più sincero.

Andrea Rivolta:

Un ringraziamento particolare al mio compagno di tesi Filippo che mi ha sopportato e aiutato a crescere in questi nove mesi passati a stretto contatto.

Il ringraziamento più caloroso va ai miei genitori che mi hanno permesso di intraprendere questo bellissimo percorso e mi hanno sempre sostenuto.

Un ringraziamento anche ai miei amici e ai compagni di studi con i quali ho condiviso questo cammino e che mi hanno accompagnato anche nei momenti più difficili incontrati.

Chapter 1 - Introduction

With the rise of e-commerce, last-mile delivery market is getting increasingly attention from investors. The attractiveness of such market is both in the volume, estimated to approximately EUR 70 billion in 2016, and in the considerable growth rates: ranging from 7 to 10% in mature markets (Germany, US, ...) in 2015, and up to 300% in evolving ones like India. The perceived quality of last-mile delivery services has been identified as a major decision criterion for online customers, and as such it is considered by the e-commerce companies as a fundamental requirement to be competitive in the parcel delivery market.

The most common approach to last mile delivery involves the use of a heavy truck with internal combustion engine; therefore, it is subjected to significant disruptions like road congestion, pollution, delivery lateness, high cost of fuel, employees, and maintenance. Hence, it is clear that a green, autonomous, cheap and fast shipment is the future of parcel delivery. That is the context of the creation of YAPE (Your Autonomous Pony Express), which is a small and compact electric AGV (Autonomous Ground Vehicle) designed by eNovia s.p.a. to accomplish parcel delivery in urban environment.



Figure 1-1 YAPE

Structurally YAPE is a two-wheeled vehicle equipped with two brushless DC motors embedded in the wheels hubs and a series of proprioceptive and exteroceptive sensors (lidars and cameras) which allows him to navigate in a crowded urban environment.

Such structure is known in the literature as a Wheeled Inverted Pendulum (WIP hereafter) and carries many advantages; first of all, the reduced footprint, together with the ability of performing turns on the spot, allow it to easily manoeuvre in the narrow paths the urban environment present; secondarily the light weight combined with the electrical power source make it a green, low cost solution to the parcel delivery problem. On the other hand, this structure is intrinsically unstable and therefore requires a feedback control action to stabilize and drive it. Moreover, the fact that a pitching motion is necessary to a WIP to accelerate and brake poses a series of problems like the reduction of field of view of lidars and cameras and a substantial risk of hitting the ground with the hulls.

Our work was related to the design of a stabilizing controller capable of tracking speed and yaw rate reference signals while accounting for the previously mentioned pitch related problems. This required a preliminary modelling phase followed by a parameters identification one aimed at reproducing at best the dynamical behaviour of the prototype we were furnished by the company.

1.1 State of the art and personal contributions

From the modelling point of view, the vehicle is a 2-wheeled inverted pendulum: this type of vehicles got more and more attention in the last few decades; for this reason, many researches about this topic are available in literature. A definitive recap of the state of the art is available in [1]. Models based on dynamic equations ([2], [3], [4], [5]) and black-box models ([9], [10], [11]) were investigated, both with or without considering the yaw motion. Particular attention has been payed to [6], [7], [8] due to the high level of similarity with the approach used in this work, namely a model with decoupled longitudinal and yaw dynamics, based on mechanical dynamical equations. Different control strategies have been proposed along the years: non-linear approach such as neural network ([12]), backstepping ([13]) and sliding mode ([14]); however, methods based on linearization such as pole placement ([6], [15]) and especially LQR control ([2], [8], [16]) are more frequently used.

Most of the mentioned publications and papers do not focus their attention out of the nominal case (except for standard parametric uncertainties). The only exceptions are few publications considering an inclined terrain ([14] – sliding mode, [17] - LQR) and a moving centre of mass ([18] - PI).

In contrast to most the prototypes used in the aforementioned publications, YAPE is a vehicle aimed to be used in daily life in an unpredictable environment; hence a further investigation of the behaviour of the system in two particular cases has been conducted:

- A non-zero slope road that can be encounter during the operative life of the vehicle: from light uphill long roads to steep ramps of the sidewalks.

- A time varying position of the c.o.g. of the vehicle due to the packages load/unload. This operation may also create an unbalanced load situation that would change in an unpredictable way the stable position of the vehicle.

Two types of control strategy were developed for such purposes, implemented and successfully tested: an LQR optimal regulator and a cascade approach.

Moreover, a solution was proposed to a problem that, to our knowledge, has been barely investigated in the literature: the pitch limitation. In fact, the possibility of imposing constraints on the maximum allowed pitch angle (FIGURE 1.2) would be crucial to minimize the occurrence of the previously mentioned pitch related problems (i.e. limitation of the exteroceptive sensors field of view, risk of hitting the ground while tilting, ...)

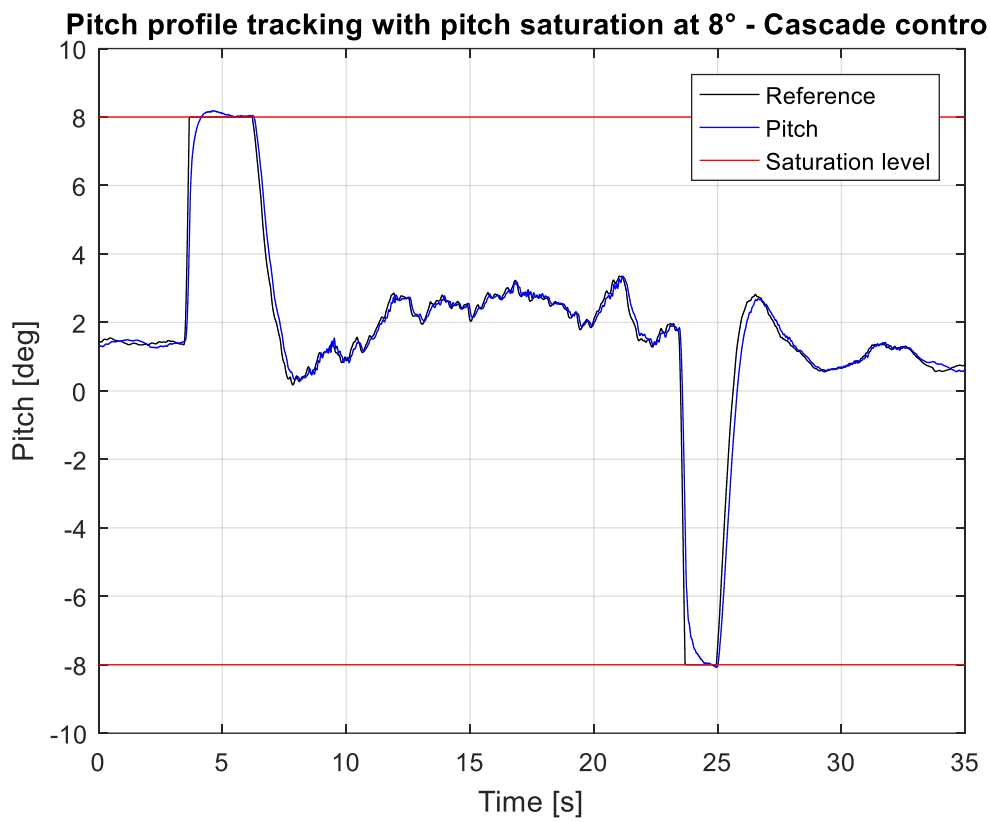


Figure 1-2 Pitch profile tracking with pitch saturation at 8° - Cascade control

1.2 Thesis structure

In the following, a brief summary of Chapters' contents is detailed.

- Chapter 2 – Vehicle setup

This chapter presents the mechanical structure of the vehicle, the available hardware and sensor. The general hardware architecture is also showed.

- Chapter 3 – Dynamical model

In this chapter all the equations that describe the dynamical behaviour of the system are derived, together with the assumed hypothesis. The starting model is the nominal one, i.e. with a flat road and balanced load (c.o.g. exactly over the wheel's hub). An analysis of the transfer functions of the linearized system is carried out.

- Chapter 4 – Effect of Loads and Slopes

In this chapter the presence of a non-zero slope road and an unbalanced load is modelled: dynamical equations are derived and their effect on the system behaviour is analysed.

- Chapter 5 – IMU calibration

This chapter shows the problematic that affect a IMU sensor used to estimate the state of the vehicle. A procedure to perform a complete calibration and compensation of errors is proposed.

- Chapter 6 – State Observers

A construction of the state observer exploiting the kinematic relationship is presented, with the solution strategies adopted to reject the noise present on data provided by sensors.

- Chapter 7 – Model identification

Detailed procedures to estimate all the parameters of the model are shown. Several tests for friction model estimation are carried out and a close loop approach for the estimation of the other parameters non-directly measurable is proposed.

- Chapter 8 – Control structure

In this chapter is presented the general control structure. The main issues that can be encountered in an urban context are presented: the ability of the controllers to face this problem are taken as performance indexes.

- Chapter 9 – Reference filtering

This chapter introduce a procedure to filter the references fed to the controller; the motivations and results of this procedure are explained.

- Chapter 10 – LQR control

In this chapter the LQR control approach is presented: starting from a theoretical introduction to the implementation. Different kind of controller are tested to fully understand their behaviour. A detailed analysis of the performances of each controller facing principal environmental disturbances is realized.

- Chapter 11 – Cascade control

An alternative approach to the LQ control is presented based on series of nested loops. The theoretical derivation of such scheme is explained; subsequently the controller is analysed with the same tests run on LQ and the obtained results are compared. Finally, an innovative approach to limit the vehicle pitch angle is proposed.

- Chapter 12 – Conclusions

Conclusions and future developments are presented.

Chapter 2 - Vehicle setup

2.1 Introduction

From a structural point of view, YAPE is a Wheeled Inverted Pendulum. It is composed of two, bicycle-like, wheels attached to a steel chassis covered with high density polystyrene hulls. (FIGURE2.1).



Figure 2-1 YAPE's structure

Each wheel contains an embedded **Brushless DC motor**, which provides the torque needed for stabilization and driving purposes. The chassis is a box-shaped one, and features a package-loading compartment. Being designed for urban autonomous driving, YAPE is equipped with a set of proprioceptive and exteroceptive sensors that are used for stabilization, speed control and trajectory planning and tracking. All the main control tasks are carried on by a central micro controller, receiving data from the sensors and communicating with the wheels by means of a CAN bus line. The vehicle is also equipped with a GPU, designed for processing the data coming from the cameras and proximity sensors.

Mechanical and electronical components, together with the main diagram of operation, are listed and described in the following.

2.2 Mechanical components:

2.2.1 The chassis

YAPE's chassis is a box-shaped, tubular frame made of welded steel. Each beam is a hollow, squared section one, of 2 cm of width and 2 cm of height. The entire frame measures 50 cm of height, for 50 cm of depth and 50 cm of length. Such measures results from a compromise between providing enough package-loading space and designing a vehicle capable of moving with ease in a complex and crowded urban environment.

The total weight of the chassis is 8 kg; the choice of welded, steel beams allowed to obtain a relatively light weighted structure still providing enough support to carry up to 70 Kg loads. The bottom part of the chassis presents two compartments for the wheels to be bolt (FIGURE 2.2).



Figure 2-2 Chassis

Right above them, in the central, lower part of the chassis, a wooden plate is screwed to the steel frame: that provides a stable surface to attach all the electronic components (Main Board, GPU, battery packs, ...).

2.2.2 The hulls

The hulls mounted on our prototype are made of high density polystyrene (FIGURE 2.3). Far from being a definitive one, this choice of material grants protection to the internal components still having a relatively small contribute on the overall weight. Despite being a temporary solution, these hulls play a crucial role in the understanding of the clearances of the vehicle, whilst providing support to the exteroceptive sensors (lidar and cameras).



Figure 2-3 Hulls

2.2.3 The wheels

The wheels are 20'', bicycle-like ones featuring an embedded electric motor mounted on the wheel's hub (FIGURE 2.4).



Figure 2-4 Wheel

They are produced by *Zehus s.p.a.* and they are defined as Smart Electric Wheels. Such wheels are all-in one products, featuring an internal electric motor, battery packs, control electronics and usually a set of sensors such as encoders, IMUs, temperature sensors (FIGURE 2.5). Communication from or to a Zehus wheel is performed through a CAN BUS port located on the central hub, that is used also for programming the internal control board.

Each wheel features:

- A lithium ion battery pack, granting up to 80 Km of autonomy at full charge.
- A BSDL motor with 70 Nm of Maximum Torque, and a reduction gearing with 1/100 transmission ratio
- A Hall's sensors based rotational encoder, which provides an incremental measure of the relative angle between the wheel and the chassis with a discretization of 0.6°
- Embedded electronics for both control and communication purposes
- A CAN bus connection that allows data stream and battery charging
- Other sensors (temperature, current, battery voltage, ...)



Figure 2-5 Embedded motor exploded view

The choice of these specific wheels was dictated by two main factors: first off all they provide a compact and complete motor pack which is capable of providing large amounts of torques, which is a very useful feature in a vehicle of this type; secondarily the relatively big rim radius allows the vehicle to overcome most of the obstacles which are presented by a urban environment (bumps, cobblestone streets, small steps, ...). An internal control loop was implemented by eNovia on the wheels mounted on our prototype in order to make them capable of following torque reference profiles: such control is characterized by a very high bandwidth of approximately 100 Hz so that from the micro controller point of view it is possible to consider them as ideal actuators.

2.3 Control architecture: general scheme

A schematic of YAPE's control architecture is depicted in FIGURE 2.6.

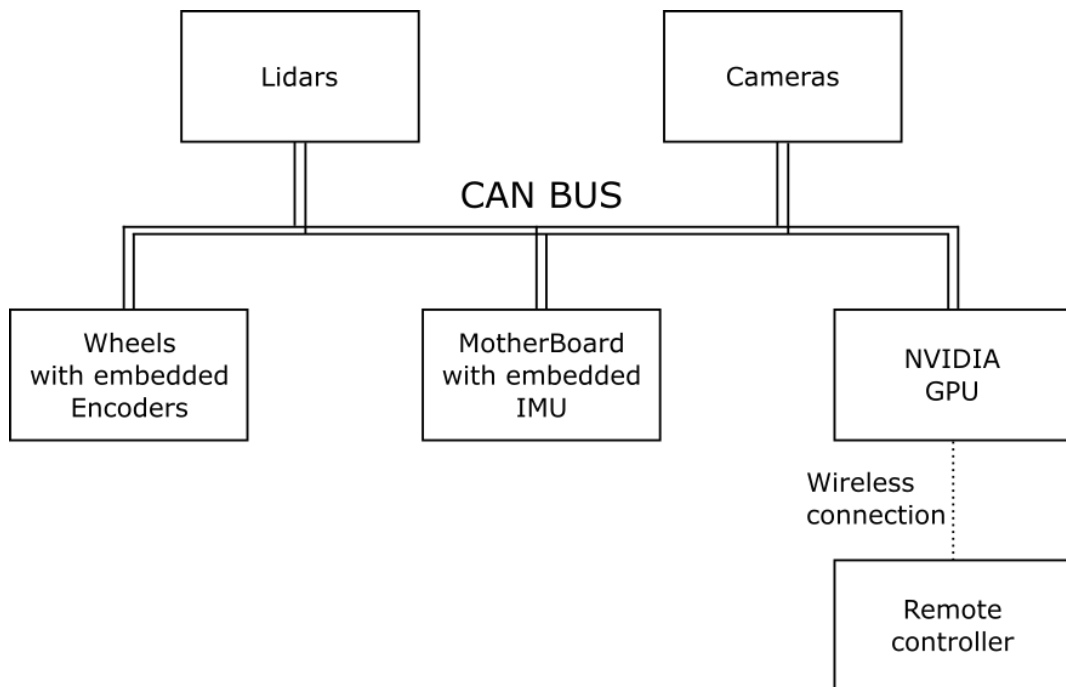


Figure 2-6 General architecture

As we can see from FIGURE 2.6 a central computational unit, the Main Board, is connected through a CAN bus to all the available sensors, actuators and communication devices. Namely, using the CAN bus, the MB receives readings from the proprioceptive sensors (IMU and encoders), computes and estimation of the actual vehicle's state, determines the amount of control action needed for stabilization and driving purposes and send a torque request to the wheels. Trajectory planning and tracking can also be performed by the MB starting from the readings of the proximity sensors (Lidars). Otherwise, speed and yaw rate requests are sent to the MB from a remote controller through the NVDIA board, thus turning YAPE into a remote-controlled vehicle.

2.4 Hardware components:

2.4.1 The mainboard

The main board is a custom-made board assembled by eNovia (FIGURE 2.7), mounting a 56F84789VLL Digital Signal Controller produced by Freescale Semiconductor, based on the 32-bit 56800EX core. The main features are listed in TABLE 2.1:

Core Frequency (Mhz)	100
Flash memory (KB)	256
FlevNVM/FlexRAM (KB)	32/2
Total flash memory (KB)	288
RAM (KB)	32
I2C/SMBus	2
FlexCan	1

Table 2-1 Mainboard datasheet extract

The mainboard is also equipped with an Inertial Measurement Unit with 6 degrees of freedom (3 axis accelerometer, 3 axis gyrometer) and can be linked through a dedicated connector to the CAN bus, achieving the possibility of exchange information with the other components of the vehicle.



Figure 2-7 Mainboard

2.4.2 The NVIDIA GPU

GPU mounted on the vehicle is a NVIDIA Jetson TX1.(FIGURE 2.8)

GPU	NVIDIA Maxwell™, 256 CUDA core
CPU	Quad ARM A57/2 MB L2
Video	4K x 2K 30 Hz Encode (HEVC) 4K x 2K 60 Hz Decode (10-bit support)
Memory	4 GB 64 bit LPDDR4 25.6 GB/s
Display	2x DSI, 1x eDP 1.4 / DP 1.2 / HDMI
CSI	Up to 6 Cameras (2 Lane) CSI2 D-PHY 1.1 (1.5 Gbps/Lane)
PCIE	Gen 2 1x4 + 1x1
Data Storage	16 GB eMMC, SDIO, SATA
USB	USB 3.0 + USB 2.0
Connectivity	1 Gigabit Ethernet, 802.11ac WLAN, Bluetooth
Mechanical	50 mm x 87 mm (400-Pin Compatible Board-to-Board Connector)

Table 2-2 NVIDIA datasheet

During our work, the NVIDIA board was only in charge of receiving the commands coming from the remote controller, translating them into a readable format for the MB and sending them on the CAN. This clearly represent a substantial underuse of its capabilities. However, the full computational power of this component will be exploited in the future for real-time elaboration of enormous amounts of data coming from lidar and cameras. It will also allow real-time streaming of the aforementioned data, and the execution of trajectory planning and tracking algorithms



Figure 2-8 NVIDIA Jetson tx1

2.4.3 The joystick

Manual control of the vehicle is performed using a Logitech F710 remote controller. This is a standard, dual-stick game controller (FIGURE 2.9)



Figure 2-9 Joystick

It is connected to the vehicle's GPU through an USB wireless receiver running at 2.40 GHz at a maximum distance of approximately 15 meters. The two sticks are used to control the vehicle speed and yaw rate, whereas all the other buttons allow to perform different actions, such as switching from manual to autonomous driving, or to switch between various inner control structures implemented on the Main Board.

2.5 Proprioceptive sensors

2.5.1 IMU

Vehicle's main board is equipped with a 6-DOF Inertial Measurement Unit, composed of three inertial accelerometers and three gyrometers, measuring accelerations and rotational speeds referred to a right handed orthogonal reference frame (sensor fixed). A peculiar feature of the accelerometers is that they measure accelerations referred to their instantaneous rest frame, which means that when the vehicle is still, an acceleration equal to the gravitational one is measured by the IMU. As will be explained in Chapter 6 this fact will actually be exploited in the estimation of the vehicle's pitch angle.

Both accelerometers and gyrometers readings are affected by different type of errors, namely:

- **Offset errors:** both accelerometers and gyros readings show an additive offset. In particular, being X any of the quantities measured by the IMU we can write:

$$X_{measured}(t) = X_{real}(t) + c \quad (2.1)$$

in which c is a constant or slowly varying noise component (time dependence of this second case was omitted for clarity). The accelerometer's offset is almost constant, and therefore quite easily corrected offline. On the other hand, the gyros are subjected to a slowly drifting offset, which can be only partially corrected at the vehicle start.

- **Gain factor errors:** They mostly affects the accelerometers, and they result in a non-unitary ratio between the actual acceleration value along one axis and the measured one. In particular, referring to the same model given in (2.1), we can write:

$$X_{measured}(t) = m X_{real}(t) + c \quad (2.2)$$

where $m \neq 1$ in general, and c is the aforementioned offset component.

- **Mounting errors:** They are ascribable to non-perfect alignment between the vehicle's and the IMU's reference frames, which result in a non-coincidence between a quantity measured on one IMU axis and that actually existing on the corresponding vehicle's axis. As will be explained in CHAPTER 5 they can be easily compensated by means of an ad hoc offline calibration procedure.

- **Noise:** High frequency noise affecting any electronic measuring device. It is typically a zero-mean white noise. By denoting this type of noise with the letter η we can finally write:

$$X_{measured}(t) = m X_{real}(t) + c + \eta(t) \quad (2.3)$$

(in FIGURE 2.10 the graphical representation of (2.3))

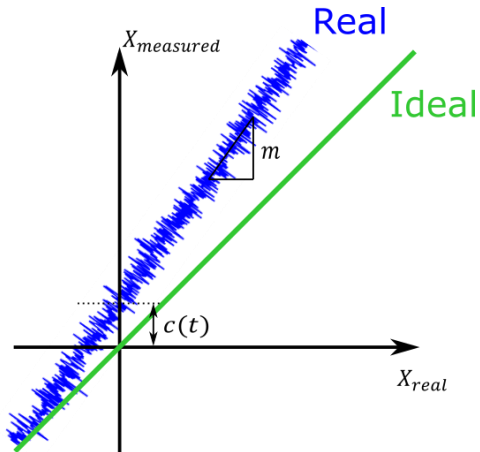


Figure 2-10 Ideal vs Real measurement curve of the IMU

2.5.2 Encoder

Each YAPE's wheel feature an embedded rotary encoder. It is an absolute encoder mounted on the motor side of the transmission gear-box (FIGURE 2.11).

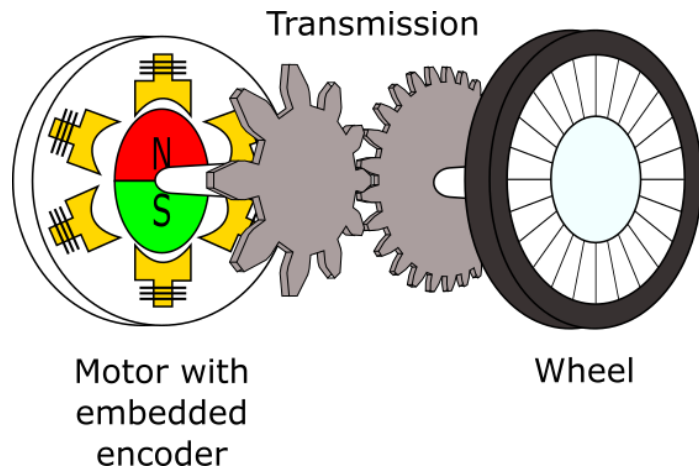


Figure 2-11 Gear box exploded view

The encoder is based on 3 Hall sensors, one for each of the three-phase stator windings of the BSCD motor (FIGURE 2.12). Each Hall sensor can detect the magnetic field vector (B) associated to the permanent magnets placed on the rotor. A logic 1 is returned by the sensor when B is in the half-circumference containing its winding, a 0 is returned otherwise. By combining the readings of the 3 sensors it is possible to compute the absolute rotor position with a discretization of 60° .

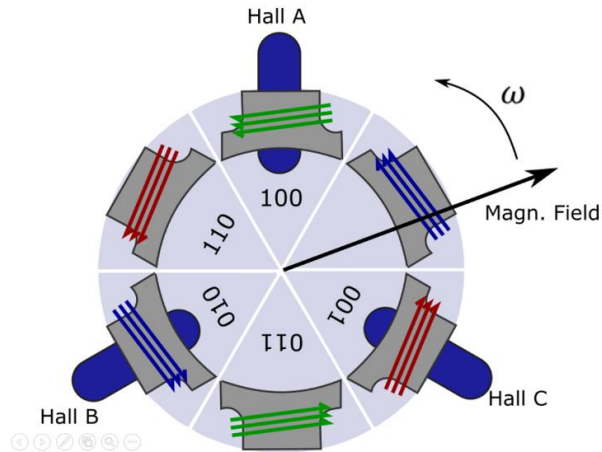


Figure 2-12 Schematic view of the encoder based on Hall sensors

Thanks to the $1/100$ gear ratio, this is translated into a measure of the wheel angular position with 0.6° quantization. This measure can't actually be used as an absolute one: in fact, each of the 6 known rotor positions correspond to 100 different wheels positions. (FIGURE 2.13)

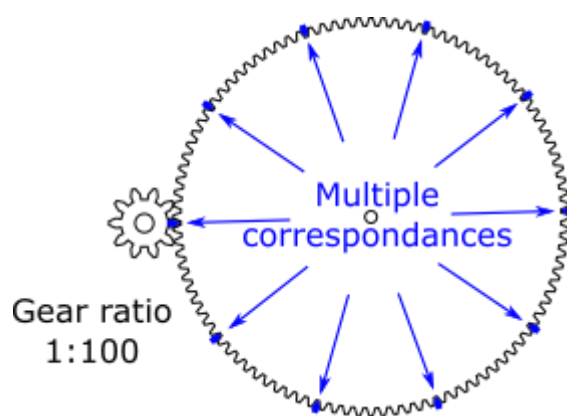


Figure 2-13 Schematic view of the gear transmission

Nevertheless, the knowledge on the Hall sequence allows to easily reconstruct a directional incremental measure for the wheel angular position as follows:

- at the start, wheel's position is set to zero
- when a clockwise rotor step is detected, wheel's position is increased by 0.6°
- when a counter clockwise rotor step, wheel's position is decreased by 0.6°

From the micro controller point of view, the encoder's output represents the relative position between the wheel and the chassis, given as an incremental and directional value with 0.6° of precision.

Due to its incremental nature this value is necessarily subjected to overflow: in particular, being encrypted in 16-bit, the measuring range is $[-2^{15}; +2^{15}]$. When the overflow occurs the measured data jumps from one extreme to the other, which is, symbolically:

$$2^{15} + 1 \text{ step} = -2^{15} \quad (2.4)$$

FIGURE 2.14 shows the evolution of an encoder reading while the vehicle is running: approximately at the 29th second the encoder reaches the overflow value, and immediately jumps to the other extreme of the scale.

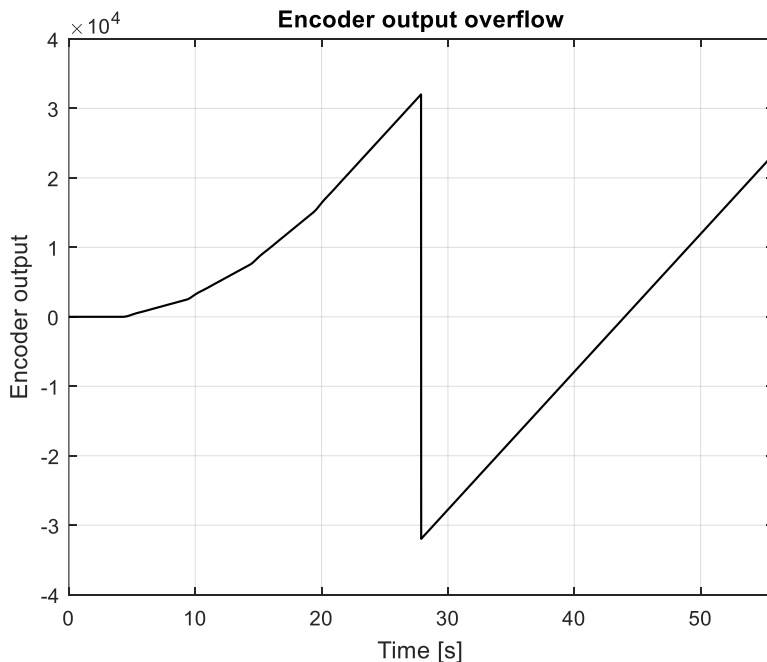


Figure 2-14 Occurrence of the overflow on one of the encoders

This type of behaviour must be considered while using encoder data in the reconstruction of the vehicle dynamic state, in order to avoid unexpected behaviours of the estimated variables.

2.5.3 Lidars

The vehicle mounts four lidar sensors, one for each side. These depth sensors are LeddarVu8 (FIGURE 2.15), with a horizontal field of view of 100° divided in 8 sectors and a vertical field of view of 3°, produced by LeddarTech Inc.

Horizontal FoV	95° \pm 5°
Vertical Fov	3.4° \pm 0.25°
Range	34 m
Number of segments	8
Accuracy	5 cm
Data refresh rate	Up to 100 Hz
Distance precision	6 mm
Distance resolution	10 mm

Table 2-3 Lidars datasheet



Figure 2-15 LeddarVu8

2.5.4 Cameras

On the vehicle are also mounted four cameras Logitech C920 HD Pro (FIGURE 2.16), which allow an operator to manoeuvre the vehicle remotely thanks to a real-time data streaming.

Full HD 1080p (up to 1920x 1080 pixels)
Photos: up to 15 megapixels
Logitech Fluid Crystal Technology
H.264 video compression
Carl Zeiss lens with 20-step autofocus
Built-in dual stereo mics with noise reduction
Automatic low-light correction
Hi-Speed USB 2.0 certified (USB 3.0 ready)

Table 2-4 Camera datasheet



Figure 2-16 Logitech c920 hd pro

2.6 Conclusions

The mechanical and electronical components of YAPE were presented in this chapter. The vehicle's control architecture was also depicted, and a brief description of the features of the various components was reported.

Chapter 3 - Dynamical model

3.1 Introduction

The aim of this chapter is to develop a mathematical model describing the dynamics of YAPE operating in nominal conditions, which means with nominal mass (no loaded package) and running on a flat road surface. The main variables characterizing the system will be presented, and then a set of nonlinear dynamic equation will be computed. Subsequently, a linearization around the chassis upright position will be performed, resulting in a 4th order linear system. Finally, the main dynamical aspects of the controlling a WIP will be presented.

3.2 Nominal model

As already mentioned in Chapter 1 and 2, YAPE is a Wheeled Inverted Pendulum, which is typically modelled as an unstable, underactuated, nonlinear system. From a kinematical point of view, it is characterized by a total of 3-DOF: two of them are related to the planar motion of the entire vehicle on the ground, and the last one to the pitching movement of the chassis along the vehicle's track. In order to describe the vehicle's kinematics two different reference frames are now introduced. First, a right handed, world fixed reference with \vec{X} - \vec{Y} plane parallel to the road surface and \vec{Z} -axis pointing upward, which will be called *world frame* and indicated with $\vec{X}_w \vec{Y}_w \vec{Z}_w$. Secondary, a right handed, chassis-fixed reference frame, in which the origin is placed at the center of the vehicle's track, the \vec{Y} -axis is parallel to the vehicle track, \vec{Z} -axis is parallel to vertical edge of the chassis, and \vec{X} -axis points forward. This will be referred as $\vec{X}_v \vec{Y}_v \vec{Z}_v$, where the subscript v stands for *vehicle frame* (FIGURE 3.1).

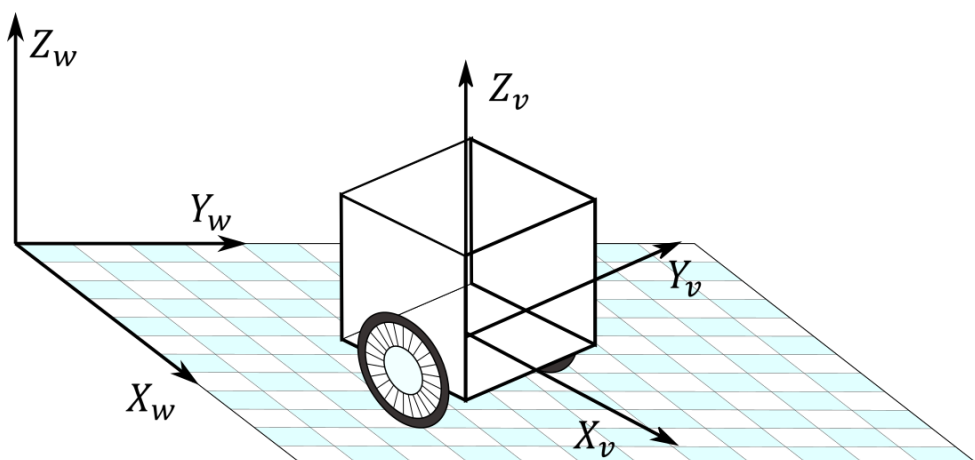


Figure 3-1 World frame and vehicle frame

At this point, let's describe the vehicle motion with respect to the *world frame*. We choose as planar coordinates the curvilinear coordinate s of the track center and the vehicle yaw angle ψ which can be computed as the angle between \vec{X}_w and the projection of \vec{X}_v on the $\vec{X}_w\vec{Y}_w$ plane (FIGURE 3.2).

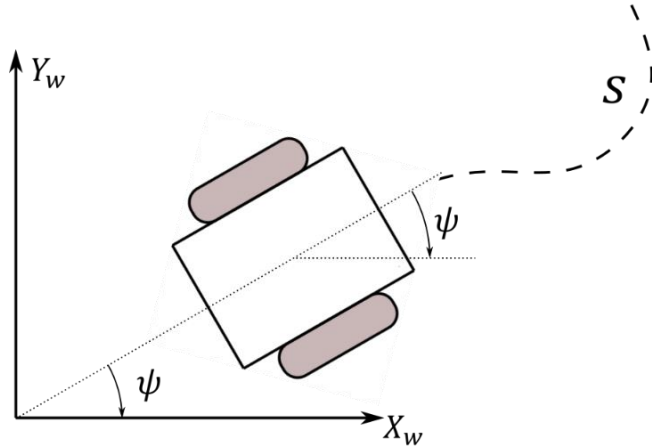


Figure 3-2 Graphical representation of curvilinear coordinate s and yaw angle ψ

Due to the rolling without sliding constraint applied to the two parallel wheels, the roto-translational motion of the vehicle can be described in terms of the longitudinal speed \dot{s} , which is always directed along the \vec{X}_v axis, and the rotational speed $\dot{\psi}$. The tilting motion occurs on the $\vec{X}_v\vec{Y}_v$ plane and its fully described by the pitch angle θ , namely the angle between \vec{Z}_v and \vec{Z}_w (FIGURE 3.3).

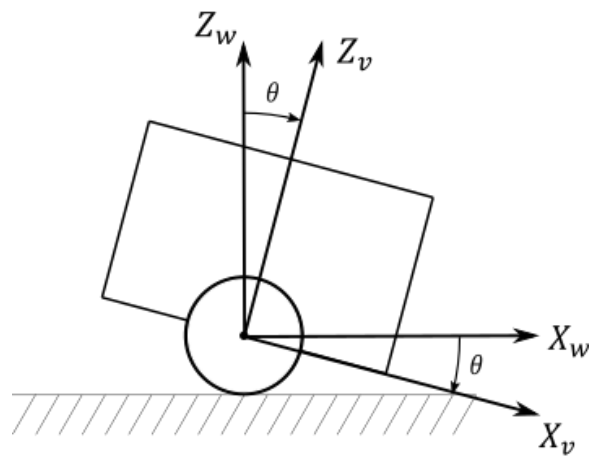


Figure 3-3 Graphical representation of pitch angle θ

Let's now consider the kinematical relations between the speed of the wheels centres and the motion of the vehicle (FIGURE 3.4). Since the chassis is a rigid body, we have that:

$$\begin{cases} \dot{s}_r = \dot{s} + \dot{\psi} \frac{d}{2} & \text{Speed of the right wheel} \\ \dot{s}_l = \dot{s} - \dot{\psi} \frac{d}{2} & \text{Speed of the left wheel} \end{cases} \quad (3.1)$$

In which d is the axle track, \dot{s}_r is the speed of the right wheel center, \dot{s}_l that of the left wheel, \dot{s} is the speed of the track's center and $\dot{\psi}$ is the yaw rate. Then, by summing and subtracting the two equations of (3.1) we get:

$$\begin{cases} \dot{s} = \frac{\dot{s}_r + \dot{s}_l}{2} \\ \dot{\psi} = \frac{\dot{s}_r - \dot{s}_l}{d} \end{cases} \quad (3.2)$$

(in FIGURE 3.4 the graphical representation of (3.2))

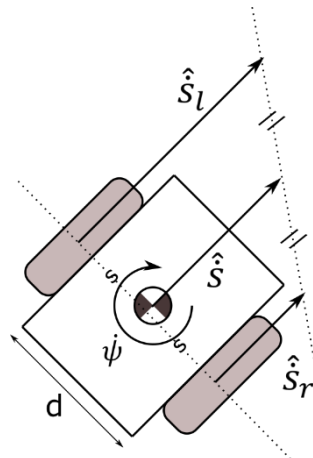


Figure 3-4 Graphic representation of the relationship between \dot{s}_r , \dot{s}_l , \dot{s} , $\dot{\psi}$.

With the aforementioned choice of variables, the vehicle dynamics can be studied by considering two different motions: a planar motion occurring in the $\vec{X}_v \vec{Z}_v$ plane, fully described by s and θ , and a rotational motion occurring on the $\vec{X}_v \vec{Y}_v$ plane, described by the variable $\dot{\psi}$. The computation of the dynamical equations was therefore carried on applying the Newton Method to these two separate motions.

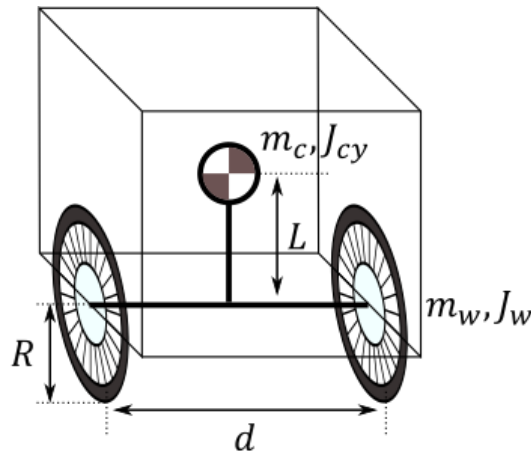


Figure 3-5 Meaning of model parameters

Before starting with the computation of the dynamical equation, the notation used to indicate the mechanical parameters of the system is introduced. Looking at FIGURE 3.5, we have that:

- m_w is the wheel mass, which is equal for both the wheels
- J_w is the wheel rotational inertia with respect to the \vec{Y}_v axis
- R is the wheel radius
- m_c is the chassis mass, intended as the sum of the chassis and hull masses
- L is the height of the chassis c.o.g computed in the $\vec{X}_v \vec{Y}_v \vec{Z}_v$ reference frame
- J_{cy} is the chassis barycentric moment of inertia with respect to an axis parallel to \vec{Y}_v
- d is the axle track

Once the mechanical parameters are defined, the computation of dynamical equation starts by considering the 2-DOF motion occurring on the $\vec{X}_v - \vec{Z}_v$ plane. The only external forces acting on this plane, are the gravitational one, and the driving torques produced by the hub motors. A planar view of the vehicle showing all the external and inertial forces and torques is presented in FIGURE 3.6. For the sake of clarity, left wheel is not shown here.

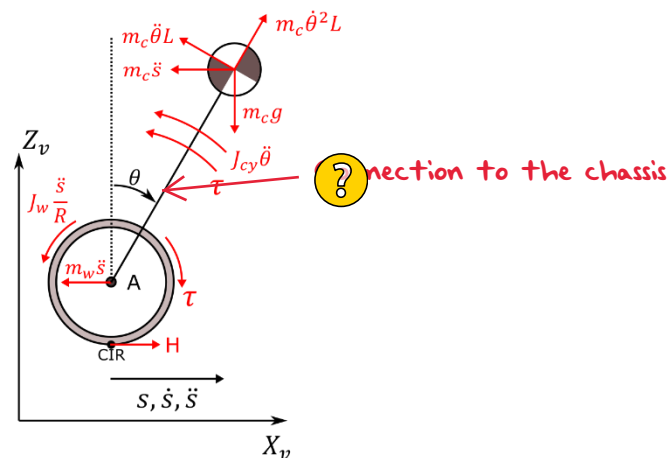


Figure 3-6 Forces and torques acting on the system

Notice that, since the driving torques can be considered as produced inside the rotational joints connecting the wheels to the chassis, two torques components are actually introduced for each wheel: one acting on the chassis, and the reaction one acting on the wheel in the opposite direction. This is the main difference between a WIP and the well-known pendulum-on-a-chassis. Let's now consider the right wheel alone. First, the rotational joint connecting it to the chassis is opened, and the corresponding internal forces are introduced together with the contact forces arising between the tyre and the ground (FIGURE 3.7)

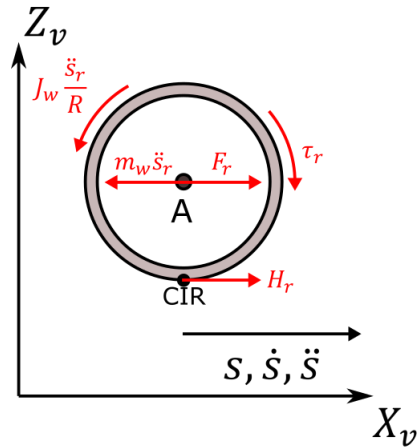


Figure 3-7 Forces and torques acting on the right wheel

It is then possible to write a balance of moments with respect to the wheel centre A:

$$\sum M_A(\text{right wheel}) = 0 \quad (3.3)$$

Yielding:

$$\tau_r = J_w \frac{\ddot{s}_r}{R} + H_r R \quad (3.4)$$

in which the subscript r trivially stands for "right-wheel". With the exact same procedure, a similar equation is obtained for the left wheel, specifically:

$$\tau_l = J_w \frac{\ddot{s}_l}{R} + H_l R \quad (3.5)$$

Still keeping the joints opened, and by looking only at the chassis, the force scheme is the one depicted in FIGURE 3.8:

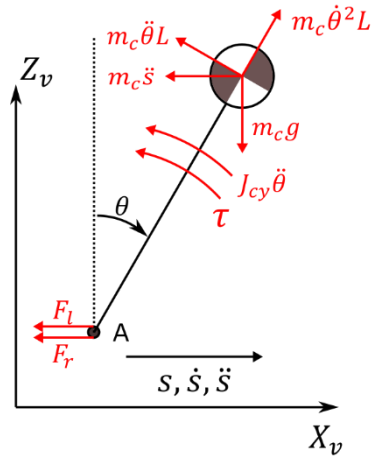


Figure 3-8 Forces and torques acting on the chassis

Therefore, another torque balance can be introduced, once again computed with respect to the rotational joint centre A:

$$\sum M_A(\text{chassis}) = 0 \quad (3.6)$$

Yielding:

$$\tau_r + \tau_l + J_{cy}\ddot{\theta} + m_c L^2 \ddot{\theta} + m_c L \ddot{s} \cos \theta = m_c g L \sin \theta \quad (3.7)$$

Finally, by closing again the rotational joints, a balance of all the horizontal forces acting on the entire vehicle is computed:

$$\sum F_{//}(\text{vehicle}) = 0 \quad (3.8)$$

yielding (see FIGURE 3.6):

$$m_c \ddot{s} + m_c L \ddot{\theta} \cos \theta + m_w \ddot{s}_r + m_w \ddot{s}_l = H_r + H_l + m_c L \dot{\theta}^2 \sin \theta \quad (3.9)$$

Summarizing, four force and torque balances are computed, namely:

$$\begin{cases} \sum M_A(\text{right wheel}) = 0 \\ \sum M_A(\text{left wheel}) = 0 \\ \sum M_A(\text{chassis}) = 0 \\ \sum F_{//}(\text{vehicle}) = 0 \end{cases} \quad (3.10)$$

This results into the following system of nonlinear equations:

$$\left\{ \begin{array}{l} \tau_r = J_w \frac{\ddot{s}_r}{R} + H_r R \\ \tau_l = J_w \frac{\ddot{s}_l}{R} + H_l R \\ \tau_r + \tau_l + J_{cy} \ddot{\theta} + m_c L^2 \ddot{\theta} + m_c L \dot{s} \cos \theta = m_c g L \sin \theta \\ m_c \ddot{s} + m_c L \ddot{\theta} \cos \theta + m_w \ddot{s}_r + m_w \ddot{s}_l = H_r + H_l + m_c L \dot{\theta}^2 \sin \theta \end{array} \right. \quad (3.11)$$

Rearranging the first two equation of (3.11), we obtain:

$$\left\{ \begin{array}{l} H_r = \frac{\tau_r}{R} - J_w \frac{\ddot{s}_r}{R^2} \\ H_l = \frac{\tau_l}{R} - J_w \frac{\ddot{s}_l}{R^2} \end{array} \right. \quad (3.12)$$

and by substituting H_r and H_l into the fourth equation of (3.11):

$$m_c \ddot{s} + m_c L \ddot{\theta} \cos \theta + m_w \ddot{s}_r + m_w \ddot{s}_l = \frac{\tau_r}{R} - J_w \frac{\ddot{s}_r}{R^2} + \frac{\tau_l}{R} - J_w \frac{\ddot{s}_l}{R^2} + m_c L \dot{\theta}^2 \sin \theta \quad (3.13)$$

rearranging, and recalling (3.2):

$$\begin{aligned} m_c \ddot{s} + m_w (\ddot{s}_r + \ddot{s}_l) + \frac{J_w}{R^2} (\ddot{s}_r + \ddot{s}_l) + m_c L \ddot{\theta} \cos \theta &= \frac{\tau_r}{R} + \frac{\tau_l}{R} + m_c L \dot{\theta}^2 \sin \theta \\ m_c \ddot{s} + 2m_w \frac{(\ddot{s}_r + \ddot{s}_l)}{2} + 2 \frac{J_w (\ddot{s}_r + \ddot{s}_l)}{2} + m_c L \ddot{\theta} \cos \theta &= \frac{\tau_r}{R} + \frac{\tau_l}{R} + m_c L \dot{\theta}^2 \sin \theta \\ m_c \ddot{s} + 2m_w \ddot{s} + 2 \frac{J_w}{R^2} \ddot{s} + m_c L \ddot{\theta} \cos \theta &= \frac{\tau_r}{R} + \frac{\tau_l}{R} + m_c L \dot{\theta}^2 \sin \theta \\ (m_c + 2m_w + 2 \frac{J_w}{R^2}) \ddot{s} + m_c L \ddot{\theta} \cos \theta &= \frac{\tau_r}{R} + \frac{\tau_l}{R} + m_c L \dot{\theta}^2 \sin \theta \end{aligned} \quad (3.14)$$

This bring us to a system of **two coupled non-linear dynamics equations** describing the longitudinal and tilting motion of the vehicle:

$$\left\{ \begin{array}{l} \tau_r + \tau_l + J_{cy} \ddot{\theta} + m_c L^2 \ddot{\theta} + m_c L \dot{s} \cos \theta = m_c g L \sin \theta \\ (m_c + 2m_w + 2 \frac{J_w}{R^2}) \ddot{s} + m_c L \ddot{\theta} \cos \theta = \frac{\tau_r}{R} + \frac{\tau_l}{R} + m_c L \dot{\theta}^2 \sin \theta \end{array} \right. \quad (3.15)$$

Linearizing around $\theta = \dot{\theta} = \ddot{\theta} = 0 \wedge \dot{s} = \ddot{s} = 0 \wedge \tau_r = \tau_l = 0$, we obtain:

$$\begin{cases} \delta\tau_r + \delta\tau_l + (J_{cy} + m_c L^2) \delta\ddot{\theta} + m_c L \delta\ddot{s} = m_c g L \delta\theta \\ (m_c + 2m_w + 2\frac{J_w}{R^2}) \delta\ddot{s} + m_c L \delta\ddot{\theta} = \frac{\delta\tau_r}{R} + \frac{\delta\tau_l}{R} \end{cases} \quad (3.16)$$

Rearranging the second equation of (3.16) (δ is omitted for sake of clarity):

$$\begin{aligned} (m_c + 2m_w + 2\frac{J_w}{R^2}) \ddot{s} + m_c L \ddot{\theta} &= \frac{1}{R} (\tau_r + \tau_l) \\ \ddot{\theta} &= -\frac{m_c + 2m_w + 2\frac{J_w}{R^2}}{m_c L} \ddot{s} + \frac{1}{R m_c L} (\tau_r + \tau_l) \end{aligned} \quad (3.17)$$

Then, substituting (3.17) into the first equation of (3.16), and rearranging:

$$\begin{aligned} \tau_r + \tau_l + \frac{J_{cy} + m_c L^2}{R m_c L} (\tau_r + \tau_l) - \frac{J_{cy} + m_c L^2}{m_c L} (m_c + 2m_w + 2\frac{J_w}{R^2}) \ddot{s} + m_c L \ddot{s} &= m_c g L \theta \\ \left(\frac{1}{m_c L} + \frac{1}{R} \frac{J_{cy} + m_c L^2}{m_c^2 L^2} \right) (\tau_r + \tau_l) - \frac{J_{cy} + m_c L^2}{m_c^2 L^2} (m_c + 2m_w + 2\frac{J_w}{R^2}) \ddot{s} + \ddot{s} &= g\theta \\ \left(\frac{1}{m_c L} + \frac{1}{R \tilde{m}} \right) (\tau_r + \tau_l) - \frac{1}{\tilde{m}} (m_c + 2m_w + 2\frac{J_w}{R^2} - \tilde{m}) \ddot{s} &= g\theta \\ \frac{1}{\tilde{m}} (m_c + 2m_w + 2\frac{J_w}{R^2} - \tilde{m}) \ddot{s} &= -g\theta + \frac{1}{\tilde{m}} \left(\frac{\tilde{m}}{m_c L} + \frac{1}{R} \right) (\tau_r + \tau_l) \\ (m_c + 2m_w + 2\frac{J_w}{R^2} - \tilde{m}) \ddot{s} &= -\tilde{m}g\theta + \left(\frac{\tilde{m}}{m_c L} + \frac{1}{R} \right) (\tau_r + \tau_l) \\ \tilde{M} \ddot{s} &= -\tilde{m}g\theta + \left(\frac{\tilde{m}}{m_c L} + \frac{1}{R} \right) (\tau_r + \tau_l) \\ \ddot{s} &= -\frac{\tilde{m}g}{\tilde{M}} \theta + \frac{\left(\frac{\tilde{m}}{m_c L} + \frac{1}{R} \right) (\tau_r + \tau_l)}{\tilde{M}} \end{aligned} \quad (3.18)$$

in which:

$$\tilde{m} = \frac{m_c^2 L^2}{J_{cy} + m_c L^2} \wedge \tilde{M} = m_c + 2m_w + 2\frac{J_w}{R^2} - \tilde{m} \quad (3.19)$$

Now, rearranging again the first equation of (3.16):

$$\begin{aligned} \frac{1}{J_{cy} + m_c L^2} (\tau_r + \tau_l) + \ddot{\theta} + \frac{m_c L}{J_{cy} + m_c L^2} \ddot{s} &= \frac{m_c L}{J_{cy} + m_c L^2} g \theta \\ \frac{\tilde{m}}{m_c^2 L^2} (\tau_r + \tau_l) + \ddot{\theta} + \frac{\tilde{m}}{m_c L} \ddot{s} &= \frac{\tilde{m}}{m_c L} g \theta \\ \ddot{\theta} &= -\frac{\tilde{m}}{m_c L} \ddot{s} + \frac{\tilde{m}}{m_c L} g \theta - \frac{\tilde{m}}{m_c^2 L^2} (\tau_r + \tau_l) \end{aligned} \quad (3.20)$$

and substituting (3.18) into (3.20) we obtain the equation for $\ddot{\theta}$ as:

$$\begin{aligned} \ddot{\theta} &= \frac{\tilde{m}^2 g}{\tilde{M} m_c L} \theta + \frac{\tilde{m}}{m_c L} g \theta - \frac{\tilde{m}}{m_c L} \frac{\left(\frac{\tilde{m}}{m_c L} + \frac{1}{R}\right)}{\tilde{M}} (\tau_r + \tau_l) - \frac{\tilde{m}}{m_c^2 L^2} (\tau_r + \tau_l) \\ \ddot{\theta} &= \frac{\tilde{m} g}{\tilde{M} m_c L} (\tilde{m} + \tilde{M}) \theta - \frac{\tilde{m}}{\tilde{M} m_c^2 L^2} \left(\tilde{m} + \frac{m_c L}{R} + \tilde{M} \right) (\tau_r + \tau_l) \end{aligned} \quad (3.21)$$

In summary, the two dynamical equations describing the motion of the vehicle in the $\vec{X}_v \vec{Z}_v$ plane are of the form:

$$\begin{cases} \ddot{s} = -a_1 \theta + b_1 \tau_r + b_1 \tau_l \\ \ddot{\theta} = a_2 \theta - b_2 \tau_r - b_2 \tau_l \end{cases} \quad (3.22)$$

in which:

$$\begin{aligned} a_1 &= \frac{\tilde{m} g}{\tilde{M}} \\ a_2 &= \frac{\tilde{m} g}{\tilde{M} m_c L} (\tilde{m} + \tilde{M}) \\ b_1 &= \frac{\left(\frac{\tilde{m}}{m_c L} + \frac{1}{R}\right)}{\tilde{M}} \\ b_2 &= \frac{\tilde{m}}{\tilde{M} m_c^2 L^2} \left(\tilde{m} + \frac{m_c L}{R} + \tilde{M} \right) \end{aligned} \quad (3.23)$$

The yaw motion is now considered. Once again, the two rotational joints are opened, and the constraint internal forces are added. FIGURE 3.9 shows a bird-eye view of the vehicle:

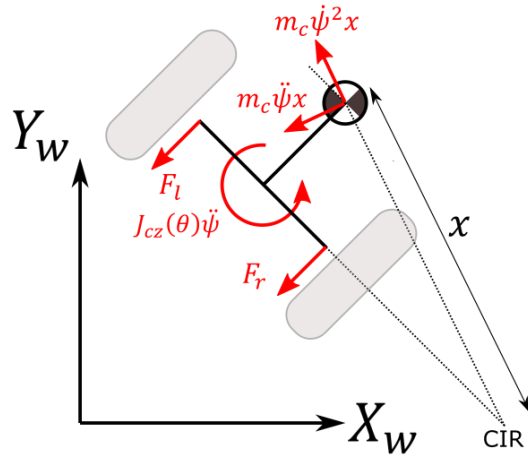


Figure 3-9 Forces and torques responsible for yaw motion

However, a simplifying hypothesis can be made by considering only the case in which the pitch angle is close to zero; as we will see in the next chapters, this assumption is perfectly acceptable provided that a good stabilization controller is implemented, and the vehicle is not requested to perform large longitudinal acceleration while turning. If θ is supposed to be very close to zero, the forces acting on the yaw motions are only the ones depicted in FIGURE 3.10.

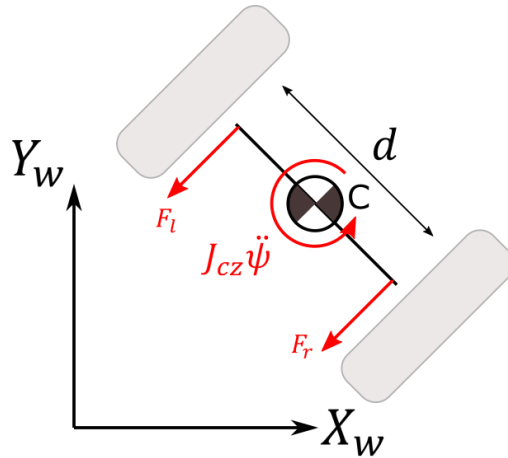


Figure 3-10 Forces and torques responsible for yaw motion - simplified model

In this case the only forces having non-null moment with respect to the axle centre C are the reaction forces F_r and F_l , and the inertial moment $J_{cz}\ddot{\psi}$. All the other gravitational or inertial forces are applied directly on the axis of rotation, and as such they do not affect the yaw dynamics. Yaw dynamic equation can then be retrieved by writing a balance of moments with respect to the track centre C:

$$\sum M_c(\text{chassis}) = 0 \quad (3.24)$$

which is:

$$\frac{(F_r - F_l)d}{2} = J_{cz}\ddot{\psi} \quad (3.25)$$

In order to compute F_r , let's consider the right wheel first. Referring again to FIGURE 3.6, we can write a balance of moments with respect to tyre contact point, (*CIR* in the figure):

$$\begin{aligned} m_w R \ddot{s}_r + \frac{J_w}{R} \ddot{s}_r &= \tau_r + F_r R \\ F_r &= \left(m_w + \frac{J_w}{R^2} \right) \ddot{s}_r - \frac{\tau_r}{R} \end{aligned} \quad (3.26)$$

Similarly, for the left wheel:

$$F_l = \left(m_w + \frac{J_w}{R^2} \right) \ddot{s}_l - \frac{\tau_l}{R} \quad (3.27)$$

Substituting (3.26) and (3.27) into (3.25), and recalling (3.2):

$$\begin{aligned} \left(m_w + \frac{J_w}{R^2} \right) (\ddot{s}_r - \ddot{s}_l) \frac{d}{2} - \frac{d}{2R} (\tau_r - \tau_l) &= J_{cz}\ddot{\psi} \\ \left(m_w + \frac{J_w}{R^2} \right) \frac{d^2}{2} \ddot{\psi} - \frac{d}{2R} (\tau_r - \tau_l) &= J_{cz}\ddot{\psi} \\ \left(\left(m_w + \frac{J_w}{R^2} \right) \frac{d^2}{2} - J_{cz} \right) \ddot{\psi} &= \frac{d}{2R} (\tau_r - \tau_l) \\ \ddot{\psi} &= \frac{d}{2R} (\tau_r - \tau_l) \end{aligned} \quad (3.28)$$

Equation (3.28) is already linear of the form:

$$\ddot{\psi} = b_3 \tau_r - b_3 \tau_l \quad (3.29)$$

in which:

$$b_3 = \frac{d}{2R\tilde{J}} \quad (3.30)$$

Finally, putting (3.22) and (3.29) together, and setting $x_1 = \dot{s}$; $x_2 = \theta$; $x_3 = \dot{\theta}$; $x_4 = \dot{\psi}$; $u_1 = \tau_r$; $u_2 = \tau_l$ the full state-space form of the system is obtained as:

$$\begin{cases} \dot{x}_1 = -a_1 x_2 + b_1 u_1 + b_1 u_2 \\ \dot{x}_2 = x_3 \\ \dot{x}_3 = a_2 x_2 - b_2 u_1 - b_2 u_2 \\ \dot{x}_4 = b_3 u_1 - b_3 u_2 \end{cases} \quad (3.31)$$

or, in the usual vector form:

$$\dot{x} = Ax + Bu \quad (3.32)$$

with state vector $x = [\dot{s} \quad \theta \quad \dot{\theta} \quad \dot{\psi}]^T$, control vector $u = [\tau_r \quad \tau_l]^T$, state matrix:

$$A = \begin{bmatrix} 0 & -a_1 & 0 & 0 \\ 0 & 0 & 1 & 0 \\ 0 & a_2 & 0 & 0 \\ 0 & 0 & 0 & 0 \end{bmatrix} \quad (3.33)$$

and input matrix:

$$B = \begin{bmatrix} b_1 & b_1 \\ 0 & 0 \\ -b_2 & -b_2 \\ b_3 & -b_3 \end{bmatrix} \quad (3.34)$$

Notice that the fourth row and the fourth column of (3.33) are null due to the dynamical decoupling between longitudinal and yaw dynamics implied in the linearization around $\theta = 0$.

3.3 Input-Output transfer function

The input-output transfer functions for the dynamical system (3.32) are now computed and analysed in order to highlight some of the peculiar aspects of WIPs that will be considered in the design phase of both the LQ and the Cascade controllers.

Starting from (3.33) and (3.34) it is possible to compute the matrix of transfer functions $G(s) = C(sI - A)^{-1}B$, setting $C = I_4$:

$$G(s) = \begin{bmatrix} \frac{b_1(s^2 - a_2 + \frac{a_1 b_2}{b_1})}{s(s^2 - a_2)} & \frac{b_1(s^2 - a_2 + \frac{a_1 b_2}{b_1})}{s(s^2 - a_2)} \\ -\frac{b_2}{s^2 - a_2} & -\frac{b_2}{s^2 - a_2} \\ -\frac{b_2 s}{s^2 - a_2} & -\frac{b_2 s}{s^2 - a_2} \\ \frac{b_3}{s} & -\frac{b_3}{s} \end{bmatrix} \quad (3.35)$$

which is of the form:

$$G(s) = \begin{bmatrix} G_{\tau s}(s) & G_{\tau s}(s) \\ G_{\tau \theta}(s) & G_{\tau \theta}(s) \\ G_{\tau \dot{\theta}}(s) & G_{\tau \dot{\theta}}(s) \\ G_{\tau \dot{\psi}}(s) & -G_{\tau \dot{\psi}}(s) \end{bmatrix} \quad (3.36)$$

Due to the particular structure of the system, it is convenient to adopt a different input vector, namely:

$$u = [\tau_c \quad \tau_d]^T \quad (3.37)$$

with

$$\tau_c = \tau_r + \tau_l$$

$$\tau_d = \tau_r - \tau_l$$

$$(3.38)$$

In this way we have:

$$G(s) = \begin{bmatrix} G_{\tau s}(s) & 0 \\ G_{\tau \theta}(s) & 0 \\ G_{\tau \dot{\theta}}(s) & 0 \\ 0 & G_{\tau \dot{\psi}}(s) \end{bmatrix} \quad (3.39)$$

and the analysis can be carried on separately for the longitudinal-pitch dynamics, on which the common torque τ_c acts, and the yaw dynamics, affected by the differential torque τ_d . FIGURE 3.11 shows a block representation of this scheme:

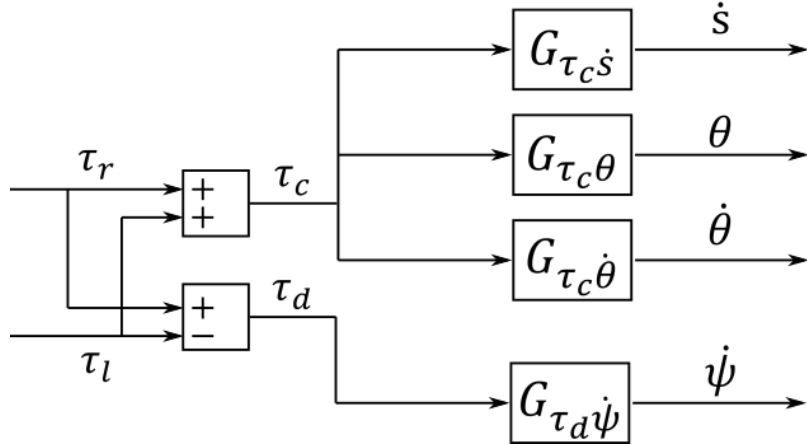


Figure 3-11 Block scheme with decoupled dynamics

3.3.1 From torque to pitch: $G_{\tau\theta}(s)$

The first transfer function to be considered is the one relating the common mode torque τ_c and the pitch θ , which is critical in the stabilization of the vehicle. Let's recall the mathematical expression for $G_{\tau\theta}(s)$:

$$G_{\tau\theta}(s) = -\frac{b_2}{s^2 - a_2} \quad (3.40)$$

Recalling (3.19), we can notice that:

$$m_c > \tilde{m} > 0 \quad (3.41)$$

and therefore:

$$\tilde{M} > 0 \quad (3.42)$$

and:

$$a_2 = \frac{\tilde{m}g}{\tilde{M}m_c L} (\tilde{m} + \tilde{M}) > 0 \quad (3.43)$$

Consequently, we can reformulate (3.40) as:

$$G_{\tau\theta}(s) = -\frac{b_2}{(s - \sqrt{a_2})(s + \sqrt{a_2})} \quad (3.44)$$

From (3.44), we can see that $G_{\tau\theta}(s)$ has 2 real poles which are symmetric to the imaginary axis: the negative pole located in $s = -\sqrt{a_2}$ is a stable pole, whereas the symmetric pole in $s = \sqrt{a_2}$ is an unstable pole. As expected, $G_{\tau\theta}(s)$ is an unstable transfer function. Moreover, the poles symmetry makes it impossible to obtain asymptotic stability for the system using a simple proportional action on the pitch. In fact, by looking at the root locus of $G_{\tau\theta}(s)$ reported on FIGURE 3.12 we can see that there is no gain for which both the closed-loop poles are located in the negative-real-part half plane.

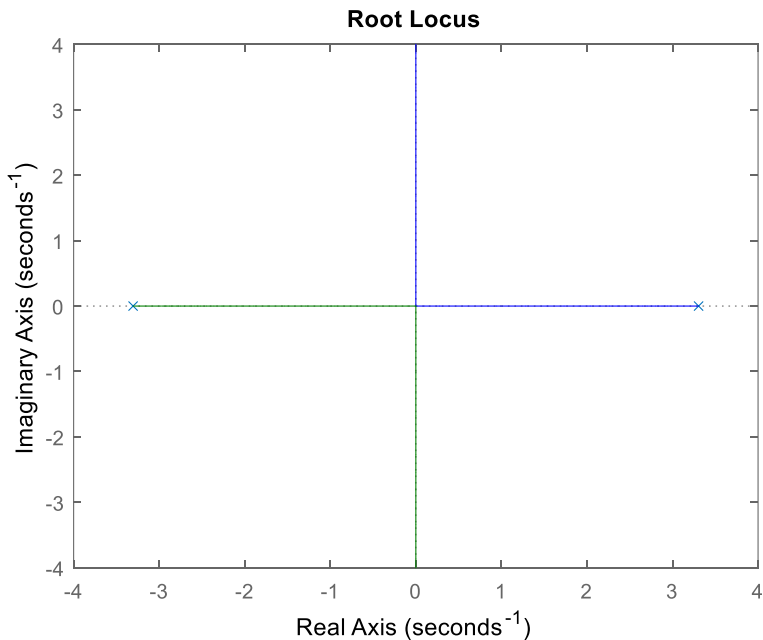


Figure 3-12 Inverse root locus of $G_{\tau_c\theta}(s)$

On the other hand, the system is easily stabilized by introducing a negative valued zero, i.e. by using a simple PD controller, which correspond to add a proportional action on the pitch rate.

Finally, we notice that, as expected $G_{\dot{\tau}\theta}(s)$ is trivially given by: eq:

$$G_{\dot{\tau}\theta}(s) = -\frac{b_2 s}{s^2 - a_2} = s G_{\tau\theta}(s) \quad (3.45)$$

3.3.2 From torque to speed: $G_{\tau\dot{s}}(s)$

Some relevant considerations can be made by looking at the transfer function relating the torque to the speed. First of all, we notice that:

$$G_{\tau\dot{s}}(s) = \frac{b_1(s^2 - a_2 + \frac{a_1 b_2}{b_1})}{s(s^2 - a_2)} = G_{\tau\theta}(s) \frac{(s^2 - a_2 + \frac{a_1 b_2}{b_1})}{s} = G_{\tau\theta}(s) G_{\theta\dot{s}}(s) \quad (3.46)$$

in which $G_{\theta\dot{s}}(s)$ can be seen as the transfer function between the pitch angle and the speed. This situation is schematically depicted in FIGURE 3.13.

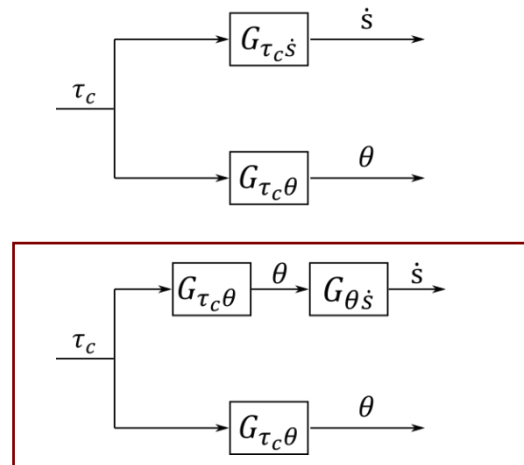


Figure 3-13 Schematic representation of the equivalence $G_{\tau\dot{s}}(s) = G_{\tau\theta}(s) G_{\theta\dot{s}}(s)$

By looking at the system in this way we can see that the vehicle can actually be driven using the pitch angle to produce a certain speed. This fact will actually be explicitly exploited in the design phase of the cascade controller, whereas it is implicitly used by the LQ regulator which acts on the whole state of the system.

Let's now analyse the transfer function $G_{\theta\dot{s}}(s)$ relating the pitch angle and the speed, which is:

$$G_{\theta\dot{s}}(s) = \frac{(s^2 - a_2 + \frac{a_1 b_2}{b_1})}{s} \quad (3.47)$$

First off all we notice the presence of pole in $s = 0$, implying the presence of an integral action between θ and \dot{s} . This can be intuitively explained by the fact that the pitch angle is directly related to the longitudinal acceleration of the vehicle, namely \ddot{s} ; since \dot{s} is the derivative of \ddot{s} the action of θ on \dot{s} will be an integral one. Another quite interesting observation can be made by looking at the numerator of $G_{\theta\dot{s}}(s)$:

$$N(s) = s^2 - a_2 + \frac{a_1 b_2}{b_1} = s^2 - \left(a_2 - \frac{a_1 b_2}{b_1}\right) \quad (3.48)$$

Since $a_2 - \frac{a_1 b_2}{b_1} > 0$, $N(s)$ can be decomposed as

$$N(s) = (s - a_{\text{nmf}})(s + a_{\text{nmf}}) \quad (3.49)$$

with

$$a_{\text{nmf}} = \sqrt{\left(a_2 - \frac{a_1 b_2}{b_1}\right)} > 0 \quad (3.50)$$

Therefore, due to the presence of a positive real-valued zero, the transfer function $G_{\theta s}(s)$ shows a non-minimum phase behavior.

The proof for $a_2 - \frac{a_1 b_2}{b_1} > 0$ is reported in the following:

Proof:

$$a_2 - \frac{a_1 b_2}{b_1} > 0 \quad (3.51)$$

by recalling (3.23), we can rewrite the inequality as:

$$\frac{\tilde{m}^2 g}{\tilde{M} m_c L} \left(1 + \frac{\tilde{M}}{\tilde{m}} - \frac{\left(\tilde{m} + \frac{m_c L}{R} + \tilde{M} \right)}{m_c L \left(\frac{\tilde{m}}{m_c L} + \frac{1}{R} \right)} \right) > 0 \quad (3.52)$$

Since $\frac{\tilde{m}^2 g}{\tilde{M} m_c L} > 0$, we the inequality becomes:

$$\begin{aligned} 1 + \frac{\tilde{M}}{\tilde{m}} - \frac{\left(\tilde{m} + \frac{m_c L}{R} + \tilde{M} \right)}{m_c L \left(\frac{\tilde{m}}{m_c L} + \frac{1}{R} \right)} &> 0 \\ 1 + \frac{\tilde{M}}{\tilde{m}} - \frac{\left(\tilde{m} + \frac{m_c L}{R} + \tilde{M} \right)}{\tilde{m} + \frac{m_c L}{R}} &> 0 \end{aligned}$$

$$\begin{aligned}
 1 + \frac{\tilde{M}}{\tilde{m}} - 1 - \frac{\tilde{M}}{\tilde{m} + \frac{m_c L}{R}} &> 0 \\
 \frac{\tilde{M}}{\tilde{m}} - \frac{\tilde{M}}{\tilde{m} + \frac{m_c L}{R}} &> 0 \\
 \frac{\tilde{M}}{\tilde{m}} &> \frac{\tilde{M}}{\tilde{m} + \frac{m_c L}{R}}
 \end{aligned} \tag{3.53}$$

which is always true due to the fact that all the variables are positive ones. This proves (3.51).

Inequality (3.53) proves that a WIP system like YAPE inevitably shows a non-minimum phase behaviour in the transfer function between pitch and speed. This fact implies that the vehicle will show a counter phase motion in the speed response (FIGURE 3.14), which is typical of such systems.

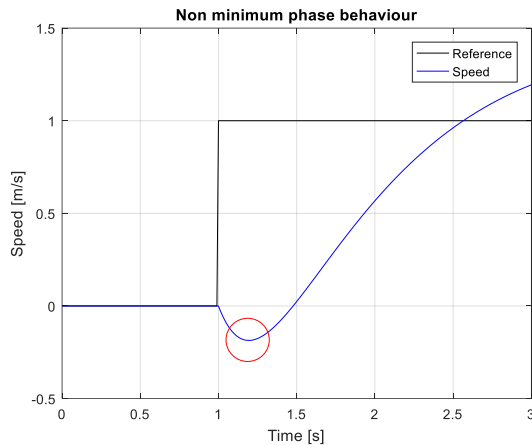


Figure 3-14 Non-minimum phase behaviour

??

The non-minimum phase behaviour can be intuitively explained as follows: if a positive speed is required, the vehicle will need to assume a positive pitch position, which correspond to a positive steady state torque and therefore to an acceleration. However, in order for the chassis to assume this position the wheels have to move backwards first; therefore, the vehicle will assume a negative speed until the steady state pitch is reached, then it will start to accelerate in the desired direction. Once again, this fact is implicitly accounted by LQ controller, whereas it will have to be explicitly considered in the design of the speed loop in the cascade approach.

Finally, by looking at (3.53) we can make some considerations on the influence of the mechanical parameters on such non-minimum-phase behaviour. In particular (3.53) puts in evidence that the absolute value of a_{nmf} increases at the increase of the difference:

$$\frac{\tilde{M}}{\tilde{m}} - \frac{\tilde{M}}{\tilde{m} + \frac{m_c L}{R}}$$

We can then state that increasing the product $m_c L$ or decreasing the value of R will cause an increase in the value of a_{nmf} , and consequently a distancing of the real-valued zero from the origin of the complex plane. This in turns reduces the non-minimum phase behaviour of the system. On the other hand, decreasing the vehicle mass, decreasing the height of the c.o.g, or increasing the wheel radius will make the positive zero to be closer to the complex plane origin, therefore accentuating the inverse response of the system.

3.4 Conclusions

The aim of this chapter was to develop a suitable model for the vehicle operating in nominal conditions, i.e. running on a flat surface with no loaded package. The nonlinear equations describing the motion of the vehicle were computed; then a linear model was obtained by means of a linearization around the unstable upright position of the chassis. An analysis of the main dynamical aspects of the system was subsequently presented starting from the transfer functions computed on the linearized system. In particular, the unstable nature of the pitch dynamics was highlighted, together with the crucial role of the pitch rate in the design of a stabilizing controller. Finally, a relation between speed and pitch was established, suggesting the possibility of driving the vehicle using the pitch as a control variable for the speed; in such relation, a peculiar non-minimum phase behaviour was also observed. In the next chapter are analysed the effects of two of the main disturbs that the vehicle will have to face, namely the package load and unload operations and the presence of sloped roads.

Chapter 4 - Effects of load and slopes

4.1 Introduction

In the previous chapter, a dynamical system was developed to model the behaviour of YAPE when it operates in nominal conditions. However, due to the particular type of tasks that the vehicle will have to perform, such model could result to be inadequate to design a suitable controller.

In particular, being YAPE a package delivery vehicle, it is expected to carry a certain amount of load, resulting in a variation of the total swinging mass and a displacement of the vehicle centre of gravity. This in turn has relevant effects both on the longitudinal and on the pitch behaviour of the vehicle. Moreover, in order to operate in an urban environment, YAPE should be able to face sloped roads, whether it is to get on a sidewalk or to overcome an overpass. Such obstacles introduce a further force component on the vehicle axle, which acts as a disturb on the longitudinal dynamics of the vehicle.

Both these disturbs are modelled and analysed in this chapter, providing results which will be useful for the regulator design phase.

4.2 Effects of loads

Since YAPE is designed to operate as a package delivery vehicle, it is expected to be subjected to occasional variations of some of the physical parameters considered in the model. In particular, the total swinging mass m_c , the moments of inertia J_{cy} and J_{cz} and the c.o.g position are actually unknown and may change as a function of the number and weight of carried loads. In this work, variations of m_c , J_{cy} and J_{cz} were considered as simple parametric uncertainties, and as such they are treated in the control design section of this work, in CHAPTER 10 and 11. Particular attention was instead dedicated to the c.o.g position variations. The nominal position of the c.o.g is defined, in the $\vec{X}_v\vec{Y}_v\vec{Z}_v$ reference frame, as:

$$p_{cog} = [0 \quad 0 \quad L] \tag{4.1}$$

which means that the c.o.g is located above the centre of the vehicle axle, at a distance L from it. Due to the load and unload operations though, p_{cog} can change to any point inside the chassis. In other terms, once a pack is loaded, the c.o.g position results to be:

$$p_{cog} = [\Delta L_x \quad \Delta L_y \quad L + \Delta L_z] \tag{4.2}$$

The vertical variation ΔL_z is basically an uncertainty on the parameter L , and as such is treated in the control-related chapters, together with the mass and moment of inertia variations. The lateral variation ΔL_y has no effect on the longitudinal and pitch dynamics; moreover, in conditions of normal usage of the vehicle, ΔL_y is supposed to have negligible effects also on the yaw dynamics. Conversely, due to the unstable nature of the vehicle, ΔL_x has a direct impact on the pitch and longitudinal dynamics. In order to study the effects of such a variation, the L-shaped pendulum depicted in FIGURE 4.1 is considered.

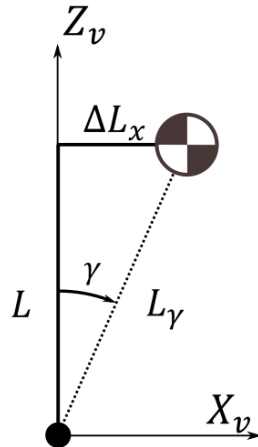


Figure 4-1 Modelling of unbalanced loads

The angle γ is defined as the angular displacement of the c.o.g with respect to the nominal position, i.e. the angle between \vec{Z}_v and the line joining the c.o.g and the pivot point. The distance between the c.o.g and the pivot point is therefore:

$$L_\gamma = \frac{L}{\cos \gamma} \quad (4.3)$$

Following the same procedure described for the nominal case, a set of balance equations can be derived also in this case:

$$\left\{ \begin{array}{l} \tau_r = J_w \frac{\ddot{s}_r}{R} + H_r R \\ \tau_l = J_w \frac{\ddot{s}_l}{R} + H_l R \\ \tau_r + \tau_l + J_{cy} \ddot{\theta} + m_c L_\gamma^2 \ddot{\theta} + m_c L_\gamma \ddot{s} \cos(\theta + \gamma) = m_c g L_\gamma \sin(\theta + \gamma) \\ m_c \ddot{s} + m_c L_\gamma \ddot{\theta} \cos(\theta + \gamma) + m_w \ddot{s}_r + m_w \ddot{s}_l = H_r + H_l + m_c L_\gamma \dot{\theta}^2 \sin(\theta + \gamma) \end{array} \right. \quad (4.4)$$

By substitution, we obtain again the system of two non-linear equations:

$$\begin{cases} \tau_r + \tau_l + J_{cy}\ddot{\theta} + m_c L_\gamma^2 \ddot{\theta} + m_c L_\gamma \dot{s} \cos(\theta + \gamma) = m_c g L_\gamma \sin(\theta + \gamma) \\ (m_c + 2m_w + 2\frac{J_w}{R^2})\ddot{s} + m_c L_\gamma \ddot{\theta} \cos(\theta + \gamma) = \frac{\tau_r}{R} + \frac{\tau_l}{R} + m_c L_\gamma \dot{\theta}^2 \sin(\theta + \gamma) \end{cases} \quad (4.5)$$

and, after the linearization (in which $\gamma = 0$ is imposed):

$$\begin{cases} \delta\tau_r + \delta\tau_l + (J_{cy} + m_c L^2)\delta\ddot{\theta} + m_c L \delta\ddot{s} = m_c g L \delta\theta + m_c g L \delta\gamma \\ (m_c + 2m_w + 2\frac{J_w}{R^2})\delta\ddot{s} + m_c L \delta\ddot{\theta} = \frac{\delta\tau_r}{R} + \frac{\delta\tau_l}{R} \end{cases} \quad (4.6)$$

Notice that, due to the linearization $L_\gamma \rightarrow L$. At this point, it is convenient to define a new variable:

$$\tilde{\theta} = \theta + \gamma \quad (4.7)$$

Since γ is considered to be constant, even if unknown parameter, it holds that $\dot{\tilde{\theta}} = \dot{\theta}$ and $\ddot{\tilde{\theta}} = \ddot{\theta}$. By substituting $\tilde{\theta}$ in the dynamical equations we get:

$$\begin{cases} \delta\tau_r + \delta\tau_l + (J_{cy} + m_c L^2)\delta\ddot{\tilde{\theta}} + m_c L \delta\ddot{s} = m_c g L \delta\tilde{\theta} \\ (m_c + 2m_w + 2\frac{J_w}{R^2})\delta\ddot{s} + m_c L \delta\ddot{\tilde{\theta}} = \frac{\delta\tau_r}{R} + \frac{\delta\tau_l}{R} \end{cases} \quad (4.8)$$

that is identical to what was found in the nominal case. Equation (4.8) can be interpreted in this way: θ is the measured geometrical pitch of the chassis whereas $\tilde{\theta}$ is the actual angular displacement with respect to the equilibrium position. Therefore, closing a loop on θ alone, would force the system to assume an unstable position. Moreover, the same transfer functions retrieved in CHAPTER 3 are obtained also in this case. In particular, we point out that:

$$G_{\tilde{\theta}\dot{s}}(s) = \frac{(s^2 - a_2 + \frac{a_1 b_2}{b_1})}{s} \quad (4.9)$$

is the transfer function between the total angle $\tilde{\theta}$ and the longitudinal speed \dot{s} , and since (4.7) holds, (4.9) is also the transfer function between the angular c.o.g displacement γ and \dot{s} . We can therefore conclude that a constant longitudinal displaced position of the c.o.g has an integral action on the speed which, if not properly controlled, leads to a drifting behaviour of the vehicle. A viable option to solve this problem is to introduce an integral action on the speed. As will be explained in CHAPTER 10 and 11, this solution can be implemented in the LQ approach by adding an integral state for the speed to the linearized model, and by including explicit integral action on the speed regulator in the Cascade approach.

4.3 Effects of slopes

One of the main difficulties that YAPE will face by operating in an urban environment is the presence of road sections with non-zero slope. In an urban environment this can be encountered from short and relatively steep sidewalk slides, to long uphill roads and overpasses. A natural requirement for any stabilization and driving controller, is then to be able to maintain certain performances when facing up a gradient. In particular, the vehicle must be able to overcome such gradients and also to keep a stationary stable position despite the presence of sloped roads.

The aim of this section is therefore to provide a mathematical tool expressing the effect of a gradient as a function of the other vehicle's parameters (masses, moments of inertia and so on). Such model will be useful in the controller design phase, and could also be used in future works as a starting point in the design of specific compensation tools. For sake of simplicity, the study was limited to the longitudinal and pitch dynamics. Nonetheless the controllers proposed in CHAPTERS 10 and 11 have shown the ability to perform turns on non-zero slope roads.

This dynamical model of the vehicle operating on a sloped road can be obtained along the lines of what was done in the nominal case. For the sake of clarity, the unbalanced load case is not considered here. In FIGURE 4.2, a schematic view of the vehicle traveling an uphill is shown on the usual $\vec{X}_w \vec{Z}_w$ plane.

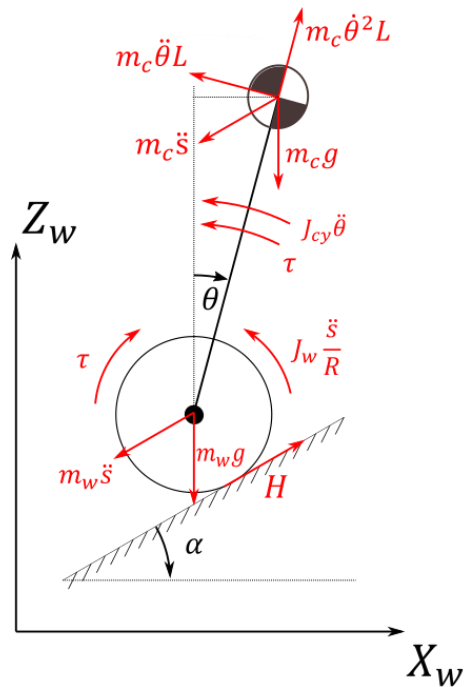


Figure 4-2 Forces and torques acting on the vehicle while travelling on uphill road

Writing the usual balance equations, we get:

$$\left\{ \begin{array}{l} \tau_r = J_w \frac{\ddot{s}_r}{R} + H_r R \\ \tau_l = J_w \frac{\ddot{s}_l}{R} + H_l R \\ \tau_r + \tau_l + J_{cy} \ddot{\theta} + m_c L^2 \ddot{\theta} + m_c L \ddot{s} \cos(\theta + \alpha) = m_c g L \sin(\theta) \\ m_c \ddot{s} + m_c L \ddot{\theta} \cos(\theta + \alpha) + m_w \ddot{s}_r + m_w \ddot{s}_l + 2m_w g \sin \alpha + m_c g \sin \alpha = \dots \\ \dots = H_r + H_l + m_c L \dot{\theta}^2 \sin(\theta + \alpha) \end{array} \right. \quad (4.10)$$

which yields:

$$\boxed{\left\{ \begin{array}{l} \tau_r + \tau_l + J_{cy} \ddot{\theta} + m_c L^2 \ddot{\theta} + m_c L \ddot{s} \cos(\theta + \alpha) = m_c g L \sin(\theta) \\ \left(m_c + 2m_w + 2 \frac{J_w}{R^2} \right) \ddot{s} + m_c L \ddot{\theta} \cos(\theta + \alpha) + (2m_w + m_c) g \sin \alpha = \dots \\ \dots = \frac{\tau_r}{R} + \frac{\tau_l}{R} + m_c L \dot{\theta}^2 \sin(\theta + \alpha) \end{array} \right.} \quad (4.11)$$

At this point, it is possible to obtain the equilibrium position for a certain value of α . First of all, we set $\tau_r = \tau_l = \bar{\tau}$, which implies no differential torque, and therefore no action on the yaw rate. Supposing that the vehicle starts with $\dot{\psi} = 0$, the previous requirement corresponds to have the vehicle proceeding in a straight line. The equilibrium point is then:

$$\left\{ \begin{array}{l} 2\bar{\tau} = m_c g L \sin(\bar{\theta}) \\ (2m_w + m_c) g \sin \alpha = 2 \frac{\bar{\tau}}{R} \end{array} \right. \quad \left\{ \begin{array}{l} 2\bar{\tau} = m_c g L \sin(\bar{\theta}) \\ \bar{\tau} = \frac{Rg(2m_w + m_c) \sin \alpha}{2} \end{array} \right. \quad \left\{ \begin{array}{l} Rg(2m_w + m_c) \sin \alpha = m_c g L \sin(\bar{\theta}) \\ \bar{\tau} = \frac{Rg(2m_w + m_c) \sin \alpha}{2} \end{array} \right. \quad \left\{ \begin{array}{l} \bar{\theta} = \sin^{-1} \left(\frac{R \sin \alpha}{L} \left(\frac{2m_w}{m_c} + 1 \right) \right) \\ \bar{\tau} = \frac{Rg(2m_w + m_c) \sin \alpha}{2} \end{array} \right. \quad (4.12)$$

As we can notice from (4.12), the equilibrium position in presence of $\alpha \neq 0$ is not $\bar{\theta} = 0 \wedge \bar{\tau} = 0$, but rather:

$$\begin{aligned} \bar{\theta} &\geq 0 \wedge \bar{\tau} \geq 0 & \text{for } 0 \leq \alpha < \frac{\pi}{2} \\ \bar{\theta} &< 0 \wedge \bar{\tau} < 0 & \text{for } -\frac{\pi}{2} < \alpha < 0 \end{aligned} \quad (4.13)$$

Equation (4.13) points out that the vehicle needs to lean forward to maintain a constant or null speed on an uphill, and conversely it has to lean backward to obtain steady state on a downhill.

This will have to be taken into account in the **controller design** phase but also in an eventual **trajectory planning phase**: in fact, as will be explained in **CHAPTER 8**, the equation (4.13) primarily poses a geometrical limit to the maximum affordable slopes.

Concerning the effects on the longitudinal speed it is possible to observe that the presence of a slope introduces a force component, parallel to ground, acting on the wheel's hub (FIGURE 4.3)

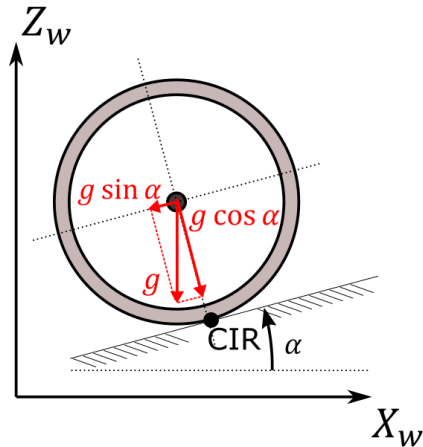


Figure 4-3 Gravitational acceleration decomposition in uphill roads

This represent a constant additive disturb on the wheel's longitudinal acceleration, and as such, a ramp disturb on the speed (due to integration occurring between the two quantities). Such considerations could be enough to solve the road-gradient problem: as long as the regulator provides an adequate rejection to ramp disturbs on the speed, the vehicle will be able to perform properly also on uphills and downhills.

4.4 Conclusions

The effects of both unbalanced loads and sloped roads were investigated in this chapter. Dynamical models were computed and confronted with the one obtained in the nominal case. The nature of both this disturbs suggests the need of an integral action on the speed controller, in order to avoid undesired drifting behaviours. The effectiveness of the regulator in facing such disturbs will be experimentally tested and used as a term of comparison between different control approaches.

Chapter 5 - IMU calibration

5.1 Introduction

The IMU is undoubtedly the most important proprioceptive sensor mounted on YAPE. It is a 6-DOF measurement unit, equipped with 3 accelerometers and 3 gyroscopes, and can therefore provide a measure of the acceleration and rotational speed components along a body-fixed right-handed frame. As will be explained in Chapter 6, IMU readings will be used to obtain an estimation of the vehicle's pitch and pitch rate. As such, a good data processing performed on the IMU has a direct and relevant effect on the vehicle stabilization and behaviour.

In the following chapter, the main error sources affecting the IMU will be treated. In particular, structural errors and mounting errors will be analysed. The firsts are intrinsic in the nature of the sensor, whereas the seconds are attributable to the misalignment between the vehicle-fixed reference frame, and the sensor-fixed one. Two offline procedures will be developed to compensate both errors, thus providing reliable measures to use in the state estimation algorithms.

5.2 Error model

Structural errors are considered first. Let $\vec{X}_s\vec{Y}_s\vec{Z}_s$ be the right-handed sensor-fixed frame to which the measurements are referred, and let the IMU be subjected to a generic acceleration A and to have a generic rotational speed W (FIGURE 5.1).

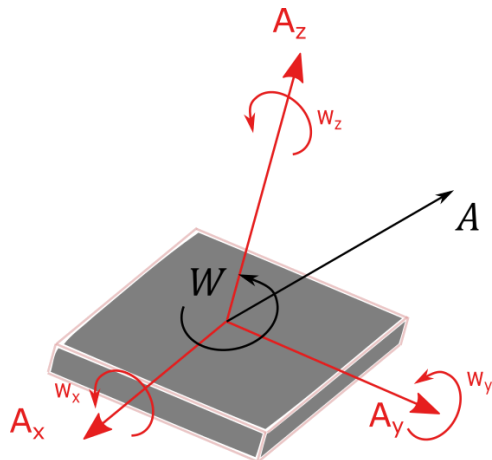


Figure 5-1 Schematic representation of IMU DoF

Then, by decomposing the acceleration and the rotational speed vectors with respect to the sensor-fixed frame, we get $A_s = [\ddot{x} \quad \ddot{y} \quad \ddot{z}]^T$ and $W_s = [\omega_x \quad \omega_y \quad \omega_z]^T$. In an ideal situation, i.e. with the sensor being affected by nothing else than electrical noise, we should have:

$$\begin{aligned} a_x &= \ddot{x} + \eta_{ax} \\ a_y &= \ddot{y} + \eta_{ay} \\ a_z &= \ddot{z} + \eta_{az} \\ g_x &= \omega_x + \eta_{gx} \\ g_y &= \omega_y + \eta_{gy} \\ g_z &= \omega_z + \eta_{gz} \end{aligned} \tag{5.1}$$

in which a_i is the value measured by the accelerometer on the i-axis, g_i is the value measured by the gyrometer on the i-axis, and $\eta_{ax}, \eta_{ay}, \dots$ are white noises affecting the measures. Although, due to causes which are intrinsic in the structure of the sensors, the actual measurements can be described as:

$$\begin{aligned} a_x &= m_{ax}\ddot{x} + q_{ax} + \eta_{ax} \\ a_y &= m_{ay}\ddot{y} + q_{ay} + \eta_{ay} \\ a_z &= m_{az}\ddot{z} + q_{az} + \eta_{az} \\ g_x &= m_{gx}\omega_x + q_{gx} + \eta_{gx} \\ g_y &= m_{gy}\omega_y + q_{gy} + \eta_{gy} \\ g_z &= m_{gz}\omega_z + q_{gz} + \eta_{gz} \end{aligned} \tag{5.2}$$

in which m_{ax}, m_{ay}, \dots are gain factor with $m_i \neq 1$ in general, and q_{ax}, q_{ay}, \dots are offset components with $q_i \neq 0$ in general. In the practice, the values of m_{gx}, m_{gy} and m_{gz} have proved to be very close to the unit value, and can therefore be neglected in the model. Hence, the final model for the 6 IMU readings is:

$$\begin{aligned} a_x &= m_{ax}\ddot{x} + q_{ax} + \eta_{ax} \\ a_y &= m_{ay}\ddot{y} + q_{ay} + \eta_{ay} \\ a_z &= m_{az}\ddot{z} + q_{az} + \eta_{az} \\ g_x &= \omega_x + q_{gx} + \eta_{gx} \\ g_y &= \omega_y + q_{gy} + \eta_{gy} \\ g_z &= \omega_z + q_{gz} + \eta_{gz} \end{aligned} \tag{5.3}$$

In addition to the uncertainties so far explained, a correct usage of the IMU measurements needs to account for the misalignment between the sensor-fixed reference frame and the chassis-fixed one (FIGURE 5.2).

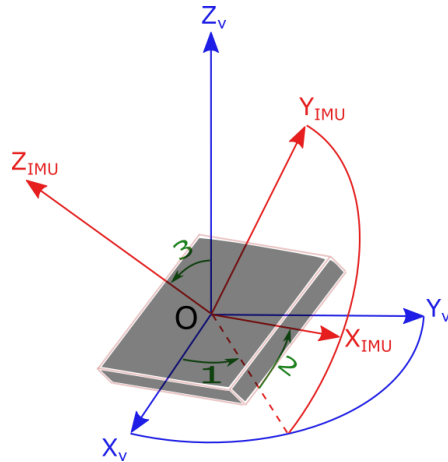


Figure 5-2 Schematic representation of misalignment between IMU frame and vehicle frame

Let $\vec{X}_v \vec{Y}_v \vec{Z}_v$ be the chassis-fixed reference frame described in CHAPTER 3. For sake of simplicity, let's suppose that $\vec{X}_v \vec{Y}_v \vec{Z}_v$ and $\vec{X}_s \vec{Y}_s \vec{Z}_s$ share the same origin, denoted with O . As will be explained in CHAPTER 6, this hypothesis has no influence on the equations used in the state estimation algorithms. Ideally, if the IMU was mounted so that to be perfectly aligned with the vehicle reference frame, it would be possible to write:

$$A_v = A_s \quad (5.4)$$

in which A_v is the acceleration of point O expressed in the chassis frame and A_s is the same acceleration expressed in the sensor frame; similarly:

$$W_v = W_s \quad (5.5)$$

in which W_v is the vehicle rotational speed expressed in the chassis reference frame and W_s is the same speed as it seen from the sensor reference frame. However, in general, $\vec{X}_v \vec{Y}_v \vec{Z}_v$ and $\vec{X}_s \vec{Y}_s \vec{Z}_s$ have different orientations, since no special attention was paid to the sensor positioning on the vehicle. Due to this fact, it is possible to write:

$$\begin{aligned} A_v &= R_{vs} A_s \\ W_v &= R_{vs} W_s \end{aligned} \quad (5.6)$$

in which R_{vs} is a rotation matrix. Equation (5.6) implies that the accelerations and rotational speed measured by the IMU are not necessarily equal to those referred to the vehicle frame, and that a rotation matrix needs to be computed in order to use them the state estimation algorithms.

In the following sections, two off-line procedures will be described: a calibration procedure designed to correct the measurement errors and a compensation procedure which computes and correct the mounting errors.

5.3 Calibration procedure

The aim of this procedure is to compute the values of the gains and offsets characterizing the sensors readings. Namely, given (5.3), the goal is to recover the values of m_{ax}, m_{ay}, m_{az} and q_{ax}, q_{ay}, q_{az} . The accelerometers are considered first. Due to the nature of these sensors, while the IMU is completely still, the total read acceleration should be equal to the gravitational one. In particular, by placing the sensor on a perfectly levelled surface, with Z_s pointing upward, the acceleration components would be $\ddot{x} = 0; \ddot{y} = 0; \ddot{z} = 9.81 \frac{m}{s^2}$. Substituting in the first three equations of (5.3) and neglecting the white noises we would obtain:

$$\begin{aligned} a_{x1} &= q_{ax} \\ a_{y1} &= q_{ay} \\ a_{z1} &= 9.18 m_{az} + q_{az} \end{aligned} \quad (5.7)$$

in which a_{x1} , a_{y1} and a_{z1} are the three values returned by the accelerometers in this first experiment. Trivially, by repeating the same experiment two more times, the first time with \vec{X}_s and the second with \vec{Y}_s pointing upward, all the gains and offsets values would then be retrieved. However, if the IMU is already mounted on the vehicle, this procedure could be particularly difficult to perform since the sensor cannot be moved freely. Since this was the case, a different procedure was designed, which does not require the knowledge of the spatial orientation of the sensor.

Also in this case, steady measurements are considered. However, if in the previous example one of the three axis was required to be perfectly vertical, in this case the magnitude of the resultant acceleration vector is exploited. In particular, given that the IMU is still, the following equation holds:

$$\ddot{x}^2 + \ddot{y}^2 + \ddot{z}^2 = 9.81^2 \quad (5.8)$$

Clearly, due to the presence of gain and offset errors, the same does not hold on the measured values:

$$|A| = \sqrt{a_x^2 + a_y^2 + a_z^2} \neq 9.81 \quad (5.9)$$

This fact is easily verified by laying the vehicle still, collecting the IMU readings and computing $|A|$. The results are shown in FIGURE 5.3.

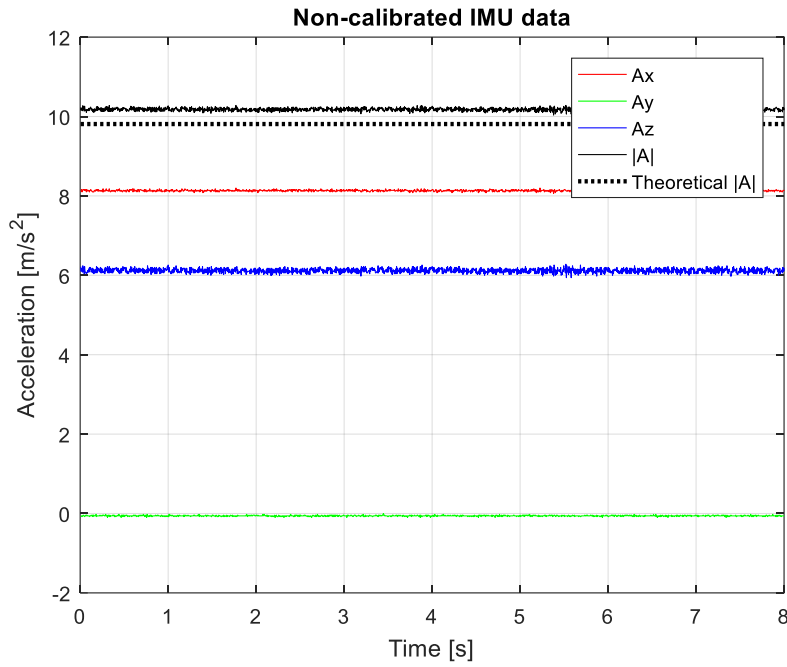


Figure 5-3 Non-calibrated IMU data

Then, by rearranging (5.3):

$$\begin{aligned}\ddot{x} &= \frac{a_x - q_{ax}}{m_{ax}} \\ \ddot{y} &= \frac{a_y - q_{ay}}{m_{ay}} \\ \ddot{z} &= \frac{a_z - q_{az}}{m_{az}}\end{aligned}\tag{5.10}$$

and substituting into (5.8)

$$\left(\frac{a_x - q_{ax}}{m_{ax}}\right)^2 + \left(\frac{a_y - q_{ay}}{m_{ay}}\right)^2 + \left(\frac{a_z - q_{az}}{m_{az}}\right)^2 = 9.81^2\tag{5.11}$$

a non-linear equation is obtained that is a function of the measurement values and of 6 unknown parameters. A cost function can then be defined as:

$$J = J(m_{ax}, m_{ay}, m_{az}, q_{ax}, q_{ay}, q_{az}) = \left(\frac{a_x - q_{ax}}{m_{ax}}\right)^2 + \left(\frac{a_y - q_{ay}}{m_{ay}}\right)^2 + \left(\frac{a_z - q_{az}}{m_{az}}\right)^2 - 9.81^2\tag{5.12}$$

At this point, 4 triplets of $[a_x \ a_y \ a_z]$ were collected by setting the vehicle in 4 different static positions. Each position was hold for a sufficient amount of time, and the triplet was then computed averaging the readings of the three accelerometers in order to minimize the effect of the measurement noise. Finally, the unknown parameters were estimated feeding the collected data to a non-linear Least Square minimization algorithm, using J as cost function. The MATLAB function `lsqnonlin()` was used at this purpose. The four static positions used in the estimation are shown in FIGURE 5.4



Figure 5-4 Four position required for IMU calibration

Notice that using the four positions depicted in FIGURE 5.4 all the axis of the IMU are excited (i.e. they measure non-null quantities) at least twice. If this requirement is not fulfilled, the Least Square minimization converges to unrealistic values of the parameters, or doesn't converge at all.

Finally FIGURE 5.5 (a) shows the raw measured accelerations, whereas FIGURE 5.5 (b) shows the same data after the calibration. Figure 5.6 shows the resultant computed before (blue line) and after the calibration (red line).

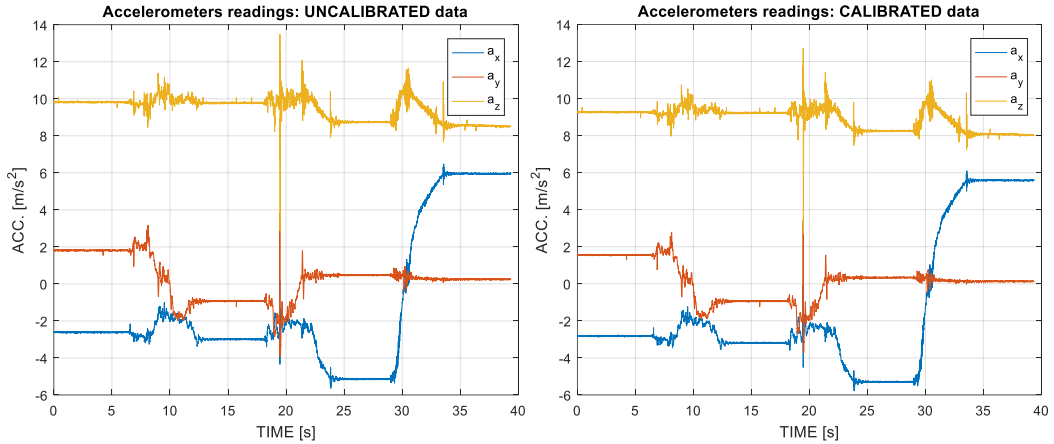


Figure 5-5 (a) Uncalibrated accelerometers readings (b) Calibrated readings

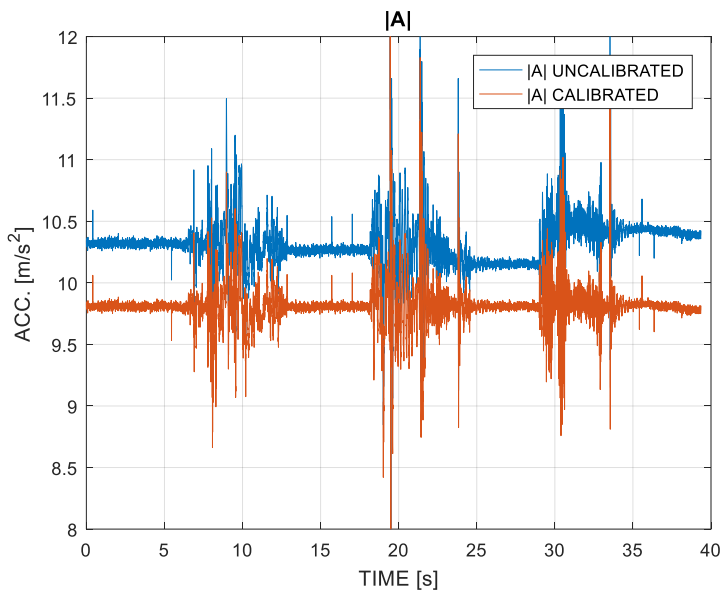


Figure 5-6 Resultant of gravity acceleration measured before and after calibration

As we can see in FIGURE 5.6 (by looking at the 4 low noise sections in which the vehicle is kept still), while the resultant of the raw measurement is not constant, and always greater than $10 \frac{m}{s^2}$, that computed from the calibrated data is constant and almost perfectly equal to $9.81 \frac{m}{s^2}$. Finally, it is worth noticing that in the last two calibration positions, the \vec{Y}_v axis of the vehicle was almost perfectly horizontal (see FIGURE 5.4). The measured accelerations for these two positions are visible in FIGURE 5.3 (b) in the 25-30 s and 35-40 s time intervals respectively. In such intervals, the measured value for a_y is not zero; this is imputable to the abovementioned misalignment between $\vec{X}_v \vec{Y}_v \vec{Z}_v$ and $\vec{X}_s \vec{Y}_s \vec{Z}_s$, that will be corrected later.

The calibration of the gyrometers is much more trivial than the accelerometer's one. In fact, recalling the error model described in (5.3), we have that:

$$\begin{aligned} g_x &= \omega_x + q_{gx} + \eta_{gx} \\ g_y &= \omega_y + q_{gy} + \eta_{gy} \\ g_z &= \omega_z + q_{gz} + \eta_{gz} \end{aligned} \quad (5.13)$$

When the vehicle is still, all the rotational speeds are equal to zero, regardless of the actual IMU position. From (5.13), this is:

$$\begin{aligned} g_x &= q_{gx} + \eta_{gx} \\ g_y &= q_{gy} + \eta_{gy} \\ g_z &= q_{gz} + \eta_{gz} \end{aligned} \quad (5.14)$$

The values of q_{gx} ; q_{gy} ; q_{gz} are then trivially retrieved by collecting data from the IMU whilst keeping the vehicle still, and then averaging the measured g_x , g_y and g_z over a sufficient amount of time in order to remove the measurement noise.

FIGURE 5.7 shows the readings of the x-axis gyrometer during the accelerometers calibration experiment. An acausal filter is applied for readability. The blue curve shows the data affected by constant offset, the red one those after the correction.

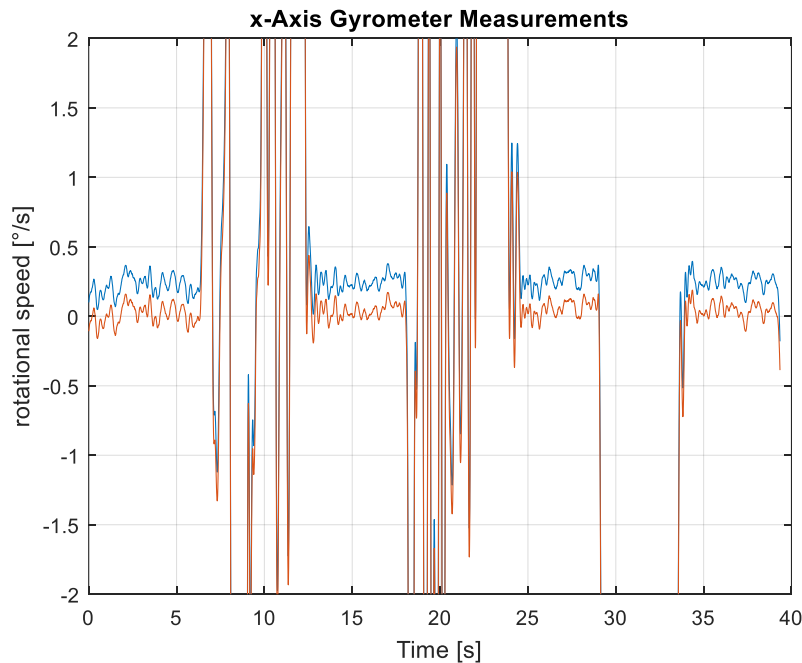


Figure 5-7 x-Axis gyrometer measurements before and after calibration

Finally, it is worth noticing that, while the accelerometers calibration parameters proved to be constant with time, the gyrometer offset components showed an important sensitivity to the environmental variables (temperature mostly) together with a slow drifting behaviour. For this reason, a new estimate of the gyro's offsets is computed at each new start of the vehicle by keeping it still for a couple of seconds. This kind of online procedure can only account for the constant part of the offset: the slowly drifting component is not corrected, and as such it has to be considered in the design of the state observers.

5.4 Compensation procedure

Once both the accelerometers and the gyrometers are calibrated, it is possible to estimate the rotation matrix R_{vs} , accounting for the misalignment between the chassis-fixed and sensor-fixed frames.

To do so, we designed a simple offline procedure that requires nothing else than the vehicle being set on an evenly flat surface. The data acquisition steps are the following:

- the vehicle is tilted along the wheel's axis until the hull touches the ground (FIGURE 5.8 (a))
- a first set of data is acquired from the IMU while the vehicle is left still
- The vehicle is then tilted all the way to the other end, until it touches the ground with the opposite side of the hull. (FIGURE 5.8 (b))
- a second set of data is acquired in this position



Figure 5-8 Compensation procedure: (a) the vehicle is tilted on one side and then (b) it is tilted all the way to the other side

Since both in the first and in the second position, the vehicle is not subjected to any force out of the gravitational one, the data coming from the accelerometers represent the components of the gravity vector with respect to the $X_s Y_s Z_s$ frame. Let's now consider the gravity vector as seen from the chassis-fixed frame. FIGURE 5.9 shows a schematic view of the vehicle in the two steady positions; $X_v Y_v Z_v$ is also depicted, together with the gravity vector for both positions.

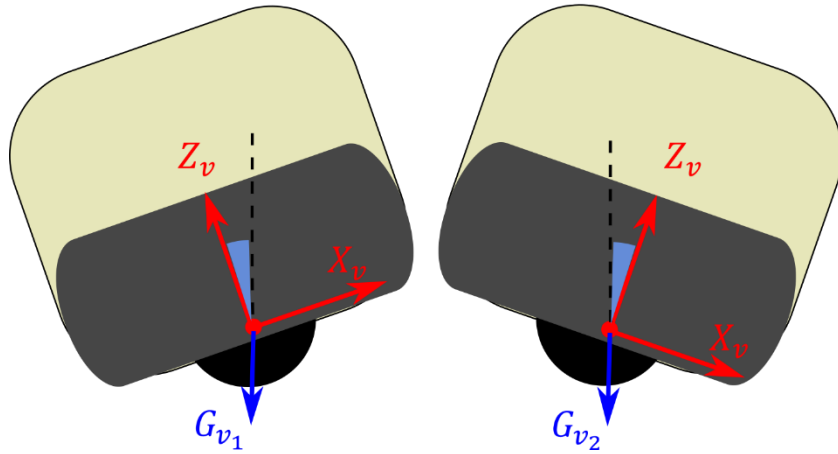


Figure 5.9 Gravity vector in steady positions

As we can see, the actual orientation of the gravity vector in the two positions depends on the geometry of the vehicle. Let G_{v1} be the gravity vector in the first position, and G_{v2} the gravity vector in the second position; both vectors are referred to the same, chassis-fixed, reference frame. We can define a rotation matrix R_{v12} mapping the first vector into the second, so that:

$$G_{v1} = R_{v12} G_{v2} \quad (5.15)$$

Since the only movement the vehicle performs during the test is around the wheel axis, which coincide with \vec{Y}_v , we can state that R_{v12} defines a rotation around the \vec{Y} axis. Moreover, due to the vehicle's symmetry, we can state that G_{v1} and G_{v2} are symmetric with respect to the $\vec{Y}_v \vec{Z}_v$ plane (FIGURE 5.10). Therefore, denoting with θ_{v1} the angle between G_{v1} and the $\vec{Y}_v \vec{Z}_v$ plane, and with θ_{v2} the angle between G_{v2} and the same plane, it holds that

$$\theta_{v1} = -\theta_{v2} \quad (5.16)$$

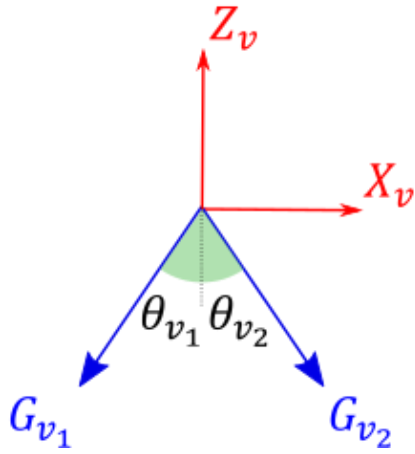


Figure 5-10 Symmetry of θ_{v_1} and θ_{v_2} wrt plane $\vec{Y}_v \vec{Z}_v$

Let's now consider the $\vec{X}_s \vec{Y}_s \vec{Z}_s$ frame: G_{s1} and G_{s2} (namely the gravity vector in the first and second position as seen from the sensor's frame) are given by the calibrated accelerometers readings of the first and second dataset. It is then possible to compute R_{s12} so that:

$$G_{s1} = R_{s12} G_{s2} \quad (5.17)$$

R_{s12} , represents a rotation occurring around a generic axis in the space; in an axis-angle representation, R_{s12} is equivalent to the tuple $(r_s; \alpha)$, where $r_s = [r_x \ r_y \ r_z]^T$ is a unity vector expressed in coordinates with respect to $\vec{X}_s \vec{Y}_s \vec{Z}_s$. It is then possible to find a rotation matrix \tilde{R} , so that:

$$\begin{bmatrix} 0 \\ 1 \\ 0 \end{bmatrix} = \tilde{R} r_s \quad (5.18)$$

By applying the rotation \tilde{R} to $\vec{X}_s \vec{Y}_s \vec{Z}_s$ we obtain a new reference frame, that we call $\tilde{X}_s \tilde{Y}_s \tilde{Z}_s$. The gravity vectors expressed in this frame are \tilde{G}_{s1} and \tilde{G}_{s2} ; due to (5.17), the rotation matrix \tilde{R}_{s12} such that:

$$\tilde{G}_{s1} = \tilde{R}_{s12} \tilde{G}_{s2} \quad (5.19)$$

represents a rotation around the \tilde{Y}_s axis. By recalling what previously said about R_{v12} , and since $G_{v1}; G_{v2}$ and $\tilde{G}_{s1}; \tilde{G}_{s2}$ are actually the same vectors seen by different reference frames, this implies that \tilde{Y}_s and \vec{Y}_v are actually aligned. Finally, it is possible to align $\tilde{X}_s \tilde{Y}_s \tilde{Z}_s$ with $\vec{X}_v \vec{Y}_v \vec{Z}_v$ by means of a rotation around \tilde{Y}_s . In other words, the rotation matrix \hat{R} that maps $\tilde{X}_s \tilde{Y}_s \tilde{Z}_s$ into $\vec{X}_v \vec{Y}_v \vec{Z}_v$ can be expressed as a rotation of a certain angle $\hat{\theta}$, around the axis $\tilde{r} = [0 \ 1 \ 0]^T$. In order to retrieve the value of $\hat{\theta}$, the symmetry constraint is exploited.

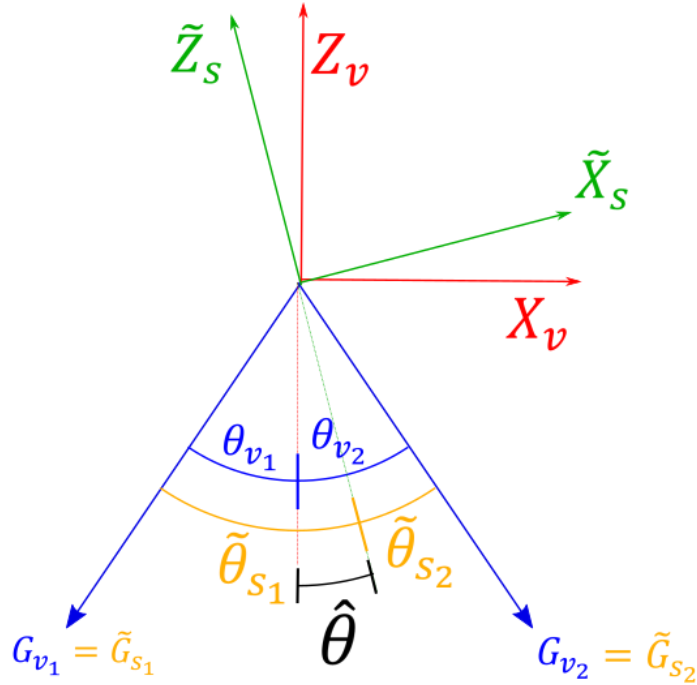


Figure 5-11 Graphical explanation of compensation procedure

In fact, $\hat{\theta}$ can be computed as:

$$\hat{\theta} = \frac{\tilde{\theta}_{s1} - \tilde{\theta}_{s2}}{2} \quad (5.20)$$

in which $\tilde{\theta}_{s1}$ and $\tilde{\theta}_{s2}$ are the angles between the plane $\tilde{Y}_s \tilde{Z}_s$ and the vectors \tilde{G}_{s1} and \tilde{G}_{s2} respectively (see FIGURE 5.11). As a result, the rotation matrix R_{vs} transforming the sensor-fixed frame $\tilde{X}_s \tilde{Y}_s \tilde{Z}_s$ into the chassis-fixed one, is given by:

$$R_{cs} = \hat{R} \tilde{R} \quad (5.21)$$

In FIGURE 5.12 are reported the acceleration measured as they result from the calibration procedure.

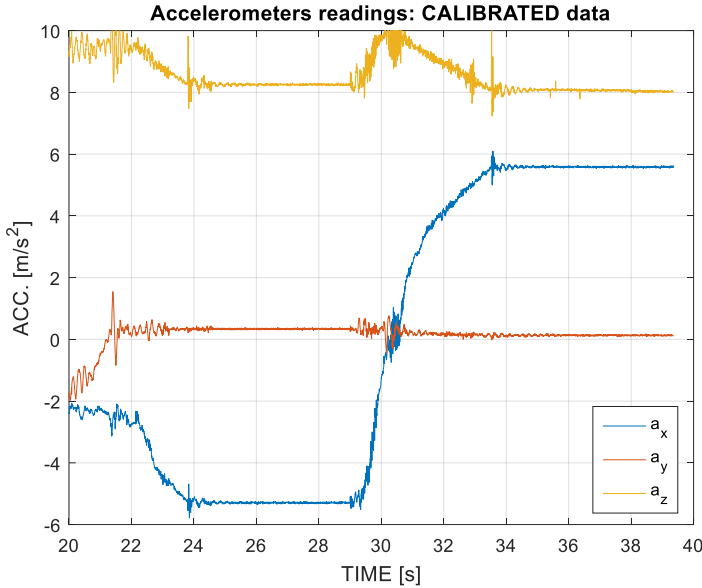


Figure 5-12 Accelerometers readings: calibrated data

Notice that the same readings coming from the last two positions of the calibration experiment are used (see FIGURE 5.8). Ideally, if $\vec{X}_s \vec{Y}_s \vec{Z}_s$ was perfectly aligned to $\vec{X}_v \vec{Y}_v \vec{Z}_v$, we should observe $a_y = 0$ (red line) in both the two static positions, namely from second 24 to 29 and from second 34 to 40. Moreover, a_z (yellow line) should be constant in both the positions, and a_x (blue line) should assume a negative value in the first position and the exact opposite value in the second. This is not the case due to the presence of the aforementioned mounting errors. In FIGURE 5.13 the same data are plotted after applying the first rotation given by \tilde{R} .

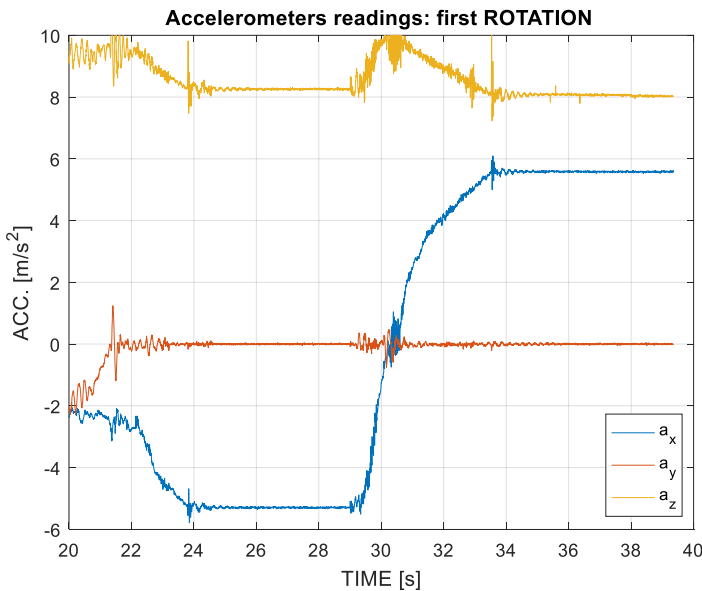


Figure 5-13 Accelerometers readings: first rotation

Notice that now $a_y = 0$, thus confirming that the \vec{Y}_s axis of the sensor is now aligned to \vec{Y}_v . Finally, in FIGURE 5.14 we can see the data as they are after the second rotation given by \hat{R} : here, a_z is constant in both the positions, and a_x assume perfectly symmetric values thus proving the alignment between the new sensor frame and the vehicle's one.

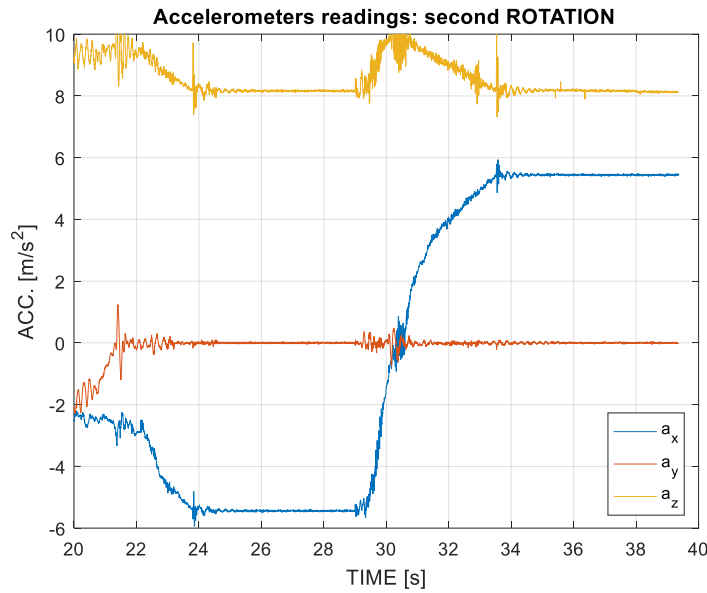


Figure 5-14 Accelerometers readings: second rotation

5.5 Conclusions

A compete analysis of the measures coming from the IMU was carried on in this chapter. Two main sources of errors were identified: structural errors, and mounting errors. The firsts are related to the nature of the sensor, and their effect is modellable with gains and offsets affecting the relation between real data and measured one. The seconds are imputable to the misalignment between sensor-fixed reference frame and vehicle-fixed one. A simple procedure was developed to correct the structural errors which only require the vehicle to be kept still in 4 different positions. Finally, a second procedure was explained to compensate also the mounting errors, which exploit the vehicle's tilt motion and its symmetry. The resulting measurements are suitable to be used in the state-estimation algorithms that will be explained in the next chapter.

Chapter 6 - State observers

6.1 Introduction

Any control scheme aiming to stabilize and drive a WIP needs the knowledge off all the main states of the dynamical system, namely the vehicle's pitch angle (θ) together with its derivative ($\dot{\theta}$), the speed of the axle track center (\dot{s}) and the yaw rate ($\dot{\psi}$). In order to achieve that, the proprioceptive sensors installed on the vehicle (namely the IMU and the encoders) can be exploited by means of some simple kinematic equations expressing the relation between sensors outputs and the system's states.

A model based, dynamical approach such as Kalman filtering would also be possible; however, such approach was discarded in this study in favour of the kinematic observers described hereafter, which have proved to be more easily implemented and still provided very satisfactory results.

6.2 Pitch Estimation

The most critical state to be estimated while controlling a Wheeled Inverted Pendulum is, for obvious reasons, the pitch angle, i.e. the angle of inclination of the chassis with respect to the vertical position (FIGURE 6.1). Notice that this is a geometrical definition for θ , so that the estimation is carried on regardless of the actual c.o.g position. Hence, since $\theta = 0$ correspond to the stable position only in case of centred c.o.g, all the considerations made in CHAPTER 4 need to be taken into account in case of unbalanced load.

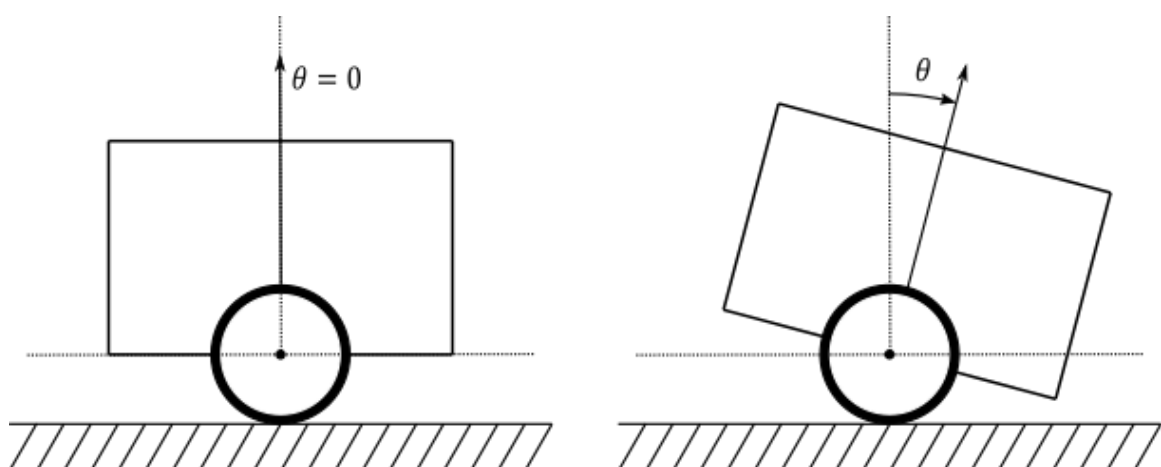


Figure 6-1 Graphical explanation of pitch angle

The estimation needs to be carried out aiming to achieve the maximum precision, while reducing the noise content in the largest frequency bandwidth achievable. In order to meet both these requirements IMU readings were fused using a Split Frequency Method, resulting into a satisfactory estimation of the pitch over a sufficiently large bandwidth.

The SFM is a sensors fusion technique that provides an estimation of a quantity by composing two complementary estimations, one performed at the low frequencies and the other at the high frequencies. Putting this into equations, being X a certain quantity to be estimated, the SFM prescribe to compute it as:

$$\hat{X} = \hat{X}_{LF} + \hat{X}_{HF} \quad (6.1)$$

where \hat{X} is the final estimate, while \hat{X}_{LF} and \hat{X}_{HF} are estimations of X at low frequency and at high frequency respectively. For the estimate to be correct though, \hat{X}_{LF} and \hat{X}_{HF} need have complementary frequency content. This requirement is well explained by the following:

$$\begin{cases} \hat{X}_{LF}(\omega) \approx X(\omega) & \omega \leq \omega_{SFM} \\ \hat{X}_{LF}(\omega) \approx 0 & \omega > \omega_{SFM} \end{cases} \quad \text{and} \quad \begin{cases} \hat{X}_{HF}(\omega) \approx 0 & \omega \leq \omega_{SFM} \\ \hat{X}_{HF}(\omega) \approx X & \omega > \omega_{SFM} \end{cases} \quad (6.2)$$

Notice that this is equivalent to require that:

$$\hat{X}_{LF}(\omega) + \hat{X}_{HF}(\omega) \approx X \quad \forall \omega \quad (6.3)$$

This is usually achieved by computing two different estimates of X and then filtering the first with a low pass filter $F_{LP}(s)$ and the second with a high pass filter $F_{HP}(s)$ such that:

$$F_{LP}(\omega) + F_{HP}(\omega) = 1 \quad \forall \omega \quad (6.4)$$

A scheme of a complete SFM approach is depicted in FIGURE 6.2 and an example of working principle in FIGURE 6.3).

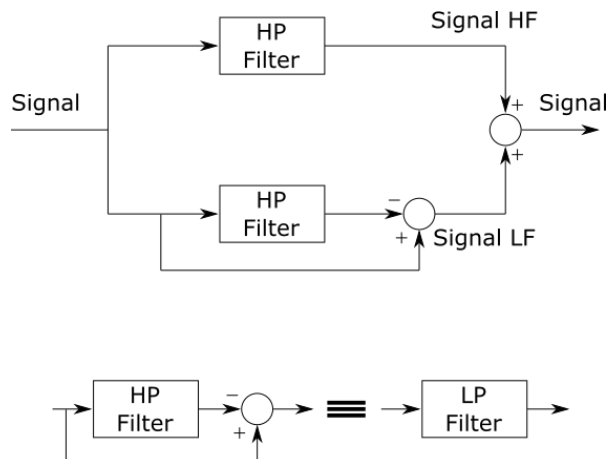


Figure 6-2 Split Frequency Method: general scheme

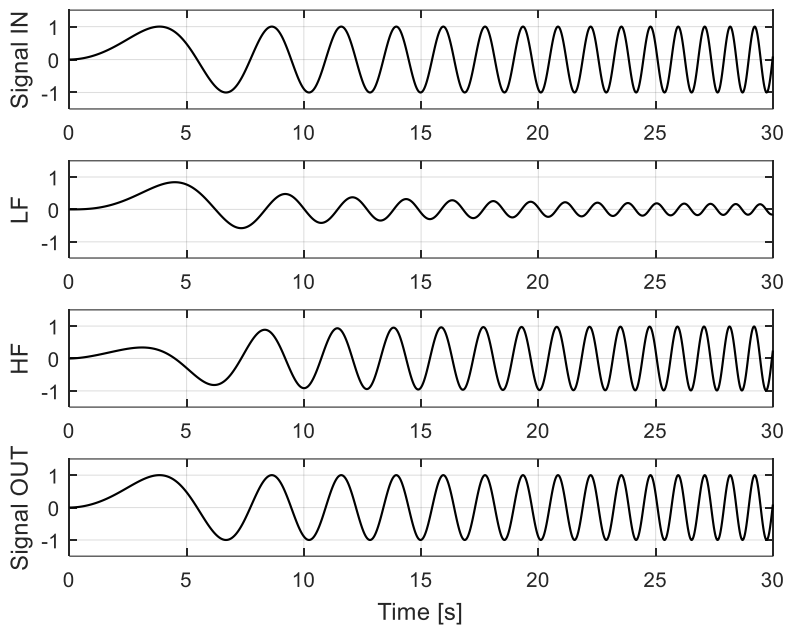


Figure 6-3 Example of working principle of SFM

The aim of SFM is to exploit only the error-free bandwidth from each measurement, and it is therefore particularly suited when two measurements are available, being affected by low frequency and high frequency noises respectively. That makes it a perfect choice for our pitch estimation problem. In fact, it will be shown that 2 different estimations can be computed starting from IMU readings: one is based on gyrometer measurements and it is mainly affected by a slowly varying offset (i.e. a very low frequency noise), and the other is obtained from accelerometers by measuring the gravitational acceleration; this is biased by spurious acceleration components and high frequency noise.

In the following chapter any zero-mean white noise will be referred to as η , whereas b will represent a constant (or slowly varying) offset.

From Chapter 5 we know that a direct measurement of the derivative of the pitch angle value is given by the y-axis gyrometer. Namely, we can state that:

$$\omega_y = \dot{\theta} + b + \eta \quad (6.5)$$

The inevitable presence of slowly varying offsets b makes unfeasible to retrieve the value of θ by means of a simple integration. In fact, integrating the full signal would give:

$$\hat{\theta} = \int \omega_y = \int \dot{\theta} + \int b + \int \eta = \theta + \int b + 0 \quad (6.6)$$

Being b an almost constant component with non-zero mean value, its integration would inevitably result into a diverging $\hat{\theta}$. Therefore, a high pass filter is applied to ω_{imu} resulting into:

$$\omega_{yHF} = \dot{\theta}_{HF} + \eta_{HF} \quad (6.7)$$

Then, recalling that η_{HF} is approximately a zero-mean white noise, it is possible to perform the integration obtaining:

$$\hat{\theta}_{HF} = \int \omega_{yHF} = \int \dot{\theta}_{HF} + \int noise_{HF} \approx \theta_{HF} + 0 = \theta_{HF} \quad (6.8)$$

Once $\hat{\theta}_{HF}$ is obtained a complementary low frequency component is needed to apply SFM. That is retrieved starting from the readings of x-axis and z-axis accelerometers.

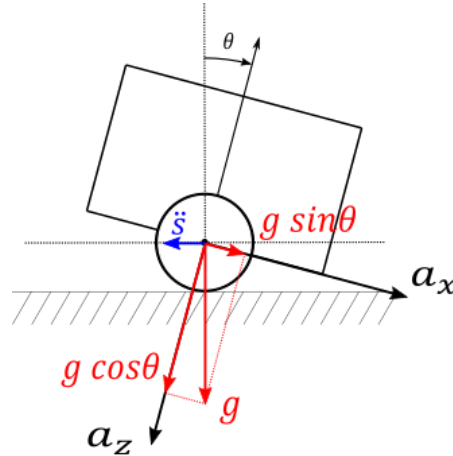


Figure 6-4 Decomposition of gravity on accelerometers while the vehicle is tilting

As we can see from FIGURE.6.4, the following expressions holds:

$$\begin{aligned} a_x &= \ddot{s} \cos \theta + g \sin \theta + \eta \\ a_z &= \ddot{s} \sin \theta + g \cos \theta + \eta \end{aligned} \quad (6.9)$$

in which a_x and a_z are the measured values for x-axis and z-axis accelerometers respectively, \ddot{s} is the longitudinal acceleration at the center of the vehicle's track, θ is the pitch angle and η is a zero-mean white noise.

In order to remove both the noise and the spurious component constituted by \ddot{s} a low pass filter is applied to both the accelerometers measurements:

$$\begin{aligned} a_{xLF} &= \ddot{s}_{LF} \cos \theta_{LF} + g \sin \theta_{LF} + \eta_{LF} \approx g \sin \theta_{LF} \\ a_{zLF} &= \ddot{s}_{LF} \sin \theta_{LF} + g \cos \theta_{LF} + \eta_{LF} \approx g \cos \theta_{LF} \end{aligned} \quad (6.10)$$

in which both \ddot{s}_{LF} and η_{LF} are supposed to be negligible with respect to g . The pitch angle is then retrieved by computing the arctangent of the ratio between $a_{x_{LF}}$ and $a_{z_{LF}}$:

$$\hat{\theta}_{LF} = \tan^{-1} \left(\frac{a_{x_{LF}}}{a_{z_{LF}}} \right) \quad (6.11)$$

At this point, since $\hat{\theta}_{LF}$ and $\hat{\theta}_{HF}$ were obtained by using complementary filters it is possible to retrieve the full-bandwidth estimation of the pitch angle as:

$$\hat{\theta} = \hat{\theta}_{LF} + \hat{\theta}_{HF} \quad (6.12)$$

In FIGURE 6.5 it is shown the complete scheme of the split frequency method applied in pitch estimation.

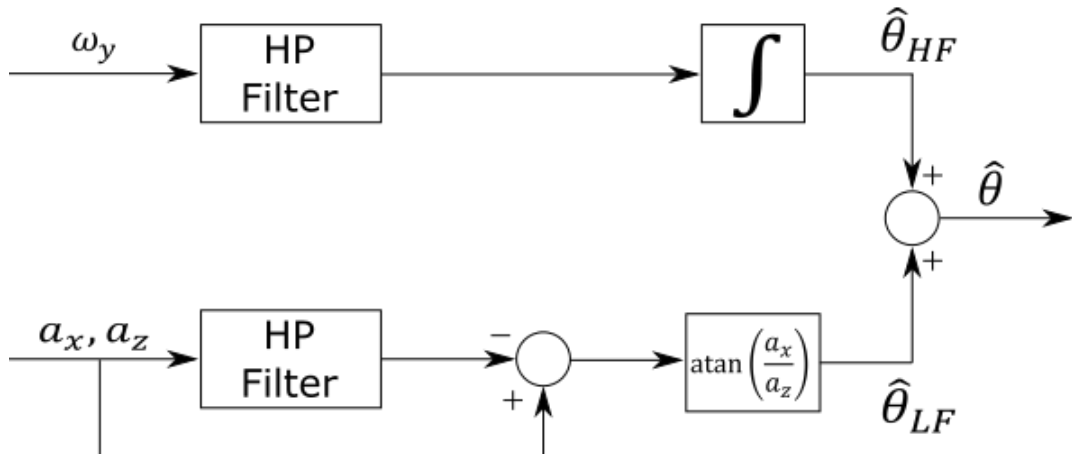


Figure 6-5 SFM applied in pitch estimation

It is quite straightforward to notice that the cut-off frequency for the two complementary filters plays a crucial role in the estimation process. Namely, a trade-off exists between the rejection of the constant bias affecting the gyro and the high frequency acceleration components: higher values of ω_{SFM} grant a better reconstruction of $\hat{\theta}_{HF}$ at the expense of a worse estimate of $\hat{\theta}_{LF}$, and vice versa.

In FIGURE 6.6 it is shown an example of the trade off in filter bandwidth choice.

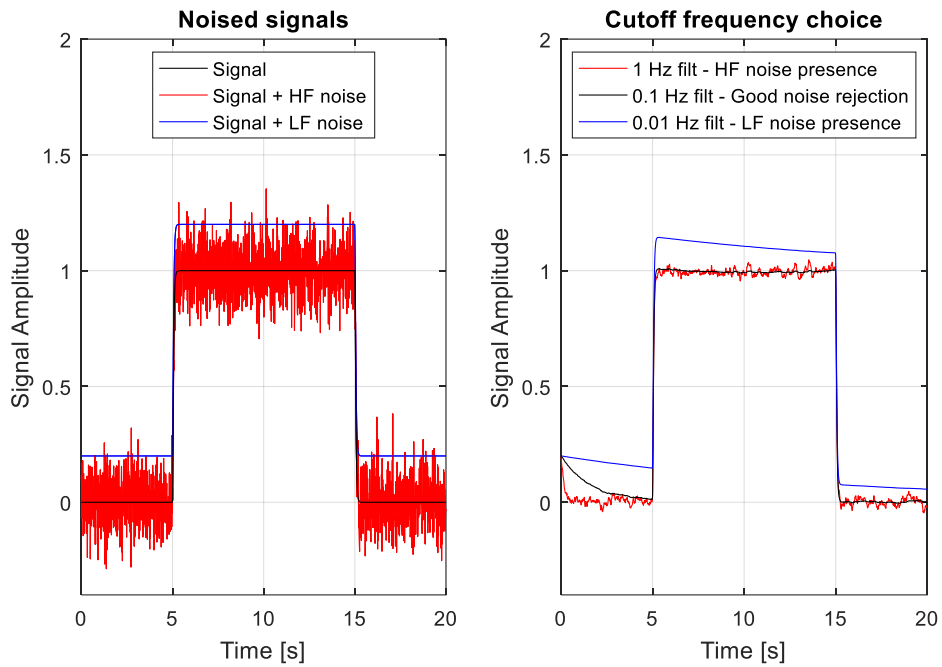


Figure 6-6 Trade off in filter bandwidth choice

The optimal value for ω_{SFM} was experimentally found by mounting a laser proximity sensor on the chassis, thus providing a direct measure for the pitch to be confronted with the estimation based on the SFM.

The experimental setup is schematically shown in FIGURE 6.7.

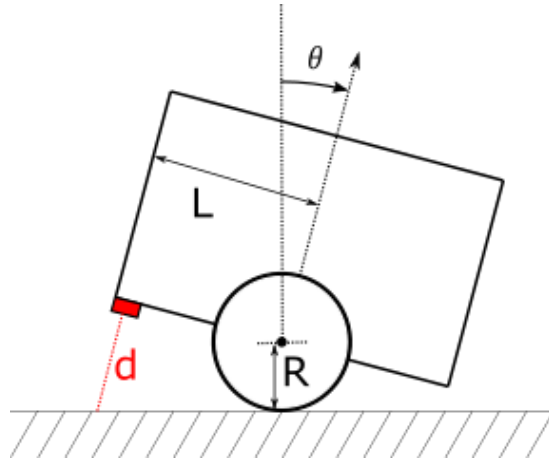


Figure 6-7 Schematic representation of mounted laser sensor

The following nonlinear equation describe the relation between the distance d measured by the laser sensor and the pitch angle θ :

$$d \cos(\theta) = R + L \sin(\theta) \quad (6.13)$$

By substitution of:

$$t = \tan \frac{\phi}{2}, \sin \theta = \frac{2t}{1+t^2}, \cos \theta = \frac{1-t^2}{1+t^2} \quad (6.14)$$

the following is obtained:

$$t = \frac{-L + \sqrt{L^2 - R^2 + d^2}}{d + R} \quad (6.15)$$

from which the pitch angle is retrieved using the arctangent:

$$\theta = 2 \arctan(t) = 2 \arctan \left(\frac{-L + \sqrt{L^2 - R^2 + d^2}}{d + R} \right) \quad (6.16)$$

Since both the exact location L of the laser sensor and the wheel radius R are known parameters, a direct measure of θ can be obtained. However, to avoid saturation phenomena occurring at the extremes of the measuring range of the laser sensor (i.e. very small and very large values of d), all the pitch readings with absolute value greater than 15° have been neglected in the tuning process. Being the considered pitch values relatively small, the following linearized equation has been used instead of (6.16):

$$\theta_{\text{lin}} = \frac{d - R}{L} \quad (6.17)$$

It's quite important to notice how θ_{lin} constitute an underestimation of θ for positive values of pitch, and an overestimation for the negative ones. This fact is shown in FIGURE 6.8.

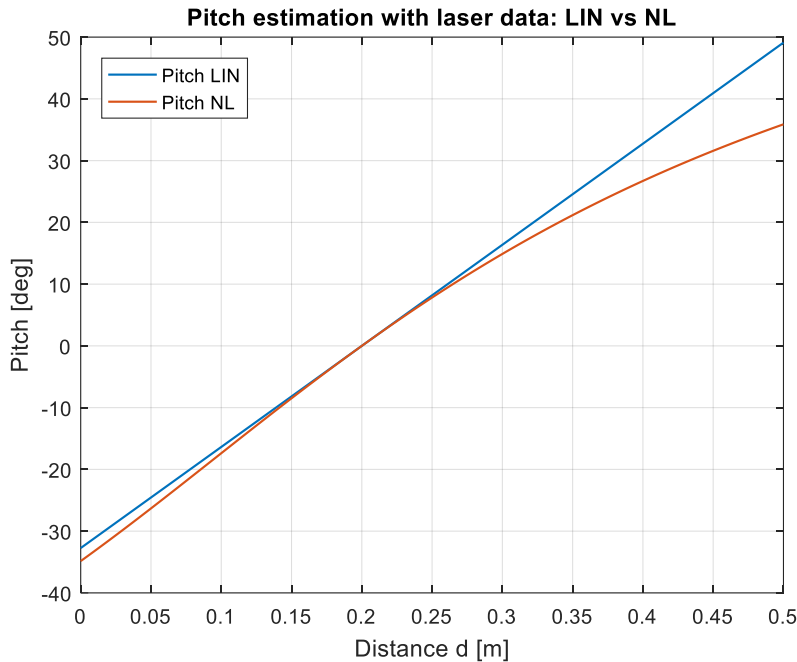


Figure 6-8 Comparison between linear and non-linear solution for pitch estimation

Given this experimental setup, two different tests were conducted, both with the stabilization controller turned off, and the vehicle being manually balanced and displaced:

1. **Test 1:** the vehicle was moved back and forward with fast and abrupt accelerations, tilting the chassis in the meanwhile
2. **Test 2:** the chassis was kept at an almost constant angle of approximately -10° , while low-intensity longitudinal accelerations were applied to the entire vehicle

Aim of test 1 was to produce the largest and most realistic value for \ddot{s} , while the second to check the accuracy of the estimator. By collecting IMU readings through all the duration of the experiments, it was possible to compute an offline SFM estimation of theta, together with the root mean square value of the estimation error given by:

$$J = \sqrt{\frac{\sum(\theta_{laser} - \hat{\theta}_{SFM})^2}{N_{samples}}} \quad (6.18)$$

The correct cut-off frequency for the SFM was then chosen as a compromise between the one minimizing the RMSE in the first experiment and that minimizing it in the second one. That corresponded to a frequency of approximately 0.03 Hz; such value allowed a good rejection of the slowly varying offset affecting the gyro and a substantial reduction of the effect of the spurious acceleration components biasing the accelerometers estimate. The comparison between pitch laser and pitch estimated is shown in FIGURE 6.9 AND 6.10.

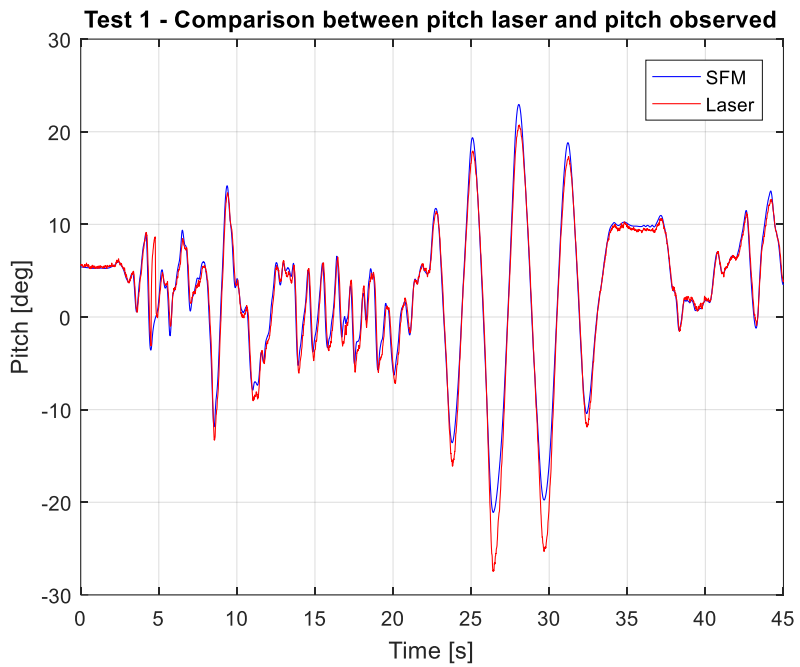


Figure 6-9 Test-1 Comparison between pitch laser and pitch observed.

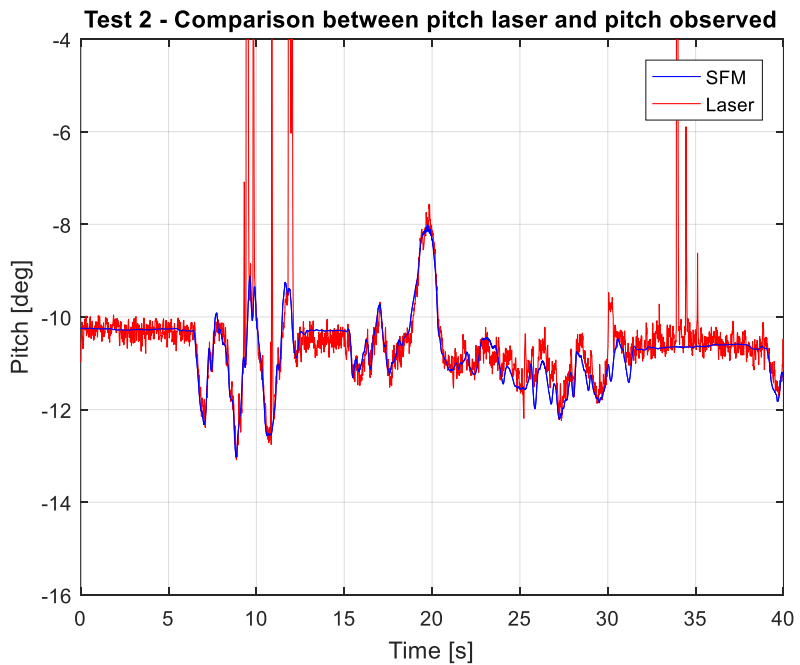


Figure 6-10 Test-2 Comparison between pitch laser and pitch observed.

6.3 Pitch Rate Estimation

As previously stated, a direct measure for $\dot{\theta}$ is available in the form of ω_y , that being the value measured by the y-axis gyrometer on the IMU:

$$\omega_y = \dot{\theta} + b + \eta \quad (6.19)$$

that is affected by a relative small white noise but relevant slowly varying offset, making necessary the application of a high pass filter to the measured valued. From the implementation point of view, the $\omega_{y_{HF}}$ value fed to the SFM algorithm was used as a direct measure of the pitch rate, i.e.:

$$\hat{\theta} = \omega_{y_{HF}} \quad (6.20)$$

This choice has proved to be well suited for control purposes despite the lack of informativity of $\hat{\theta}$ in the low frequency bandwidth; in fact, provided that a satisfactory closed loop controller is running with a good pitch control, the low frequency component of $\dot{\theta}$ has small absolute value, so that it is possible to neglect it.

6.4 Speed Estimation

The estimation of \dot{s} , namely track center speed, is carried on using the data coming from the two rotational encoders mounted on the wheels.

As already mentioned, they provide an incremental, directional measure of the relative angle between the wheel and the chassis:

$$\alpha_r = \theta + \frac{s_r}{R} \quad (6.21)$$

in which α_r is the angle measured by the right-wheel encoder, θ is the absolute pitch and $\frac{s_r}{R}$ the absolute right-wheel angular displacement. By subtracting the estimated pitch angle and computing the derivative on the result, a measure of the rotational wheel speed is obtained. Finally, the longitudinal wheel speed is retrieved by multiplying that by the wheel radius.

$$\hat{s}_r = R \frac{d(\alpha_r - \hat{\theta})}{dt} \quad (6.22)$$

From \hat{s}_r and \hat{s}_l (right and left wheel speeds respectively) it is possible to obtain the speed at the track's centre is obtained by exploiting the simple cinematic relation introduced in Chapter 3, namely:

$$\hat{s} = \frac{\hat{s}_r + \hat{s}_l}{2} \quad (6.23)$$

which is also shown in FIGURE 6.11.

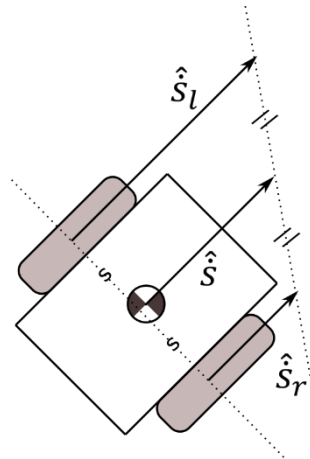


Figure 6-11 Graphical explanation of kinematic relation (6.23)

Due to discretization and sampling errors, the value is useless as it is; a second order low pass filter is then applied. A frequency of 4 Hz has been chosen as a compromise between noise rejection and phase delay. (FIGURE 6.12)

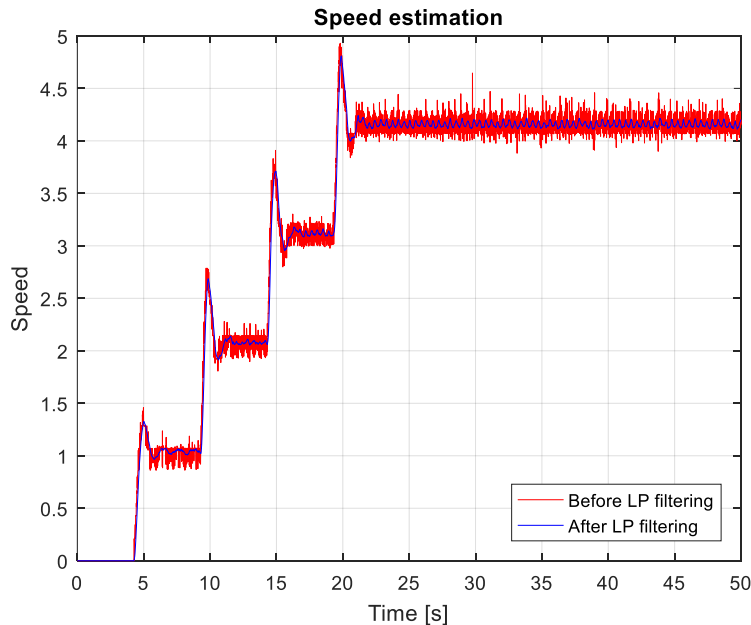


Figure 6-12 Speed estimation before and after LP filtering

6.4.1 The overflow

Being based on encoder readings, this type of estimation is subjected to a critical issue: the overflow. Namely, when any of the two encoders overshoots the maximum value of 2^{15} steps, the counter is immediately moved to the opposed extreme (specifically -2^{15} steps). This produces an enormous differential between the actual position and the previous one that would result into a very dangerous spike in the speed value. This, if not correctly managed, could bring the controller to produce an impulsive action, thus saturating the actuators and possibly destabilizing the entire vehicle. In order to prevent this issue a speed threshold of 25 Km/h has been set: when the system detects a spike in the speed estimation overshooting the threshold the actual estimation is set to the last acceptable value, which in formulae is:

$$\text{if } \hat{s}(k) > \ddot{s}_{MAX} \text{ then } \hat{s}(k) = \hat{s}(k - 1) \quad (6.24)$$

This simple adjustment solves the overflow problem (FIGURE 6.13). Thresholding the speed provides also a good rejection of speed spikes possibly deriving from wheel slip phenomena.

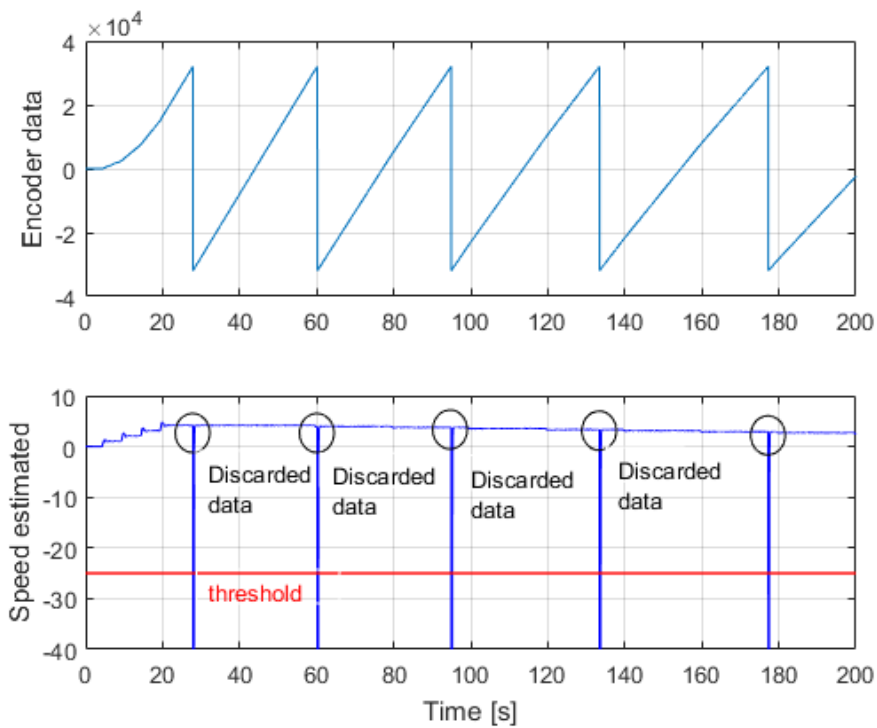


Figure 6-13 Overflow management

6.5 Yaw Rate Estimation

For the yaw rate estimation two possible approaches are available. The first is based on z-axis gyrometer readings through:

$$\omega_z = \dot{\psi} \cos(\theta) + b + \eta \approx \dot{\psi} + b + \eta \quad \text{for } \theta \sim 0 \quad (6.25)$$

in which the cosine of θ can either be neglected by supposing the vehicle to be almost vertical while turning, or computed using the value of $\hat{\theta}$ coming from the SFM estimator.

The second, follows the same procedure used for the speed estimation: starting from \hat{s}_r and \hat{s}_l the yaw rate is computed using the kinematic relation expressed in Chapter 3, namely:

$$\hat{\psi} = \frac{\hat{s}_L - \hat{s}_R}{d} \quad (6.26)$$

which is also shown in FIGURE 6.14.

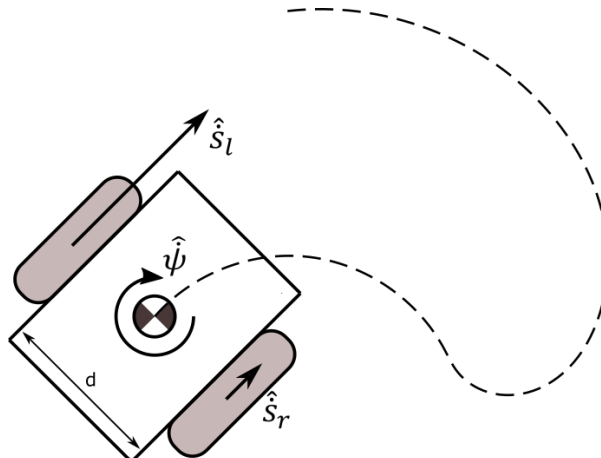


Figure 6-14 Graphical explanation of kinematic relation (6.25)

Both the two measures exhibit pros and cons: gyrometer based estimation shows low variance white noise and small slowly variable offset, while the encoder based estimation has larger noise but with zero mean value. Due to this fact it is possible to implement an SFM estimator in a similar fashion to what has been done for the pitch angle, by taking the gyro-based measure as high frequency estimation and the encoder-based value as low frequency one. In this way the good high frequency performances of the gyro are exploited still avoiding the non-zero mean noise, which could possibly lead to a drifting behaviour of the vehicle. In this case the cut-off frequency for the SFM estimator was experimentally tuned to 0.3 Hz, which has shown a total rejection of the gyro's offset (see FIGURE 6.15).

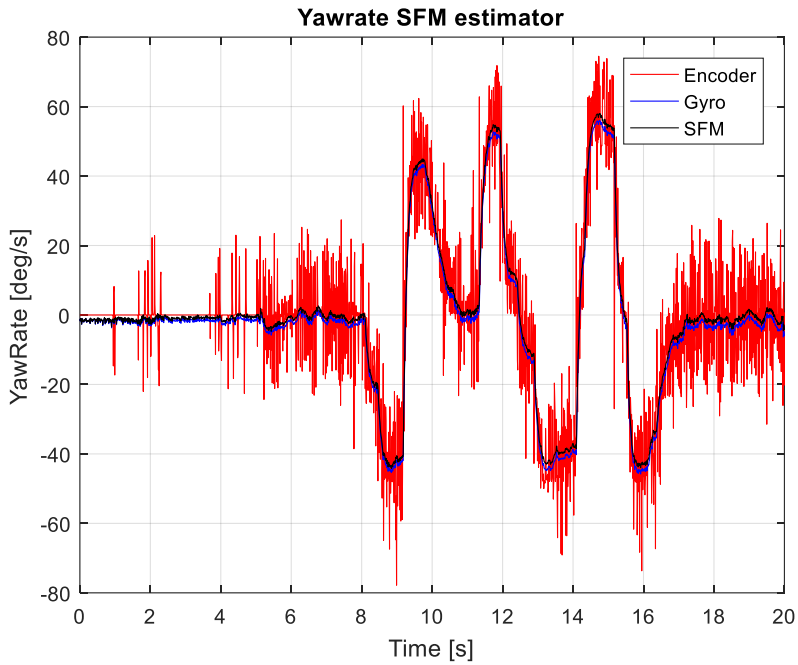


Figure 6-15 SFM for yawrate estimation

6.6 Conclusions

Starting from the available sensor, a full set of observers has been designed and tested in order to provide a reliable estimation for all the states of the dynamical system modelling YAPE's behaviour. An efficient sensor fusion algorithm was implemented to exploit the full performances of the IMU in estimating the pitch angle, whereas encoders were used to obtain a simple but still valid estimation of the vehicle speed and yaw rate. All the data coming from the observers were used both in the control feedback loops and to compare the behaviour of the real system with the results obtained on the simulator, thus providing a viable way of testing the validity of the latter. Moreover, they have proven to be useful in the model identification process that will be explained in the next Chapter.

Chapter 7 - Parameters Identification

7.1 Introduction

The dynamical model derived in Chapter 3 is characterized by the presence of many parameters which numerical values affects in a relevant way the overall behaviour of the system. A numerical assessment of these parameters is then needed in order to have a complete, reliable model, both for control design purposes and for setting up an accurate simulation environment for the vehicle. Most of these parameters are directly or indirectly measurable, whereas for a couple of them a model-based regression was needed.

In addition to the already depicted dynamical model, a friction model will be introduced, accounting for all the main dissipation effects occurring on YAPE. The presence of frictions and dissipation effects on a WIP is addressed in literature in three possible ways: the first is to consider them as totally negligible [23], the second is to design specific procedures to compensate their effects and to add them to a nominal controller [19], [21]. Our work follows a third approach ([20], [22]); namely, even if the nominal model is used in the controller design phase, a friction model is introduced and numerically assessed in this Chapter. By implementing such a model in the simulator will then be possible to test the rejection capabilities of the nominal controller to friction-related disturbs, such as limit cycles and non-null steady state torques. Finally, even if no specific compensation procedure was designed during our work, the present dissipation-model will be useful to possible future developments on this matter.

7.2 Dissipation effects: friction model

Dissipation effects occurring on YAPE are manly related to the wheels supporting the vehicle, and they are crucial in explaining and reproducing some non-linear behaviours that the vehicle shows in practice, like the presence of limit cycles in zero-speed conditions. Two main causes of dissipations have been identified: first the friction torques occurring inside the rotational joint between each wheel and the chassis, and secondary the rolling friction of the tyres. The numerical assessment of the entire friction model has been carried on using ad hoc experiments that do not require the knowledge of all the other mechanical parameters characterizing the vehicle.

In order express the friction torques arising in the wheels hinges a Coulomb-Stribeck model has been selected. This is basically a classic Coulomb model, with a static and a dynamic friction component, an additional viscous component (i.e. proportional to the wheel's rotational speed) and non-linear Stribeck effect occurring at low speeds. (FIGURE 7.1)

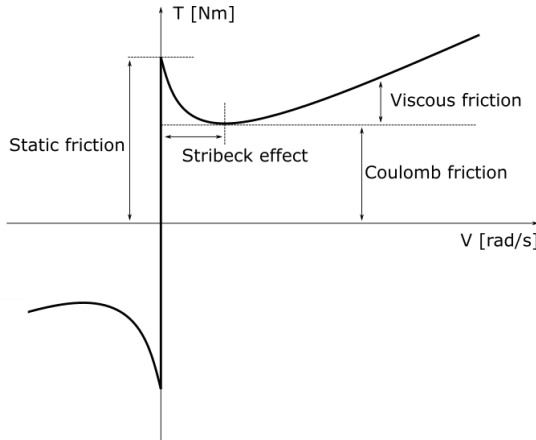


Figure 7-1 Friction model

The mathematical form of this model is given by:

$$T_{frict}(T_{ext}, v) = \begin{cases} T_{ext} & v = 0, T_{ext} \leq T_s \\ T_C + (T_s - T_C)e^{-\alpha_s v} + T_{visc}v & v > 0 \\ -T_C + (T_C - T_s)e^{\alpha_s v} - T_{visc}v & v < 0 \end{cases} \quad (7.1)$$

Hence an additional constant term T_{roll} is added to the dynamical part of the model, representing the dissipations caused by the tyres rolling friction. The resulting complete friction model is then:

$$T_{frict}(T_{ext}, v) = \begin{cases} T_{ext} & v = 0, T_{ext} \leq T_s \\ T_C + (T_s - T_C)e^{-\alpha_s v} + T_{visc}v + T_{roll} & v > 0 \\ -T_C + (T_C - T_s)e^{\alpha_s v} - T_{visc}v - T_{roll} & v < 0 \end{cases} \quad (7.2)$$

Where:

- T_{ext} is the external torque applied to the wheel.
- T_s is the static friction torque.
- T_C is the torque due to Coulomb friction.
- T_{visc} is the torque due to viscous friction.
- T_{roll} is the rolling resistance torque.
- α_s is the Stribeck coefficient.

The model is a 5-parameters one ($T_s, T_C, T_{visc}, \alpha_s, T_{roll}$), and has to be applied to both the wheels in both the direction, thus resulting in a total of 20 parameters to be estimated. In the following sections, all these parameters will be numerically identified; the static friction will be investigated first, then the hinge related dynamical forces will be assessed and finally the rolling resistance will be considered.

Through all the experimental activity detailed below, a measure of the torque has been recovered from current measures on the motor's armature circuit; since such measures are affected by relevant high frequency noise they have been offline processed in a MATLAB environment using an acausal filter (*filtfilt()* MATLAB function). In FIGURE 7.2 the result of such filtering action.

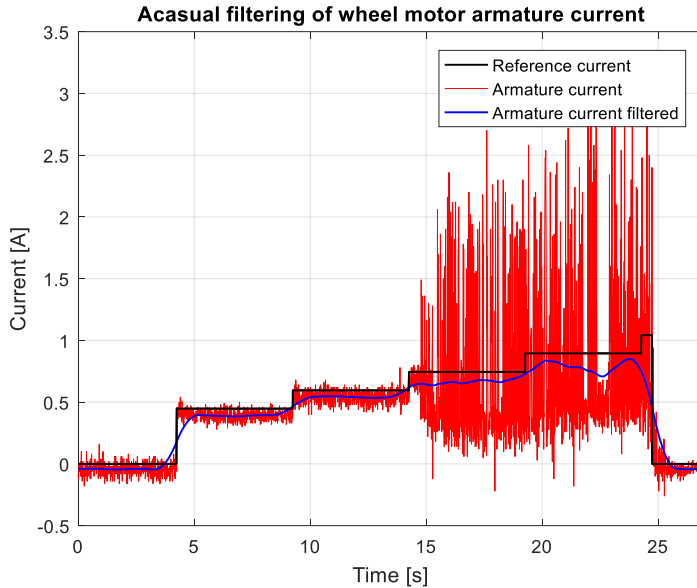


Figure 7-2 Acausal filtering of wheel motor armature current

7.2.1 Static Friction

The static friction region constitutes the first part of the friction model. The friction torques equals the driving torque as long as the latter reaches the value of T_s :

$$T_{frict} = T_{ext} \quad \text{for } T_{ext} \leq T_s \quad (7.3)$$

As soon as this happens the wheel starts its motion and the friction reduces rapidly following the Stribeck curve shown in FIGURE 7.3.

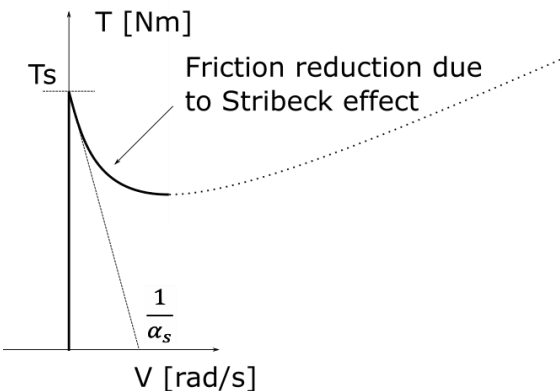


Figure 7-3 Friction model – Stribeck effect

Therefore, the estimation of T_s has been carried on by setting up an ad hoc procedure designed to compute the minimum torque required to start the motion of each wheel. First of all, the vehicle is set sitting on the floor in a stable position with the wheels pointing up and free to spin without any obstacle (FIGURE 7.4).



Figure 7-4 Setup friction tests.

In this position the wheel is only subjected to the driving torques and to the resisting torques caused by joint frictions (i.e. it is not subjected to any tyre-related torque/force). A discretized torque ramp is requested to each motor, starting from a value of 0.3 [Nm] and increasing with steps of 0.3 [Nm] each 5 seconds. As soon as the wheel starts to rotate the torque request is reset to zero. The procedure is repeated 10 times on each wheel for both the rotation directions (FIGURE 7.5).

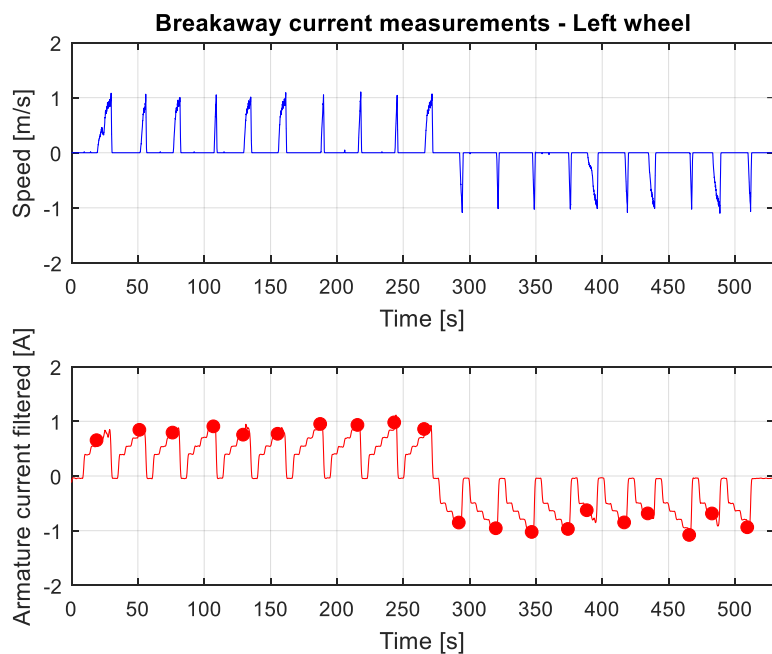


Figure 7-5 Breakaway current measurements

Four values for T_s were computed by averaging the detachment torques through the conversion Ampere-Torque with the motor constant torque $k_m = 0.67 \left[\frac{Nm}{A} \right]$ over the entire set of tests. The results are shown in TABLE 7.1

Wheel/Direction	Left / Positive	Left / Negative	Right / Positive	Right / Negative
Test – 01 [Nm]	0.42	-0.58	0.71	-0.51
Test – 02 [Nm]	0.55	-0.64	0.58	-0.62
Test – 03 [Nm]	0.52	-0.69	0.59	-0.46
Test – 04 [Nm]	0.59	-0.65	0.70	-0.59
Test – 05 [Nm]	0.49	-0.42	0.58	-0.54
Test – 06 [Nm]	0.50	-0.57	0.58	-0.59
Test – 07 [Nm]	0.62	-0.46	0.53	-0.53
Test – 08 [Nm]	0.61	-0.73	0.49	-0.59
Test – 09 [Nm]	0.64	-0.46	0.54	-0.60
Test – 10 [Nm]	0.56	-0.63	0.60	-0.64
Mean [Nm]	0.55	-0.58	0.59	-0.57

Table 7-1 Breakaway torques

7.2.2 Dynamic friction

In the dynamic region, the value of the friction torque is a function of the speed. Therefore, the estimation of the dynamic friction component requires the wheel to reach an equilibrium speed $v = \bar{v}$, in which the driving torque equals the friction torque:

$$T_{mot} = T_{frict} = T_{frict}(\bar{v}) \quad (7.4)$$

In order to achieve this speed, a PI speed controller was designed (see APPENDIX A).

The experimental setup was the same adopted for the static friction estimation, with the vehicle set on the side and the wheels being free to rotate without contact with the ground. Each wheel was then required to follow a speed profile starting from a value of 20 [rad/s] down to 3 [rad/s], and successively from 2.5 [rad/s] down to 0.25 [rad/s]: each value was hold for 20 seconds (see FIGURE 7.6), in order to allow to the wheel to reach the steady state value and to keep it long enough to obtain a fair value of the required torque. The choice of a downward speed trajectory was dictated by the presence of the static torque, which is higher than the dynamic one at low speeds; this, together with the fact that a very basic speed controller was implemented, leads the wheel to a limit cycling behaviour when low speeds are requested from a standing start. Conversely, the limit cycle is trivially avoided by reaching the low speed values only when the wheel is already spinning.

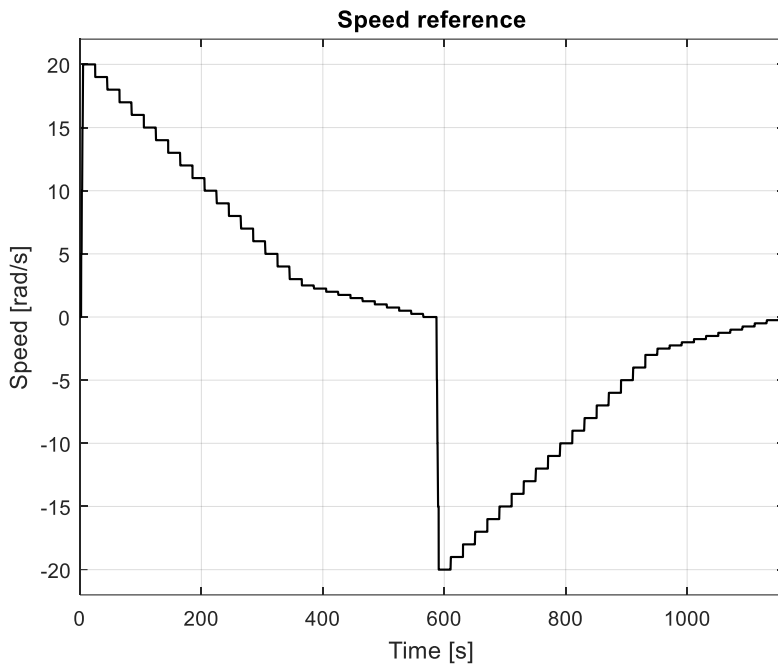


Figure 7-6 Speed reference for each wheel in viscous friction tests

Starting from the collected speed-torque tuples, it was possible to obtain the values for T_C , α_s , T_{visc} , by means of a non-linear regression of the equation (7.1). The actual implementation involved the use of *fitnlm()* MATLAB function, which fits a nonlinear regression model

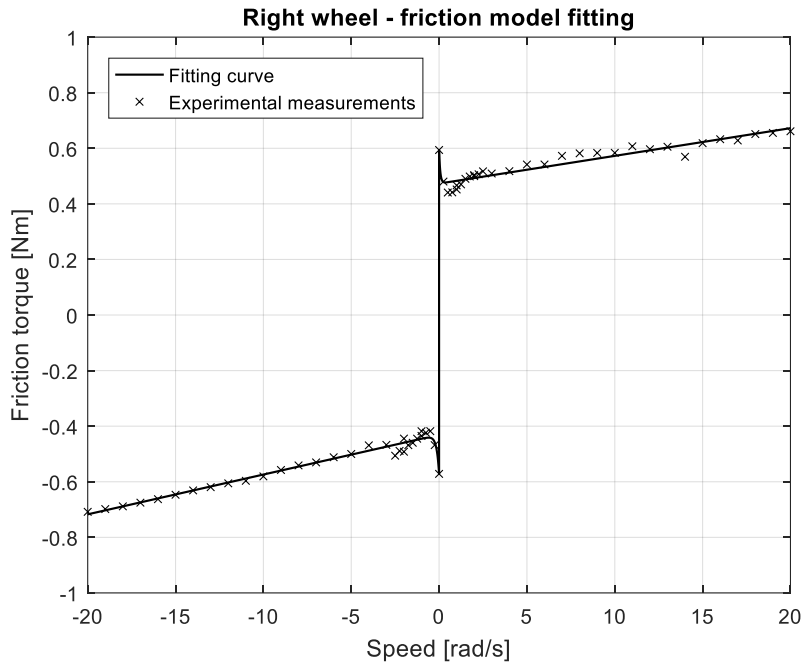


Figure 7-7 Friction model fitting – Right wheel

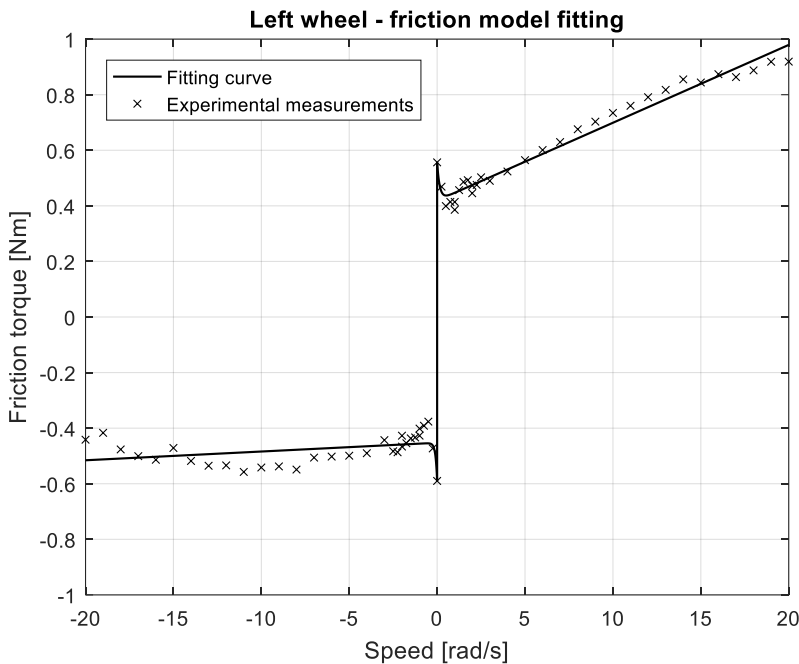


Figure 7-8 Friction model fitting – Left wheel

Left Wheel Positive		Left Wheel Negative	
Parameter	Value	Parameter	Value
T_s	0.55 [Nm]	T_s	-0.58 [Nm]
T_c	0.41 [Nm]	T_c	-0.47 [Nm]
T_{visc}	0.02 [Nms/rad]	T_{visc}	0.01 [Nms/rad]
α_s	6.87 [s/rad]	α_s	14,99 [s/rad]

Table 7-2 Estimated friction model parameters – Left wheel

Right Wheel Positive		Right Wheel Negative	
Parameter	Value	Parameter	Value
T_s	0.59 [Nm]	T_s	-0.57 [Nm]
T_c	0.45 [Nm]	T_c	-0.43 [Nm]
T_{visc}	0.003 [Nms/rad]	T_{visc}	0.01 [Nms/rad]
α_s	11.00 [s/rad]	α_s	7.16 [s/rad]

Table 7-3 Estimated friction model parameters – Right wheel

From table 7.2 and 7.3 it is possible to state that the two wheels present similar values of friction at low or null speed; in the high-speed region the right wheel shows reduced friction in positive direction, while the left wheel shows a symmetrical behaviour.

In FIGURE 7.7 and FIGURE 7.8 the experimental data together with the model-based curves are shown; it is possible to notice how a satisfactory fitting was obtained, thus validating the choice made for the friction model. An even better fit, however, was obtained by substituting the linear viscous term with one depending on the square root of the speed (FIGURE 7.9 and FIGURE 7.10).

$$T_{frict}(T_{mot}, v) = \begin{cases} T_{ext} & v = 0, T_{ext} \leq T_s \\ T_C + (T_s - T_C)e^{-\alpha_s v} + T_{visc}\sqrt{|v|} & v > 0 \\ -T_C + (T_C - T_s)e^{\alpha_s v} - T_{visc}\sqrt{|v|} & v < 0 \end{cases} \quad (7.5)$$

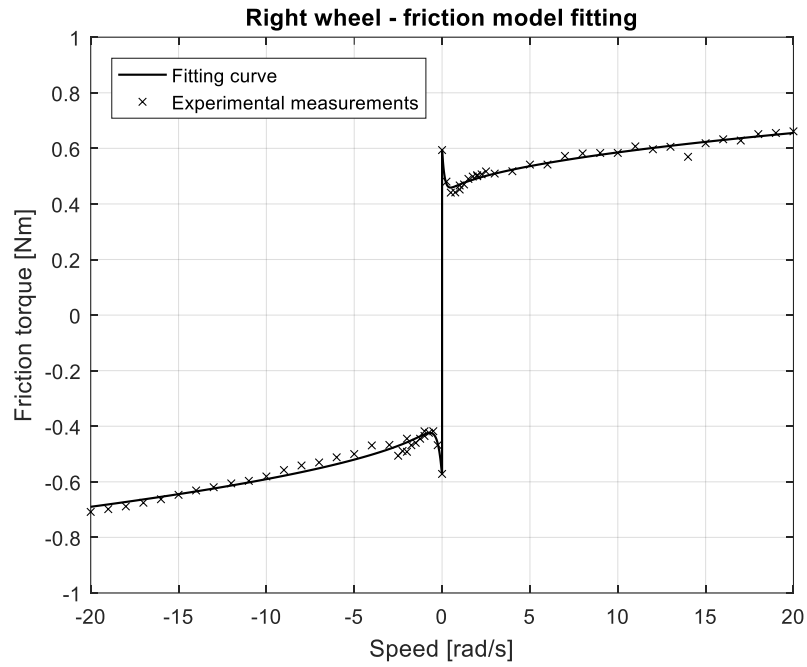


Figure 7-9 Friction model (viscous - root squared) fitting – Left wheel

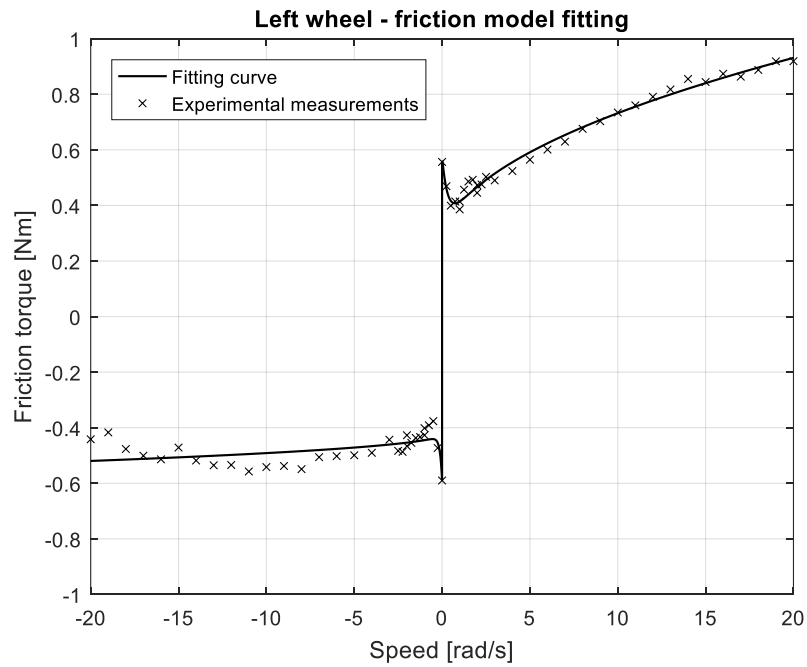


Figure 7-10 Friction model (viscous - root squared) fitting – Right wheel

Left Wheel Positive		Left Wheel Negative	
Parameter	Value	Parameter	Value
T_s	0.55 [Nm]	T_s	-0.58 [Nm]
T_c	0.25 [Nm]	T_c	-0.35 [Nm]
T_{visc}	0.15 [Nms/rad]	T_{visc}	0.07 [Nms/rad]
α_s	3.34 [s/rad]	α_s	4.42 [s/rad]

Table 7-4 Estimated friction model (viscous - root squared) parameters – Left wheel

Right Wheel Positive		Right Wheel Negative	
Parameter	Value	Parameter	Value
T_s	0.59 [Nm]	T_s	-0.57 [Nm]
T_c	0.41 [Nm]	T_c	-0.42 [Nm]
T_{visc}	0.05 [Nms/rad]	T_{visc}	0.02 [Nms/rad]
α_s	7.26 [s/rad]	α_s	8.39 [s/rad]

Table 7-5 Estimated friction model (viscous - root squared) parameters – Right wheel

Since this slight modification provides a relevant improvement in the model fitting, the choice of using the square root of the speed has been accepted as the correct one, and will be used hereafter.

7.2.3 Rolling Friction

The last friction component to be identified is the one deriving from the tyre rolling resistance. However, in order to obtain that, the vehicle needs to be standing in upright position, and to proceed at constant speed for a sufficient span of time. An LQ controller was used to achieve that (see Chapter 10 for the controller design).

By measuring the requested torque in the constant speed phase, and subtracting the torque needed to compensate the viscous and Coulomb frictions, T_{roll} was obtained. Since that torque is known to be independent from the speed, different tests were run at different speeds; in particular steady state speeds of 0.5, 1 and 1.5 m/s were requested to the controller. The results are shown in TABLE 7.6.

	0.5 m/s	1.0 m/s	1.5 m/s	Mean value [Nm]
Test 1 – Right wheel	0.2380	0.3151	0.2567	0.2699
Test 2 – Right wheel	0.2113	0.2768	0.2783	0.2555
Test 1 – Left wheel	0.5058	0.5187	0.4563	0.4936
Test 2 – Left wheel	0.4149	0.5084	0.4931	0.4721

Table 7-6 Rolling resistance – Test results

In order to have a check on the reliability of the test, a lower inflation pressure was imposed to the left tyre: this should result into higher values of the resisting torques, a fact that can be actually seen in the table.

7.2.4 Friction model: Conclusions

The experimental activity has shown how it is possible to perform a numerical assessment of a model describing all the main dissipation effects occurring on the vehicle. Such a model can be included in a simulation environment in order to reproduce otherwise missing behaviours such as limit cycling (FIGURE 7.11) and non-zero steady state torques. It could also be used to design a compensator for such effects, or to provide models of the energy consumption of the vehicle.

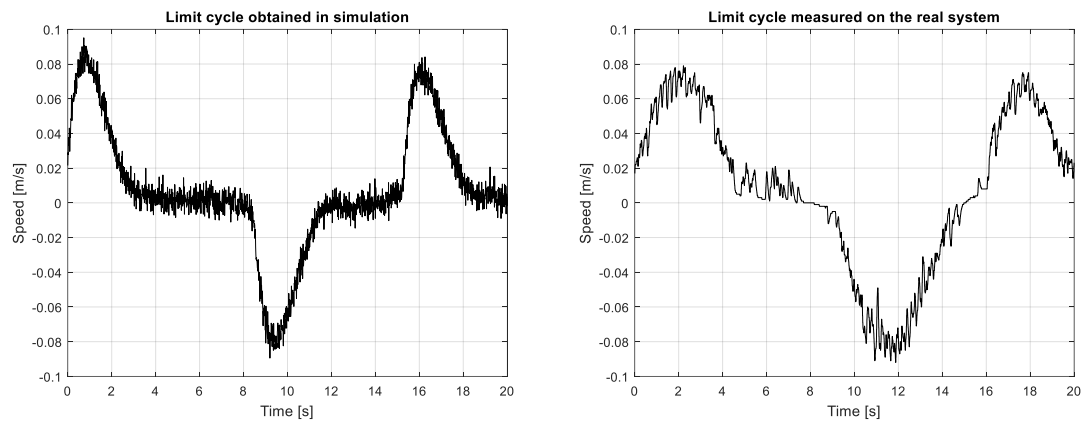


Figure 7-11 Simulated and measured limit cycle comparison

A more rigorous estimation procedure for the static and dynamic friction would require the vehicle to be standing, thus accounting for the weight of the chassis acting on the joint. However, this would imply non-trivial computations to separate the stabilization-torques from the friction related ones, making the procedure practically unfeasible.

The estimated rolling friction is actually heavily affected by environmental factors, such as temperature, material and conditions of the road and also by the tyre inflation pressure. For any control related purpose, an online estimation procedure would be required in order to obtain up to date values for this parameter. This constitute, in our judgement, a too heavy computational effort given the relatively small advantages coming from the knowledge of such a parameter.

Aerodynamics dissipations effects were neglected due to the relatively low speeds at which YAPE is designed to operate.

Magnetic effects resulting from anisotropies in the motor internal structure were not modelled as separate effects but rather considered as included in the adopted mechanical friction model, thus resulting in an easier but anyway expressive mathematical structure.

7.3 Mechanical Parameters:

7.3.1 Direct Measure

Most of the mechanical and physical parameters characterizing our model are quite easily measured. Among them we have all the lengths and the masses, whereas the moment of inertia and the c.o.g position had to be estimated in a different fashion.

All the lengths were measure using a standard measuring tape with 0.01 m precision, whereas masses where measured using a scale with 0.1 Kg precision. The obtained measures are listed below:

- Wheel's Radius: $R = 0.2 [m]$
- Axle Track: $d = 0.49 [m]$
- Wheel's Mass: $m_w = 4.0 [Kg]$
- Upper Hull Mass: $m_w = 6.0 [Kg]$
- Lateral Hull Mass: $m_2 = 1.1 [Kg]$ (x2)
- Chassis + Battery Pack + Lower Hull Mas: $m_3 = 18.2 [Kg]$
- Total swinging mass: $m_c = m_1 + 2 m_2 + m_3 = 26.4 Kg$
- Total Vehicle Mass: $m_t = 34.4 [Kg]$

7.3.2 Mechanical Parameters: Indirect Measure

The wheels Moment of Inertia where measured by approximating them with homogeneous discs, for which we have a radial M.o.I of:

$$J_w = \frac{1}{2} M_w R^2 = 0.0722 [Kg m^2] \quad (7.6)$$

Actually, the wheel shows a mass concentration near the rotation axis, due to the presence of the hub motor and the battery pack, which should result into a smaller value of J_w . Nevertheless, we considered this variation to have negligible effects on the vehicle dynamics, and (7.6) was accepted as factual value.

7.3.3 Mechanical Parameters: Model Fitting

The last parameters needed to provide a full numerical assessment of the model are the height of the centre of gravity (L) and the chassis M.o.I around the y-axis (J_{cy}). These parameters are of difficult calculation without having very precise measuring instruments, therefore they required a model-based estimation procedure.

Experimental numerical assessment is usually carried on by fitting the open loop response of a real system to a set of different inputs (typically steps and sine waves) with the one obtained from the same inputs in a simulated environment. (FIGURE 7.12)

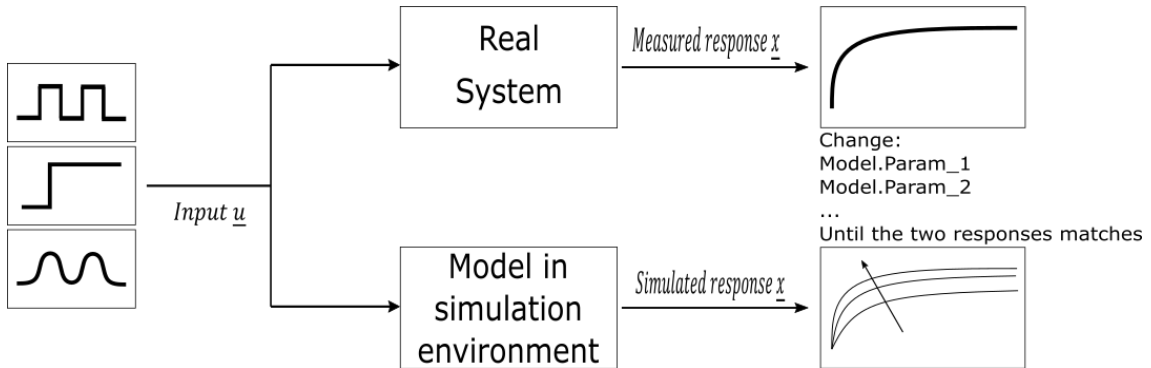


Figure 7-12 General scheme for parameters estimation in open loop procedure

However, being a WIP an unstable system, this type of procedure is not feasible in our case. A closed-loop identification was then set up, in which a stabilizing loop is closed, and an additive torque disturb is imposed to excite the vehicle's dynamics (FIGURE 7.13). The additive disturb was composed of sine waves at different frequencies, followed by steps and squared waves. All the disturb components had an amplitude of 5 Nm.

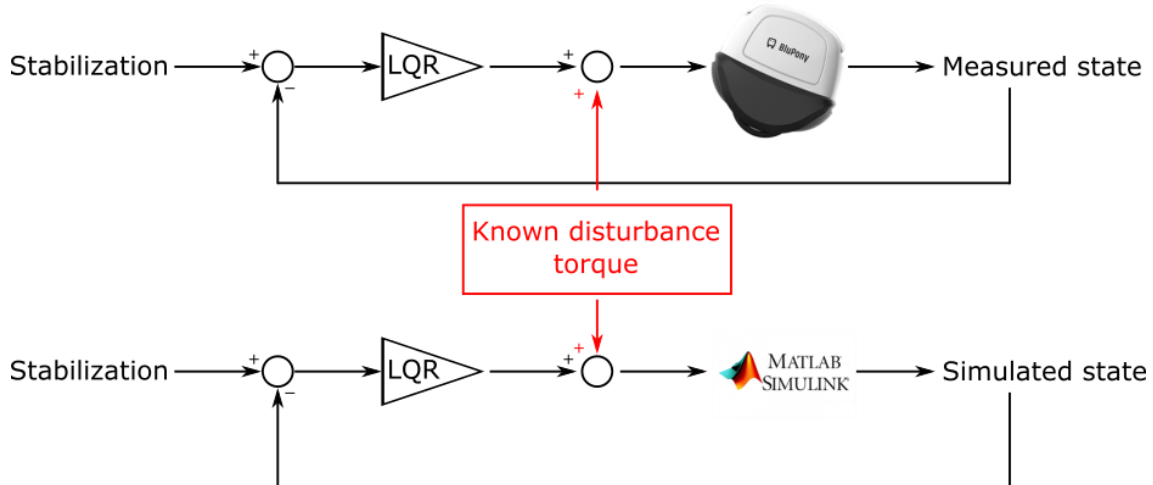


Figure 7-13 General scheme adopted for parameters estimation

By reproducing the same experiment in a Simulink environment, it was possible to make a comparison between the measured and the simulated state behaviour. In particular Pitch, Speed and Torques behaviours were compared. As a figure of merit, the Root Mean Square Error between real response and simulated one was computed:

$$f = \sqrt{\frac{\sum(x_{real} - \hat{x}_{simulated})^2}{N_{samples}}} \quad (7.7)$$

Different simulations were run for different values of L and J_{cy} , and their actual value was then retrieved by means of a minimization procedure on f . In the following an example of minimization results obtained with a squared wave disturbance.

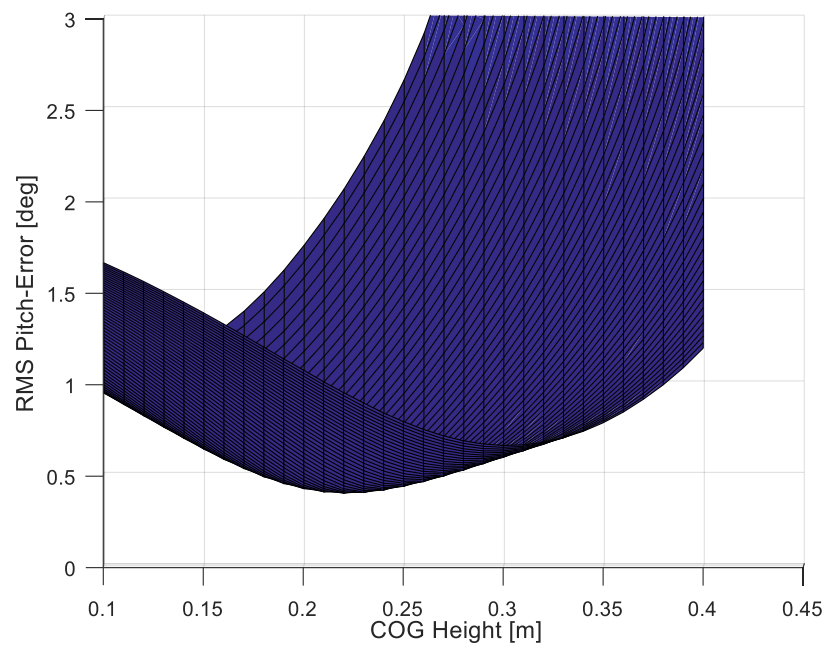


Figure 7-14 Example of RMSE sensitivity to c.o.g. height variations

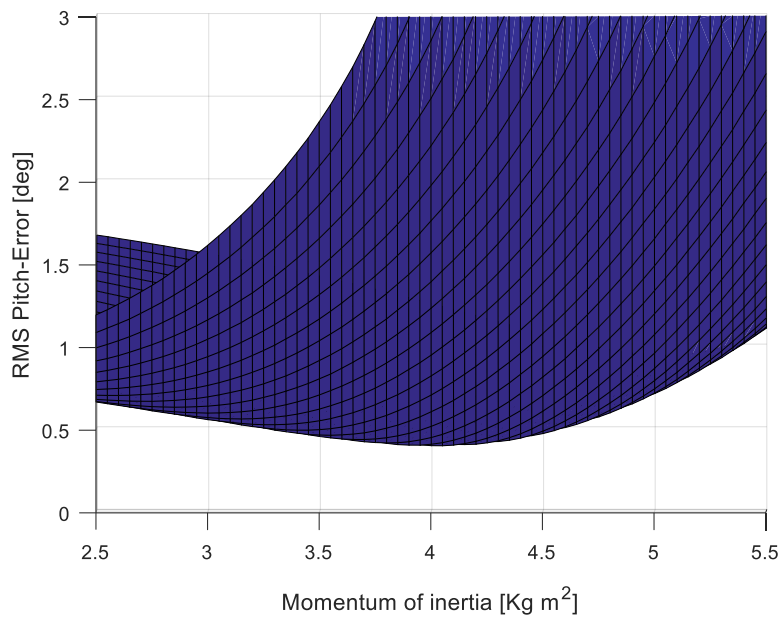


Figure 7-15 Example of RMSE sensitivity to moment of inertia variations

As we can notice from FIGURE 7.14 and FIGURE 7.15, the parameters value that better fit the response measured are:

- $L = 0.2 \text{ m}$
- $J_{cy} \approx 4 [\text{kg m}^2]$

The system response (and therefore the RMSE), is very sensitive to variations in the cog height, and much less sensitive to J_{cy} variations. It follows that the obtained estimate for J_{cy} is less reliable than the one obtained for L . However, this also means that poor knowledge on the nominal value of J_{cy} will not affect in a relevant way the closed loop behavior of the system, thus making acceptable the current estimate of $4 [\text{Kg m}^2]$ for J_{cy} .

7.4 Conclusion

In this Chapter it was shown how to achieve a satisfactory numerical assessment of all the physical parameters characterizing the dynamical model chosen for our system. The identified model will be used in the design phase of the stabilizing and driving controller. Moreover, together with the previously mentioned friction model, the obtained values for the mechanical parameter allowed to implement a quite reliable simulation environment for YAPE, thus providing a platform for tentative controllers to be tested safely and economically (FIGURE 7.16, 7.17, 7.18).

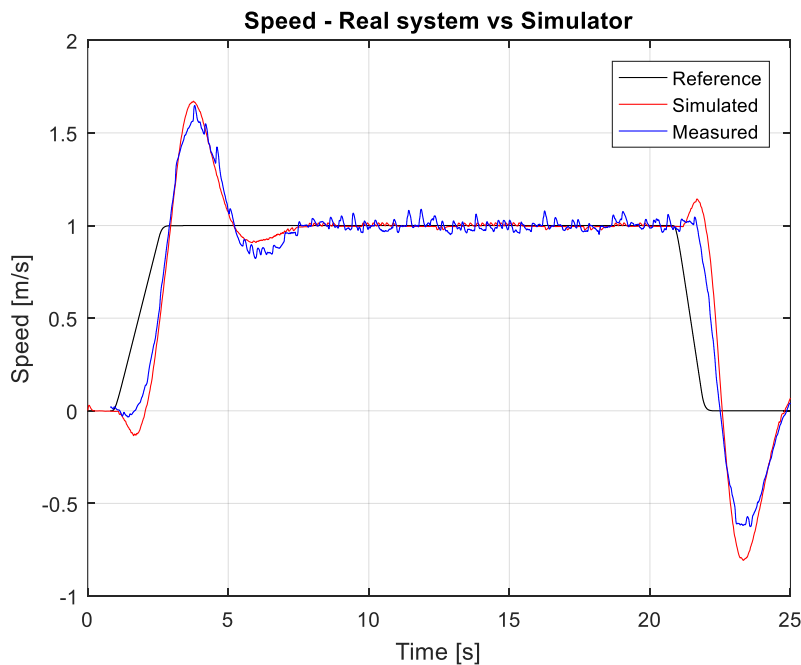


Figure 7-16 Real system versus simulator in following a trapezoidal speed profile. Speed analysis

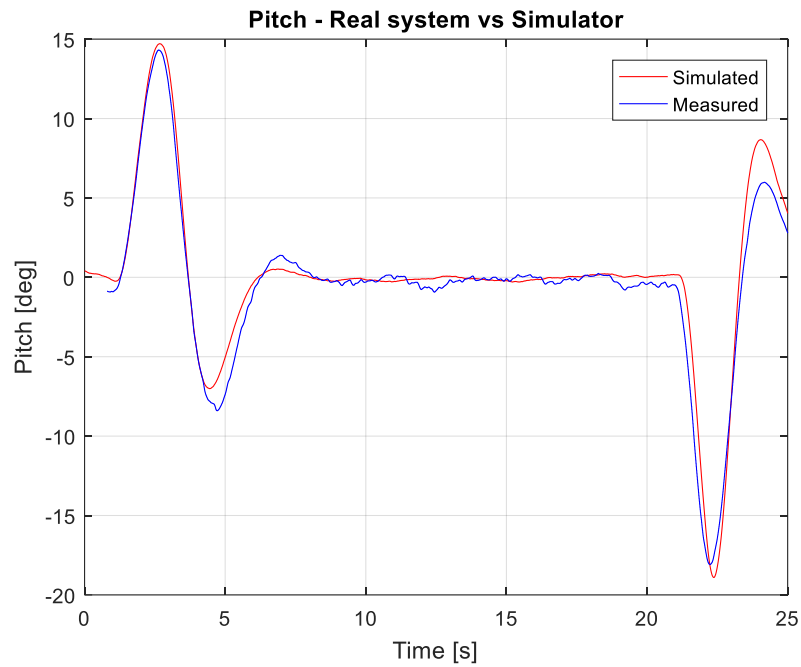


Figure 7-17 Real system versus simulator in following a trapezoidal speed profile. Pitch analysis

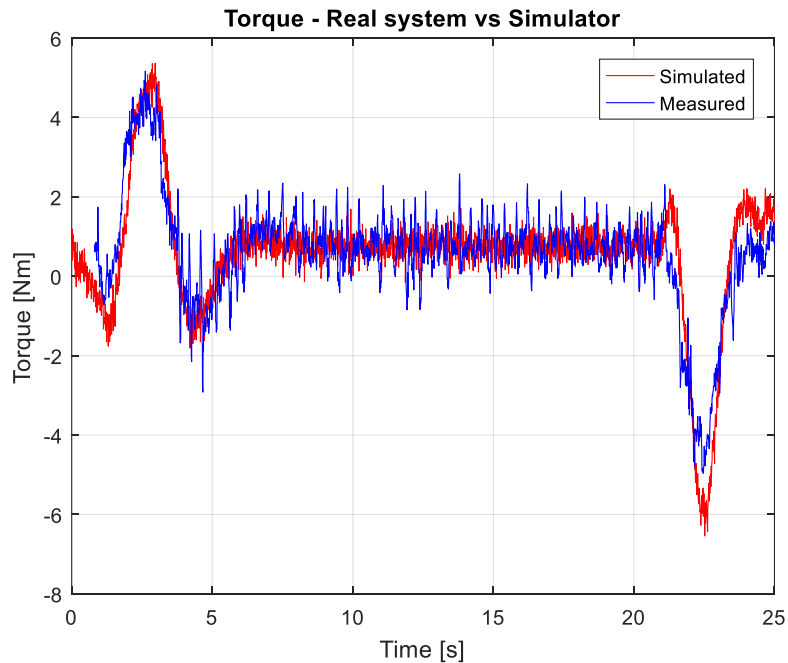


Figure 7-18 Real system versus simulator in following a trapezoidal speed profile. Torque analysis

Appendix A: PI controller

The transfer function between torque and wheel's speed was modelled as a first order system. Starting from the balance equation:

$$\tau_{mot} = J \ddot{\theta} + V_{fric} \dot{\theta} \quad (7.8)$$

where J is the wheel's moment of inertia, V_{fric} is the viscous friction coefficient, τ is the torque, $\dot{\theta}$ and $\ddot{\theta}$ are the wheel's rotational speed and acceleration respectively, the following transfer function is obtained:

$$G_{\tau\theta} = \frac{1}{V_{frict} + Js} \quad (7.9)$$

Based on G , a PI regulator $R(s) = \frac{s+3.12}{s}$ was designed with a bandwidth of 2 Hz.

Chapter 8 - Control structure

8.1 Introduction

As already mentioned, YAPE is a small autonomous, electric vehicle, designed for last-mile delivery in urban environment. The short-term goal for YAPE company is to make it operational as a remote-controlled prototype in which a human operator drives the vehicle having access to a data streaming coming from the cameras and the lidar Sensors on board.

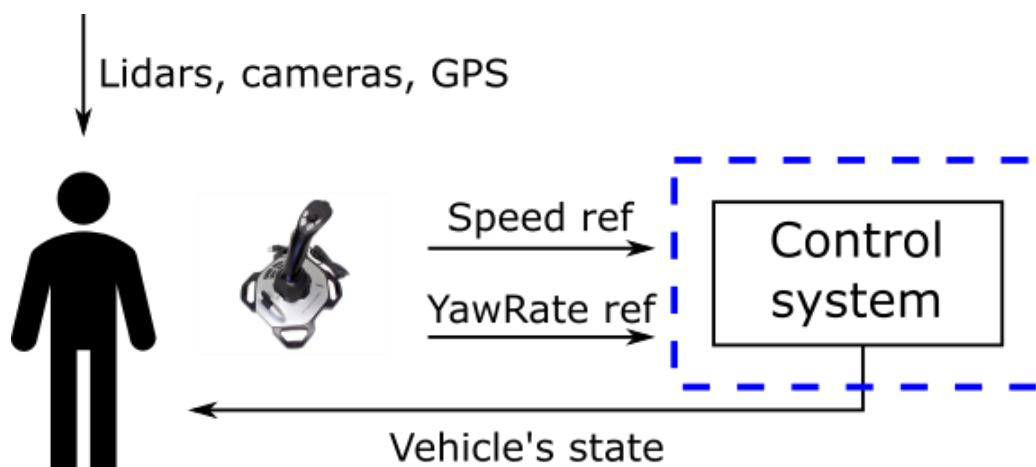


Figure 8-1 Control structure with human driving.

A medium-long term objective is that of making the vehicle fully autonomous and capable of reaching a desired place while autonomously planning an appropriate trajectory.

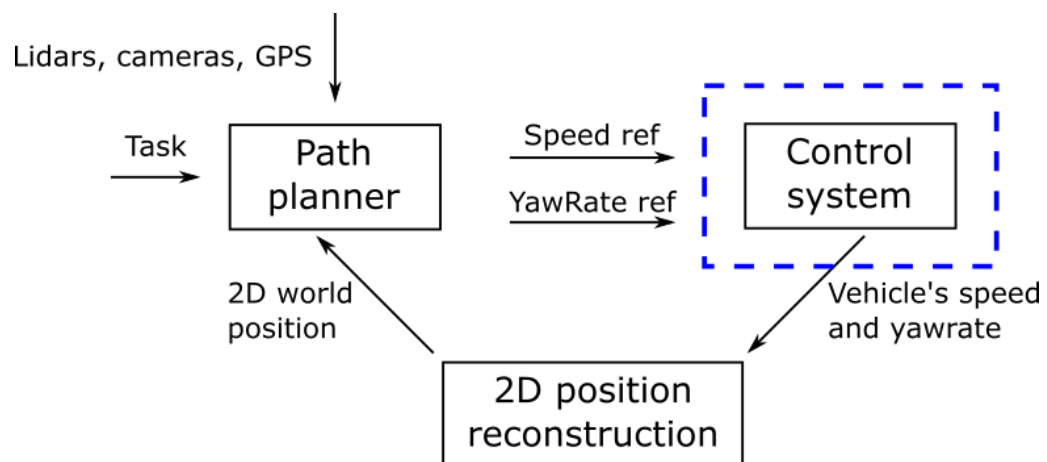


Figure 8-2 Control structure with autonomous driving

As already mentioned, the purpose of our work was to design and test the internal feedback control system (blue block in FIGURE 8.1 and FIGURE 8.2), capable of tracking speeds and yaw rate profiles in both these application cases. A schematic representation of the internal structure of such control system is presented in FIGURE 8.3

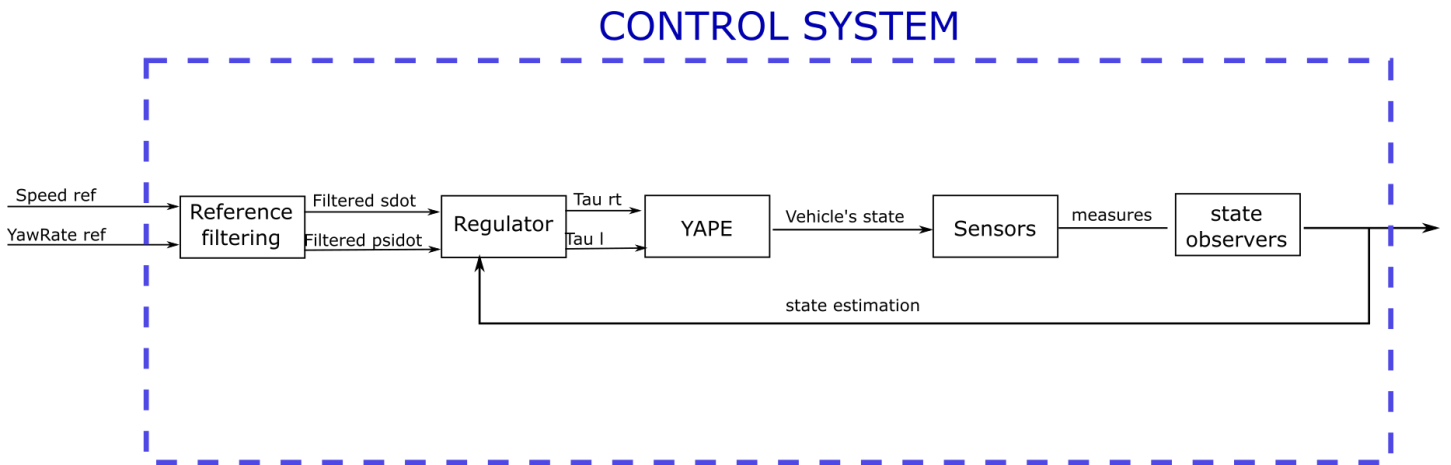


Figure 8-3 Control system expanded scheme

Most of the blocks constituting the scheme of FIGURE 8.3 were treated in the previous chapters of this work: first of all, a model for YAPE was developed in CHAPTERS 3, 4 AND 7; the sensors were analysed in CHAPTER 2, and a calibration procedure for them was explained in CHAPTER 5; finally, a set of reliable state observes was designed and tested in CHAPTER 6.

In the following sections, a brief presentation of the practical and theoretical aspects behind the reference filtering and the regulator blocks will be reported, followed by a description of the aspects that will be tested on each regulator. Then, a more in-depth analysis for each block will be covered in next two chapters: the reference filtering block will be explained in CHAPTER 9, and two possible control approaches for designing the regulator block will be presented in CHAPTERS 10 AND 11.

8.2 Reference filtering block

Limiting as much as possible the pitch dynamics is particularly important for YAPE, which needs to avoid damages to the carried packs and to maintain the maximum possible field of view for the exteroceptive sensors. The relation between \ddot{s} and θ observed in CHAPTER 3 and suggest the possibility of achieving that by means of a reference filtering process. In particular, the aim of such block is to produce a smoother pitch behaviour and to minimize the possibilities of reaching the maximum pitch angle, crashing the hull on the ground. This is obtained by filtering the high frequency components of the reference signals, and limiting the maximum required acceleration. The second action is particularly critical when the LQ controller is used, whereas it is possible to replace it with a faster and more efficient technique when using a Cascade controller.

8.3 Regulator block

From a control theory point of view, YAPE is a typical non-linear, under actuated, MIMO system. In fact, three states (namely the speed, the yaw rate, and the pitch angle) need to be controlled using only two control variables, namely the two torques provided by the wheels. The control problem was addressed using two different approaches: a MIMO Linear Quadratic controller, and a Cascade approach with multiple SISO controllers acting on nested loops. The LQ regulator is one of the most frequently adopted approaches in WIP control; it is a state-feedback MIMO controller which requires a reasonably small effort to be designed, since it involves only a linear model for the system and the definition of two positive definite weight matrices. As reported in many examples that can be found in literature, LQ provides quite satisfactory results when applied to WIPs, both in terms of pure speed tracking performances and of rejection of disturbs such as sloped roads. On the other hand, it lacks a simple and reliable way of imposing a limitation to the pitch angle; this typically leads to a deliberate reduction of the speed performances in order to minimize the risk of the vehicle hitting the ground. This particular aspect prompted us to explore the possibility of a Cascade approach. The goal is that of creating two different control loops: a first internal loop to stabilize and control the vehicle pitch, and an outer speed loop which, based on the considerations made in Chapter 4, uses the pitch to impose the desired speed. With such an approach, pitch limitation could be achieved by means of a saturation on the pitch reference signal produced by the speed regulator (FIGURE 8.4)

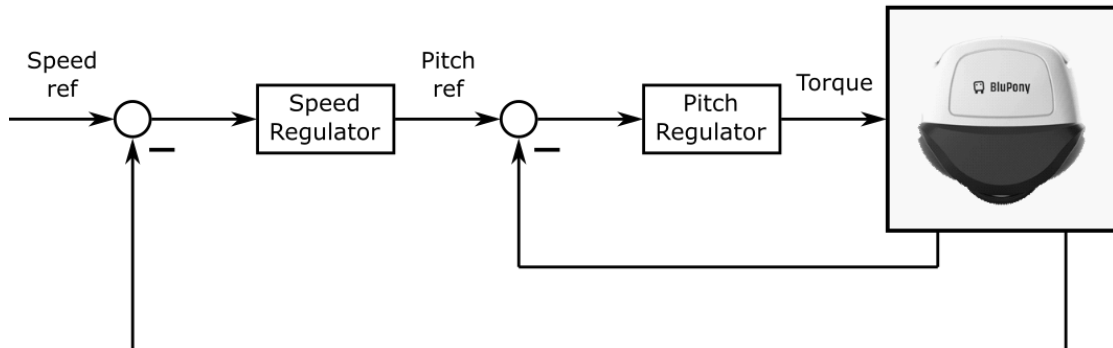


Figure 8-4 Cascade control architecture

In the following section, some measures of the effectiveness of each controller are introduced.

8.4 Regulator performance indexes

To provide a suitable way of confronting the performances of the two approaches, a series of test was designed accounting for all the major requirements that YAPE's control task presents.

First of all, being YAPE a WIP vehicle, all its longitudinal motions are coupled with a tilting motion of the chassis; that implies the need for the controller to limit the pitch in accordance to the hull

clearances, in order to avoid hitting the ground with it. Secondary, since the vehicle is designed for package delivery, it will be subjected to possibly relevant mass and c.o.g. position variations, so that any stabilizing controller needs to be robust to this type of disturbances. Finally, since YAPE is expected to move into an urban environment it needs to be able to face several challenging situations, including intricated paths, inclines, and small steps (see CHAPTER 4).

To consider all these problematics, 5 different requirements were tested on each controller:

- Pitch Limitation
- Start and Station Keeping:
- Turn-on-the-spot capabilities
- Unbalanced Load handling
- Uphill roads handling

8.4.1 Pitch Limitation

The pitch limitation problem is quite easy to understand: due to the geometrical shape of the hulls, any pitch angle greater than 30° would result into the vehicle hitting the ground (FIGURE 8.5), leading to instability and possibly to a total system failure. Moreover due to the presence of lidars and cameras whose field of view reduces as the pitch increases, the pitch limitation of problem is particularly critical for YAPE.

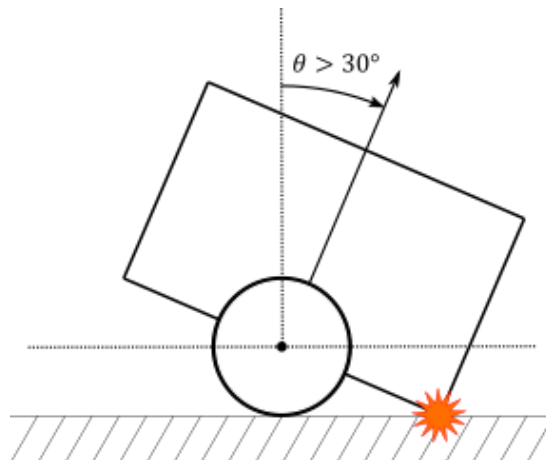


Figure 8-5 Pitch angle limit.

The occurrence of this problem is related to two main causes: a poor pitch controller and a too aggressive speed controller. If the first is quite straightforward to understand, the second is less intuitive, as it is related to the dynamic nature of WIPs. In fact, as already noticed in CHAPTER 3 and CHAPTER 4, the pitch and speed dynamics of a WIP are inevitably coupled. Putting it simply, at any steady state pitch angle correspond a steady state torque, which in turns produces a certain longitudinal acceleration. Vice versa, if the vehicle needs to undergo a specific acceleration, a certain torque is required, which correspond to a unique, non-zero, stable pitch position. This implies that requesting strong accelerations to YAPE could lead it to overshoot the maximum allowed pitch angle.

Handling this type of dynamics is the first problem that will be issued for both the controllers, using slightly different techniques leading to different results.

8.4.2 Start and station keeping

In order to limit the energy consumption, YAPE's stabilization control is likely to be shut down in certain situations, such as the load and unload of a package. For this reason, the vehicle needs to be able to lean on the ground when turned off, and rise from there when switched back on (FIGURE 8.6). Even if the first manoeuvre was not addressed in our work, the second one was instead tested on each controller implemented on YAPE.

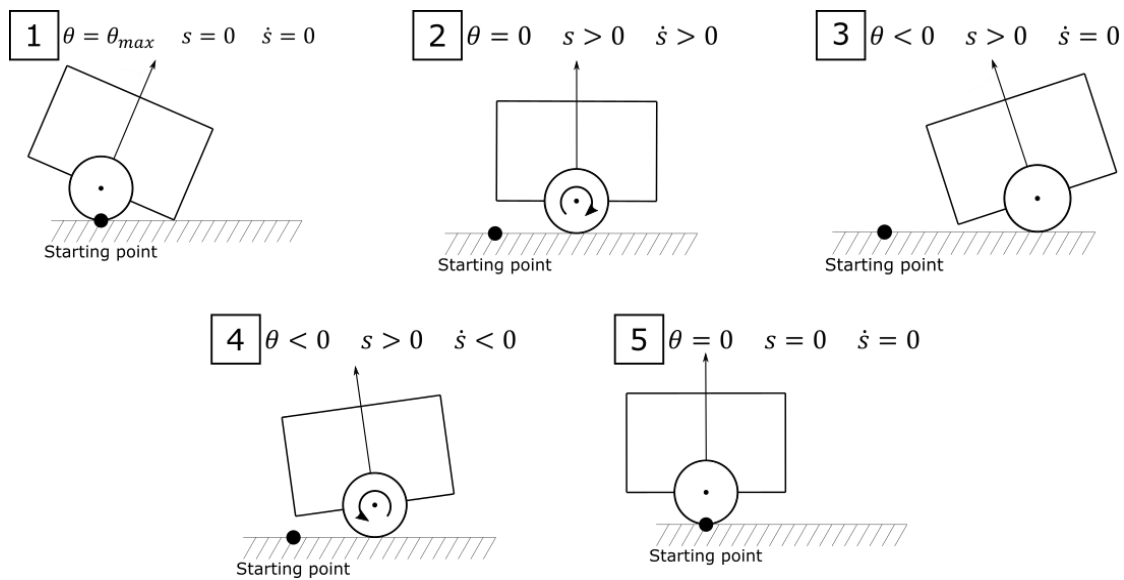


Figure 8-6 Start-up procedure schematization

Once standing up, the vehicle needs to be able to maintain the equilibrium pitch angle whilst keeping its position. This has been referred as station keeping. Due to the unstable nature of the vehicle, together with the presence of frictions and non-idealities in general, station keeping requires continuous pitch adjustments: this implies that the vehicle enters almost inevitably into a limit cycle behaviour, making it oscillate around the equilibrium position. The capability of reducing these limit cycles was another criterion used in the confront of the various attempted controllers.

8.4.3 Turn-on-the-spot capabilities

One of the characteristics that distinguishes YAPE from many of his competitors is the ability to perform turns on the spot. In fact, due to his two-wheeled structure, YAPE is endowed with a great manoeuvrability, which allows it to follow complex path also in a crowded environment. This capability was one of the main reasons driving the developers to choose a WIP structure for this vehicle. (FIGURE 8.7)

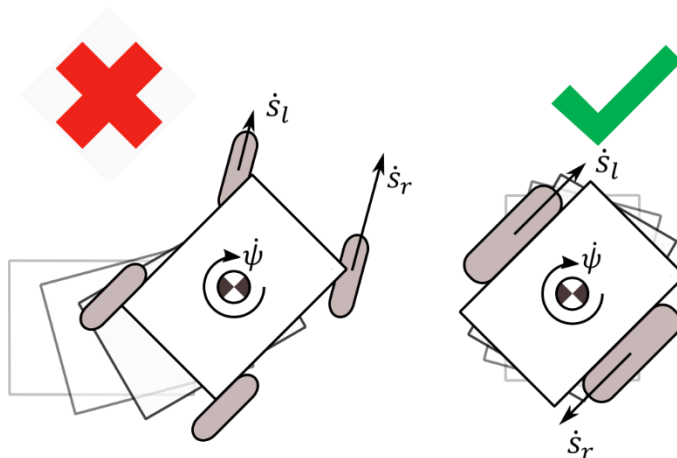


Figure 8-7 Two wheel – Four wheel vehicle turning comparison

Ideally, having two parallel, symmetric wheels, YAPE should be able to turn on the spot, i.e. having zero speed at the track centre, simply by applying opposite torques to the two wheels. However, this capability is impaired by many factors, such as different inflation pressure of the tyres, actuators nonidealities or the two wheels being on grounds with different grips. Errors in the estimation of the vehicle's dynamic state can also affect turn-on-the-spot capabilities. Finally, poor pitch stabilization performances are also reducing the capability of the vehicle to turn on the spot, due to the non-symmetric torques needed to bring the vehicle back to vertical position.

The ability to react to all these possible error sources and grant the minimum curve radius is another criterion used to confront the performances of the various controllers.

8.4.4 Unbalanced Load handling

Due to non-symmetric mass distributions, the c.o.g. is very unlikely to be perfectly centred with respect to the wheel axis. Moreover, because of the loading and unloading of packages, this position will also necessarily be subjected to occasional and unpredictable variations. (in FIGURE 8.8 a graphic view of unbalanced load).

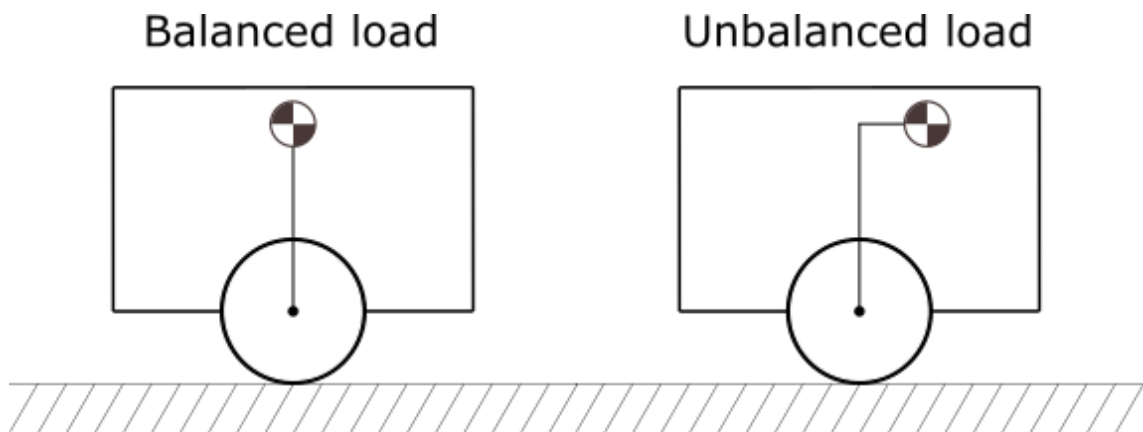


Figure 8-8 Schematic view of balanced and unbalanced load.

As already mentioned in CHAPTER 4, the pitch equilibrium position consequently results to be unknown and, in general, different from zero. From a practical point of view, the system is modelled as an L-shaped pendulum, where γ , i.e. the angular displacement of the c.o.g. with respect to the vehicle vertical axis, is an unknown parameter.

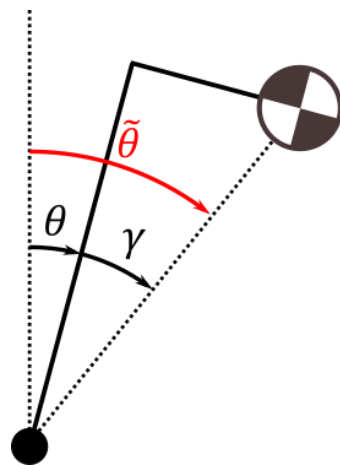


Figure 8-9 Angle offset introduced by unbalanced load in pitch behaviour

Recalling Chapter 4, the c.o.g. pitch angle with respect to the gravitational reference system is then given by:

$$\tilde{\theta} = \theta + \gamma \quad (8.1)$$

in which θ is the measured pitch angle, i.e. the angular displacement of the chassis with respect to the gravity-referred vertical position, and γ is the unbalanced load angle (FIGURE 8.9). This results in an unknown equilibrium position of:

$$\theta = -\gamma \quad (8.2)$$

Once again, the ability to react to random changes in the equilibrium position is one of the aspects that have been investigated on each controller.

8.4.5 Uphill roads handling

Being designed to operate in an urban environment, YAPE must be able to overcome occasional uphills and downhills. This type of obstacle can be present in different fashions, from short and relatively steep sidewalk slides, to long uphill roads and overpasses.

Italian law provides for a maximum slope for each step category:

Law	Description	Values	
		Type of road	Maximum slope
Decreto Ministero delle Infrastrutture e dei Trasporti – D.M. 05/11/2001	This law regulates the maximum slope of roads accessible by cars.	AUTOSTRADA EXTRAURBANA PRINCIPALE EXTRAURBANA SECONDARIA URBANA DI SCORRIMENTO URBANA DI QUARTIERE LOCALE	6% 6% 7% 6% 8% 10%
Decreto del Ministro dei lavori pubblici 14 giugno 1989, n. 236	This law regulates the maximum slope of the ramp inside public and housing complex in order to grant accessibility to wheelchair users.	<ul style="list-style-type: none"> - Max slope: 8%; - Slopes of not more than 15% are permitted for a maximum height of 15 cm. 	
Lombardia - LEGGE REGIONALE 20 febbraio 1989 , N. 6 (Adopted by most of Italian regions)	This law regulates the maximum slope of ramps of sidewalks.	<ul style="list-style-type: none"> - For ramps up to m. 0.50 the maximum permissible slope is 12%; - For ramps up to m. 2.00 the maximum permissible slope is 8%; - For ramps up to m. 5.00 the maximum permissible slope is 7%; - Beyond the m. 5.00 the maximum permissible slope is 5%. 	
<i>Decreto ministeriale 1° febbraio 1986 (G.U. n. 38 del 15 febbraio 1986)</i>	This law regulates the maximum slope of ramps inside public or private garages (capacity > 9 vehicles).	Maximum slope allowed = 20%.	

The first problem to be addressed while designing a controller to be capable of facing non-zero slope roads is a geometrical one. In fact, in CHAPTER 4 it was proved that the vehicle needs to tilt forward during uphills, and backward during downhills in order to contrast the effects of gravity.

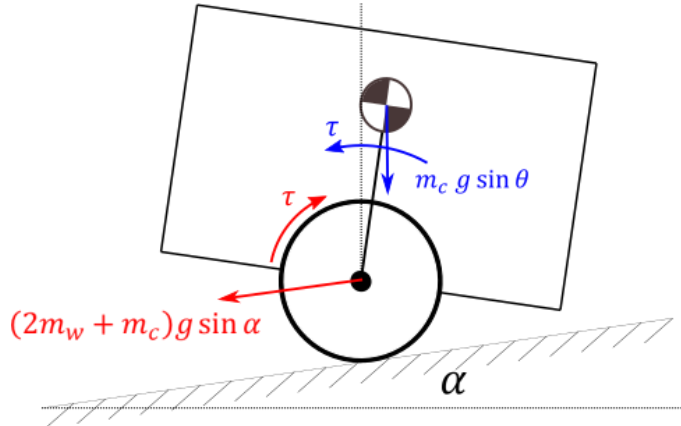


Figure 8-10 Forces acting on the vehicle at constant speed on uphill road.

In particular, looking at FIGURE 8.10 the equilibrium pitch angle was computed as:

$$\theta = \arcsin\left(\frac{R(2m_w + m_p)\sin\alpha}{Lm_p}\right) = \arcsin\left(\frac{R\sin\alpha}{L} \left(1 + \frac{2m_w}{m_p}\right)\right) \quad (8.3)$$

As we can see from (8.3), the equilibrium angle is a function of the road slope α , of the swinging mass m_c and of the c.o.g height L (wheel's mass and radius are considered as constant parameters).

Starting from (8.3), and knowing that the vehicle has a clearance angle of 30° , it is possible to compute the maximum slope the vehicle can overcame in nominal conditions. By defining as r the straight line connecting the wheel's contact point with the chassis vertex, we have that:

$$\epsilon = \theta_{MAX} - \theta - \alpha \quad (8.4)$$

is the angle between r and the ground, i.e. the residual clearance angle.

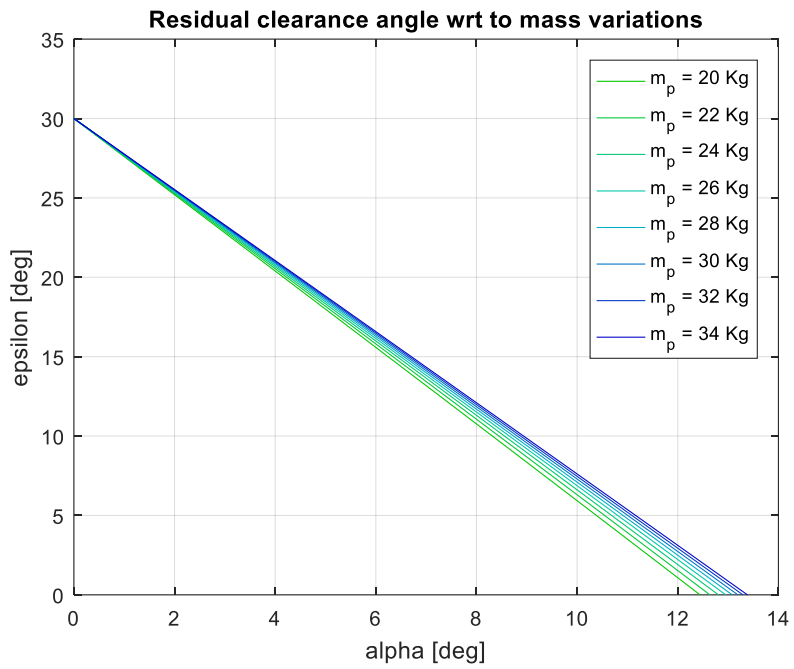


Figure 8-11 Residual clearance angle wrt mass variations

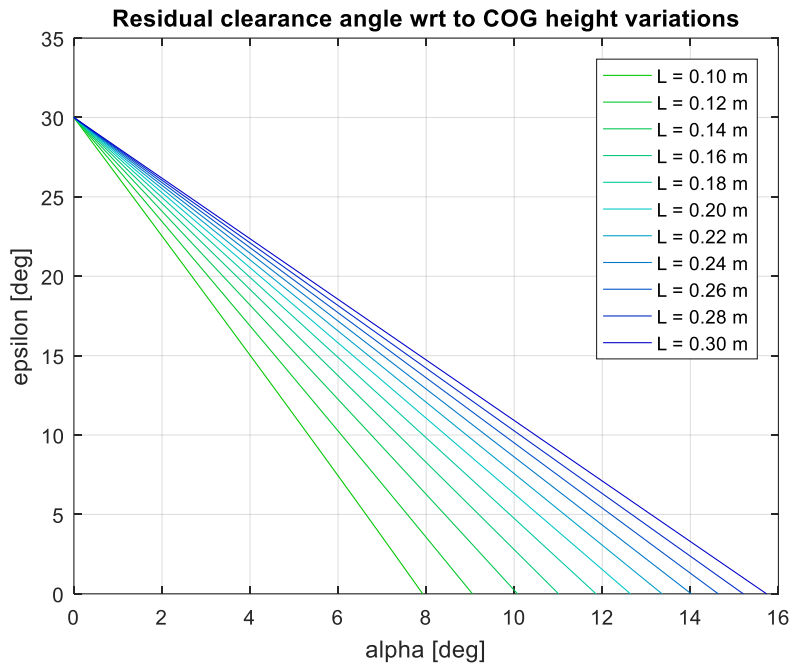


Figure 8-12 Residual clearance angle wrt c.o.g. height variations

By setting:

$$\epsilon = 0 \quad (8.5)$$

we can compute the maximum affordable slope as:

$$\alpha = \theta_{MAX} - \theta \quad (8.6)$$

With our experimental setup we have:

- $m_w = 4 \text{ Kg}$
- $R = 0.2 \text{ m}$
- $m_p = 24 \text{ Kg}$
- $L = 0.2 \text{ m}$
- $\theta_{MAX} = 30^\circ$

resulting into a maximum affordable slope of 12.8° (i.e. an 22.7% slope uphill). In practice, this value must be reduced in order to leave a margin to the pitch and speed controller to act tilting the vehicle in order to brake or accelerate it. FIGURES 8.11 AND 8.12 report the value of the clearance angle as a function of the slope angle α ; in particular, FIGURE 8.11 shows the sensitivity of the clearance angle to mass variations, whereas FIGURE 8.12 accounts for L variations. Notice that increasing the mass or the c.o.g height actually produces an increase in the maximum geometrically affordable slope (which is the intersection of the curves with the horizontal axis). FIGURE 8.13 shows the clearance angle of uphill road used during experimental tests.



Figure 8-13 Clearance angle of the uphill road used during experimental tests

8.5 Conclusions

The general control scheme for YAPE was presented in this chapter. Two control approaches for stabilize and drive the vehicle were briefly presented, together with a set of specifications that the vehicle needs to comply with in order to suitably perform the operations for which it was designed. All these considerations will be taken into account in the next chapters, in which the actual controller design phase is reported

Chapter 9 - Reference filtering

9.1 Introduction

The first goal of any WIP controller is to keep the vehicle in a vertical and stable position; this is particularly important for YAPE, which needs to limit as much as possible the pitch dynamics in order to avoid damages to the carried packs. However, as we noticed in Chapters 3 and 4, there is a direct relation between the speed dynamics and the pitch ones; therefore, in order to produce big accelerations, the vehicle needs to assume deeply tilted positions. This suggest the possibility of moderating the pitch behaviour by means of a reference filtering process.

In particular, two different actions were implemented: a low pass filtering action and a limitation of the reference speed rate. The first aims at producing a smoother pitch behaviour by limiting the high frequency components of the reference signals, and it is particularly needed in case of human driver. The second is intended to minimize the possibilities of reaching the maximum pitch angle by limiting the maximum required acceleration. As will be explained in CHAPTERS 10 AND 11, this rate limiting action is fundamental when the LQ controller is used, whereas it is possible to replace it with a faster and more efficient technique when using a cascade controller.

9.2 Rate limiter

Since in WIPs the pitch angle is directly related to the longitudinal acceleration, it is possible to act on the speed reference to limit the maximum steady state angle that the vehicle will assume. This is simply achieved by limiting the maximum required acceleration to a specific value, corresponding to the maximum affordable pitch.

In order to obtain the relation between steady state pitch and acceleration, the nonlinear dynamical equations obtained in CHAPTER 3 are used, namely:

$$\begin{cases} \tau_r + \tau_l + J_{cy}\ddot{\theta} + m_c L^2 \ddot{\theta} + m_c L \ddot{s} \cos \theta = m_c g L \sin \theta \\ (m_c + 2m_w + 2\frac{J_w}{R^2})\ddot{s} + m_c L \ddot{\theta} \cos \theta = \frac{\tau_r}{R} + \frac{\tau_l}{R} + m_c L \dot{\theta}^2 \sin \theta \end{cases} \quad (9.1)$$

At steady state speed we can impose:

$$\ddot{\theta} = \dot{\theta} = 0 \quad (9.2)$$

Obtaining the following system of equation:

$$\begin{cases} \tau_r + \tau_l + m_c L \ddot{s} \cos \theta = m_c g L \sin \theta \\ (m_c + 2m_w + 2 \frac{J_w}{R^2}) \ddot{s} = \frac{\tau_r}{R} + \frac{\tau_l}{R} \end{cases} \quad (9.3)$$

Getting $(\tau_r + \tau_l)$ from the first equation, substituting it in the second one, and rearranging we can obtain the equation relating the pitch angle and the acceleration of the system at steady state:

$$\ddot{s}(\theta) = \frac{m_c g L \sin \theta}{m_c L \cos \theta + 2 R \left(\frac{J_w}{R^2} + m_w \right) + m_c R} \quad (9.4)$$

Using (9.4) it is possible to compute the acceleration corresponding to the maximum acceptable steady state angle as:

$$\ddot{s}_{MAX} = \frac{m_c g L \sin \theta_{MAX}}{m_c L \cos \theta_{MAX} + 2 R \left(\frac{J_w}{R^2} + m_w \right) + m_c R} \quad (9.5)$$

Therefore, calling \ddot{s}_R the derivative of the speed reference signal, it is possible to impose:

$$\ddot{s}_R \leq \ddot{s}_{MAX} \quad (9.6)$$

which grants that the steady state pitch of the vehicle will not be greater than θ_{MAX} .

Notice that even if this holds, there is actually no guarantee that the pitch will always be smaller than θ_{MAX} . The first reason for this is that the equations are referred to a steady state situation which implies that, depending on the controller, the vehicle could easily overshoot θ_{MAX} before actually reaching it. Secondarily, since the acceleration limit is only imposed on the speed reference and not on the actual speed, there is no actual guarantee that the controller will not impose bigger acceleration to the vehicle trying to reach the reference value \dot{s}_R . Since this has proved to be particularly true for the LQ controller, a relatively small value of θ_{MAX} had to be chosen in order to grant safety margins to the pitch angle. Conversely, the cascade approach suggested the possibility of removing the rate limiter and replacing it with a more efficient closed loop solution that will be explained in CHAPTER 11.

In the implementation, different values of θ_{MAX} were selected for acceleration and for braking; namely, a bigger value of θ_{MAX} was imposed during braking phase, in which a contact with the ground is preferable to a too small braking action causing the vehicle to crash against an eventual obstacle. In particular, the maximum acceleration during acceleration was set to 0.6 m/s^2 (that correspond to $\theta_{MAX} = 8.68^\circ$), while maximum braking was set to -1 m/s^2 (that is $\theta_{MAX} = -14.45^\circ$).

FIGURE 9.1 shows how a square wave and a sinusoidal speed profile are processed by the rate limiter.

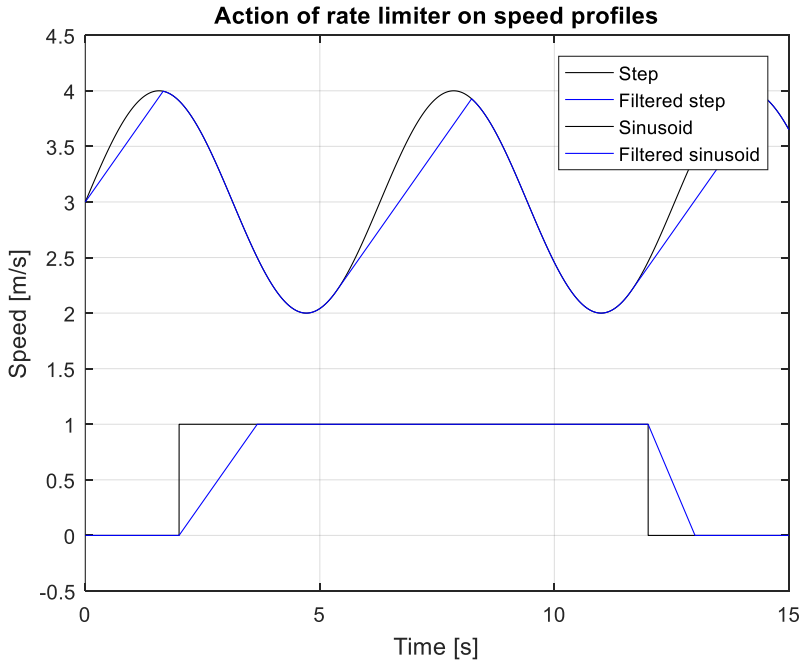


Figure 9-1 Action of rate limiter on speed profiles

It is clear that, in principle, the rate limiter action could be delegated to the pilot itself, which could adopt a less aggressive driving style in order to limit the maximum pitch. However, this would be practically unfeasible for the human driver, for whom the introduction of a rate limiter resulted in a significant improvement of the vehicle drivability.

9.3 Low-Pass filtering

Due to the already noticed relation between accelerations and pitch, the presence of high frequency component in the speed reference signal reflects in an oscillatory pitch behaviour of the vehicle.

In order to reduce such undesired behaviour, the speed reference is filtered using a low pass filter

The sources of high filter noise on the speed reference are mainly related to the human driver: in our case they were associative to small undesired thumb movements on the joystick stick. The cut-off frequency was therefore experimentally chosen as 2.5 Hz, a value which constitutes a tradeoff between oscillation rejection and vehicle reactivity.

FIGURE 9.2 shows a speed reference produced by a human driver trying to keep a constant speed.

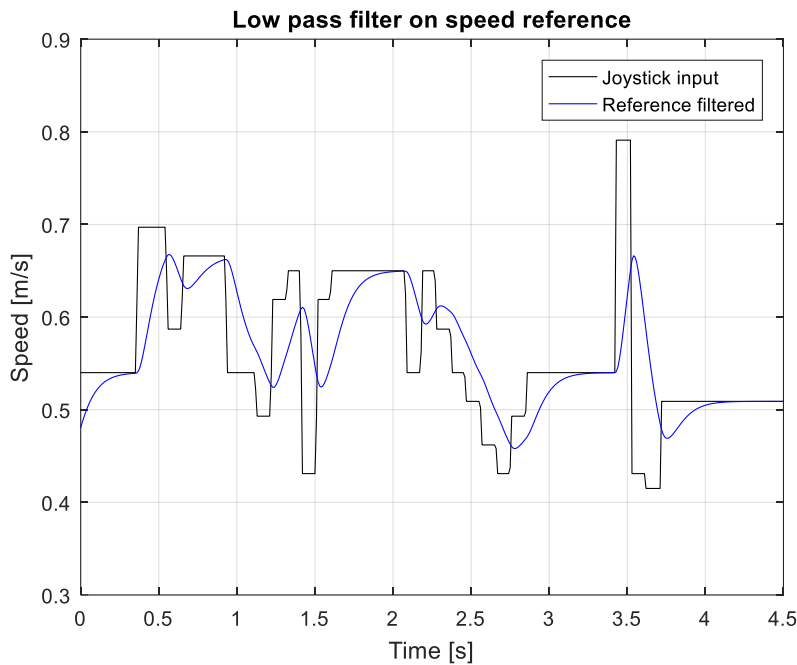


Figure 9-2 Low pass filter on speed reference

Finally, it's worth noticing that such low pass filter action can be applied also to the yaw rate reference signal, resulting in an additional improvement of the vehicle driveability. The overall reference filtering scheme is reported in FIGURE 9.3.

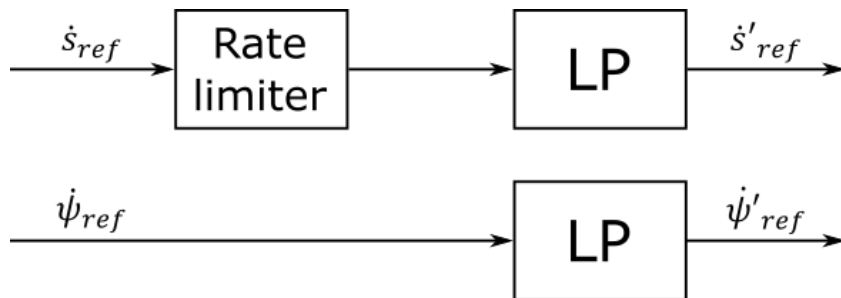


Figure 9-3 Overall scheme of reference filtering

9.4 Conclusions

In this chapter it was shown how a reference filtering procedure was created in order to reduce the vehicle oscillation and minimize the risk of a contact between the hull and the ground. Such procedure is particularly needed in case of a human pilot since it significantly increases the vehicle driveability. Nevertheless, especially for what concerns the rate limiter, this filtering action causes a reduction of performances in the vehicle; as such, an attempt of overcoming its limitations will be presented in CHAPTER 11.

Chapter 10 - LQ Controller

10.1 Introduction

From a control theory point of view, YAPE is a time-invariant underactuated MIMO system, with two inputs, namely the torques produced by the hub motors, and 3 outputs, which are the longitudinal speed, the vehicle pitch, and the vehicle yaw rate. A natural choice for controlling this type of systems is the Linear Quadratic Regulator, a particular type of optimal control which provides a fast and efficient way of designing a well performing regulator also for unstable MIMO systems. The LQ control is actually the most widely used control structure for WIP vehicles ([2], [8], [9], [16], [17], [23]).

In the following chapter, the main theoretical aspects of Linear Quadratic regulation will be recalled; then an LQ regulator will be designed for YAPE starting from the linearized dynamical model presented in CHAPTER 3. After a brief discussion on the tuning of the regulator, the sensitivity of the closed loop system with respect to the uncertainties on the model parameters will be investigated using a simulator developed in a Simulink environment. Finally, a series of tests will be presented, in which all the main performance indexes discussed in CHAPTER 8 will be measured on 10 different LQ controllers.

10.2 LQR theory

Given a non-linear time invariant system described by:

$$\dot{x}(t) = f(x(t), u(t)), \quad x \in R^n, \quad u \in R^m \quad (10.1)$$

in which f is continuously differentiable and x is measurable, a control is defined to be optimal for the system if its control law $u^0(t)$, $t \in [t_0, T]$, minimize the performance index:

$$J(x(t_0), u(.), t_0) = \int_{t_0}^T l(x(\tau), u(\tau)) d\tau + m(x(T)) \quad (10.2)$$

in which l and m are continuously differentiable functions. Let's now define:

$$\frac{\partial J^0(x, t)}{\partial t} = - \min_u \left\{ l(x, u) + \frac{\partial J^0(x, t)}{\partial x} f(x, u) \right\} \quad (10.3)$$

This partial differential equation is known as Hamilton-Jacobi-Bellman (HJB hereafter). It is possible to prove that the optimal control problem can be solved in two steps, namely:

1. Compute the value u^0 minimizing :

$$\left\{ l(x, u) + \frac{\partial J^0(x, t)}{\partial x} f(x, u) \right\} \quad (10.4)$$

2. find the function $J^0(x, t)$ satisfying the HJB equation, in which u^0 is substituted to u .

The Linear Quadratic control is a particular case of the optimal control in which the controlled system is time-invariant linear one, like:

$$\dot{x}(t) = Ax(t) + Bu(t), \quad x \in R^n, \quad u \in R^m \quad (10.5)$$

with quadratic cost function given by:

$$J(x_0, u(\cdot), 0) = \int_0^T (x'(\tau) Q x(\tau) + u'(\tau) R u(\tau)) d\tau + x'(T) S x(T) \quad (10.6)$$

In which $Q \geq 0 \wedge R > 0 \wedge S \geq 0$.

The LQ problem is that of finding the control law which minimize J over the selected time interval.

The solution of this problem is based on the HJB (10.3).

From the theory of optimal control, we have that the LQ problem is solved by following these steps:

1. compute u by solving the minimization problem:

$$\min_u \left\{ x^T Q x + u^T R u + \frac{\partial J^0(x, t)}{\partial x} (Ax + Bu) \right\} \quad (10.7)$$

In this case, since the term to be minimized is quadratic in u , R and R is positive definite, the solution is trivially found by setting the partial derivative equal to zero, which gives:

$$u^0 = -\frac{1}{2} R^{-1} B^T \left(\frac{\partial J^0(x, t)}{\partial x} \right)^T \quad (10.8)$$

2. compute the function $J^0(x, t)$ fulfilling the HJB equation.

By setting $J^0(x, t) = x^T P(t)x$, the HJB equation reduces to:

$$\dot{P}(t) + Q - P(t)BR^{-1}B^TP^T(t) + P(t)A + A^TP^T(t) = 0 \quad (10.9)$$

which is known as the differential Riccati equation.

The resulting control law:

$$u^0(t) = -R^{-1}B^TP^T(t)x(t) = -K(t)x(t) \quad (10.10)$$

solves the LQ problem. Notice that this is a time varying control law, which is often useless since it would require to be computed at each time instant, possibly saturating the computational capability of the microcontroller. A time invariant control law can therefore be computed solving the optimal problem for $T \rightarrow \infty$, in which the performance index is expressed as:

$$J(x_0, u(\cdot), 0) = \int_0^\infty (x^T(\tau)Qx(\tau) + u^T(\tau)Ru(\tau))d\tau \quad (10.11)$$

in which $Q \geq 0 \wedge R > 0$, and the terminal penalty S is set to zero in order to grant asymptotical stability. It is then possible to prove that, if the pair (A, B) is reachable, and the pair (A, C_q) is observable (where C_q is such that $Q = C_q^T C_q$), then:

1. the optimal control law is given by:

$$u(t) = -R^{-1}B^T\bar{P}x(t) = -\bar{K}x(t) \quad (10.12)$$

where $\bar{P} > 0$ is the unique solution of the stationary Riccati equation:

$$0 = A^T\bar{P} + \bar{P}A + Q - \bar{P}BR^{-1}B^T\bar{P} \quad (10.13)$$

2. The closed loop system:

$$\dot{x}(t) = (A - B\bar{K})x(t) \quad (10.14)$$

is asymptotically stable.

It is also possible to prove that the LQ control grants stability also in case of:

1. phase variations up to 60°
2. gain variations in the interval $(\frac{1}{2}; +\infty)$

Note that there are no guarantees for contemporary gain and phase variations in any input.

Summing up, given a linear system of equation:

$$\dot{x}(t) = Ax(t) + Bu(t), \quad x \in R^n, \quad u \in R^m \quad (10.15)$$

the only thing that is needed to compute the LQ control for the system, is the definitions of two matrices, namely Q and R . Then, the LQ gain matrix \bar{K} is computed using the Riccati equation. The control is implemented using the following state-feedback scheme (FIGURE 10.1):

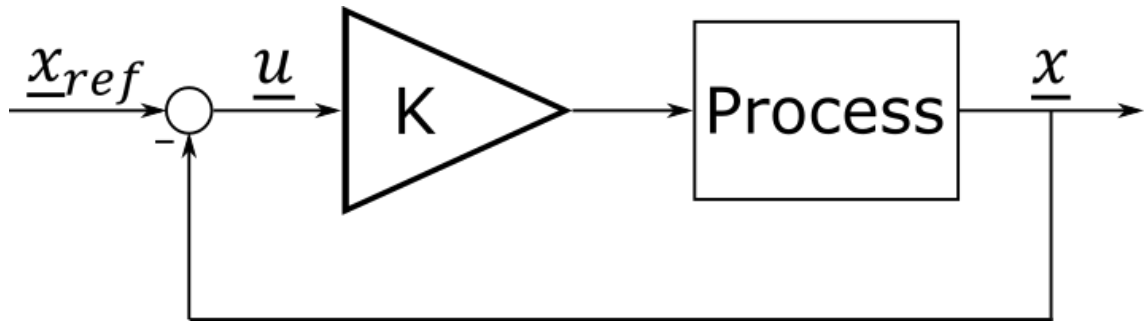


Figure 10-1 Control scheme with LQ regulator

and the resulting closed loop system is asymptotically stable with a 60° margin, and a gain margin of $(\frac{1}{2}; +\infty)$.

10.3 LQ implementation

As explained in the previous section, the LQ is a state-feedback proportional controller, which means that the control action computation requires the knowledge of the full state of the system. In our case, the system is the 4th order one computed in CHAPTER 3, namely:

$$\dot{x} = Ax + Bu \quad (10.16)$$

with state vector $x = [\dot{s} \quad \theta \quad \dot{\theta} \quad \dot{\psi}]^T$, control vector $u = [\tau_r \quad \tau_l]^T$, state matrix:

$$A = \begin{bmatrix} 0 & -a_1 & 0 & 0 \\ 0 & 0 & 1 & 0 \\ 0 & a_2 & 0 & 0 \\ 0 & 0 & 0 & 0 \end{bmatrix} \quad (10.17)$$

and input matrix:

$$B = \begin{bmatrix} b_1 & b_1 \\ 0 & 0 \\ -b_2 & -b_2 \\ b_3 & -b_3 \end{bmatrix} \quad (10.18)$$

However, in accordance to the considerations made on CHAPTER 4 regarding the rejection of the disturbances presented by unbalanced roads and uphills, an integral action on the speed and on the yaw rate is also required. This, in a LQ scheme, is achieved by introducing integral states in correspondence of those quantities on which an integral action is required. In particular we introduced:

$$\begin{cases} s = \int \dot{s} \\ \psi = \int \dot{\psi} \end{cases} \quad (10.19)$$

This result in a 6th order system with state vector:

$$x = [s \quad \dot{s} \quad \theta \quad \dot{\theta} \quad \psi \quad \dot{\psi}]^T \quad (10.20)$$

and state matrix:

$$A = \begin{bmatrix} 0 & 1 & 0 & 0 & 0 & 0 \\ 0 & 0 & -a_1 & 0 & 0 & 0 \\ 0 & 0 & 0 & 1 & 0 & 0 \\ 0 & 0 & a_2 & 0 & 0 & 0 \\ 0 & 0 & 0 & 0 & 0 & 1 \\ 0 & 0 & 0 & 0 & 0 & 0 \end{bmatrix} \quad (10.21)$$

The input vector and input matrix are unchanged. Then, according to the theoretical results reported in the previous section, the LQ control law is given by:

$$u(t) = -R^{-1}B^T \bar{P}x(t) = -\bar{K}x(t) \quad (10.22)$$

where $\bar{P} > 0$ is the unique solution of the stationary Riccati equation:

$$0 = A^T \bar{P} + \bar{P}A + Q - \bar{P}B R^{-1} B^T \bar{P} \quad (10.23)$$

in which Q is a 6×6 semi-positive definite matrix and R a 2×2 positive definite one. The choice of Q and R , which are the only two tunable quantities of an LQR, will be treated in the following section. Finally, since an acceptable estimate of all the needed states is available thanks to the state observers developed in CHAPTER 6, the LQ controller can be implemented on the vehicle in accordance to the following scheme (FIGURE 10.2):

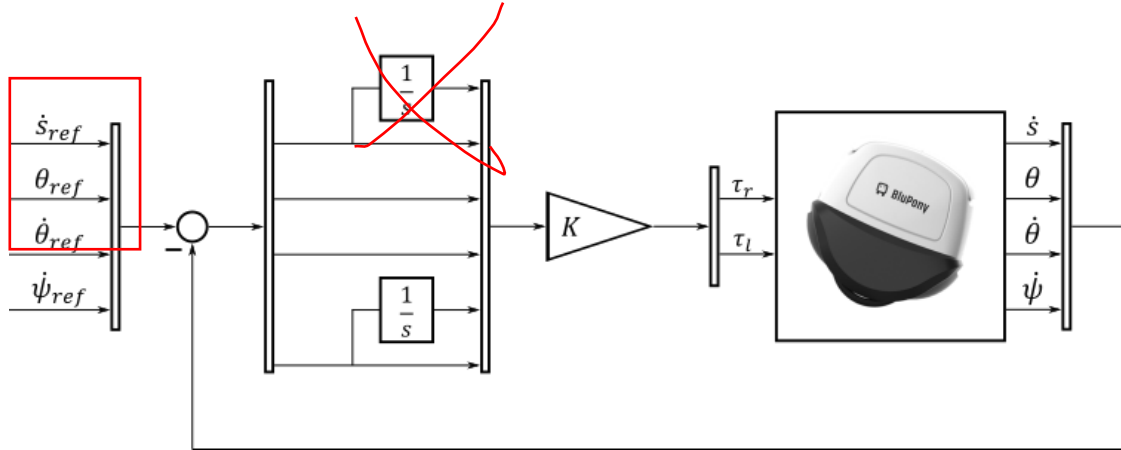


Figure 10-2 Schematic representation of LQR implementation

Notice that the errors on s and ψ are not computed as the difference between a reference signal and a measure of the corresponding state. This is due to the fact that, while the vehicle is running, the reference signals for s and ψ would increase continuously, possibly up to infinity. Due to memory limitations, this would inevitably lead to overflow phenomena. For this reason, the errors on the integral states s and ψ are computed as the integral of the errors on the speed and on the yaw rate: in this way the overflow does not occur and the integral action on speed and yaw rate is still granted. For what concerns the reference signals for pitch and pitch rate, they were set to zero in order to keep in an upright and stable position.

10.4 LQ tuning

As explained in the previous sections, the only task to be performed while designing an LQR is the choice of the weighting matrices Q and R . This actually constitutes the only drawback of the LQ method, due to the lack of a particular tuning technique granting the optimal choice for these weights. In order to understand how to proceed, the role of these two matrices in computing the performance index is further analysed in the following.

First of all, Q and R are chosen as diagonal matrices:

$$Q = \begin{bmatrix} q_1 & 0 & 0 & 0 & 0 & 0 \\ 0 & q_2 & 0 & 0 & 0 & 0 \\ 0 & 0 & q_3 & 0 & 0 & 0 \\ 0 & 0 & 0 & q_4 & 0 & 0 \\ 0 & 0 & 0 & 0 & q_5 & 0 \\ 0 & 0 & 0 & 0 & 0 & q_6 \end{bmatrix} \quad R = \begin{bmatrix} r_1 & 0 \\ 0 & r_2 \end{bmatrix} \quad (10.24)$$

In this way $Q \geq 0$ is granted by $q_i \geq 0 \forall i$, and $r_i > 0 \forall i$ implies $R > 0$. The performance index J is then rearranged in a sum of scalars, namely:

$$\begin{aligned} J &= \int_0^\infty (x^T(\tau) Q x(\tau) + u^T(\tau) R u(\tau)) d\tau = \\ &= \int_0^\infty (x_1^2(\tau) q_1 + x_2^2(\tau) q_2 + x_3^2(\tau) q_3 + x_4^2(\tau) q_4 + x_5^2(\tau) q_5 + x_6^2(\tau) q_6 + u_1^2(\tau) r_1 + u_2^2(\tau) r_2) d\tau \end{aligned} \quad (10.25)$$

From (10.25) we can see that the greater is the value of q_i , the more the state x_i will be weighted in the performance index. The same goes for r_i and the control variables u_i . Since the LQ control law is the one minimizing J , the highest is a certain weight (q_i or u_i), the more the controller will try to keep the corresponding variable close to its steady state value. This means that the weights q_i can be used to decide what system states are to be controlled most, whereas the weights r_i can be used to moderate the corresponding control variables.

It is clear that the choice of these parameters heavily affects the behaviour of the closed loop system. However, especially in the case of unstable systems with important coupling effects as YAPE is, this choice represents a non-trivial problem. One of the most intuitive methods to be used is the weights normalization. Supposing to know the maximum value that each state or control variable can assume, we can rewrite the weights as:

$$q_i = \frac{\tilde{q}_i}{x_{MAX_i}^2}, i = 1, \dots, n, \quad r_i = \frac{\tilde{r}_i}{u_{MAX_i}^2}, i = 1, \dots, m, \quad \tilde{q}_i \geq 0, \quad \tilde{r}_i > 0 \quad (10.26)$$

in which $|x_i| < x_{MAX_i}$, $i = 1, \dots, n$ and $|u_i| < u_{MAX_i}$, $i = 1, \dots, m$. The performance index is then:

$$J = \int_0^\infty \left(\frac{x_1^2(\tau)}{x_{MAX_1}^2} \tilde{q}_1 + \frac{x_2^2(\tau)}{x_{MAX_2}^2} \tilde{q}_2 + \frac{x_3^2(\tau)}{x_{MAX_3}^2} \tilde{q}_3 + \frac{x_4^2(\tau)}{x_{MAX_4}^2} \tilde{q}_4 + \frac{x_5^2(\tau)}{x_{MAX_5}^2} \tilde{q}_5 + \frac{x_6^2(\tau)}{x_{MAX_6}^2} \tilde{q}_6 \right. \\ \left. + \frac{u_1^2(\tau)}{u_{MAX_1}^2} \tilde{r}_1 + \frac{u_2^2(\tau)}{u_{MAX_2}^2} \tilde{r}_2 \right) d\tau \quad (10.27)$$

Notice that in this way, the values of \tilde{q}_i and \tilde{u}_i are weighting quantities in the interval (0,1]. In this sense, \tilde{q}_i and \tilde{u}_i represent the importance the designer gives to a certain state or control variable, regardless of the absolute value and the unit of measure of that quantity.

In our case, the extreme values used for the normalization, together with the motivation for each choice are:

- Position: $x_{MAX_1} = 1 [m] \rightarrow$ Maximum desired error
- Speed: $x_{MAX_2} = 5.55 \left[\frac{m}{s} \right] = 20 \left[\frac{km}{h} \right] \rightarrow$ Maximum speed YAPE is assumed to reach
- Pitch: $x_{MAX_3} = 0.61 [rad] = 30 [deg] \rightarrow$ Geometrical limit
- Pitch Rate: $x_{MAX_4} = 4.36 \left[\frac{rad}{s} \right] = 250 \left[\frac{deg}{s} \right] \rightarrow$ Free fall speed
- Yaw: $x_{MAX_5} = 0.34 [rad] = 20 [deg] \rightarrow$ Maximum desired error
- Yaw Rate: $x_{MAX_6} = 6.14 \left[\frac{rad}{s} \right] = 360 \left[\frac{deg}{s} \right] \rightarrow$ Maximum desired rotational speed
- Torques: $u_{MAX_1} = u_{MAX_2} = 10 [Nm] \rightarrow$ Saturation limit imposed during the test

With this choice of maximum values, a set of 14 tentative controllers was computed by varying the values of \tilde{q}_i and \tilde{r}_i . The first 10 controllers were used to understand the action of the weights on the longitudinal behaviour of the vehicle, whereas the last 4 were used to tune the controller on the yaw dynamics. In particular, the first controller was obtained by giving the same weight to all the states and inputs, namely:

$$\tilde{q}_i = \tilde{r}_j = 1 \quad \forall i = 1, \dots, 6 \wedge j = 1, 2 \quad (10.28)$$

whereas in the controllers from 2 to 5 one of the states is prevalent on the other: s , \dot{s} , θ and $\dot{\theta}$ are prioritized in controllers $K_{LQ}02$, $K_{LQ}03$, $K_{LQ}04$ and $K_{LQ}05$ respectively. Then, for the controllers $K_{LQ}06$ up to $K_{LQ}10$ the same values of \tilde{q}_i are repeated but with a higher weight on the control actions. On the same way, $K_{LQ}11$ and $K_{LQ}12$ are privileging ψ and $\dot{\psi}$, and $K_{LQ}13$ and $K_{LQ}14$ are their counterparts with high control action. Weights and resulting control matrices are reported in TABLE 10.1

Most weighted state		$[\tilde{q}_1 \tilde{q}_2 \tilde{q}_3 \tilde{q}_4 \tilde{q}_5 \tilde{q}_6 \tilde{r}_1 \tilde{r}_2]$	Control matrix K
Klq01	Uniform	[1 1 1 1 1 1 10 10]/10	$\begin{bmatrix} -2.2 & -5.4 & -41.2 & -12.7 & 6.4 & 2.7; \\ -2.2 & -5.4 & -41.2 & -12.7 & -6.4 & -2.7 \end{bmatrix}$
Klq02	Position	[100 1 1 1 1 1 10 10]/100	$\begin{bmatrix} -22.3 & -26.6 & -82.0 & -26.9 & 6.4 & 2.7; \\ -22.3 & -26.6 & -82.0 & -26.9 & -6.4 & -2.7 \end{bmatrix}$
Klq03	Speed	[1 100 1 1 1 1 10 10]/100	$\begin{bmatrix} -2.2 & -7.1 & -45.9 & -14.3 & 6.4 & 2.7; \\ -2.2 & -7.1 & -45.9 & -14.3 & -6.4 & -2.7 \end{bmatrix}$
Klq04	Pitch	[1 1 100 1 1 1 10 10]/100	$\begin{bmatrix} -2.2 & -6.2 & -50.9 & -14.3 & 6.4 & 2.7; \\ -2.2 & -6.2 & -50.9 & -14.3 & -6.4 & -2.7 \end{bmatrix}$
Klq05	Pitch Rate	[1 1 1 100 1 1 10 10]/100	$\begin{bmatrix} -2.2 & -5.5 & -42.7 & -14.1 & 6.4 & 2.7; \\ -2.2 & -5.5 & -42.7 & -14.1 & -6.4 & -2.7 \end{bmatrix}$
Klq06	Uniform	[1 1 1 1 1 1 10 1]	$\begin{bmatrix} -7.0 & -11.7 & -54.8 & -17.3 & 20.2 & 4.9; \\ -7.0 & -11.7 & -54.8 & -17.3 & -20.2 & -4.9 \end{bmatrix}$
Klq07	Position	[100 1 1 1 1 1 1 1]/100	$\begin{bmatrix} -70.7 & -68.4 & -155.6 & -52.3 & 20.2 & 4.9; \\ -70.7 & -68.4 & -155.6 & -52.3 & -20.2 & -4.9 \end{bmatrix}$
Klq08	Speed	[1 100 1 1 1 1 1 1]/100	$\begin{bmatrix} -7.0 & -19.2 & -76.3 & -24.8 & 20.2 & 4.9; \\ -7.0 & -19.2 & -76.3 & -24.8 & -20.2 & -4.9 \end{bmatrix}$
Klq09	Pitch	[1 1 100 1 1 1 1 1]/100	$\begin{bmatrix} -7.0 & -17.1 & -102.0 & -24.5 & 20.2 & 4.9; \\ -7.0 & -17.1 & -102.0 & -24.5 & -20.2 & -4.9 \end{bmatrix}$
Klq10	Pitch Rate	[1 1 1 100 1 1 1 1]/100	$\begin{bmatrix} -7.0 & -13.5 & -69.0 & -27.5 & 20.2 & 4.9; \\ -7.0 & -13.5 & -69.0 & -27.5 & -20.2 & -4.9 \end{bmatrix}$
Klq11	Yaw	[1 1 1 1 100 1 10 10]/100	$\begin{bmatrix} -2.2 & -5.4 & -41.2 & -12.7 & 64.0 & 8.5; \\ -2.2 & -5.4 & -41.2 & -12.7 & -64.0 & -8.5 \end{bmatrix}$
Klq12	Yaw Rate	[1 1 1 1 1 100 10 10]/100	$\begin{bmatrix} -2.2 & -5.4 & -41.2 & -12.7 & 6.4 & 4.4; \\ -2.2 & -5.4 & -41.2 & -12.7 & -6.4 & -4.4 \end{bmatrix}$
Klq13	Yaw	[1 1 1 1 100 1 1 1]/100	$\begin{bmatrix} -7.0 & -11.7 & -54.8 & -17.3 & 202.5 & 15.1; \\ -7.0 & -11.7 & -54.8 & -17.3 & -202.5 & -15.1 \end{bmatrix}$
Klq14	Yaw Rate	[1 1 1 1 1 100 1 1]/100	$\begin{bmatrix} -7.0 & -11.7 & -54.8 & -17.3 & 20.2 & 12.2; \\ -7.0 & -11.7 & -54.8 & -17.3 & -20.2 & -12.2 \end{bmatrix}$

Table 10-1 List of controller tested

The aim of this study over a relatively large number of controllers is that of understanding how each weight influences the behaviour of the whole system, in order to have guidelines in the design of the definitive LQ controller

In the following sections, the 14 controllers are tested with different conditions and with different tasks. All the required performances described in CHAPTER 8 are considered, namely: pitch limitation capabilities, station keeping capabilities, turn on the spot capabilities, unbalanced load handling and the uphill roads handling.

10.5 Station Keeping

The first test we present is a stabilization test: the controller is turned on, and the vehicle is stabilized; speed and yaw rate reference signals are set to zero for 30 seconds, and the behaviour of the system is analysed.

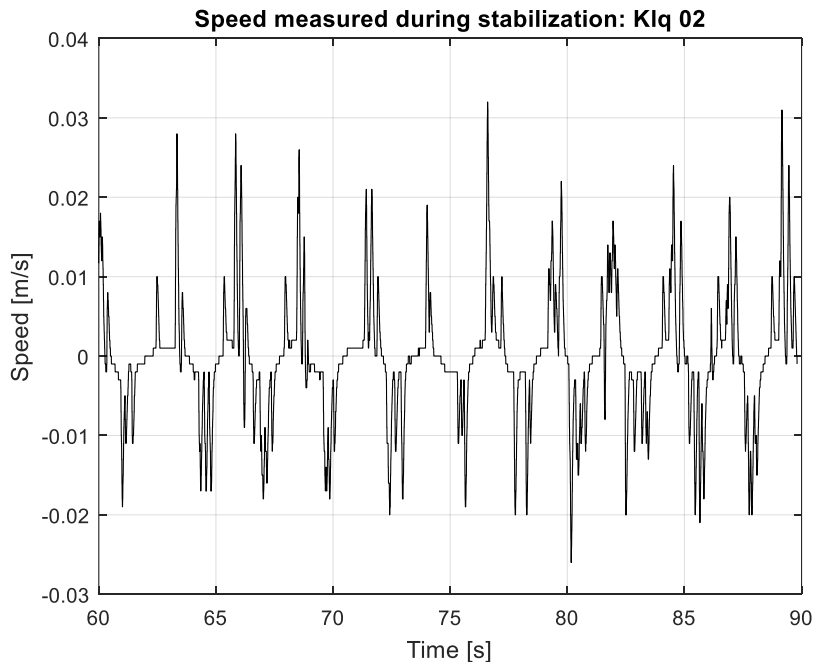


Figure 10-3 Speed measured during stabilization: Klq02

The ideal behaviour in this case would be for the vehicle to be perfectly still with the load on balance in upright position. However, as anticipated in CHAPTER 8, a limit cycle on the speed is usually detected. We can observe the occurrence of such behaviour in the vehicle speed (FIGURE 10.3), and pitch (FIGURE 10.4).

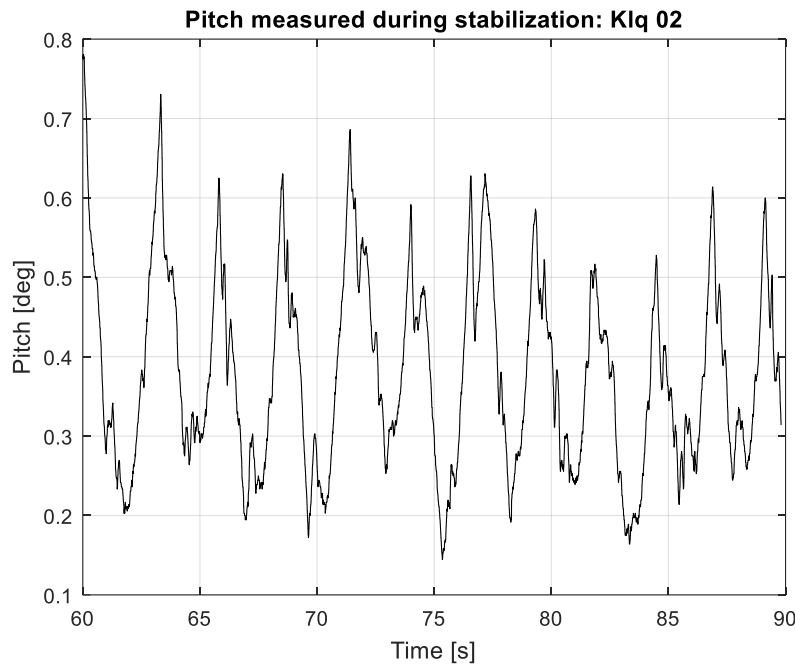


Figure 10-4 Pitch measured during stabilization: Klq02

FIGURE 10.3 and FIGURE 10.4 report the results of a stabilization test run on controller Klq02. The results obtained on all the other controllers are not reported for sake of brevity; they are qualitatively comparable to what is depicted in FIGURE 10.3 and FIGURE 4. .

Frequency and amplitude of the limit-cycle oscillations, were taken as a measure of effectiveness of each controller; in order to retrieve them a Fourier decomposition was computed on the measured speed, pitch and requested torques. An estimate of the displacement was also computed based on the encoders readings; this is sufficiently reliable due to the shortness of the test, which does not allow the occurrence of drifting phenomena which are typical of such estimate. The results are reported on the following TABLE 10.2:

Controller	Oscillation frequency [Hz]	Oscillation period [s]	Speed amplitude [m/s]	Position amplitude [m]	Max pitch [deg]	Max torque [Nm]
Klq01	0.06	15.00	0.10	0.16	1.55	1.40
Klq02	0.36	2.72	0.03	0.01	0.39	1.46
Klq03	0.13	7.50	0.04	0.02	1.43	1.43
Klq04	0.13	7.50	0.04	0.02	1.28	1.31
Klq05	0.10	10.00	0.05	0.08	0.83	0.98
Klq06	0.20	5.00	0.02	0.01	0.76	1.13
Klq07	0.63	1.57	0.03	0.01	0.24	8.68
Klq08	0.30	3.33	0.02	0.01	0.57	1.22
Klq09	1.66	6.00	0.01	0.04	0.29	1.38
Klq10	0.26	3.75	0.03	0.01	0.43	1.37

Table 10-2 Results of stabilization tests - LQR

By inspection of the table we can state that:

- The controller with a strong control action (Klq06-10) present higher oscillation frequencies than the corresponding weak ones (Klq01-05); the amplitude of the speed oscillations and the peak value for the pitch are, in general, smaller
- The controllers with a higher weight on the position (Klq02 and Klq07) present the smallest amplitude of oscillation: the registered values of $\pm 1 \text{ cm}$ are in the order of magnitude of the discretization used in the CAN bus acquisition
- The maximum wheel rotational speed during the limit cycle is in the order of few cm/s for all the tested controllers
- In the practice, the Klq07 controller, corresponding to maximum weight on the position, presents an extremely nervous behaviour. This can be observed in the high registered value for the torque. Potentially dangerous mechanical vibrations arise while using this controller; on the other hand, the improvements on the vehicle performances are not significative

It is therefore possible to conclude that controllers with an elevated weight on the torques present better general performances; a strong weight on the position reduces the amplitude of limit-cycle oscillations, at the cost of more nervous behaviour (up to the arising of undesirable vibrations); increasing the weight on speed, pitch and pitch rate has less relevant influence on the station keeping performances.

10.6 Speed tracking

The second test aims to study the speed tracking capabilities of the controller while the vehicle is running on a flat surface. The required speed profile is shown in FIGURE 10.5:

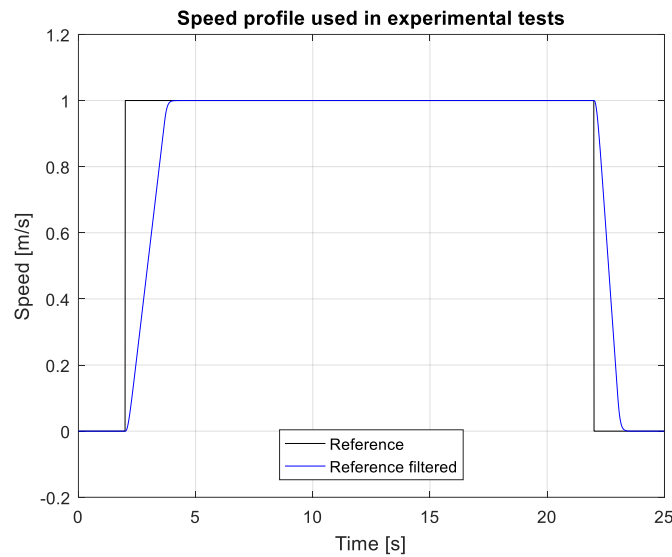


Figure 10-5 Speed profile used in experimental tests

The original reference is a step of 1 m/s amplitude with a duration of 20 seconds. Due to the presence of the reference filtering block explained in CHAPTER 9, the resulting profile is a smooth trapezoidal one, with a maximum acceleration of $0.6 \frac{m}{s^2}$ (corresponding to a steady state angle of $\theta_{ss_acc} = 7.8^\circ$), and a maximum deceleration of $1 \frac{m}{s^2}$ ($\theta_{ss_brak} = -12.9^\circ$).

The measured speeds and pitch for this test are shown in FIGURES from 10.6 to 10.10

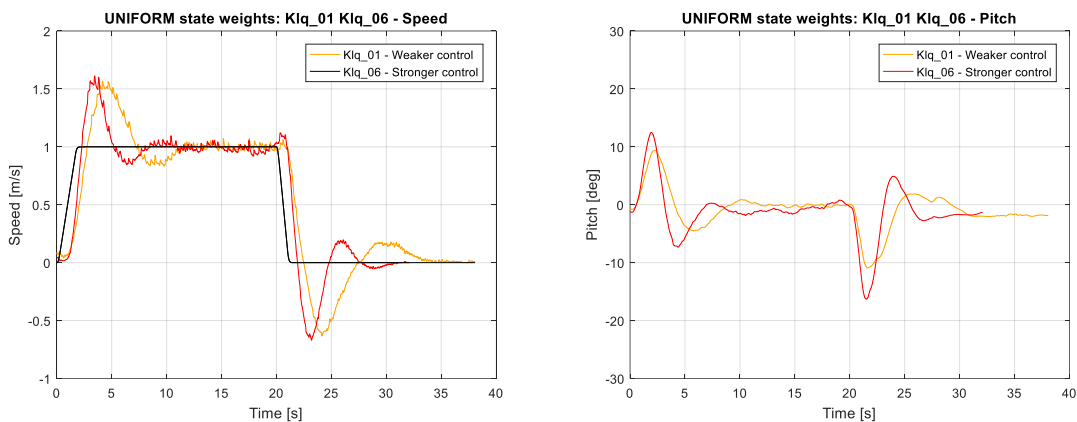


Figure 10-6 Speed and pitch in speed tracking test – Klq 01 and Klq 06

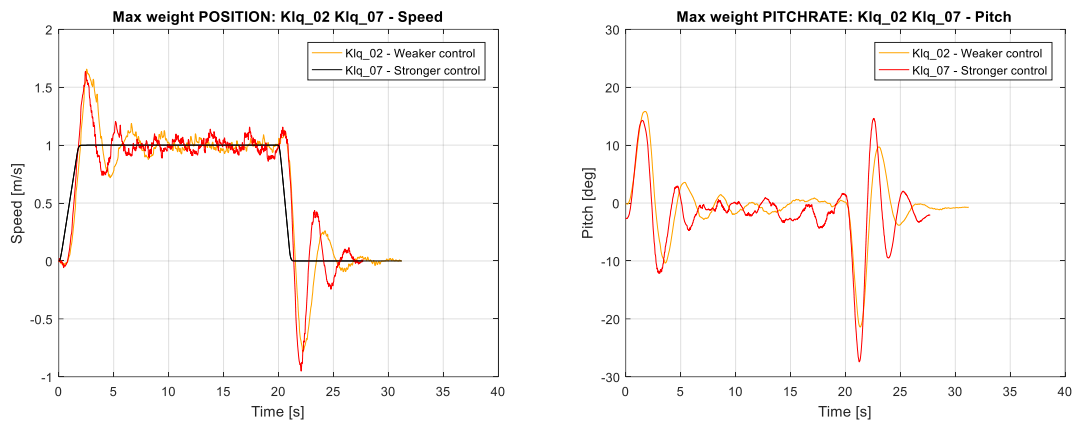


Figure 10-7 Speed and pitch in speed tracking test – Klq 02 and Klq 07

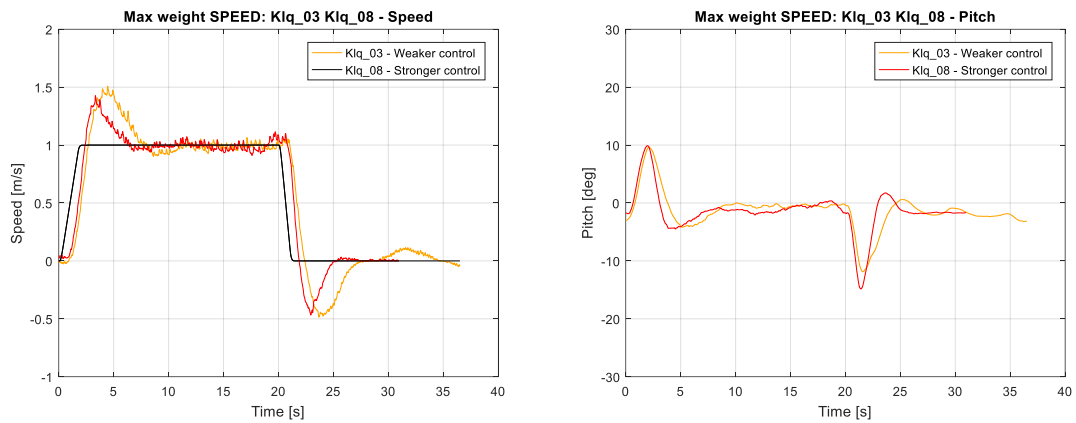


Figure 10-8 Speed and pitch in speed tracking test – Klq 03 and Klq 08

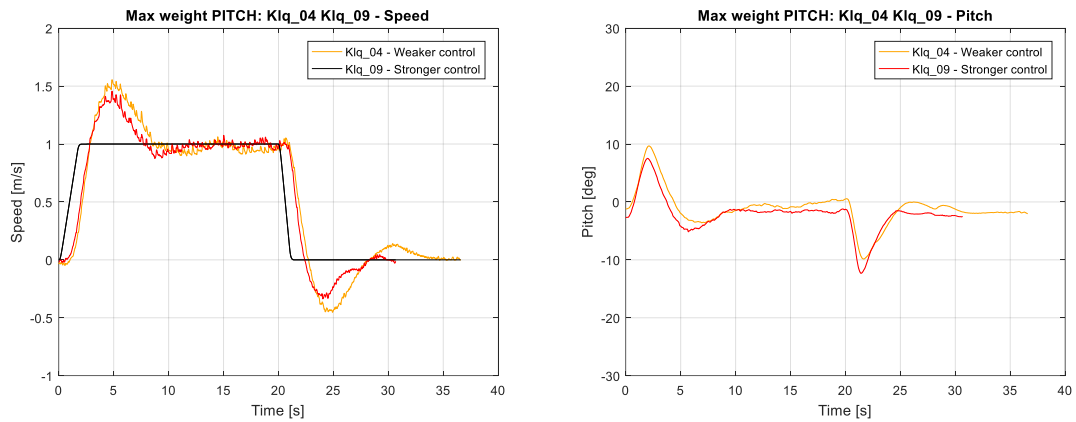


Figure 10-9 Speed and pitch in speed tracking test – Klq 04 and Klq 09

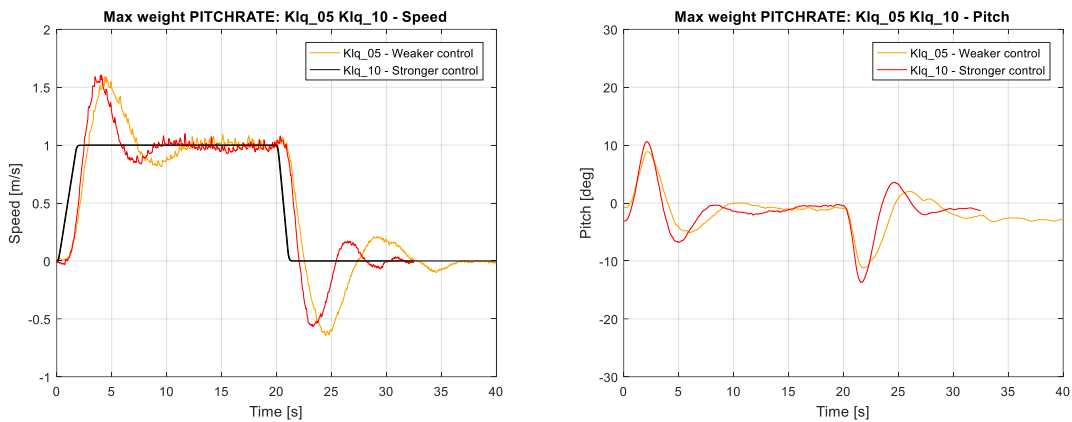


Figure 10-10 Speed and pitch in speed tracking test – Klq 05 and Klq 10

As we can see, the LQ controller is able to track the speed reference profile. All the controllers cause an overshoot of the steady state value, possibly followed by one or more damped oscillations. Non-minimum phase behaviour predicted by the theory in CHAPTER 3 is present in the first few seconds of motion. Most importantly, we can observe that the pitch systematically overshoots the steady state value imposed by the rate limiter up to +10° during acceleration and up to -12° while braking.

The main performance measures for this test are summarized in Table 10.2

Controller	Speed overshoot [%]	Max pitch [deg]	Response delay [s]	Rising time (10%-90%) [s]	Number of oscillations
Klq01	56	9.36	0.85	1.47	1
Klq02	65	15.8	0.77	0.81	3
Klq03	50	9.59	1.00	1.18	1
Klq04	55	9.67	1.15	1.25	1
Klq05	59	8.88	0.99	1.35	1
Klq06	61	12.47	0.94	0.91	1
Klq07	63	14.62	0.67	0.71	5
Klq08	42	9.88	0.74	1.15	0
Klq09	45	7.52	0.92	1.42	0
Klq10	60	10.61	1.08	1.01	0

Table 10-3 Results of speed profile tracking tests - LQR

According to the obtained results we can state that:

- all the controllers present an overshoot on the speed profile in the range of 50-60%; trivially, the best controllers in this regard are those with a higher speed weight.
- The speed overshoot is generally larger during braking due to the bigger absolute value of the deceleration with respect to the acceleration. This negative overshoot is also heavily influenced by the system's state at the beginning of the braking phase.
- The pitch behaviour is heavily affected by the controller choice: a more aggressive control on speed and position brings to YAPE to reach higher pitch values. An increase of almost 50% in the pitch peak is detected for these controllers. On the other hand, the controllers with the highest weight on the pitch and pitch rate keep the pitch below 10° in acceleration and 15° in deceleration.
- All the previous phenomena are amplified for the strong controllers (Klq06-10) with respect to the corresponding weak ones (Klq01-05).
- A strong position control can lead to the arise of speed oscillations around the steady state value.
- As previously noted, the Klq07 controller causes the arise of mechanical vibrations due to the very strong torque request

In conclusion, we can state that a high weight on speed and position causes, as expected, a more reactive behaviour of the system in following the speed profiles. A shorter rising time is usually obtained in these cases, at the cost of greater speed overshoots and higher pitch peak values. In the worst case an oscillatory response is obtained. A higher weight on pitch and pitch rate is required to moderate the pitch response, at the cost of increasing the system's response time. In the end, we can state that a compromise needs to be found between the response time, the speed overshoot magnitude and the maximum allowed pitch.

10.7 Speed Tracking: slopes

This experiment aims to test the capabilities of the controller in rejecting the disturbances caused by the presence of non-zero slope road profiles (see CHAPTER 4). The requested speed profile is exactly the same of the previous test, but this time the test was executed on a road with 20% slope (i.e. a slope angle of approximately 11.3°). FIGURE 10.11 shows the slope of the road used during experimental tests.



Figure 10-11 Slope during experimental tests

The Klq07 controller was not used in this case due to its nervous behaviour combined to the very limited available angle between the road and the vehicle's hulls (see CHAPTER 8).

Results are reported in FIGURES from 10.12 to 10.16 and in TABLE 10.4

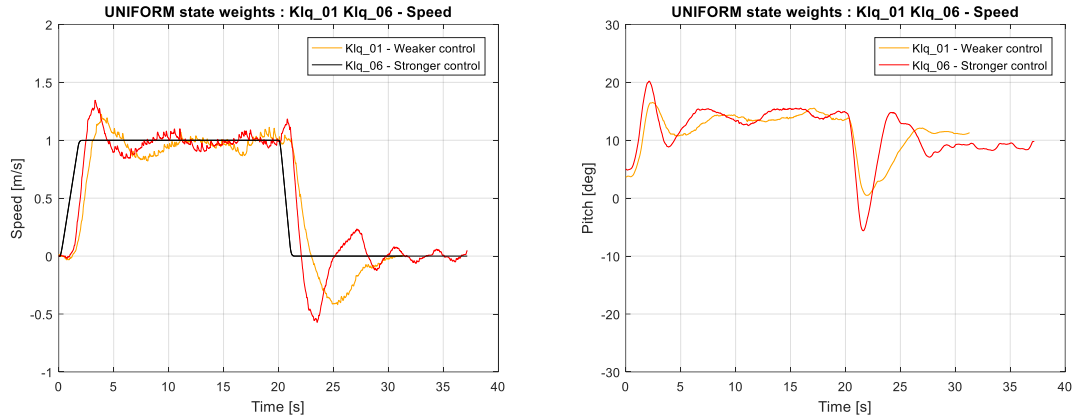


Figure 10-12 Speed and pitch in speed tracking test on uphill road– Klq 01 and Klq 06

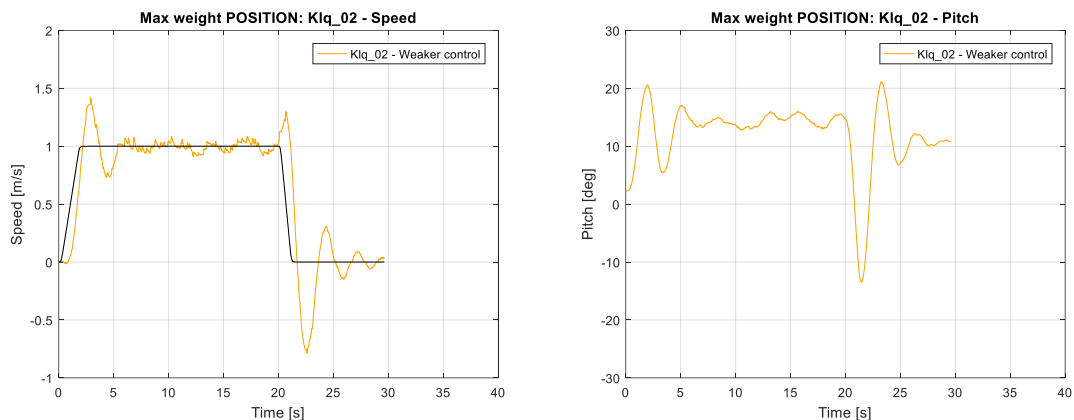


Figure 10-13 Speed and pitch in speed tracking test on uphill road– Klq 02

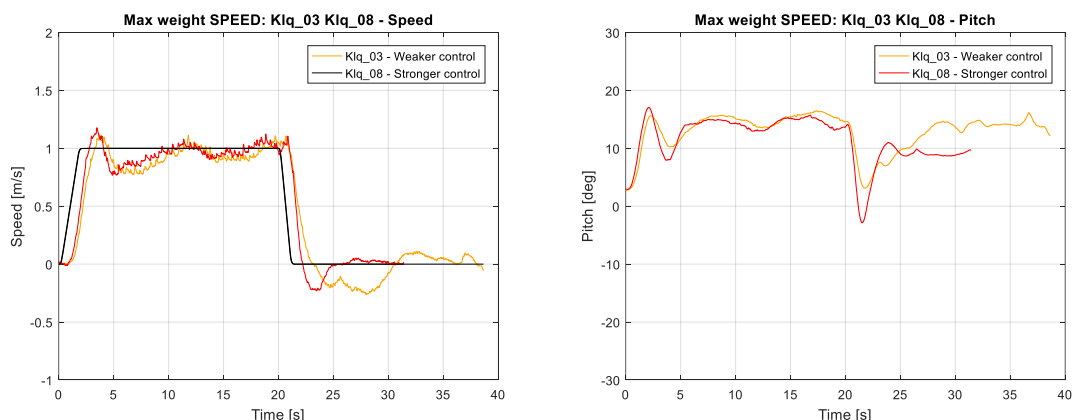


Figure 10-14 Speed and pitch in speed tracking test on uphill road– Klq 03 and Klq 08

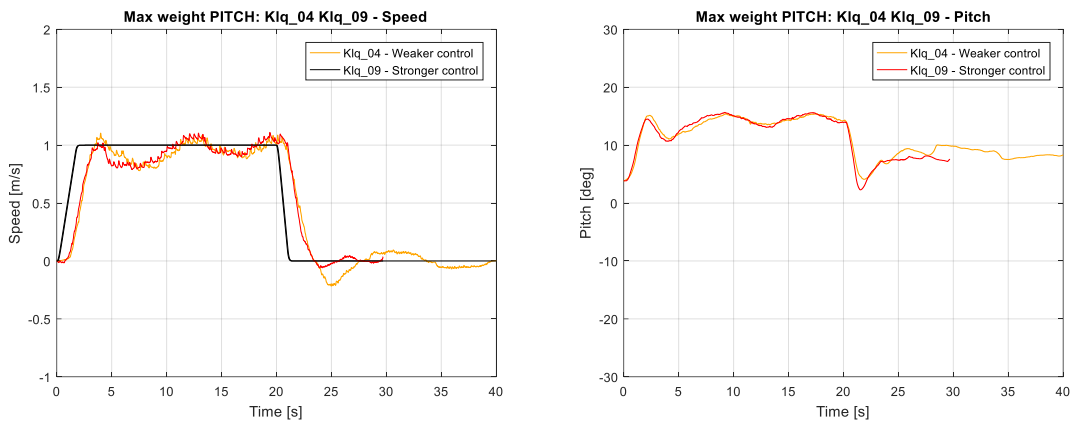


Figure 10-15 Speed and pitch in speed tracking test on uphill road – Klq 04 and Klq 09

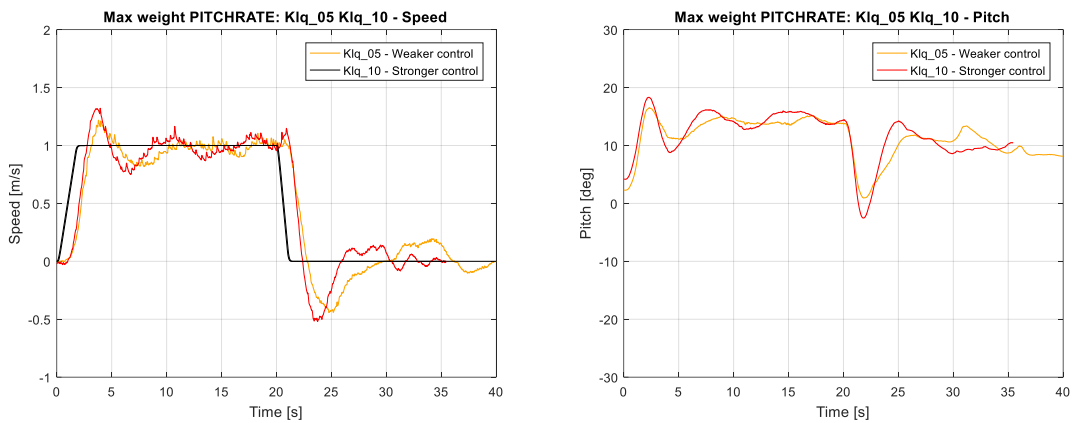


Figure 10-16 Speed and pitch in speed tracking test on uphill road – Klq 05 and Klq 10

Controller	Speed overshoot [%]	Max pitch [deg]	Response delay [s]	Rising time (10%-90%) [s]
Klq01	22	16.53	1.33	1.26
Klq02	42	21.13	0.78	0.90
Klq03	11	16.48	1.12	1.39
Klq04	10	15.45	1.12	1.59
Klq05	21	16.55	1.18	1.41
Klq06	34	20.21	1.10	0.88
Klq07	/	/	/	/
Klq08	17	17.07	0.93	1.17
Klq09	11	15.65	0.92	1.86
Klq10	32	18.31	1.01	1.17

Table 10-4 Results of speed profile tracking on uphill road tests - LQR

As we can deduct from FIGURES 10.12 -10.16, a general rejection of the disturb is obtained with all the tested controllers: in fact, the steady state speed value is reached with all tested controllers despite the fact that the vehicle is running on a quite challenging sloped road. All the other considerations made for the previous test hold also in this case. Clearly, due to the uphill, the reached values are different, namely: smaller speed overshoots, directly imputable to the gravity force resisting to the motion, and higher pitch peaks, caused by the non-zero steady state pitch value corresponding to this specific road slope (see CHAPTER 8). In conclusion, we can state that the LQ controller with integral action on the speed shows a satisfactory rejection of the disturb presented by a non-zero slope road profile.

10.8 Unbalanced load

The last test run to assess the longitudinal and pitch performance of the controller was that of simulate the load and unload of a package on the vehicle.

First of all, the theoretical behaviour of the LQR in this case is presented, in order to better understand the experimental result presented right after.

As already explained in CHAPTERS 3 and 4, we can model the vehicle with an unbalanced load as one having an offset on the pitch angle. In this case, the position of geometrical pitch equal to zero is an unstable one; the stable position is the one in which the pitch corresponds to the opposite of the unbalancing angle of the cog.

An LQ regulator with integral action on the speed is capable of autonomously reach the equilibrium position. In order to understand this it is sufficient to analyse the LQ control law, which is $\bar{u} = -K\delta\bar{x}$ or, explicitly:

$$\begin{bmatrix} u_1 \\ u_2 \end{bmatrix} = \begin{bmatrix} k_{11} & k_{12} & k_{13} & k_{14} & k_{15} & k_{16} \\ k_{21} & k_{22} & k_{23} & k_{24} & k_{25} & k_{26} \end{bmatrix} \begin{bmatrix} \delta s \\ \delta \dot{s} \\ \delta \theta \\ \delta \dot{\theta} \\ \delta \psi \\ \delta \dot{\psi} \end{bmatrix} \quad (10.29)$$

In the equilibrium position both $\delta\dot{x}_0$ e $\delta\dot{\theta}$ must be equal to zero. For simplicity, let's assume that $\delta\psi$ e $\delta\dot{\psi}$ are equal to zero too. Since in stabilization the requested speed is null, $\delta\dot{x}_0 = 0$ must hold in order to have the vehicle to be steady on place; moreover, in absence of other disturbs, also the requested torques have to be null. Al this considering we have:

$$\begin{bmatrix} 0 \\ 0 \end{bmatrix} = \begin{bmatrix} k_{11} & k_{12} & k_{13} & k_{14} & k_{15} & k_{16} \\ k_{21} & k_{22} & k_{23} & k_{24} & k_{25} & k_{26} \end{bmatrix} \begin{bmatrix} \delta s \\ 0 \\ \delta \theta \\ 0 \\ 0 \\ 0 \end{bmatrix} \quad (10.30)$$

Which correspond to the two equations

$$\begin{aligned} 0 &= k_{11}\delta s + k_{13}\delta\theta \\ 0 &= k_{21}\delta s + k_{23}\delta\theta \end{aligned} \quad (10.31)$$

which, since $k_{11} = k_{21}$ and $k_{13} = k_{23}$, are actually the same equation. Then, rearranging the first of the two equations:

$$\delta s = -\frac{k_{13}}{k_{11}} \delta\theta = -\frac{k_{13}}{k_{11}} \gamma \quad (10.32)$$

from which we understand that the LQ controller compensate for error on the pitch given by the unbalanced load with an error on the position. In practice, this means that if a package is loaded on the vehicle causing a variation in the longitudinal position of the COG the vehicle assumes automatically the correct pitch position, at the cost of a longitudinal displacement. The amount of longitudinal displacement needed for a c.o.g angular displacement γ is given by (10.32) imposing that:

$$\delta\theta = -\gamma \quad (10.33)$$

which yields:

$$\delta s = -\frac{k_{13}}{k_{11}} \gamma \quad (10.34)$$

Clearly, the requested displacement depends directly from the gains k_{11} and k_{13} : namely, δx_0 is inversely proportional to the gain on the position error, and directly proportional to the one on the pitch. FIGURE 10.17 graphically shows the (10.34)

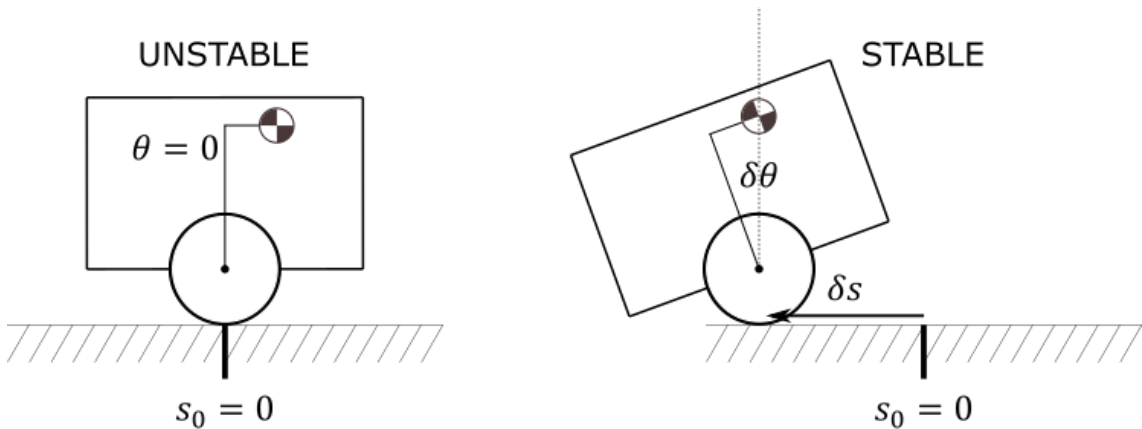


Figure 10-17 Stable position in case of unbalanced load

The experiment used to test this behaviour was carried on using weights of 2 Kg. First of all, the vehicle is put in station keeping mode; then the load is added on the top of the frontal side of the hulls, causing the longitudinal displacement of the COG; once the vehicle reaches the new equilibrium position the load is removed, and the vehicles moves back to the nominal equilibrium position. The load and unload operations were executed trying to simulate at best the occurrence of a step-like disturbance.

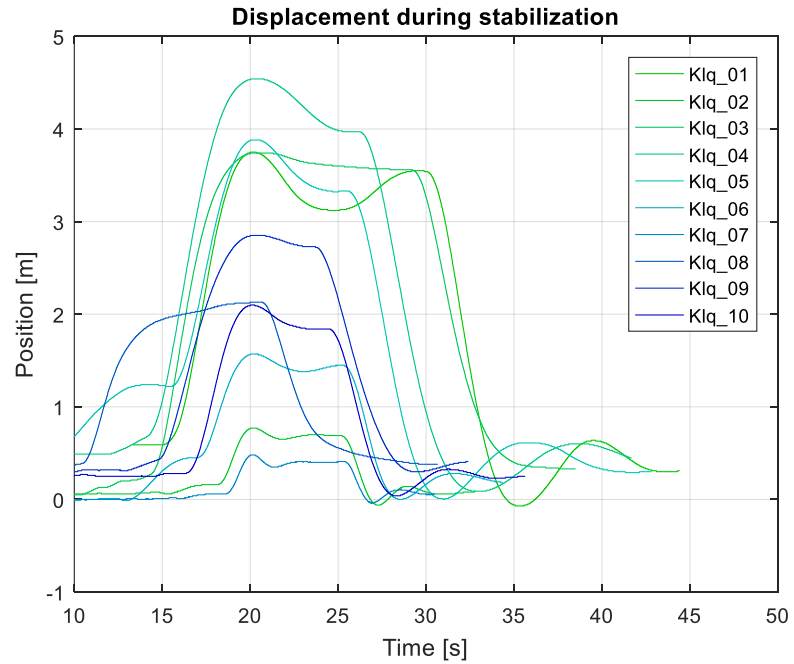


Figure 10-18 Displacements during stabilization tests - LQR

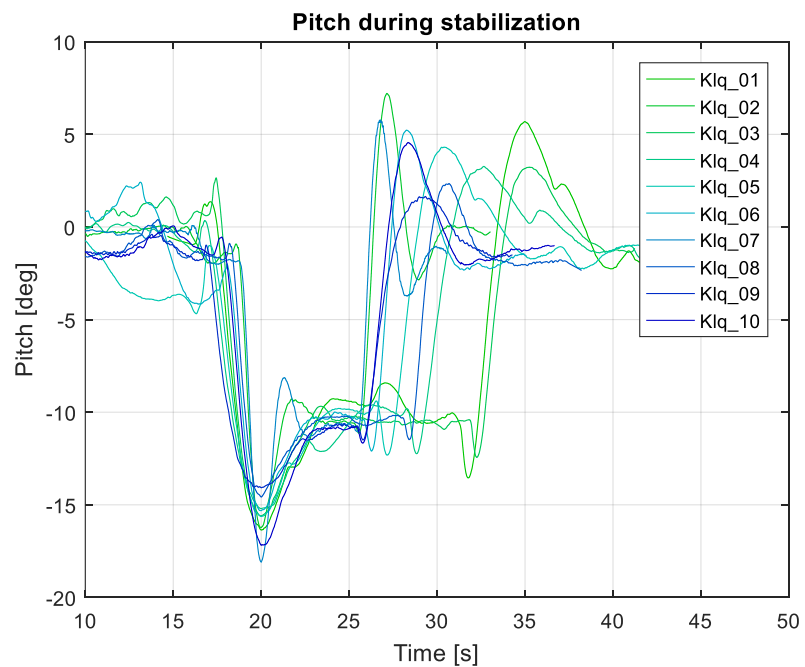


Figure 10-19 Pitch during stabilization tests

FIGURE 10.18 shows the vehicle longitudinal displacement during the test; the curves were aligned in order to have the maximum displacement occurring at the same time instant. In FIGURE 10.19 the corresponding pitch behaviour is depicted.

The performance indexes of this test are reported in Table 10.4

Controller	Max pitch [deg]	Theoretical displacement [m]	Measured displacement [m]	Steady – state pitch [deg]
Klq01	-16.36	3.29	3.16	-10.24
Klq02	-16.22	0.65	0.74	-10.33
Klq03	-15.59	3.67	3.82	-10.43
Klq04	-15.20	4.06	4.60	-10.02
Klq05	-15.62	3.41	3.90	-10.19
Klq06	-15.31	1.38	1.61	-10.16
Klq07	-18.09	0.39	0.49	-10.59
Klq08	-14.58	1.92	2.01	-10.19
Klq09	-14.07	2.56	2.89	-10.56
Klq10	-17.18	1.73	2.05	-10.77

Table 10-5 Results of stabilization with unbalanced load tests - LQR

By inspection of the results we can notice that:

- The steady state pitch equilibrium point is successfully reached by all the controllers. The pitch equilibrium position is clearly invariant with respect to the used controller (the variations are imputable to the non-exact repeatability of the experiment). On the other hand, the displacement needed to reach such equilibrium is heavily affected by the choice of the controller.
- The actual displacement is almost identical to what predicted by (10.34).
- The main difference between the various controllers is given by the peak value reached by the pitch during the transition phase. All the controllers produced an overshoot on the steady state value; this phenomenon is trivially minimized by the controller having a higher weight on the pitch and pitch rate

10.9 Turn on the spot

The last experiment aims to test the performances of the LQ controller in tracking a yaw rate profile. The last 4 controllers are therefore used. A filtered step of yaw rate profile (see CHAPTER 9) is requested to the vehicle, whilst keeping the longitudinal speed reference to zero. This correspond to the turn-on-the-spot manoeuvre described in CHAPTER 8.

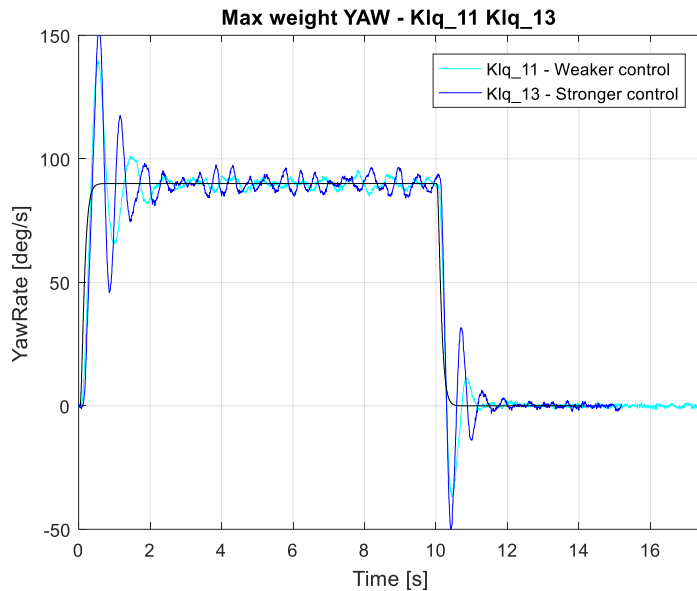


Figure 10-20 Yawrate in yawrate profile tracking test - KIq 11 and KIq 13

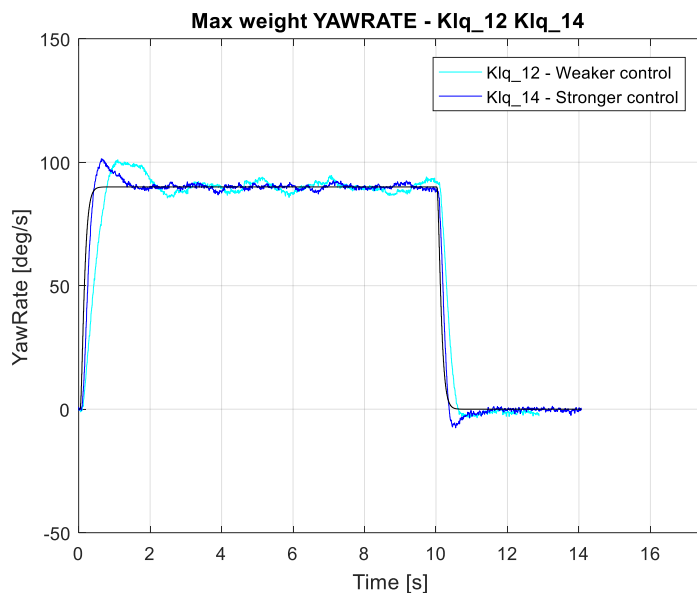


Figure 10-21 Yawrate in yawrate profile tracking test - KIq 12 and KIq 14

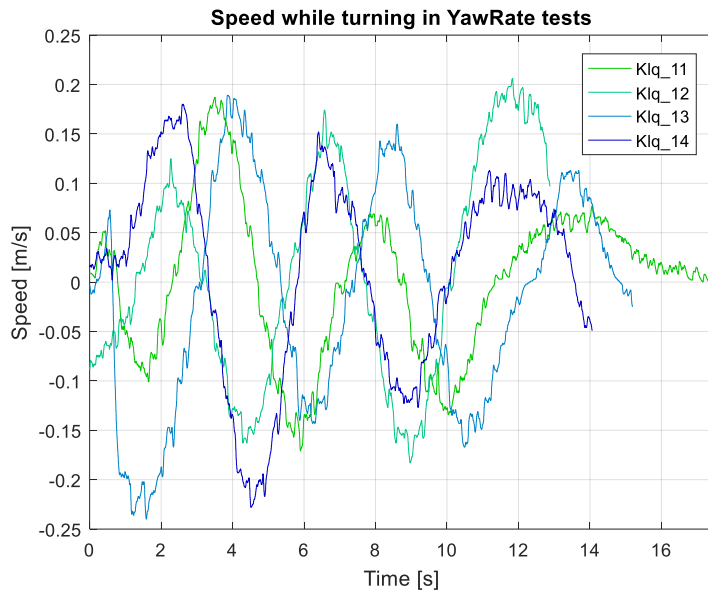


Figure 10-22 Speed in yawrate profile tracking test - Klq 11,12,13,14

The measured yaw rate is reported in FIGURE 10.20 and 10.21; the longitudinal speed for both the tests are reported in FIGURE 10.22.

From the analysis of the results we can state that:

- The controller is able to track yaw rate profiles in spite of all the disturbances to which the system is subjected, such as different inflation pressure of the wheels, slip phenomena or different traction properties of the road surface.
- Increasing the control weight on ψ makes the controller more reactive, but causes also an oscillatory behaviour.
- The amplitude of the oscillations is directly related to the weights of the control action: The less are the weights r_i , the stronger is the control action, the bigger is the amplitude of the oscillations.
- Better performances are related to the controllers with a higher weight on the yaw rate: a very good reference tracking is achieved, with a limited overshoot (approximately 10%) and no relevant oscillations
- The longitudinal speed behaviour is not influenced by the variations of the control weights on the yaw dynamics: through all tests that is approximated by a sinusoidal with 0.1 amplitude and a period of 5 seconds. The presence of such a behaviour is actually very undesired since it invalidates the vehicle's capability of turning on the spot, but is trivially removed by improving the control action on the speed.

10.10 Conclusion on the choice of LQR

Summarizing the considerations made on all the tests, we can state that a trade-off clearly exists between weighting the two speeds (\dot{s} and $\dot{\psi}$) and the corresponding integral states (s and ψ). A strong weight on the integral states is needed in order to provide good station keeping performances together with a good response reactivity. Moreover, a high weight on the position influence the displacement needed to manage the occurrence of eventual unbalanced load. A too high integral action though, can lead to mechanical vibrations and oscillatory behaviours. Sufficiently high weights on the pitch and pitch rate are also needed: they reduce the system reactivity to longitudinal speed requests, but they also provide the needed disturb rejection and pitch moderation that prevents the vehicle from hitting the ground.

A final controller was then chosen with weights: $q = [50 \ 50 \ 100 \ 50 \ 10 \ 100]/100$ and $r = [1 \ 1]$, resulting into:

$$K_{LQ} = \begin{bmatrix} -15.8 & -22.2 & -79.6 & -25.2 & 20.2 & 5.9 \\ -15.8 & -22.2 & -79.6 & -25.2 & -20.2 & -5.9 \end{bmatrix} \quad (10.35)$$

The Station Keeping performances of K_{LQ} are reported in FIGURE 10.23 (a), whereas FIGURE 10.23 (b) shows its Speed Tracking capabilities on a plane road. FIGURE 10.24(a) shows the yawrate profile tracking and FIGURE 10.24(b) the speed value during this test.

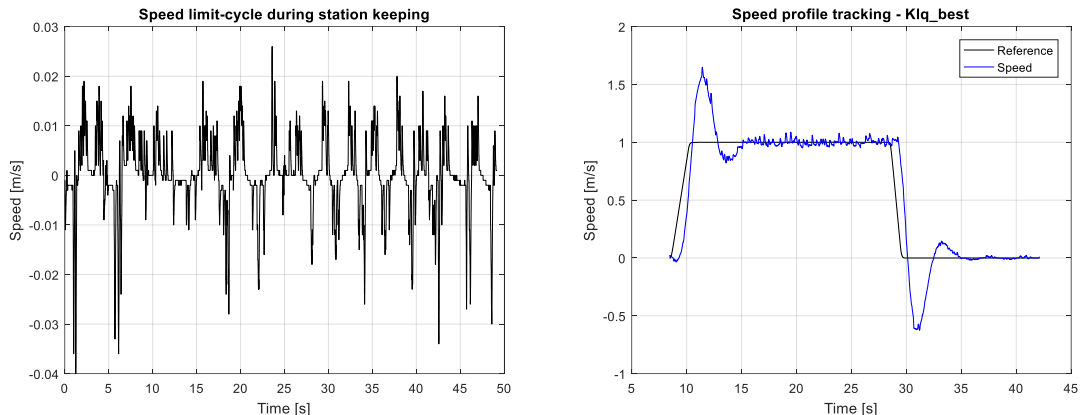


Figure 10-23 K_{LQ}_best: (a) Speed during stabilization (b) Speed profile tracking

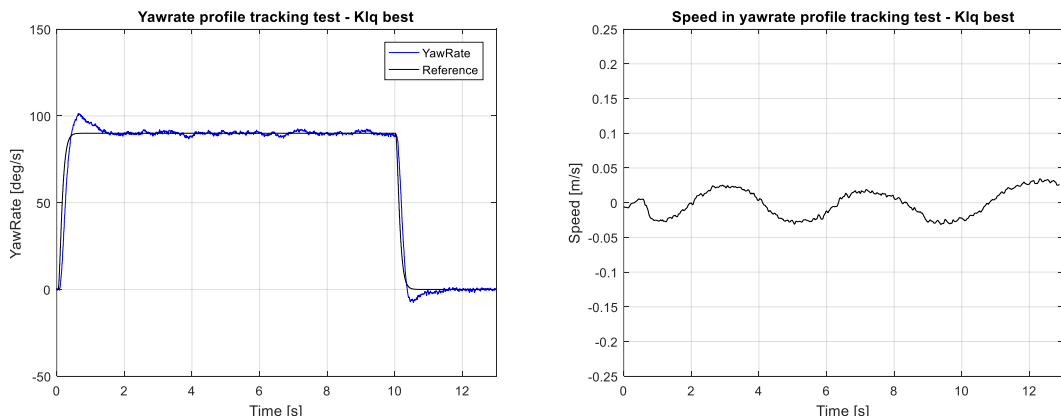


Figure 10-24 K_{LQ}_best: (a) Yawrate profile tracking (b) Speed

10.11 Robustness analysis.

As already mentioned, YAPE is subjected to a number of parametric uncertainties. In particular, the parameters which are mostly influenced by the load and unload operations are: the chassis mass (m_c), the value of the moments of inertia (J_{py}) and the c.o.g height (L). Moreover, both L and J_{py} are obtained by means of a model identification procedure, which is naturally affected by uncertainties (see CHAPTER 7)

In order to assess the controller's robustness to these parametric uncertainties a series of simulated tests were run. In particular, the definitive controller Klq_{best} of equation (10.34) was used. Then, the usual speed profile was requested to the controller acting on the nominal system. The result of this test will be used as a term of comparison. Finally, the test was repeated on the simulator, in which the nominal parameters were changed. In particular, a first set of tests was run by changing one parameter at a time, and then a final test was made, in which all the parameters were subjected to a variation compatible with the load of a standard package. A saturation of 10Nm on the torques was imposed during all the test, in order to be coherent with the test so far described for the real vehicle.

10.11.1 Mass variation test:

The nominal value for the chassis mass m_c is 24 Kg, which is increased up to 56 Kg during the test. The speed, pitch and torque profiles generated with this test are reported in FIGURES 10.25, 10.26 AND 10.27.

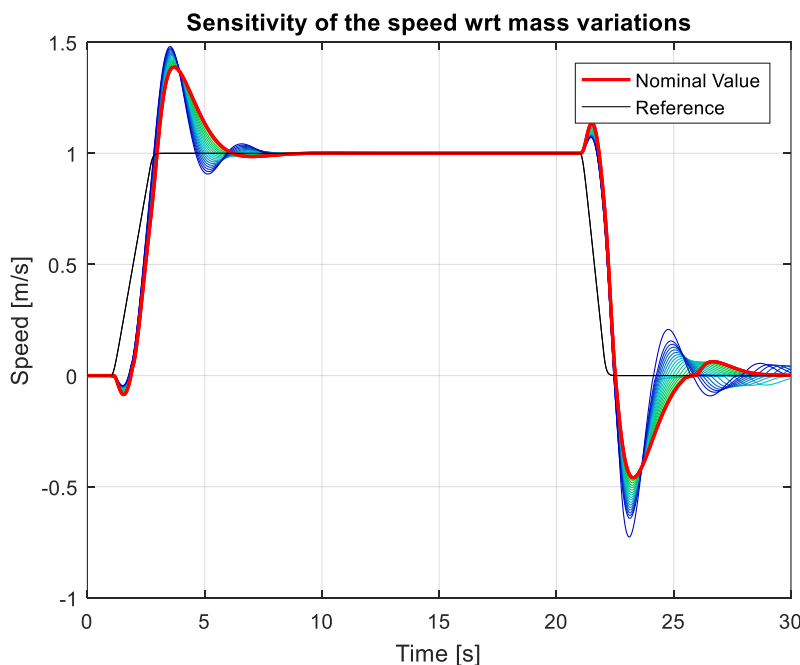


Figure 10-25 Sensitivity of the speed wrt mass variations

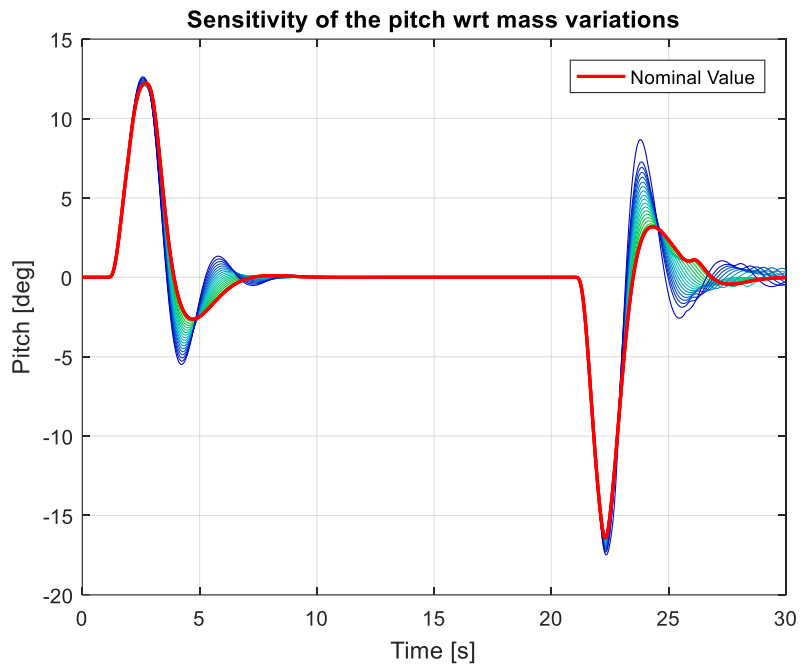


Figure 10-26 Sensitivity of the pitch wrt mass variations

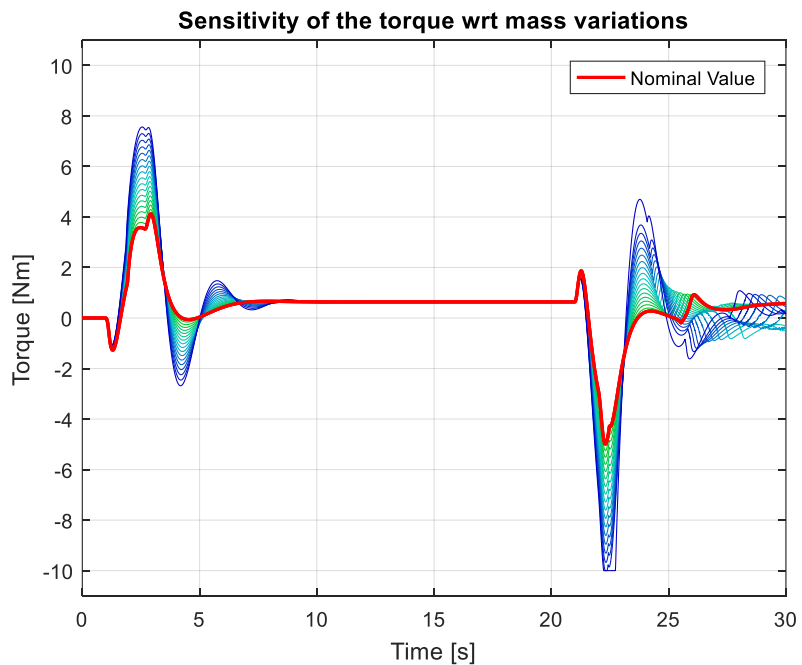


Figure 10-27 Sensitivity of the torque wrt mass variations

In the reported plots, we can see the nominal response reported in red, and all the other responses in a colour scale that goes from green to blue as the mass increases. From the test results we can notice that:

- the m_c variation does not impair the stability of the system.
- the system shows a less sensitivity in acceleration than in braking phase. (6.65% speed overshoot variation in acceleration versus 73.25% during braking and stabilization),
- as m_c increases the damping of speed oscillations is decreased.
- the only evident variation in the pitch behaviour is in the damping of the oscillations arising when the chassis is brought back to the vertical position.
- the maximum required torque increases almost linearly with the mass (5% increase for each 2Kg added to the vehicle)
- as the mass reaches 50Kg the torque saturates during the braking phase; even in this case the controller is able to maintain the stability of the vehicle.

It is also important to notice that if the mass is further increased up to 58Kg, the controller is not able of keeping the vehicle on balance: in fact, during the braking phase, the torque saturation impairs the stabilization capabilities of the controller, and the vehicle falls (FIGURE 10.28)

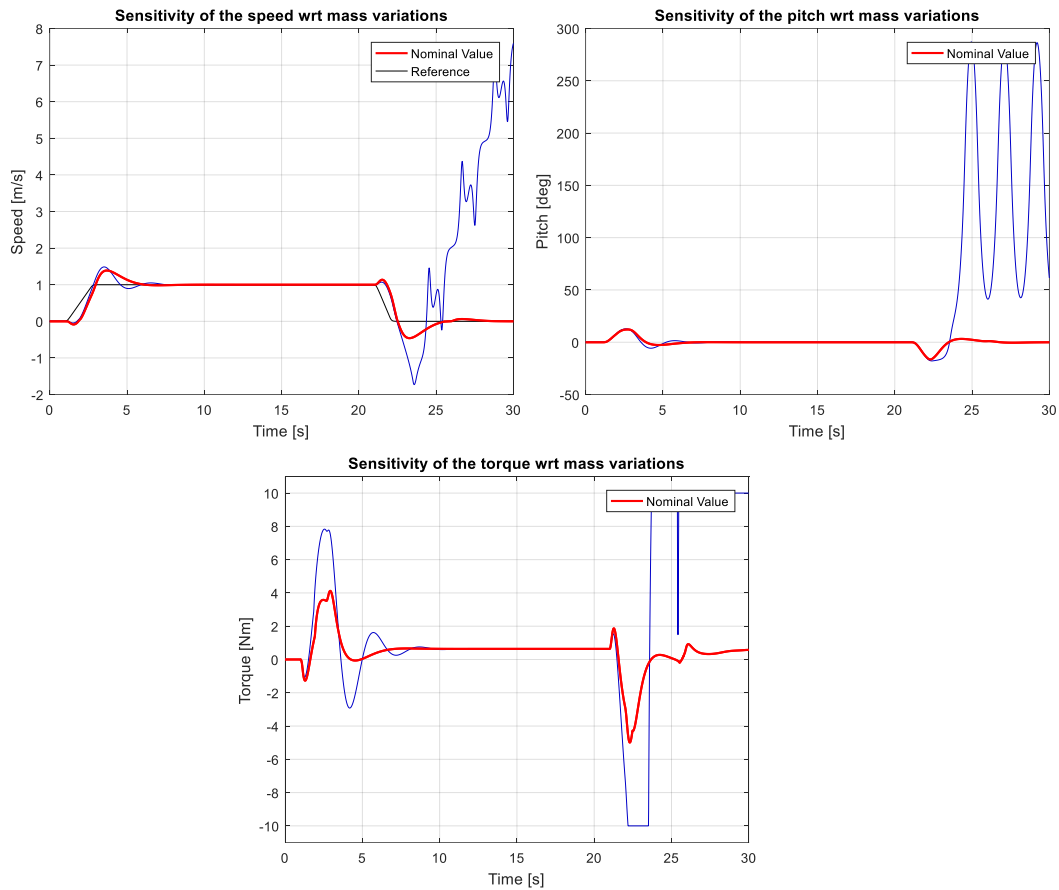


Figure 10-28 Loss of stability in case of too high mass variation

10.11.2 C.O.G height variation test:

Regarding the c.o.g height (L) , whose nominal value is 20 cm, an interval of 10-50 cm was used, in order to account both for positive and for negative variations. The results are shown in FIGURES 10.29,10.30,10.31.

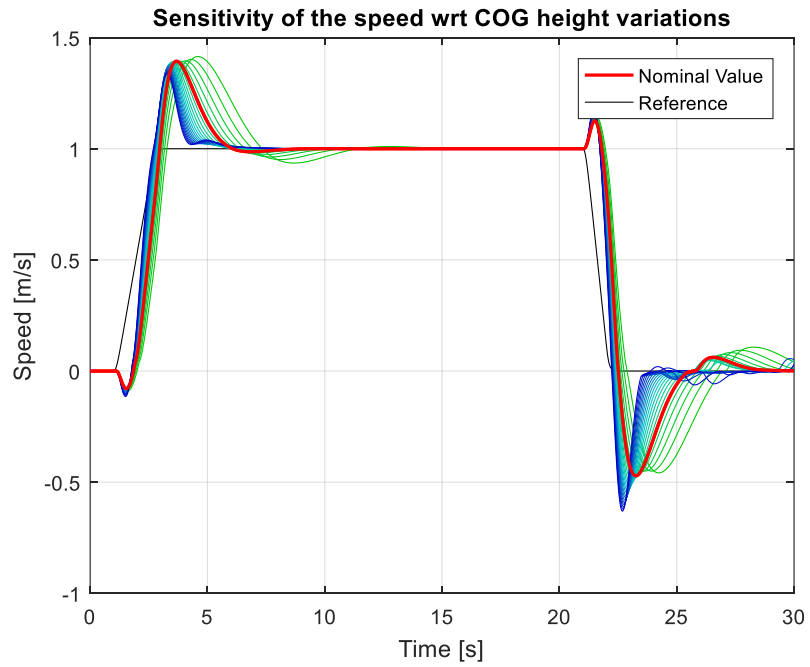


Figure 10-29 Sensitivity of the speed wrt c.o.g. height variations

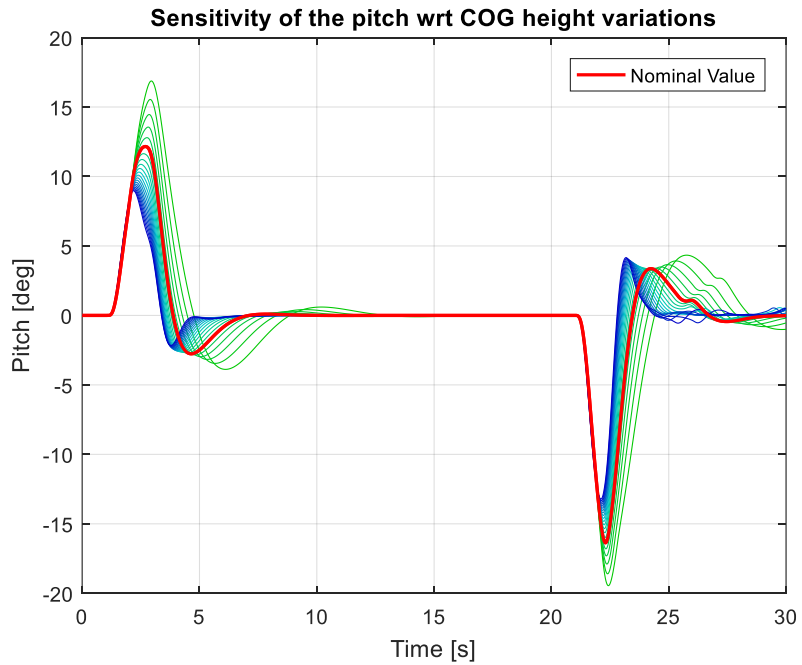


Figure 10-30 Sensitivity of the pitch wrt c.o.g. height variations

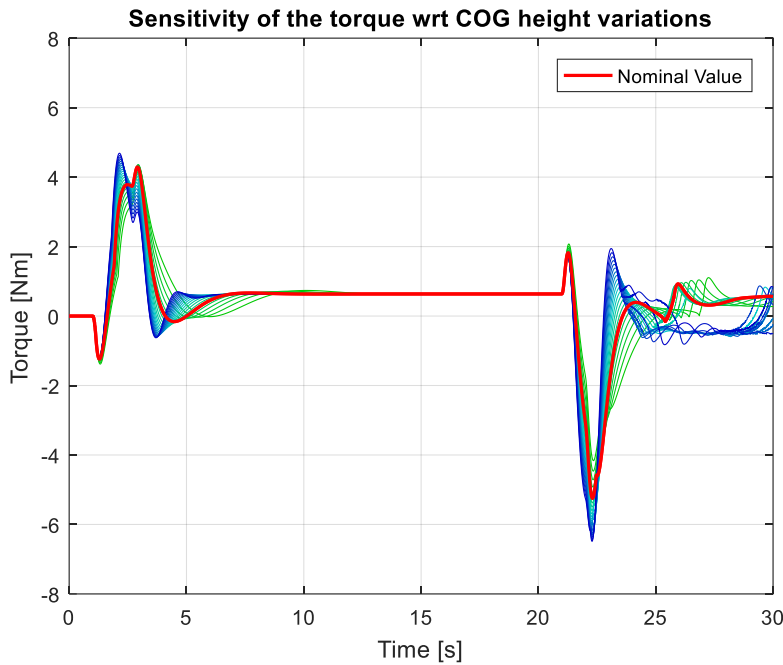


Figure 10-31 Sensitivity of the torque wrt c.o.g. height variations

Also in this case, the red curve represents the nominal response, whereas the colour goes from green to blue as L is increased from 10 to 50cm.

This test shows that:

- The speed and torque profiles show a limited sensitivity to the L variations.
- The pitch curve highlights an interesting behaviour of the LQR: the regulator is very sensible to negative variations of the parameter, and shows worse performances for values of L which are smaller than the nominal one with respect to the nominal case.
- A 50% decrease of L produces a 38% increase on the maximum overshoot. Conversely, a 50% increase of L produces a reduction of 15% of the peak pitch value. In other words, if the actual system requires a less intense control action with respect to the one on which the controller is designed, the torque excess results into a more oscillatory behaviour. On the contrary, a more requiring system is well managed by the feedback action.

We can conclude that during the controller design phase it is better to underestimate the value of L; in this way, any load/unload operation will produce an increase of the c.o.g. height with respect to the nominal value, and will be managed easily by the controller.

10.11.3 Moment of Inertia

An interval of 1-8 [kg m²] was considered for the moment of inertia J_{cy} , which has an estimated nominal value of 4 [kg m²]. The results are shown in FIGURES 10.32,10.33,10.34.

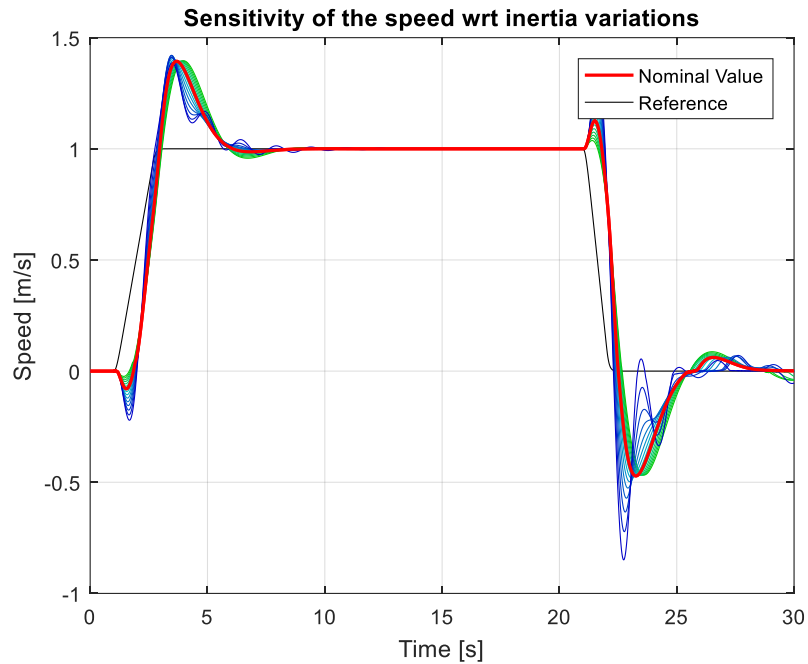


Figure 10-32 Sensitivity of the speed wrt to inertia variations

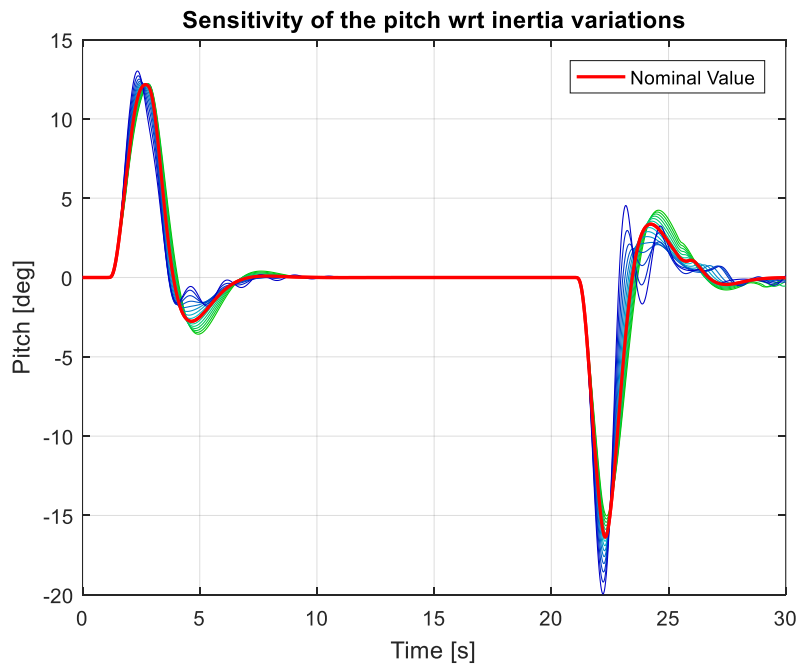


Figure 10-33 Sensitivity of the pitch wrt to inertia variations

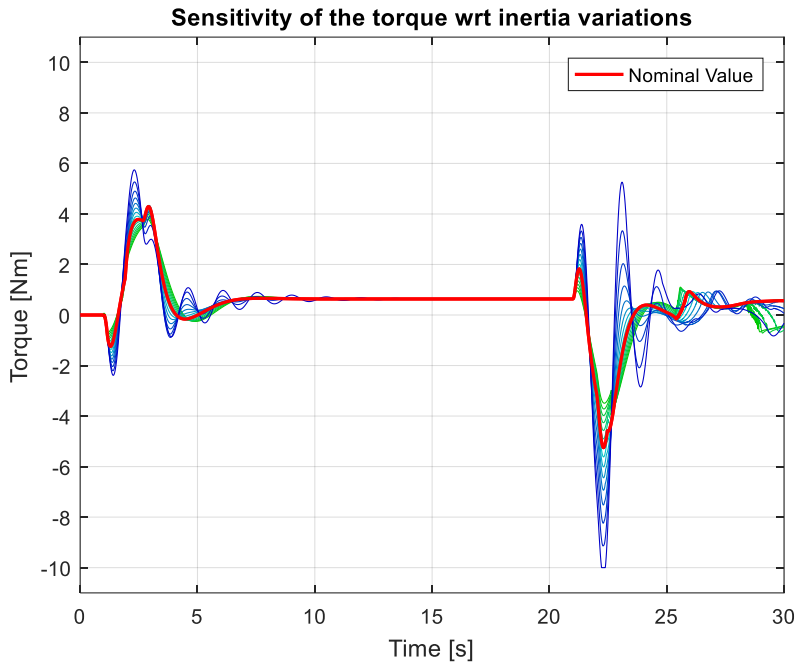


Figure 10-34 Sensitivity of the torque wrt to inertia variations

The effect of a variation of J_{cy} is far from being linear: in the range from 1-4 [kg m^2] the system behaviour is practically unchanged, which confirms what was noticed in CHAPTER 7. However, as the value of J_{cy} increases, its influence on the systems behavior grows bigger and bigger. The most affected dynamics is the pitch one; this reflects also on the requested torques, which easily reach the saturation limit. In general, a less damped behaviour is observed on the whole system.

10.11.4 Package load test

As a final test, the load of a regular package is simulated: the presence of the load will affect the chassis mass (m_c), the value of the moments of inertia (J_{cy}) and the c.o.g height (L). The results are shown in FIGURES 10.35,10.36,10.37.

The pack is supposed to be a uniform cube of 20 kg mass, and a 30cm side. The position of the pack is supposed to be such that the c.o.g. height is increased of 10 cm, resulting in $L = 30 \text{ cm}$. The total rotational inertia of the chassis was computed using the Huygens theorem:

$$I_{rot} = I_{cog} + m_{pack}L^2 = \frac{1}{12}m_{pack}(l^2 + l^2) + m_{pack}L^2 \quad (10.36)$$

As in the previous tests, the nominal values of the vehicle's parameters are:

- $m_{c_n} = 24 \text{ [Kg]}$
- $L_n = 0.2 \text{ [m]}$
- $J_{cy_n} = 4 \text{ [Kg m}^2]$

whereas the perturbed ones become:

- $m_c = m_{cn} + m_{pack} = 44 \text{ [Kg]}$
- $L = 0.30 \text{ [m]}$
- $J_{cy} = J_{cy_n} + \frac{1}{12}m_{pack}(l^2 + l^2) + m_{pack}L^2 = 6.10 \text{ [Kg m}^2]$

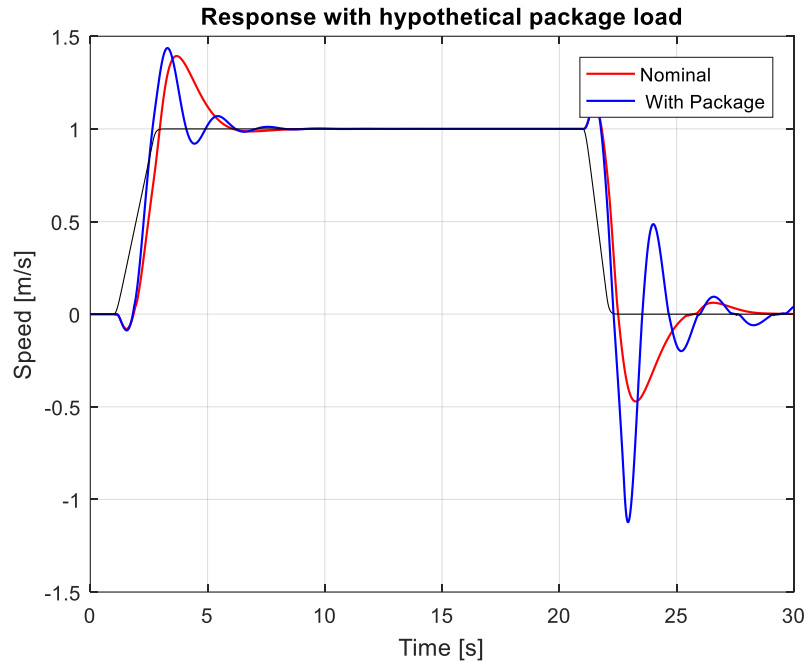


Figure 10-35 Response with hypothetical package load - speed

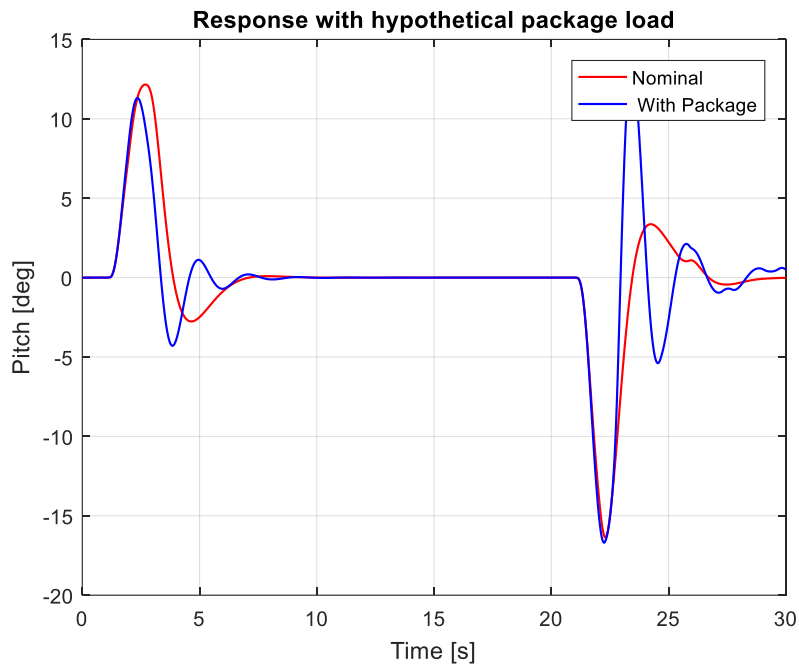


Figure 10-36 Response with hypothetical package load - pitch

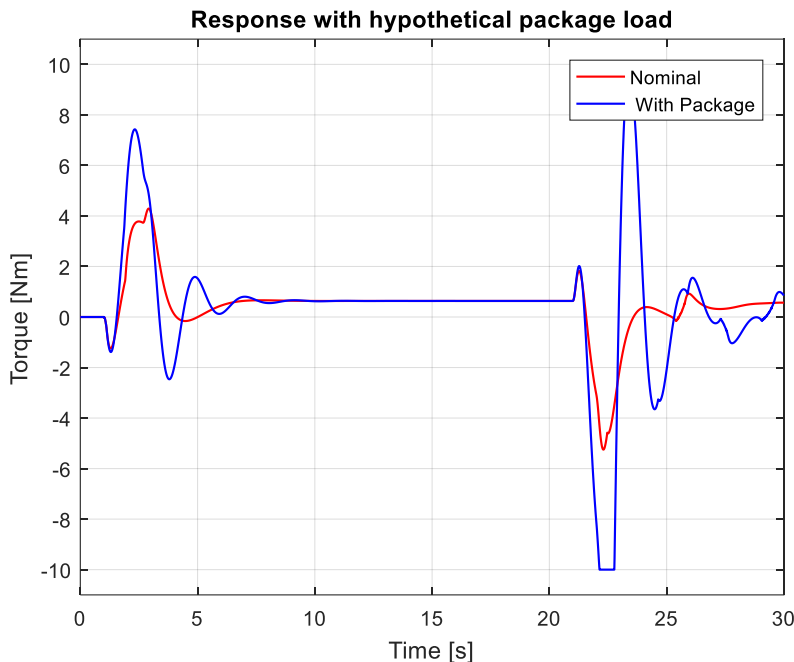


Figure 10-37 Response with hypothetical package load – torque

	Max speed	Min speed	Max pitch	Min pitch	Max torque	Min Torque
Package	+3 %	+138%	+10%	+2%	+125%	+90%

Table 10-6 Comparison with/without package

For the analysis of the response we notice that:

- The entity of the speed overshoot is not affected by the presence of the pack during the acceleration, whereas a significative worsening of the performances is shown in the braking phase: the combination of an increased mass and inertia, with a higher c.o.g result in a large, low damped oscillatory behaviour during the final stabilization phase
- The abovementioned oscillatory behaviour causes the temporary saturation of the torques, which though does not result in the system instability. This saturation indicates the fact the such a package pushes the controller to the maximum of its capabilities (with this particular torque saturation value): a further mass increase could bring to instability
- The controller could handle heavier loads by removing the torque saturations; this won't anyway remove the oscillatory behaviour. In order to reduce those, a controller tuned on a higher value of m_c mass could be used, but this would have even worse performances as soon as the pack is unloaded. A feasible solution would be the implementation of a scheduled controller, in which the proper gain matrix is chosen from time to time based on a mass measure or at least some sort of mass estimation.

10.12 Feedforward

A possible improvement of LQ scheme is related to the pitch reference signal. In fact, during all the test considered so far, the LQ controller was fed with a pitch reference equal to zero. This value is often not coherent with what is required by the reference speed: in fact, in order to track non-zero speed profiles, the vehicle needs to perform accelerations or decelerations which cannot happen without a forward or backward pitch motion. This incoherence between the two reference signals makes the pitch control interfere in some way with the speed one, decreasing the reactivity and the efficiency of the latter. Better performances can be obtained by including a feed forward action in the form of an open loop estimation of the required pitch angle to follow a specific speed profile.

In order to implement this feed forward block, the relation between acceleration and pitch computed in CHAPTER 9, is recalled first:

$$\ddot{s} = \frac{m_p g L \sin \theta}{m_c L \cos \theta + 2 R \left(\frac{J_w}{R^2} + m_w \right) + m_c R} \quad (10.37)$$

Then, by defining:

$$\begin{aligned} a &= m_c g L \\ b &= m_c L \\ c &= 2 R \left(\frac{J_w}{R^2} + m_w \right) + m_c R \end{aligned} \quad (10.38)$$

It is possible to rewrite the (10.37) as:

$$\ddot{s}(\theta) = \frac{a \sin \theta}{b \cos \theta + c} \quad (10.39)$$

Substituting:

$$t = \tan \frac{\theta}{2}, \quad \sin \theta = \frac{2t}{1+t^2}, \quad \cos \theta = \frac{1-t^2}{1+t^2} \quad (10.40)$$

Into (10.39), we get:

$$\ddot{s} b \frac{1-t^2}{1+t^2} + \ddot{s} c = a \frac{2t}{1+t^2} \quad (10.41)$$

Rearranging:

$$\ddot{s} (c - b) t^2 - 2 a t + \ddot{s} (b + c) = 0 \quad (10.42)$$

Which solution is:

$$t = \frac{a \pm \sqrt{a^2 - \ddot{s} (c^2 - b^2)}}{\ddot{s} (c - b)} \quad (10.43)$$

Substituting (10.43) into the first equation of (10.40) we can finally write:

$$\theta(\ddot{s}) = 2 \tan \frac{a - \sqrt{a^2 - \ddot{s}(c^2 - b^2)}}{\ddot{s}(c - b)} \quad (10.44)$$

Which express the steady state pitch angle as a function of the requested acceleration.

The implementation of the feed forward action is then carried on as follows: by differentiating the speed reference signal the requested acceleration is obtained; then, by using the corresponding steady state pitch angle is computed; such value is then used as pitch reference. The approach is schematically presented in FIGURE 10.38.

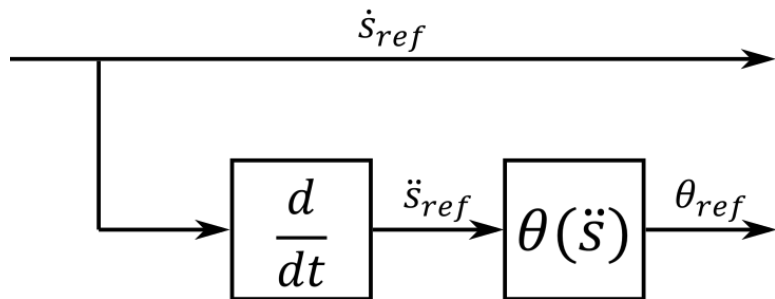


Figure 10-38 Pitch feedforward scheme

This control approach was tested using the usual trapezoidal speed profile, with the following results:

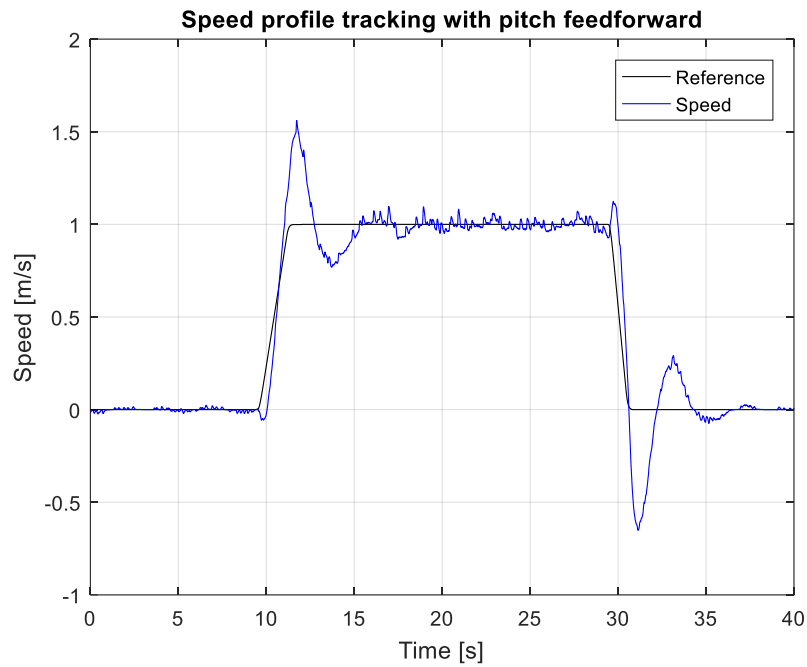


Figure 10-39 Speed profile tracking with pitch feedforward

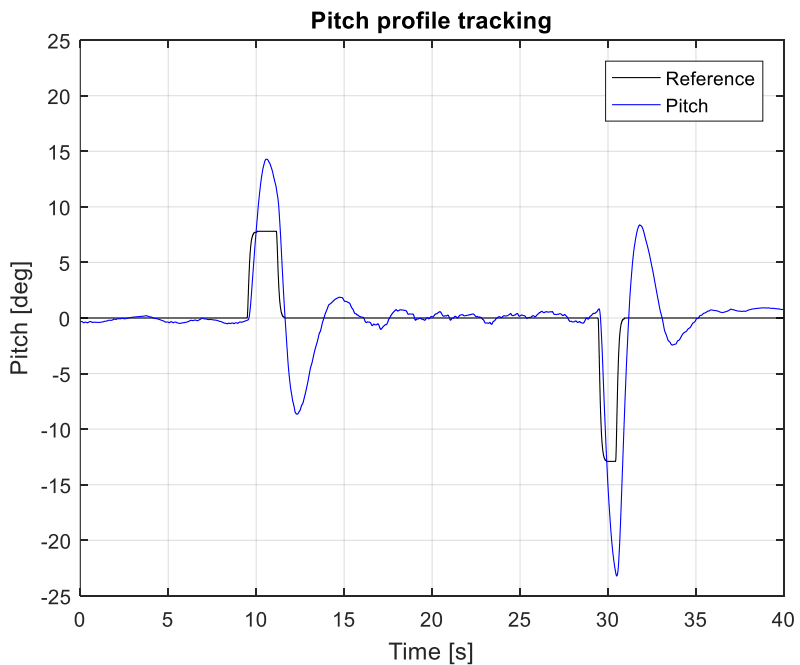


Figure 10-40 Pitch profile tracking

From FIGURES 10.39 AND 10.40 we can notice that:

- the speed profile is tracked with a superior reactivity with respect to what is done by the same controller without the feed forward action: the time delay related to the non-minimal phase behaviour is reduced, together with the rising time;
- the speed overshoot is practically unchanged.
- The pitch angle makes a big overshoot with respect to the required one (almost an 100% overshoot). A reduction of this value was obtained on the simulator by considerably increasing the weight on the pitch with respect to other states; such a solution was not tested on the real system, since this type of controller was verified to be very nervous and to cause mechanical vibrations in the system.

10.13 Conclusions

The LQ control approach was explained in this chapter. Theoretical results were presented explaining the nature of an LQR together with a method of tuning the weights matrices. A set of tests was then introduced, together with the experimental results acquired from the vehicle. In addition to that, a sensitivity analysis of the closed loop system to model parametric uncertainties was carried on the simulator. Finally, a feed forward approach was presented as a mean of improving the LQ performances.

From all the data presented in this chapter, we can conclude that the LQ represents a good control approach for a WIP vehicle. It grants satisfactory performances and an adequate rejection of the main disturbances the vehicle can encounter in an urban environment. However, since LQ does not allow to explicitly limit the pitch excursions of the chassis with a good confidence, large margins of performances are lost in order to minimize the possibilities of a crash. The cascade controller presented in the next chapter is intended to overcome this weakness; it aims at granting the good disturbance rejection performances observed with the LQR while providing a way of computing and limiting the expected pitch behaviour.

Chapter 11 - Cascade Control

11.1 Introduction

In the previous chapter, an LQR approach was presented and its performances in controlling the vehicle were analysed. It was noticed that the main flaw of this regulator is the lack of a simple way of prescribing a maximum allowed value for the pitch angle. In order to avoid crashes, the vehicle performances are therefore limited by means of a rate limiter on the speed reference signal, which minimize the possibilities of reaching the maximum pitch by limiting the required accelerations. In order to overcome this problem, an alternative control approach is presented in this chapter.

The main idea behind this approach is that of creating two different loops: an internal loop whose goal is that of stabilizing the vehicle controlling the pitch, and an external one aiming at controlling the speed by using the pitch as a control variable. In order to do so, the results obtained in CHAPTER 3 concerning the transfer function between pitch and speed will be used. The same test run on the LQR will be repeated on this type of controller, and the performances of the two will be compared. Finally, a simple pitch limitation technique will be introduced and discussed.

11.2 CASCADE control: theory

The cascade controller was designed starting from the transfer functions derived in CHAPTER 3. First of all, the longitudinal and yaw dynamics were controlled separately, using the change of control variable introduced in CHAPTER 3; namely, the sum of the two torques $\tau_c = \tau_r + \tau_l$ was used to control the longitudinal and pitch dynamics, whereas the differential torque $\tau_d = \tau_r - \tau_l$ was used to control ψ and $\dot{\psi}$. An input-output scheme for this choice is presented in FIGURE 11.1

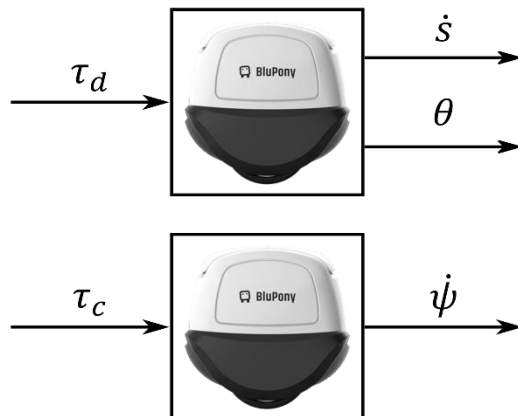


Figure 11-1 I/O representation of cascade control

In particular, due to the satisfactory performances obtained by the LQ regulator in controlling the yaw dynamics, the cascade controller for τ_d was trivially obtained using the components of the LQ control matrix Klq_{best} which were relative to the yaw dynamics:

$$\tau_d = k_{15}\delta\psi + k_{16}\dot{\delta\psi} \quad (11.1)$$

In this way the cascade approach grants the same yaw performances observed in the previous chapter on LQ; therefore, the yaw controller will not be treated in this chapter, which will be focused on the longitudinal and pitch dynamics. For this reason, from now on we will use τ to refer τ_c .

The objective of the longitudinal controller is that of designing two control loops: the first is closed on the pitch, with the intent of stabilizing the system using the torques as control variables; the second one is closed on the speed, and tracks a speed reference profile using the pitch as a control variable. Such control scheme is depicted in FIGURE 11.2 in which $G_{\tau\dot{s}}(s)$ is the transfer function between torque and pitch, and $G_{\tau\dot{s}}(s)$ is the transfer function between torque and speed (see CHAPTER 3).

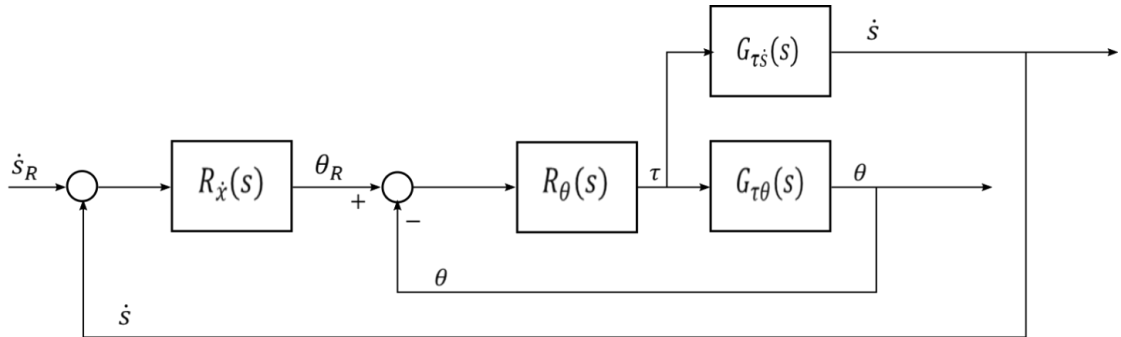


Figure 11-2 Block scheme of cascade control

As we can notice from FIGURE 11.2, this control scheme is not in the classical form of a cascade control scheme. Therefore, by means of simple block manipulation, we have to rewrite it as (FIGURE 11.3):

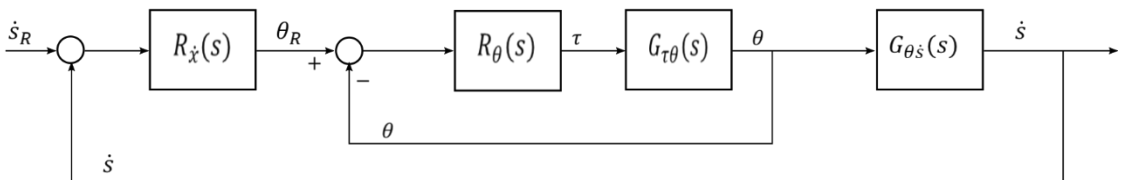


Figure 11-3 Block scheme of cascade control: classical form

in which $G_{θs̄}(s)$, is the non-minimum-phase transfer function between pitch and speed computed in CHAPTER 3.

The control design phase will be explained in the following sections, starting from the design of the inner pitch loop, and following with the external speed loop.

11.3 CASCADE: pitch loop

The internal loop controller is designed on the transfer function relating the torque to the vehicle's pitch, namely:

$$G_{\tau\theta}(s) = -\frac{b_2}{(s + \sqrt{a_2})(s - \sqrt{a_2})} \quad (11.2)$$

As noted in CHAPTER 3, this transfer function presents two symmetrical poles, a negative, stable one and a positive and unstable one. For this reason, the classical tools used in the design phase (such as Bode diagrams) are of no use in this case. For this reason, a convenient solution [24] is that of designing a two-loop controller as depicted in FIGURE 11.4

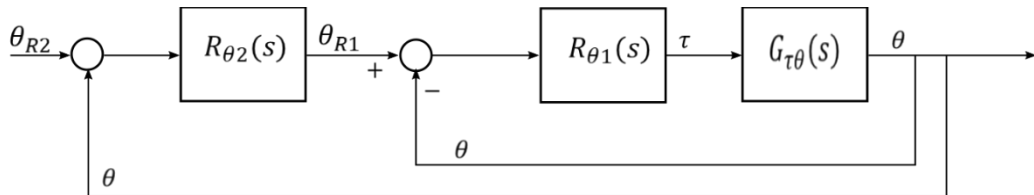


Figure 11-4 Pitch control loop

The goal of $R_{\theta 1}(s)$ is only to stabilize the system, so that $R_{\theta 2}(s)$ can be designed on the resulting, stable transfer function with the goal of providing the required performances.

The first controller was designed using the root-locus technique. As we can see from the inverse root locus of $G_{\tau\theta}(s)$ reported in FIGURE 11.5 the system is not stabilizable with a simple proportional regulator:

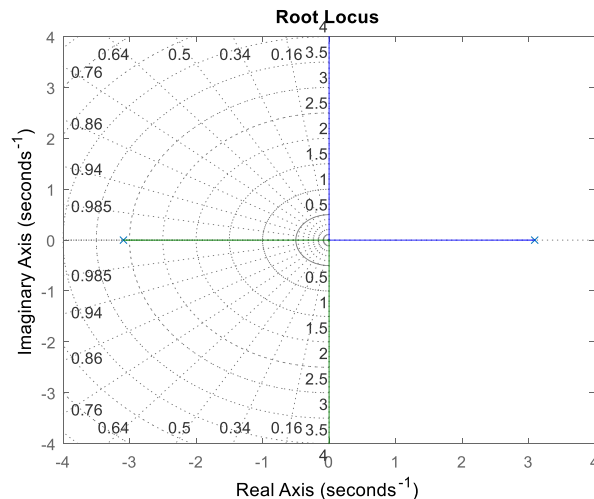


Figure 11-5 Inverse root locus of $G_{\tau\theta}(s)$

The reason for this, is the perfect symmetry between the stable and the unstable pole of the system. A possible solution is therefore to cancel the stable pole of the system, and replace it with a higher frequency one. A regulator accomplishing that is given by:

$$R_{\theta 1}(s) = k_1 \frac{s + \sqrt{a_2}}{s + p_1} \quad (11.3)$$

in which k_1 and p_1 can be used as free design parameters. The corresponding root-locus would be the one depicted in FIGURE 11.6

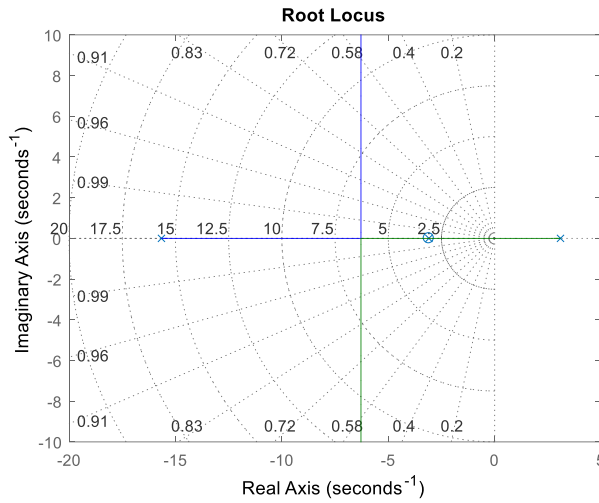


Figure 11-6 Inverse root locus of $G_{\tau\theta}(s)$ after pole replacement

The values of k_1 and p_1 , were then tuned to obtain coincident closed loop poles having a natural frequency $\omega_{p\theta}$. In order to do so, the characteristic polynomial $\rho_{\theta 1}$ of the closed-loop system is used. In particular, we have that:

$$\rho_{\theta 1}(s) = s^2 + s(p_1 - \sqrt{a_2}) - p_1\sqrt{a_2} - b_2k_1 \quad (11.4)$$

It is then possible to prescribe coincident closed loop poles by setting to zero the discriminant of the quadratic equation, yielding:

$$p_1^2 + a_2 - 2p_1\sqrt{a_2} + 4p_1\sqrt{a_2} + 4b_2k_1 = 0 \quad (11.5)$$

which in turn gives:

$$k_1 = -\frac{(p_1 + \sqrt{a_2})^2}{4b_2} \quad (11.6)$$

If (11.6) holds, the two roots of $\rho_{\theta 1}(s)$, i.e. the closed loop poles of the system, are coincident and given by:

$$s_{1,2} = \frac{-p_1 + \sqrt{a_2}}{2} \quad (11.7)$$

Prescribing the poles to be located at $s = -\omega_{p\theta}$, we obtain

$$-\omega_{p\theta} = \frac{-p_1 + \sqrt{a_2}}{2} \quad (11.8)$$

and, rewriting:

$$p_1 = 2\omega_{p\theta} + \sqrt{a_2} \quad (11.9)$$

Once p_1 is known, it is possible to compute k_1 from (11.6):

$$k_1 = -\frac{(p_1 + \sqrt{a_2})^2}{4b_2} = -\frac{(2\omega_{p\theta} + 2\sqrt{a_2})^2}{4b_2} \quad (11.10)$$

In conclusion, choosing:

$$\begin{cases} R_{\theta 1}(s) = k_1 \frac{s + \sqrt{a_2}}{s + p_1} \\ p_1 = 2\omega_{p\theta} + \sqrt{a_2} \\ k_1 = -\frac{(2\omega_{p\theta} + 2\sqrt{a_2})^2}{4b_2} \end{cases} \quad (11.11)$$

the closed loop transfer function is:

$$F_{\theta 1}(s) = -\frac{b_2 k_1}{(s + \omega_{\theta 1})^2} \quad (11.12)$$

The second regulator can now be designed on $F_{\theta 1}(s)$. In this case, we decided to use a standard PID regulator of the form

$$R_{\theta 2}(s) = k_2 \frac{(s + \omega_{z1})(s + \omega_{z2})}{s} \quad (11.13)$$

using the two zeros to cancel the double pole of $F_{\theta 1}(s)$ and then tuning the gain k_2 to obtain the desired bandwidth. In particular, having:

$$R_{\theta 2}(s) = k_2 \frac{(s + \omega_{\theta 1})^2}{s} \quad (11.14)$$

the open loop transfer function is

$$L_{\theta 2}(s) = -\frac{b_2 k_1 k_2}{s} \quad (11.15)$$

that is a simple integrator with cut-off frequency $\omega_c = -b_2 k_1 k_2$. Then, by imposing

$$\omega_c = \bar{\omega}_{c\theta} \quad (11.16)$$

we obtain a value for k_2 of:

$$k_2 = -\frac{\bar{\omega}_{c\theta}}{b_2 k_1} \quad (11.17)$$

The final closed loop transfer function for the pitch is then

$$F_{\theta 2}(s) = \frac{\bar{\omega}_{c\theta}}{s + \bar{\omega}_{c\theta}} \quad (11.18)$$

which is a first order low pass filter with unitary gain and a bandwidth of $(0; \bar{\omega}_{c\theta})$ (FIGURE 11.7)

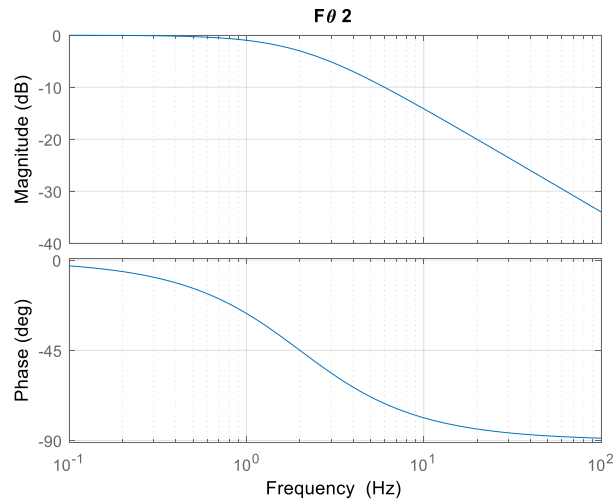


Figure 11-7 Bode diagram of closed loop pitch transfer function

It can be shown that the total control sensitivity function is then:

$$Q_\theta(s) = -\frac{\bar{\omega}_{c\theta}}{b_2} \frac{s^2 - a_2}{s + \bar{\omega}_{c\theta}} \quad (11.19)$$

The bode diagram of the modulus of $Q_\theta(s)$ is shown in FIGURE 11.8.

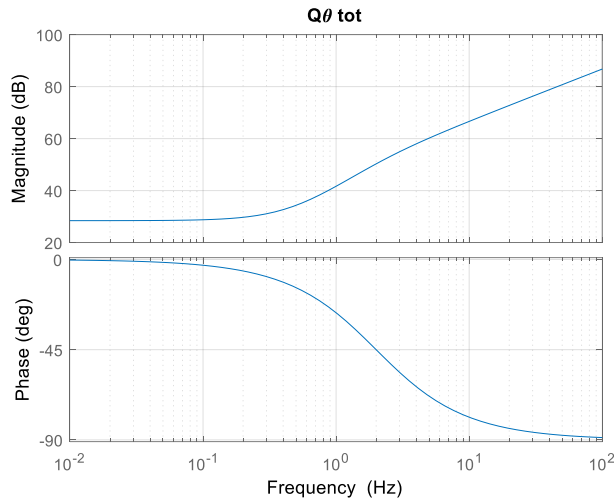


Figure 11-8 Bode diagram of control sensitivity function of pitch loop

As expected, the bigger $\bar{\omega}_{c\theta}$ the higher is the maximum requested control in the frequency range of interest. The cut-off frequency $\bar{\omega}_{c\theta}$ has therefore to be chosen as result of a tradeoff between the speed required to minimize the interference of the pitch loop with the speed loop and the moderation of the control action. In addition to that, the PID scheme was implemented applying the derivative action directly to the state rather than to the error (see FIGURE 11.9), as is common practice to improve the moderation of the control action at the high frequencies.

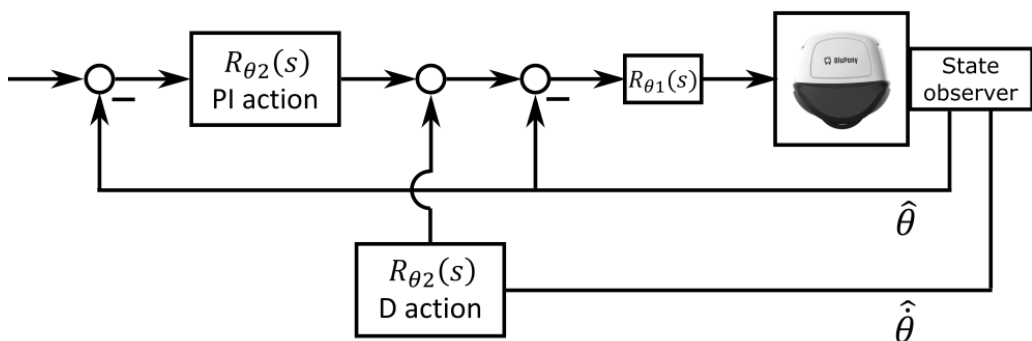


Figure 11-9 Overall control scheme pitch loop

11.4 CASCADE: speed loop

Once the internal speed loop is closed, the external, speed regulator can be designed. The control scheme is reported in FIGURE 11.10

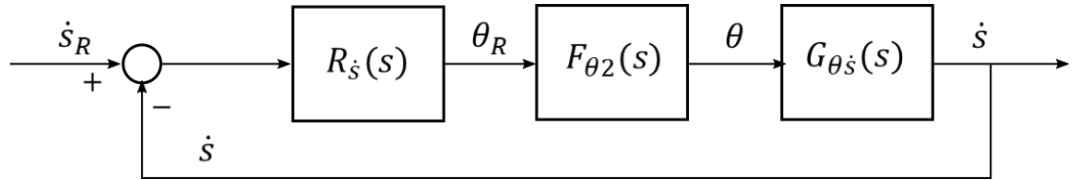


Figure 11-10 Scheme speed control loop

In this scheme, $F_{\theta_2}(s)$ is the closed loop transfer function for the pitch, whereas $G_{\theta\dot{s}}(s)$ is the pitch-speed transfer function derived in CHAPTER 3, namely:

$$G_{\theta\dot{s}}(s) = -\frac{b_1(s + a_{nmf})(s - a_{nmf})}{b_2 s} \quad (11.20)$$

As proved in CHAPTER 3, $G_{\theta\dot{s}}(s)$ shows a non-minimum phase behavior due to the positive valued real zero located at $s = a_{nmf}$. The total transfer function that has to be controlled is then:

$$G_{\theta_R\dot{s}}(s) = F_{\theta_2}(s)G_{\theta\dot{s}}(s) = -\frac{b_1\bar{\omega}_{c\theta}}{b_2}\frac{(s + a_{nmf})(s - a_{nmf})}{s(s + \bar{\omega}_{c\theta})} \quad (11.21)$$

which is the transfer function between the pitch reference and the vehicle speed once the internal loop is closed. The bode diagrams of $G_{\theta_R\dot{s}}(s)$ are depicted in FIGURE 11.11.

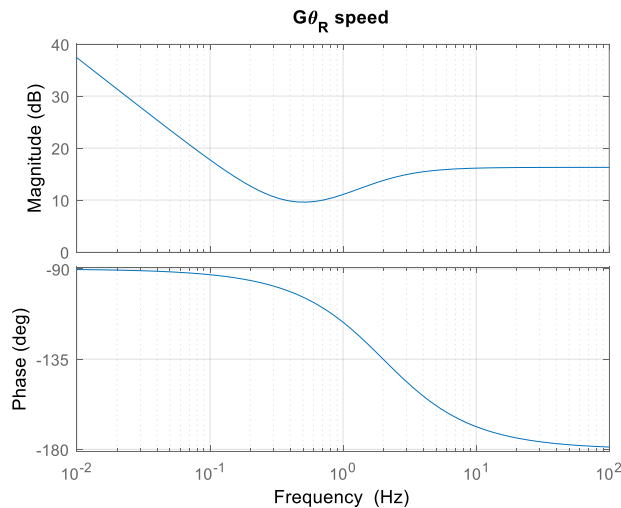


Figure 11-11 Bode diagrams of $G_{\theta_R\dot{s}}(s)$

As we can see both from the (11.21) and from the bode diagrams, $G_{\theta_R \dot{s}}(s)$ already contains an integral action. This is due to the fact that YAPE is controlled using torques, which directly acts on the vehicle's acceleration, i.e. on the derivative of the speed. However, following the same reasonings made on the LQR, a further integral action is needed to provide a rejection to disturbances such as unbalanced loads or non-zero slope road profiles. A tentative controller for $R_s(s)$ is then given by:

$$R_s(s) = k_3 \frac{\frac{s}{\omega_{z3}} + 1}{s(\frac{s}{\omega_{p3}} + 1)} \quad (11.22)$$

in which k_3 , ω_{z3} and ω_{p3} are tuning parameters. The zero located in ω_{z3} was added to compensate the -90° contribute of phase given by the integrator, whereas the pole in ω_{p3} is needed to allow the crossing of the unity gain line. In particular, the zero and the pole were chosen so that $\omega_{z3} < \omega_{nmf}$ and $\omega_{nmf} < \omega_{p3} < \bar{\omega}_{c\theta}$. The bode diagrams for one of the choices of k_3 , ω_{z3} and ω_{p3} is presented in FIGURE 11.12

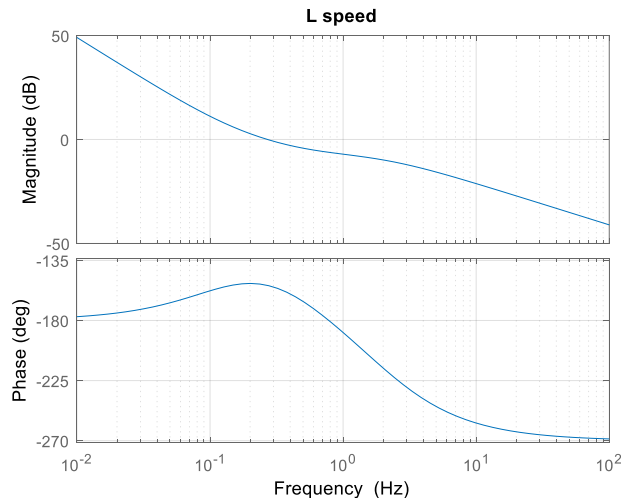


Figure 11-12 Speed open loop Bode diagram

In the following sections of the chapter, the testing phase of the controllers will be presented. The same test run on the LQ controller will be repeated for the cascade controller, so that a comparison between the results can be established. A set of 8 cascade controllers will be used. The internal loop will be kept constant; namely, $R_{\theta 1}$ and $R_{\theta 2}$ are designed so as to obtain

$$F_{\theta 2}(s) = \frac{2\pi f_c}{s + 2\pi f_c} \quad (11.23)$$

with cut-off frequency $f_c = 2$ Hz.

The 8 speed regulators were designed to test different cut-off frequencies and different disturbance rejection capabilities. In the first 4 controllers the pole and the zero of $R_s(s)$ were kept constant, and k_3 was used to change the speed cutoff frequency. Then, the pole frequency ω_{p3} was fixed together with the cutoff frequency, whereas k_3 and ω_{z3} were changed so to obtain different disturbance rejection capabilities. The parameters for the controller are reported in TABLE 11.1

Name	ω_{p3} [rad/s]	ω_{p3} [rad/s]	k_3	Resulting Cutoff frequency ω_{cs} [rad/s]	Resulting Cutoff frequency f_{cs} [Hz]
R_{01}	4.5	0.2	0.011	0.3	0.048
R_{02}	4.5	0.2	0.032	0.8	0.127
R_{03}	4.5	0.2	0.052	1.4	0.224
R_{04}	4.5	0.2	0.061	1.8	0.290
R_{05}	4.5	0.3	0.092	1.9	0.300
R_{06}	4.5	0.5	0.149	1.9	0.300
R_{07}	4.5	1	0.271	1.9	0.300
R_{08}	4.5	1.5	0.356	1.9	0.300

Table 11-1 List of cascade controller

11.5 Station Keeping

As for the LQ regulator, the first test presented is the station keeping (see CHAPTER 9). Also in this case and oscillating behaviour is observed. The results are reported on the following table:

Controller	Oscillation frequency [Hz]	Oscillation period [s]	Speed amplitude [m/s]	Position amplitude [m]	Max pitch [deg]	Max torque [Nm]
R_{01}	0.43	2.31	0.02	0.1	0.14	1.39
R_{02}	0.39	2.50	0.02	0.1	0.13	1.31
R_{03}	0.53	1.87	0.02	0.1	0.21	1.74
R_{04}	0.46	2.14	0.02	0.1	0.15	1.04
R_{05}	0.56	1.76	0.02	0.2	0.37	1.06
R_{06}	0.53	1.87	0.03	0.1	0.21	1.18
R_{07}	0.46	2.14	0.03	0.1	0.33	1.29
R_{08}	0.46	2.14	0.3	0.1	0.40	1.52

Table 11-2 Results of stabilization tests – CASCADE

By inspection of the table we can state that:

- The oscillation frequency is almost constant and approximately equal to 0.5 Hz, and no relevant trend is observable in the amplitude of pitch or speed oscillations as a function of the adopted controller
- The maximum speed during the limit cycle is in the order of few cm/s, and is comparable with what was obtained with the LQ controllers
- Position oscillation are of the same order of magnitude of those observed with the LQ controllers

We can therefore conclude that no relevant difference is observable between the LQ and the Cascade approach with regard to the Station Keeping Capabilities

11.6 Speed tracking

The second test aims to study the speed tracking capabilities of the controller while the vehicle is running on a flat surface. (see CHAPTER 8). The same speed reference profile introduced for the LQ controller was used also in this case. First, the controllers R_{01} to R_{04} , i.e. those having an increasing cutoff frequency, are analyzed; speed responses obtained using such controllers are reported in FIGURE 11.13, whereas the corresponding pitch curves are depicted in Figure 11.14.

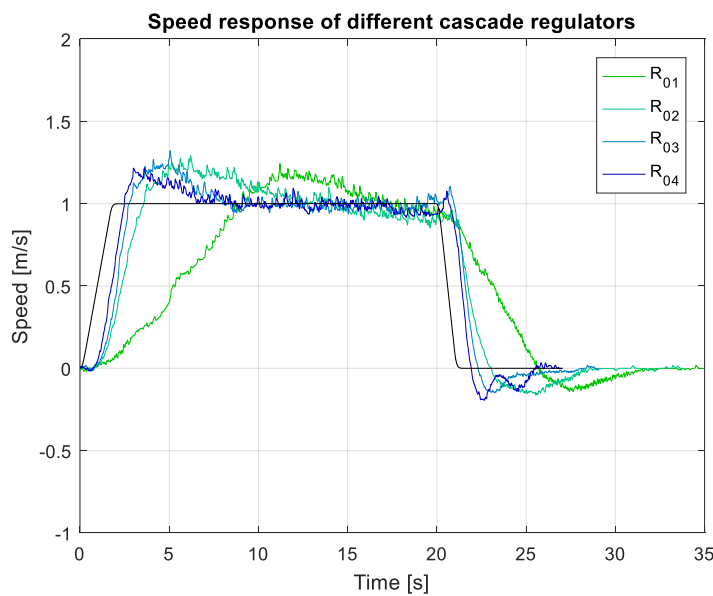


Figure 11-13 Speed tracking test – $R_{01}, R_{02}, R_{03}, R_{04}$ - Speed

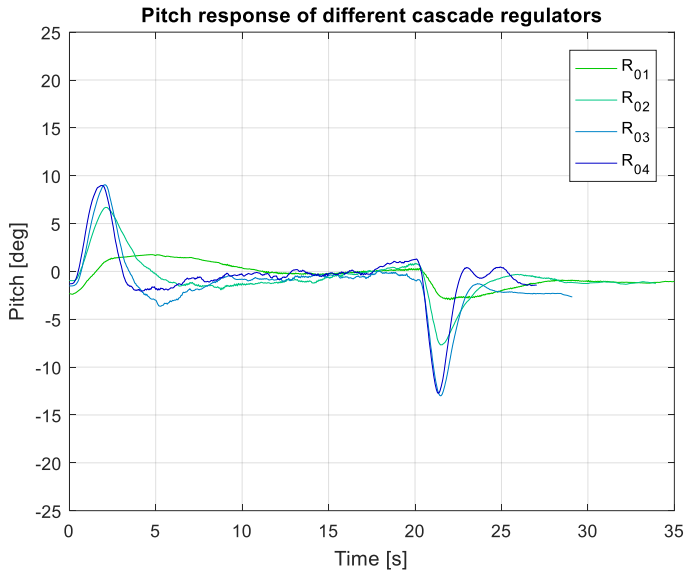


Figure 11-14 Speed tracking test – $R_{01}, R_{02}, R_{03}, R_{04}$ – Pitch

From FIGURES 11.13 AND 11.14 we can observe that:

- as expected, the rise time decreases as the cut-off frequency increases, going from approximately 10 seconds with R_{01} to less than one second with R_{04} . This last result is comparable to what was obtained using LQ
- The speed overshoot is almost constant, with a peak value of 1.2 m/s, corresponding to the 20% of the steady state value. This represent an improvement with respect to LQ, which shown overshoots in the range of 50-60%
- The pitch peaks range from 2° to 9° in acceleration, and from -3° to -13° while braking: these results are comparable with the best results obtained using LQ

The results obtained using regulators R_{05} to R_{08} , designed to have the same cutoff frequency but different disturbance rejection, are shown in FIGURES 11.15 AND 11.16.

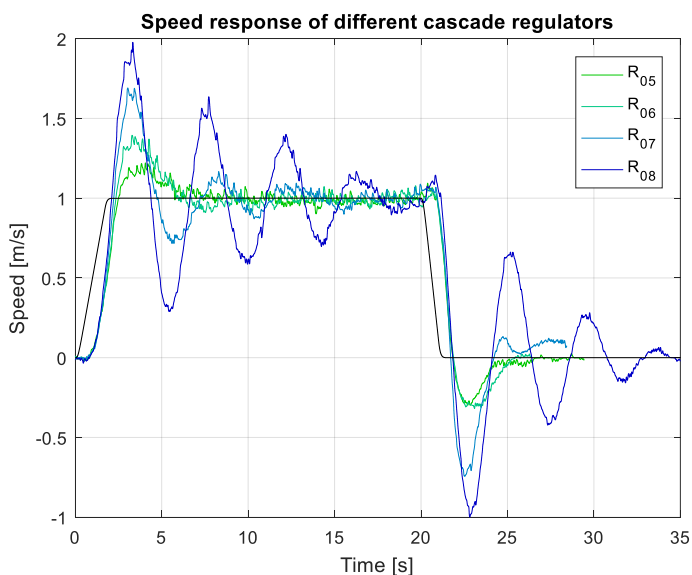


Figure 11-15 Speed tracking test – $R_{05}, R_{06}, R_{07}, R_{08}$ – Speed

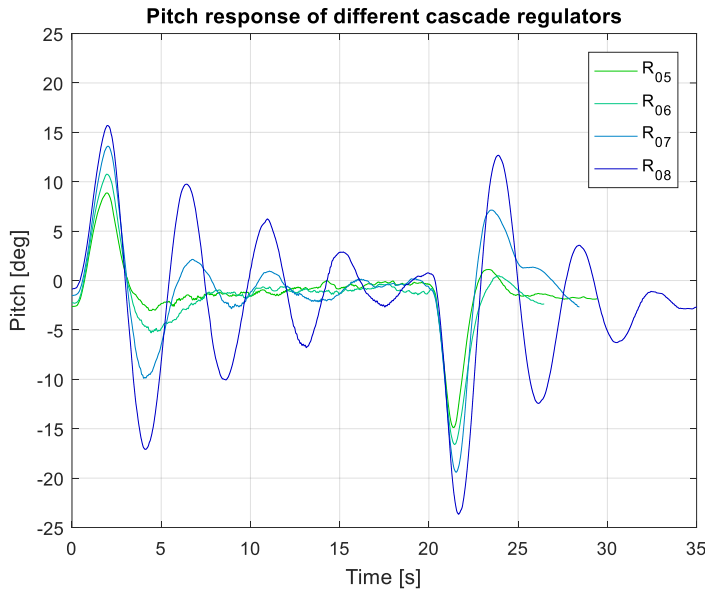


Figure 11-16 Speed tracking test – $R_{05}, R_{06}, R_{07}, R_{08}$ – Pitch

- As expected, the rise time is almost constant and comparable to what obtained with R_{04} , namely ~ 1 s.
- The speed overshoot increases, and an oscillatory behaviour arises going from R_{05} to R_{08} . This is explained by the fact that, in order to increase the disturbance rejection, the zero ω_{z3} of the speed regulator is moved closer and closer to the cutoff frequency; this results in a reduction of the phase margin, which in turn is manifested as a less damped system.
- R_{08} produces pitch peaks of 15° in acceleration, and -23° while braking; all the other regulators produce a positive peak of approximately 10° and a negative one of almost 15°.

In conclusion, we can state that cascade regulators R_{03} up to R_{06} show satisfactory speed tracking performances whilst keeping the pitch limited to the lowest values obtained with LQ. Conversely, R_{01}, R_{02} are too slow, whereas R_{07}, R_{08} are too aggressive and result in an undesirable oscillatory behavior of the speed. The best controller is therefore a compromise between regulators R_{03} up to R_{06} , which has to take into account the disturbance rejection capabilities that will be investigated in the next sections.

A final interesting observation can be made by looking at FIGURE 11.17, in which is depicted the time evolutions of the pitch reference signals produced by regulator R_{05} , together with the actual vehicle pitch.

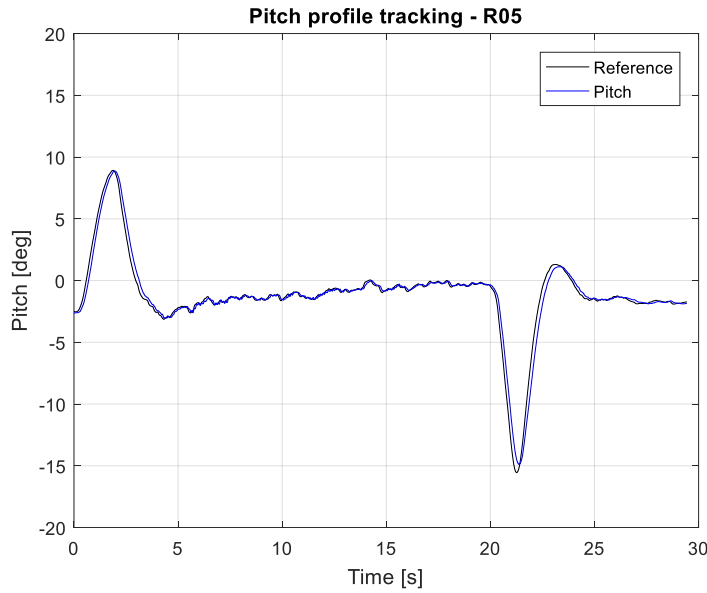


Figure 11-17 Pitch profile tracking R_{05}

As we can see, the inner pitch controller performs an almost perfect reference tracking, which suggest the possibility of removing the reference rate limiter and substituting it with a saturation on the pitch reference. The theoretical aspects and results of such technique will be investigated in the last section of this chapter.

11.7 Speed Tracking: slopes

Once again, the same speed profile used in the previous experiment is then tested on a non-zero slope road. For sake of brevity, the results related to the first 7 regulators are reported in FIGURE 1.18 AND 11.19. Regulator R_{08} was not tested on the slope for safety reasons.

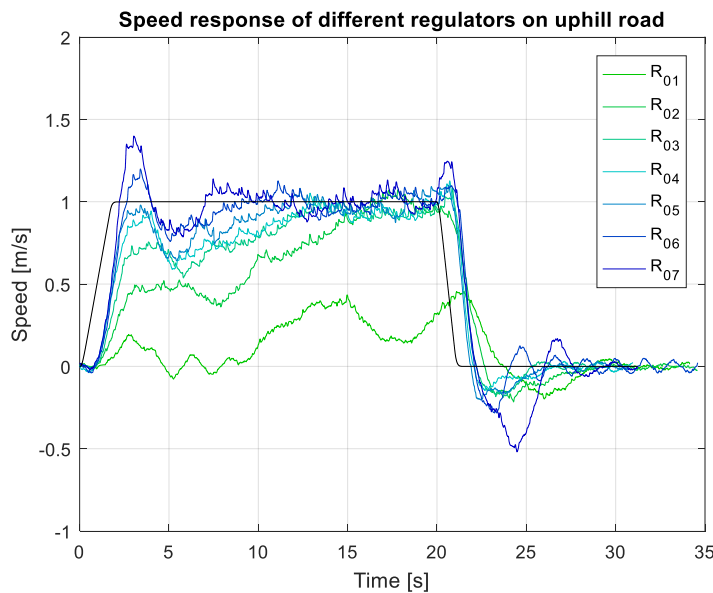


Figure 11-18 Speed response of different regulators on uphill road

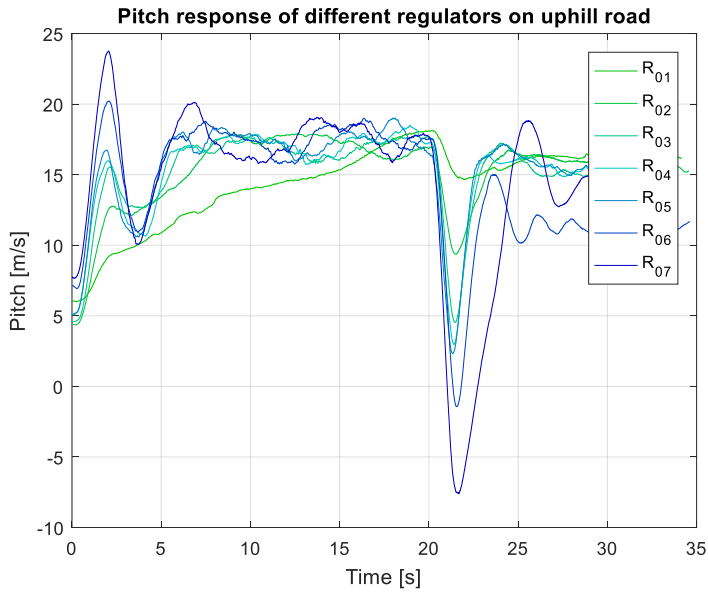


Figure 11-19 Pitch response of different regulators on uphill road

- The rejection of the disturb increases as expected going from regulator R_{01} , which fails at reaching the steady state speed value, up to R_{07} which efficiently opposes to the gravity force component and successfully tracks the required speed.
- Settle time, which ranged between 5 and 10 seconds in LQ, goes from almost 20 seconds using R_{01} to approximately 10 seconds for R_{05} , R_{06} and R_{07}
- The steady state pitch, which is approximately equal to 17° is reached by all controllers, even if with different time and dynamics.

Once again it is possible to appreciate the good reference tracking capabilities of the pitch controller by looking at FIGURE 11.20, which report the evolution of the pitch reference produced by R_{05} while facing the sloped road profile.

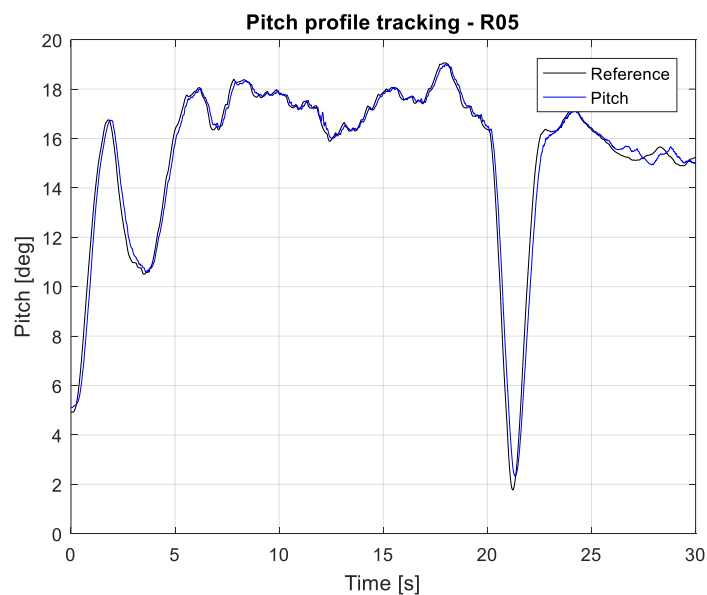


Figure 11-20 Pitch profile tracking R_{05} uphill road

In addition to what previously noticed about the pitch saturation, such reference tracking performances for the pitch suggest the possibility of introducing a feed forward action to increase the performances of the vehicle on uphills and downhills; such approach, which was not treated in our work, is part of the possible future developments of YAPE control structure.

11.8 Unbalanced load

As previously done with LQ controllers, a package load/unload operation is simulated. The behaviour of the vehicle using a cascade controller was qualitatively comparable to that observed in CHAPTER 10.

The time evolution of the vehicle displacement is reported in FIGURE 11.21, and the corresponding pitch curves are depicted in FIGURE 11.22. The experimental results are then summarized in the TABLE 11.3

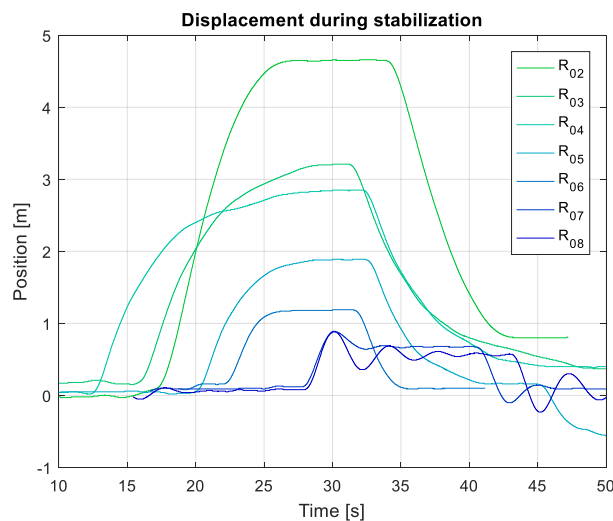


Figure 11-21 Displacements during stabilization tests - CASCADE

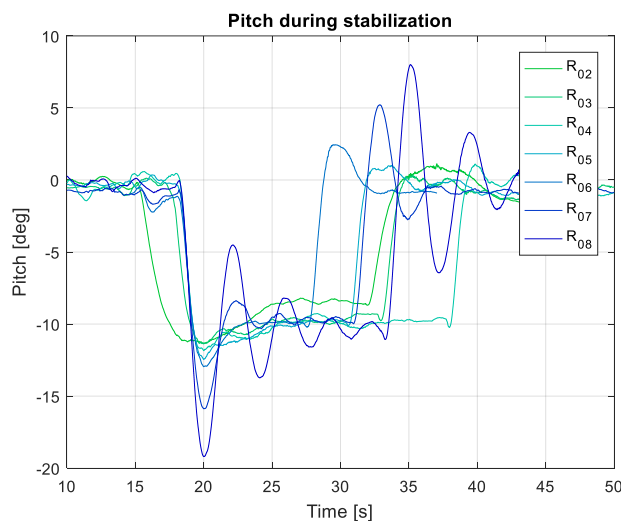


Figure 11-22 Pitch during stabilization tests – CASCADE

Controller	Max pitch [deg]	Measured displacement [m]	Steady – state pitch [deg]
R_{01}	-12.27	15.43	-9.40
R_{02}	-11.34	4.68	-8.38
R_{03}	-11.37	3.08	-9.85
R_{04}	-11.84	2.80	-9.93
R_{05}	-12.45	1.82	-10.05
R_{06}	-12.95	1.10	-9.82
R_{07}	-15.87	0.82	-9.72
R_{08}	-19.19	0.91	-10.24

Table 11-3 Results of stabilization with unbalanced load tests – CASCADE

- The equilibrium is achieved by all the controllers
- R_{01} , showed a total displacement of approximately 14 meters and is therefore not reported in FIGURE 11.21 for sake of clarity
- All the other controllers showed displacements which are comparable to the results obtained using LQ
- R_{05} and R_{06} , which proved to be the best controllers in all the previous tests, need a displacement of 1 and 2 meters respectively to reach the equilibrium position
- Once again, a feed forward action on the pitch reference could result in a general improvement of the performances, especially for what concerns the vehicle displacement. Such action, together with that mentioned concerning the slopes, is treated in the possible future developments section of this work

11.9 Pitch saturation

It should be clear from what has been discussed in this work, that an accurate and efficient control of the pitch dynamics is of paramount importance in the control of any WIP vehicle and even more so in the control of YAPE. To our knowledge, there are no examples in the literature of specific methods to impose a limit to the maximum pitch angle that the vehicle is allowed to assume. As explained in CHAPTER 10, such problem is particularly challenging using a traditional LQ control: namely, even with a particularly well-tuned version of the controller, there was no actual guarantee on the fact that the pitch wouldn't reach the geometrical limit of 30°. The reference rate limiter explained in CHAPTER 9 has proved to have only limited effectiveness in solving the problem, nonetheless introducing relevant reductions in the overall vehicle performances.

Conversely, our cascade approach offers an easy way of imposing a constraint on the maximum allowed pitch by means of a simple saturation on the pitch reference signal (FIGURE 11.23). Consequently, the observance of a constraint on the maximum pitch can be predicted in terms of the performances of $R_\theta(s)$. In particular, thanks to the good reference tracking capabilities exhibited by the pitch loop in the previous tests (FIGURE 11.17 AND 11.20), it can be concluded with high degree of confidence that the pitch won't exceed any limit that will be imposed.

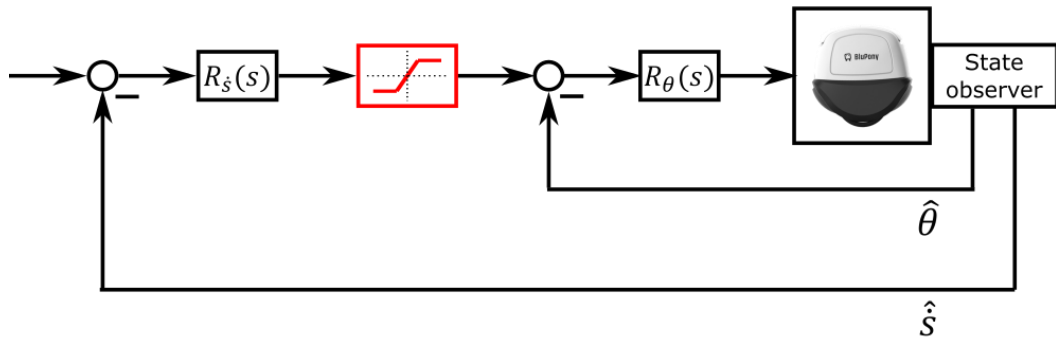


Figure 11-23 Scheme with pitch reference saturation

In order to test such method, a speed tracking test was run on R_{04} by removing the rate limiter and introducing a saturation on the pitch reference. In particular, since the rate limiter was set to $0.6 \frac{m}{s^2}$ which corresponds to a steady state angle of $\theta_{MAX} = 7.8^\circ$, a pitch reference saturation of 8° was used.

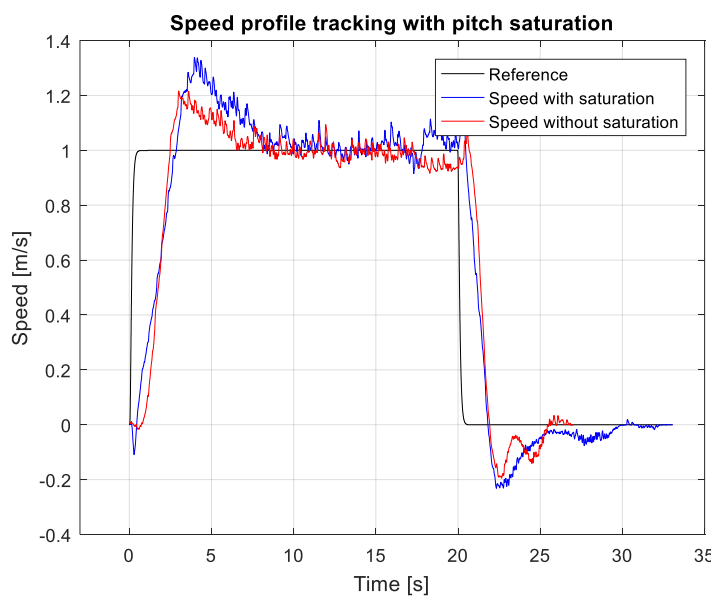


Figure 11-24 Speed profile tracking with pitch saturation

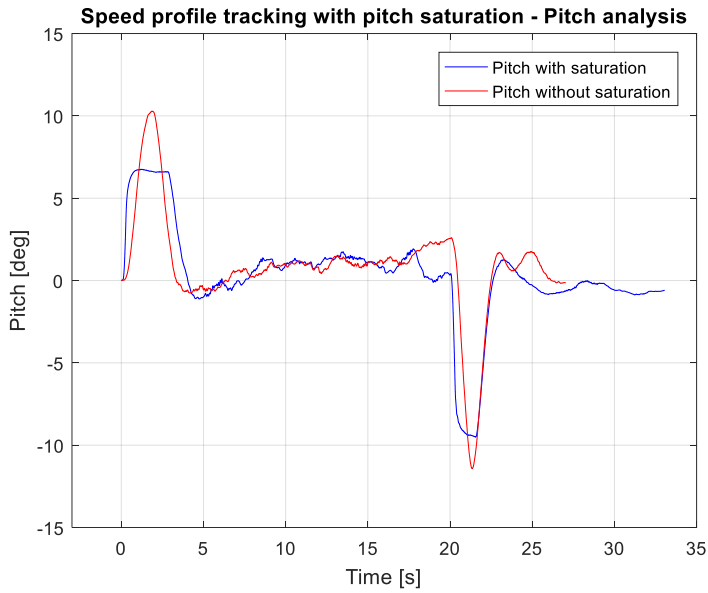


Figure 11-25 Speed profile tracking with pitch saturation – Pitch analysis

The saturated controller (blue line in FIGURE 11.24 AND 11.25) fulfilled the pitch limitation whilst granting good speed tracking capabilities.

Notice that the introduction of a saturation on the pitch reference should require the implementation of an anti-wind-up scheme for the integral action of $R_s(s)$. Such scheme would prevent potentially dangerous behaviors related to the saturation of the integral action. To understand that it is sufficient to consider the case of an emergency braking request: in this case, the integral windup of θ_R would result in a dangerous delay in the beginning of the braking phase, possibly causing the vehicle to hit an eventual obstacle. Due to lack of time, the anti-wind-up scheme was not designed nor implemented in our work. Hence, even if better speed tracking capabilities could be obtained using higher saturation values no other test was run on the vehicle for safety reasons.

11.10 Conclusions

In this Chapter a cascade approach to stabilize and drive a WIP was presented. Such approach requires the design of an inner stabilization loop based on a pitch feedback, and of an outer driving loop which tracks the speed reference signal using the pitch as a control variable. The performances of this control scheme were tested on the same test described in Chapter 10; in general, the obtained results may compete with those obtained using LQ regulators. Moreover, it was shown how the cascade approach offers a simple and reliable way of limiting the pitch angle by means of a saturation on the pitch reference signal. Finally, since the LQ regulator has shown slightly improved capabilities in the rejection of the disturbs presented by sloped roads and unbalanced loads, eventual future developments could be related to the insertion of feed forward actions in the cascade scheme in order to improve its performances in this respect.

Chapter 12 - Conclusions and Future Developments

The results obtained in this thesis project can be used to model and control a Wheeled Inverted Pendulum subjected to mass variations and operating in an urban environment. Our work was focused on a compact, electric WIP designed for last-mile parcel delivery in urban environment. All the main difficulties related to WIP while pursuing parcel delivery tasks together with the major obstacles presented by an urban environment were addressed. This chapter will summaries all the work that has been reported in this paper, starting from the considered problems, following with the adopted solutions and the obtained results. Finally, some possible future developments will be presented.

12.1 Conclusions

Our work involved two phases: model identification and controller design. The first required the use of mechanical systems modelling techniques, and of numerical assessment procedures aimed to obtain a reliable model for our specific prototype. Such model was of great importance both in the controller design phase and in the creation of a simulator to be used as a test bench for tentative controllers. In the control design phase two main approaches were investigated: first an LQ regulator, which is the most common solution in controlling WIPs, and secondly a cascade approach. The latter is less used in the literature of WIPs: on this matter we contributed by investigating the possibility of imposing constraints to the maximum allowed pitch angle.

In the following each phase of our work will be described, highlighting problems and relative solutions.

12.2 Model identification

The model identification phase was based on standard techniques. First, in Chapter 3, a system of nonlinear dynamics equations was computed using the Newton method. Such model describes the vehicle behaviour while operating in nominal conditions, i.e. without carrying loads and running on a flat surface. Contextually, it was assumed a decoupling between the longitudinal dynamics (those related to pitch and longitudinal speed) and the rotational ones (related to the yaw rate). Such assumption was based on the hypothesis that the vehicle assumes small pitch angles while turning, and proved to be valid in the testing phase on the real vehicle. Consequently, a linear model was obtained by means of a linearization around the unstable equilibrium position, which correspond to the vehicle being vertical and proceeding at any constant speed. Some considerations were made on the various input-output transfer functions; in particular, the instability of the system was assessed, together with a relation between the pitch and the speed which was useful in the following control design phase. Such relation showed a peculiar non-minimum phase structure. A numerical

assessment procedure was then applied to the obtained model; that required the direct or indirect quantification of all the measurable quantities, and the estimation of the unmeasurable ones; namely, model fitting techniques based on the minimization of the difference between measured system responses and simulated ones were used. During this phase a friction model was also introduced in order to account for all the main dissipation effects occurring on the vehicle; ad hoc experiments were used to obtain the identification of such friction model. Such model was therefore implemented in the simulator in order to achieve better correspondence of the latter with the real system, especially at low speeds.

12.3 Disturbs modelling

Chapter 4 focused on the effects of two of the most important events causing the vehicle behaviour to deviate from the nominal one: the presence of unbalanced loads and of sloped road profiles. The first is related to the type of operations that will be required to our prototype; namely, being YAPE a parcel-carrying robot, it is likely that the total mass is subjected to occasional variations as a result of the loading and unloading operations. Such variations almost inevitably affect also the c.o.g position. The modelling phase has shown how this event can be treated as an additive constant disturb acting on the measured geometrical pitch angle. The second source of disturbs has been identified in the presence of sloped road profiles, which the vehicle will have to face in an urban environment. In chapter 3 was shown how the dynamical effect of such disturb can be summarized as an additive force component opposing to the vehicle longitudinal motion. The effects of a sloped road on the equilibrium position were also investigated; in particular it was observed how the vehicle must lean forward to maintain constant or null speed on an uphill and conversely to lean backward to do the same on a downhill. Consequently, in section 8.4.5, a geometrical analysis was carried on establishing the maximum affordable slope angle, which resulted to be 12.8° (23% sloped road); such result was also compared with the values of slope provided by the Italian law for the various road elements. In sections 3.2 and 3.3 it was explained how the presence of an integral action in the speed regulator constitute a viable solution to reject both these disturbs.

12.4 Controller design, standard techniques

The second part of our work was related to the actual controller design process. The first considered approach was a Linear Quadratic Regulator, which is the most commonly used in controlling WIP vehicles. The only issue presented by such method was the choice of the weighting matrices, which was addressed in Chapter 10 by means of a normalization technique and a trial and error procedure. A set of experiments was designed to test all the requirements needed by our vehicle, namely: the ability to limit the pitch angle, the ability of tracking speed and yaw rate profiles possibly in turn-on-the-spot manoeuvres, the ability of managing unbalanced loads and the capacity of facing sloped road profiles. The LQ controller showed satisfactory results with respect to all these requirements, with the exception of the pitch limitation capabilities. In particular, the impossibility

of explicitly imposing a constraint on the maximum allowed pitch angle was delineated; in order to compensate to this deficiency, a reference filtering algorithm was introduced in Chapter 9. Such method bounds the steady state angle reached by the vehicle by imposing a limit to the maximum allowed longitudinal acceleration. Even so, large safety margins need to be left to the pitch dynamics; hence a relatively small value of maximum acceleration is imposed, thus sensibly reducing the vehicle performances.

12.5 Controller design, innovative techniques

A cascade controller was designed in Chapter 11 as an alternative to the classical LQ approach. This control scheme is based on the construction of an inner loop to stabilize and control the pitch, and an outer loop which drives the vehicle using the pitch to produce the required speed. The cascade controller was tested on the same experiments run on the LQ controller, and a comparison between the two was therefore established. The obtained results show that the cascade approach can compete with LQ regulators, with only a small reduction of the disturbance rejection capabilities. Then, in section 11.9, an innovative and simple way of limiting the pitch is introduced. Namely, thanks to the excellent performances provided by the internal loop, a constraint on the maximum allowed pitch is imposed using a saturation on the pitch reference signal produced by the speed controller. Such method produced promising results when tested on the real vehicle. As such, it could represent an important contribution to the WIP control techniques, due to the lack in the literature of simple ways of explicitly limiting the vehicle pitch angle.

12.6 Future developments

The future developments of our work are mainly related to the improvement of the proposed pitch saturation technique and to the development of feed forward actions to be added to the cascade controller in order to enhance its performances. Some of the possible developments are listed below:

12.6.1 Pitch Saturation

Pitch reference saturation technique has shown very promising results in limiting the pitch angle of a WIP whilst maintaining satisfactory speed tracking performances. However, further researches are needed in order to make this method a viable solution to be used in a real vehicle. In particular, an anti wind-up scheme has to be developed in order to avoid the occurrence of unexpected and potentially dangerous behaviours such as time delays in the speed response; such scheme should anyway provide the same rejection capabilities of the standard cascade scheme to the unbalanced load and sloped road problems.

12.6.2 Feed forward compensation of sloped roads

The ability of the vehicle of facing sloped roads is strictly related to capability of reaching the correct steady state pitch angle for each different slope. Using the cascade approach, it would therefore be possible to obtain a faster rejection of the disturb by means of the scheme presented in FIGURE 12.1

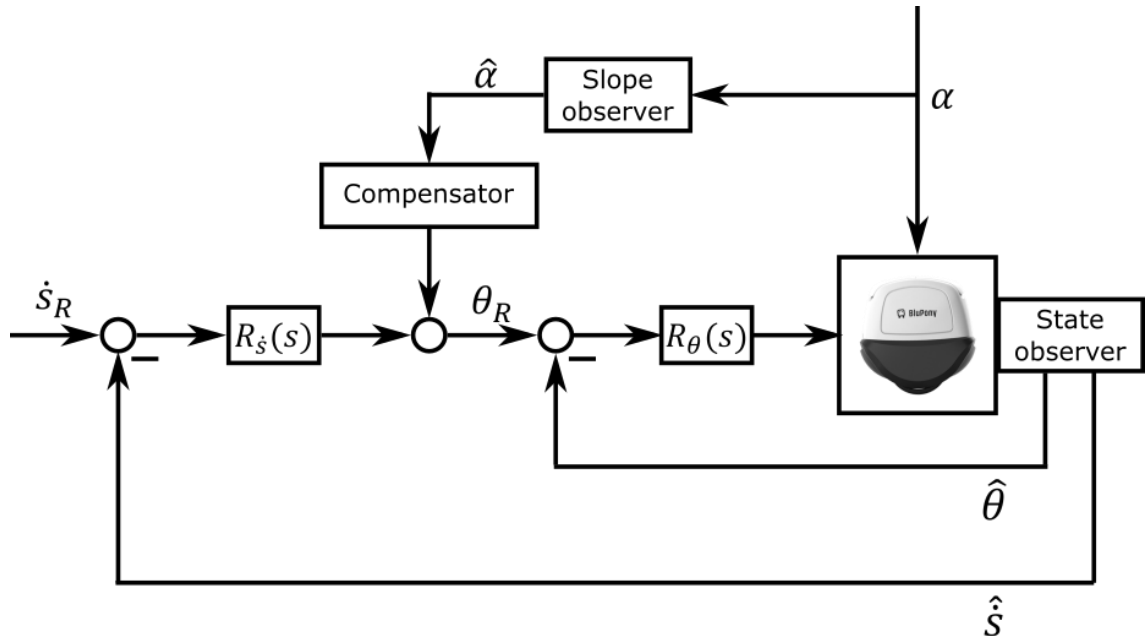


Figure 12-1 Feed forward compensation of sloped roads

As we can see in FIGURE 12.1 this would require the creation of a disturbance observer to produce an estimate of the slope angle based on measurements of the vehicle inputs and states. Once that is known, a feed forward compensation term could be computed and added to the pitch reference angle.

12.6.3 Feed forward compensation of unbalanced loads

In a similar fashion to what was just said on sloped roads, also unbalanced loads effects could be compensated by means of a feed forward action on the cascade approach. A scheme implementing such solution presented in FIGURE 12.2

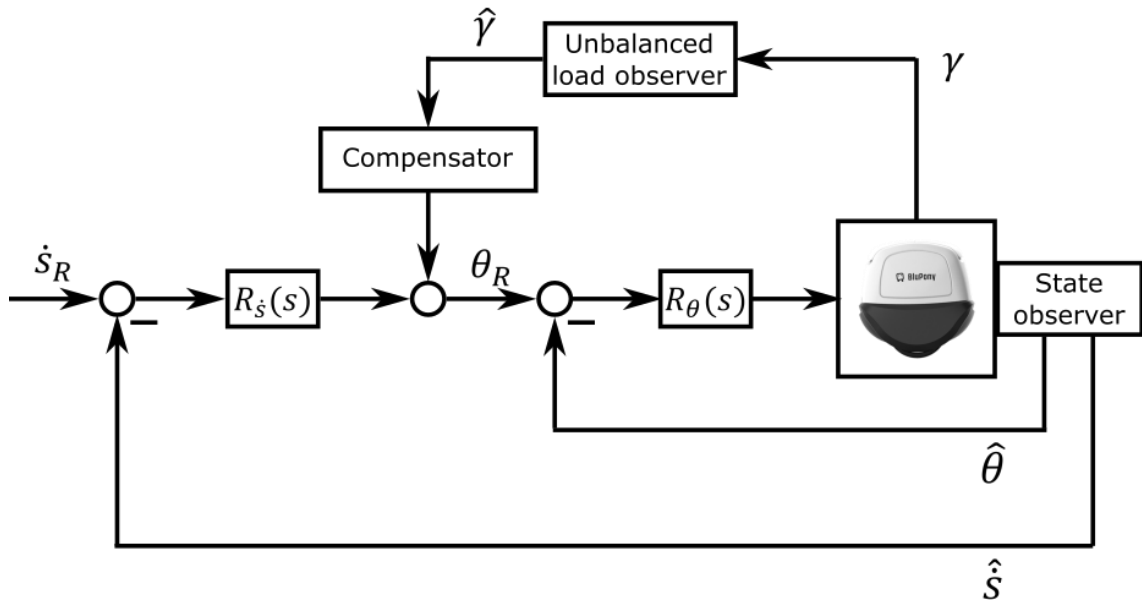


Figure 12-2 Feedforward compensation of unbalanced loads

Once again, the compensation would require the estimation of the c.o.g displacement angle, followed by the creation of a feed forward compensation term to be added to the pitch reference angle.

The efficiency of both these methods would be granted by the considerably good performances showed by the pitch control loop; in case of a less performing pitch loop the effectiveness of such actions should be further investigated.

12.6.4 Scheduled controller

The sensitivity analysis reported in Chapter 10 for the LQ regulator has shown a performance degradation when the vehicle is subjected to relevant variations in the mass and c.o.g position. Such reduction, which does not impair the stability and general speed tracking capabilities of the vehicle, suggest the possibility of creating a scheduled controller for the vehicle. Such approach, which would very easily apply to the LQ case should be further investigated using the cascade scheme. In any case, the choice of the appropriate control from a large schedule of possibilities should be based on an estimation of the mass of the loaded parcels. Such estimation could be constituted both by a direct measurement or by the output of a state observer (possibly a Kalman filter).

Bibliography

- [1] Ronald Ping Man Chan, Karl A. Stol, C. Roger Halkyard (2013). Review of modelling and control of two-wheeled robots.
- [2] Åkesson, J., Blomdell, A., & Braun, R. (2006). Design and control of YAIP – An inverted pendulum on two wheels robot. In International conference on control applications (pp. 2178–2183). Munich, Germany.
- [3] Han, J. H., Zhao, S. S., Li, J. S., & Li, H. (2008). Research on developed parallel twowheeled robot and its control system. In Proceedings of the IEEE international conference on automation and logistics (ICAL) (pp. 2471–2475). Qingdao.
- [4] Kim, Y., Lee, S.-H., & Kim, D.H. (2011). Dynamic equations of a wheeled inverted pendulum with changing its center of gravity. In 11th international conference on control, automation and systems (ICCAS), 2011 (pp. 853–854).
- [5] Lien, J., Tu, L., Ross, W., & Burvill, C. (2006). Implementation issues for an inexpensive inverted-pendulum mobile robot. In International conference on information and automation, 2006, ICIA 2006 (pp. 372–377).
- [6] Grasser, F., D'arrigo, A., Colombi, S., Ruffer, A., & Mobile, JOE: A (2002). Inverted pendulum. IEEE Transactions on Industrial Electronics, 49, 107–114.
- [7] Hu, J. S., & Tsai, M. C. (2008). Design of robust stabilization and fault diagnosis for an auto-balancing two-wheeled cart. Advanced Robotics, 22, 319–338.
- [8] Takei, T., Immura, R., & Yuta, S. (2009). Baggage transportation and navigation by a wheeled inverted pendulum mobile robot. IEEE Transactions on Industrial Electronics, 56, 3985–3994.
- [9] Alarfaj, M., and Kantor, G., 2010. Centrifugal force compensation of a two-wheeled balancing robot,” in Control Automation Robotics & Vision (ICARCV), 2010 11th International Conference on, pp. 2333-2338.
- [10] Jahaya, J., Nawawi, S. W., & Ibrahim, Z. (2011). Multi input single output closed loop identification of two wheel inverted pendulum mobile robot. In IEEE student conference on research and development (SCOReD), 2011 (pp. 138–143).
- [11] Qin, Y., Liu, Y., Zang, X., & Liu, J. (2011). Balance control of two-wheeled selfbalancing mobile robot based on TS fuzzy model. In 6th International forum on strategic technology (IFOST), 2011 (pp. 406–409).
- [12] Zhao, J.-w., & Ruan, X.-g. (2008). Research of dynamic model of flexible two-wheel upright self-balance humanoid robot. In International conference on intelligent computation technology and automation (ICICTA), 2008 (pp. 1121–1125).
- [13] Thao, N. G. M., Nghia, D. H., & Phuc, N. H. (2010). A PID backstepping controller for two-wheeled self-balancing robot. In International forum on strategic technology (IFOST), 2010 (pp. 76–81).

- [14] Nasrallah, D. S., Michalska, H., & Angeles, J. (2007). Controllability and posture control of a wheeled pendulum moving on an inclined plane. *IEEE Transactions on Robotics*, 23, 564–577.
- [15] Shiroma, N., Matsumoto, O., Kajita, S., & Tani, K. (1996). Cooperative behavior of a wheeled inverted pendulum for object transportation. In *Proceedings of the 1996 IEEE/RSJ international conference on intelligent robots and systems '96, IROS 96* (vol. 2, pp. 396–401).
- [16] Coelho, V., Liew, S., Stol, K., & Liu, G. (2008). Development of a mobile two wheel balancing platform for autonomous applications. In *15th international conference on mechatronics and machine vision in practice (M2VIP08)*. Auckland.
- [17] Kausar, Z., Stol, K., & Patel, N. (2012b). Effect of terrain inclination on performance and stability region of two wheeled mobile robots. *IJARS*.
- [18] Takahashi, Y., Ishikawa, N., & Hagiwara, T. (2001). Inverse pendulum controlled two wheel drive system. In *Proceedings of the 40th SICE annual conference. International session papers SICE 2001* (pp. 112–115).
- [19] Altpeter, (1999). Friction modelling, identification and compensation. Master thesis.
- [20] Cerkala, Jadlovska (2001). Mobile robot dynamics with friction in Simulink.
- [21] Armstrong (1988). Friction: Experimental determination, modelling and compensation.
- [22] Garcia, Gonzalez de Santos (2002). Velocity dependence in the cyclic friction arising with gears.
- [23] Kim, Kim, Kwak (2005). Dynamic Analysis of a nonholonomic two wheeled inverted pendulum robot.
- [24] P.Bolzern, R. Scattolini, N. Schiavoni, *Fondamenti di Controlli Automatici*, 4th Edition, Milan, Italy.